

WASHINGTON UNIVERSITY
SEVER INSTITUTE
SCHOOL OF ENGINEERING AND APPLIED SCIENCE
DEPARTMENT OF ENERGY, ENVIRONMENTAL, AND CHEMICAL
ENGINEERING

Hydrodynamics, back-mixing, and Mass Transfer in a Slurry Bubble Column
Reactor for Fischer-Tropsch Alternative Fuels

by

Lu Han

Prepared under the direction of Professor M. H. Al-Dahhan

A thesis presented to the Sever Institute of
Washington University in partial fulfillment of the
requirements for the degree of

DOCTOR OF SCIENCE

May 2007

Saint Louis, Missouri

SEVER INSTITUTE OF TECHNOLOGY

Doctor of Science Degree

DISSERTATION ACCEPTANCE
(To be submitted by the graduation approval deadline)

DATE: April 10, 2007

STUDENT'S NAME: LU HAN

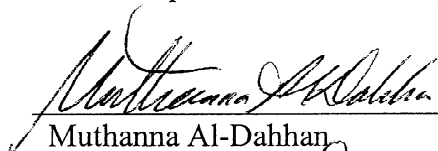
E.R.S. CODE:

This student's dissertation, entitled:

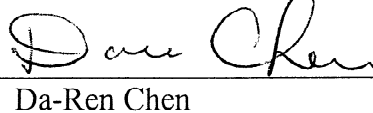
“Hydrodynamics and Mass Transfer in a Slurry Bubble Column Reactor”

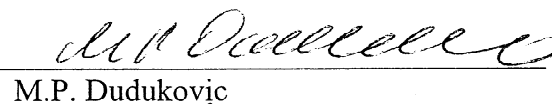
has been examined by the undersigned committee of six faculty members and has received full approval for acceptance in partial fulfillment of the requirements for the degree Doctor of Science.

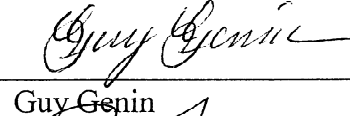
Signatures:

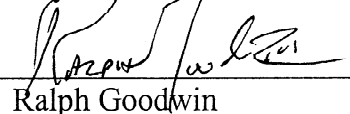

Muthanna Al-Dahhan

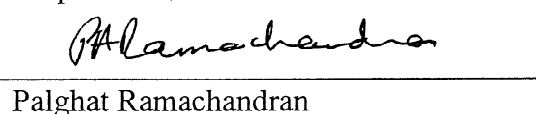
Chairman


Da-Ren Chen


M.P. Dudukovic


Guy Genin


Ralph Goodwin


Palghat Ramachandran

Distribution:

- 6 – Dissertation copies
- 1 – Candidate
- 1 – Department
- 1 – Dean's Office
- 1 – Registrar

WASHINGTON UNIVERSITY
SEVER INSTITUTE
SCHOOL OF ENGINEERING AND APPLIED SCIENCE
DEPARTMENT OF ENERGY, ENVIRONMENTAL, AND CHEMICAL
ENGINEERING

ABSTRACT

Hydrodynamics, back-mixing, and Mass Transfer in a Slurry Bubble Column Reactor
for Fischer-Tropsch Alternative Fuels

by

Lu Han

ADVISOR: Professor M. H. Al-Dahhan

May 2007

St. Louis, Missouri

As one of the alternative energy sources, Fischer-Tropsch (FT) processes convert synthesis gas into clean hydrocarbon fuels and chemicals. The slurry bubble column reactor (SBCR) is a promising reactor type for the low temperature FT process, due to its many advantages compared to other multiphase reactors. The hydrodynamics, phase mixing, and transports which may affect the reactor performance in FT SBCRs remain difficult to predict due to the complex phase interactions and flow turbulence. Experimentation is essential in obtaining and extending the knowledge of SBCRs' behavior with respect to different variables.

In an air-C₉C₁₁-FT catalyst system selected to mimic the physical properties in a real FT SBCR, this work investigated the phase holdup distribution, velocity field, and turbulence parameter profiles using computed tomography (CT) and computer automated radioactive particle tracking (CARPT) techniques. A new CT/CARPT

occurrence method was presented for three-phase CT reconstruction using single-source scans. The impact of using FT catalyst, instead of the glass beads used in the previous studies, on the hydrodynamics was quantified. Such a detailed hydrodynamics study not only provides insight into the physical behavior of SBCRs, but also serves as a benchmark with FT significance for the future computational fluid dynamics modeling.

Also investigated in the mimicked FT SBCR were the back-mixing of phases and the gas-liquid mass transfer. Significant impacts of the FT catalyst and high pressure on the back-mixing of phases were quantified using tracer techniques and various reactor models. A virtual tracer response method was developed and implemented to estimate dispersion parameters in reactor models using the CARPT data, among which the dispersion parameters in a mechanistic model were for the first time estimated. The k_{1a} values of various gas species were obtained in the same mimicked FT SBCR, using the developed optical oxygen probe and gaseous tracer techniques and selected reactor models. A square root $k_{1a} \sim D_{AB}$ relation was observed, and a k_{1a} correlation was developed based on the Higbie's penetration theory. The k_{1a} values of H_2 and CO in the mimicked FT SBCR were predicted using the developed correlation at various conditions.

Contents

List of Tables	vi
List of Figures	vii
List of Abbreviations	xii
Nomenclature	xiv
Acknowledgements	xvii
Chapter 1. Introduction	1
1.1. Motivation.....	3
1.2. Research Objectives.....	7
1.3. Structure of the Dissertation	10
Chapter 2. Background	12
2.1. Phase Holdup Profiles Investigations	13
2.2. Velocity Field and Turbulence Parameters Investigations	18
2.3. Liquid and Solids Phase Back-Mixing Investigations.....	23
2.4. Gas Phase Back-Mixing Investigations	29
2.5. Gas-Liquid Mass Transfer Investigations.....	31
Chapter 3. Hydrodynamics in the Mimicked FT SBCR	39
3.1. Scope.....	39
3.2. Selection of Three-Phase Systems.....	41
3.2.1. Gas Phase Selection.....	41
3.2.2. Liquid Phase Selection	42
3.2.3. Solids Phase Selection	42
3.3. Reactor Setup.....	43
3.4. CT Experiments	47
3.4.1. CT Setup	47
3.4.2. CT Experimental Conditions	49
3.4.3. CT Reconstruction Algorithms.....	51
3.5. CARPT Experiments	54
3.5.1. Radioactive Tracer Particles	54
3.5.2. CARPT Setup and Procedures.....	57
3.5.3. CARPT Experimental Conditions	59

3.5.4. CARPT Reconstruction Algorithm.....	60
3.6. CT/CARPT Occurrence Reconstruction Method	60
3.7. Hydrodynamic Parameters at the Main Mimicked FT Condition	62
3.7.1. Phase Holdup Distribution using Two Reconstruction Algorithms	62
3.7.2. Trajectories and Velocity Field	71
3.7.3. Velocity Probability Density Functions.....	73
3.7.4. Turbulence of the FT Catalyst Particles	75
3.8. Evaluation of Two FT Mimicking Liquids (Therminol vs. C ₉ C ₁₁)	79
3.9. Differences in Hydrodynamics using FT Catalyst and Glass Beads	83
3.10. Comparison of Three Different Systems (Air-Water-Glass Beads, Air- Therminol-Glass Beads, and Air-C ₉ C ₁₁ -FT Catalyst)	89
3.11. Comparison of the Effects of Operating Parameters on the Hydrodynamics... 93	
3.11.1. Effects of the Superficial Gas Velocity	93
3.11.2. Effects of the Operating Pressure	93
3.11.3. Effects of the Solids Loading	94
3.12. Summary.....	97
Chapter 4. Back-Mixing of Phases.....	99
4.1. Scope.....	99
4.2. Gas Phase Back-Mixing	100
4.2.1. Reactor Setup and Experimental Conditions.....	100
4.2.2. The Developed Gaseous Tracer Technique.....	101
4.2.3. Estimation of the Gas Mixing in the Distributor Plenum	105
4.2.4. Estimation of the Gas Axial Dispersion in the Reactor.....	107
4.2.5. Investigation of the Effects of Operating Parameters on Gas Phase Back- Mixing.....	110
4.2.6. Summary of the Gas Phase Back-Mixing Investigation.....	114
4.3. Liquid Phase Back-Mixing using a Virtual Tracer Response Method.....	115
4.3.1. The Developed Virtual Tracer Method.....	116
4.3.2. Parameter Estimation for the Axial Dispersion Model.....	118
4.3.3. Parameter Estimation for a Mechanistic Model	121
4.3.4. Summary of the Liquid Phase Back-Mixing Investigation	126
4.4. Solids Phase Back-Mixing using the Virtual Tracer Response Method.....	127
4.4.1. Solids Virtual Tracer Response Curves for the Transient Method.....	127
4.4.2. Sedimentation-Dispersion Model and its Parameter Fitting.....	127
4.4.3. Solids Phase Axial Dispersion in the Mimicked FT SBCR	129
4.4.4. Summary of the Solids Phase Back-Mixing Investigation	130

Chapter 5. Gas-Liquid Mass Transfer.....	131
5.1. Scope.....	131
5.2. Gas-Liquid Mass Transfer of Oxygen	132
5.2.1. Reactor Setup and Experimental Conditions.....	132
5.2.2. Optical Oxygen Probe Technique.....	134
5.2.3. Oxygen-Enriched Air Dynamic Method	137
5.2.4. Reactor Models.....	139
5.2.5. Results and Analysis.....	144
5.3. Gas-Liquid Mass Transfer of Various Species.....	146
5.3.1. Gaseous Tracer Technique for Mass Transfer Measurements	146
5.3.2. Experimental Conditions	147
5.3.3. The reactor Scale Model and k_{La} Fitting.....	148
5.3.4. Results and Analysis.....	149
5.4. A k_{La} Correlation using the Higbie Penetration Theory	151
5.5. Summary.....	156
Chapter 6. Conclusions and Recommendations	157
6.1. Summary of Conclusions.....	157
6.1.1. Investigation of the Hydrodynamics in the Mimicked FT SBCR	157
6.1.2. Investigation of the Phase Back-Mixing in the Mimicked FT SBCR	158
6.1.3. Investigation of the Mass Transfer in the Mimicked FT SBCR.....	159
6.2. Overall Presentation of the Effects of Different Variables.....	159
6.3. Recommendations for Future Work	160
6.3.1. Effects of Different Solids.....	161
6.3.2. Validation of the CT/CARPT Occurrence Reconstruction Method	161
6.3.3. Validation of the Bubble Dynamic Parameters Estimations	161
Appendix A. Additional CT/CARPT Data in the Mimicked FT SBCR.....	163
Appendix B. Operating Procedures and Technical Information of the Two	
Developed Techniques.....	182
Appendix C. Solids Axial Dispersion with a Steady State Method	188
Appendix D. Development of Two Empirical k_{La} Correlations.....	196
References.....	202
Vita.....	224

List of Tables

2-1.	Tomography studies in SBCRs.....	16
2-2.	Correlations for the liquid axial dispersion coefficient in BCRs.....	24
2-3.	Experimental studies of the liquid axial dispersion in BCRs.....	25
2-4.	Experimental studies of the solids axial dispersion.....	27
2-5.	Reported measurements of gas axial dispersion coefficient in BCRs.....	30
2-6.	Correlations for the gas axial dispersion coefficient.....	31
2-7.	Correlations for k_{1a} and k_l in BCRs or SBCRs.....	32
3-1.	Gas phase densities.....	41
3-2.	Physical properties of various liquids.....	42
3-3.	List of the CT experimental conditions.....	50
3-4.	Coordinates of the CARPT detectors.....	58
3-5.	List of the CARPT experimental conditions.....	59
3-6.	Values of the steepness factor n obtained at CT conditions.....	70
3-7.	Apparent physical properties of the pseudo- slurries.....	92
4-1.	List of gas back-mixing experimental conditions (helium tracer).....	101
4-2.	The designed four measurements for the gaseous tracer technique.....	104
4-3.	Obtained values of the liquid axial dispersion coefficient.....	120
4-4.	Obtained values of the RCFD dispersion coefficients.....	125
4-5.	Obtained values of the solids axial dispersion coefficient.....	130
5-1.	Experimental conditions of oxygen mass transfer measurements.....	133
5-2.	Properties of various tracer gases ($P=101.325$ kPa, $T=298.2$ K).....	147
5-3.	Experimental conditions of mass transfer measurements (gas tracer).....	148
5-4.	Measured k_{1a} values of CH_4 , CO_2 , and Ar with used model parameters....	150
6-1.	Overall representation of the effects of various variables.....	160
D-1.	Dimensionless numbers considered for the k_{1a} correlation development...	197
D-2.	Parameter ranges of the collected data.....	200

List of Figures

1-1.	Slurry bubble columns in different flow regimes.....	3
1-2.	Schematic structure of the work.....	10
3-1.	Schematic diagram of the reactor setup.....	44
3-2.	a). SBCR (I): 6-inch stainless steel slurry bubble column reactor (plain design); b). SBCR (II): 6-inch stainless steel slurry bubble column reactor (with ports).....	45
3-3.	Schematic diagram of the gas distributor (holes shown not to scale).....	47
3-4.	Schematic diagram of the single source CT technique.....	48
3-5.	Parylene N coated Sc particle and polypropylene ball with dimensions...	55
3-6.	3-D demonstration of the CARPT setup for the 6" SBCR.....	58
3-7.	a) Cross-sectional distributions of the gas and solids holdups using reconstruction method (I) – the CT/overall gas holdup method, air-C ₉ C ₁₁ -FT catalyst, 25% vol., 0.30 m/s, 1.0 MPa.....	65
	b) Cross-sectional distributions of the gas and solids holdups using reconstruction method (II) – the CT/CARPT occurrence method, air-C ₉ C ₁₁ -FT catalyst, 25% vol., 0.30 m/s, 1.0 MPa.....	66
3-8.	Radial profiles of the gas and solids holdups using reconstruction method (I) – the CT/overall gas holdup method, air-C ₉ C ₁₁ -FT catalyst, 25% vol., 0.30 m/s, 1.0 MPa.....	67
3-9.	Radial profiles of the gas and solids holdups using reconstruction method (II) – the CT/CARPT occurrence method, compared with results of method (I), air-C ₉ C ₁₁ -FT catalyst, 0.30 m/s, 1.0 MPa, 25% vol.....	68
3-10.	Radial profiles of the solids concentration in slurry using reconstruction method (II) – the CT/CARPT occurrence method, compared with results of method (I), air-C ₉ C ₁₁ -FT catalyst, 0.30 m/s, 1.0 MPa, 25% vol.....	69
3-11.	Lagrangian trajectories and a 2-D velocity vector map, air-C ₉ C ₁₁ -FT Catalyst, 0.30 m/s, 25% vol., 1.0 MPa.....	72
3-12.	Radial profiles of the solids velocities in three directions, air-C ₉ C ₁₁ -FT Catalyst, 0.30 m/s, 25% vol., 1.0 MPa.....	73
3-13.	PDFs of instantaneous solids velocities in three directions, air-C ₉ C ₁₁ -FT Catalyst, 0.30 m/s, 25% vol., 1.0 MPa.....	75
3-14.	Radial profiles of the stresses, air-C ₉ C ₁₁ -FT Catalyst, 0.30 m/s, 25%	

	vol., 1.0 MPa.....	77
3-15.	Radial profiles of the TKE, air-C ₉ C ₁₁ -FT Catalyst, 0.30 m/s, 25% vol., 1.0 MPa.....	78
3-16.	Radial profiles of the eddy diffusivities, air-C ₉ C ₁₁ -FT Catalyst, 0.30 m/s, 25% vol., 1.0 MPa.....	79
3-17.	Effects of the two liquids on the gas holdup radial profiles, air-Therminol vs. air-C ₉ C ₁₁ , 0.20 m/s, AARD=1% at 0.1 MPa, AARD=7% at 1.0 MPa.....	80
3-18.	Effects of the two liquids on gas holdup radial profiles, method (I), air-Therminol vs. air-C ₉ C ₁₁ , 0.30 m/s, AARD=3% at 0.1 MPa, AARD=2% at 1.0 MPa.....	80
3-19.	Effects of the two liquids on gas holdup radial profile, method (I), air-Therminol-FT catalyst vs. air-C ₉ C ₁₁ -FT catalyst, 0.30 m/s, 25% vol., AARD=6% at 0.1 MPa, AARD=5% at 1.0 MPa.....	81
3-20.	Effects of the two liquids on solids velocity and turbulence parameters, air-C ₉ C ₁₁ -FT Catalyst vs. air-Therminol-FT Catalyst, 0.30 m/s, 25% vol., 1.0 MPa.....	83
3-21.	Gas holdup radial profiles using FT catalyst and glass beads, method (I).....	85
3-22.	Differences of FT catalyst and glass beads in the resulting solids velocities and turbulence parameters, air-Therminol-FT Catalyst vs. air-Therminol-glass beads, 0.30 m/s, 25% vol., 1.0 MPa.....	87
3-23.	Comparison of the gas holdup in three systems (method I) - air-water-glass beads, air-Therminol-glass beads, and air-C ₉ C ₁₁ -FT catalyst, 0.30 m/s, 1.0 MPa, 9.1% vol.....	89
3-24.	Comparison of the gas holdup in three systems (method I) - air-water-glass beads, air-Therminol-glass beads, and air-C ₉ C ₁₁ -FT catalyst, 0.30 m/s, 0.1 MPa, 9.1% vol.....	90
3-25.	Comparison of the velocity and turbulence parameters in three different systems - air-water-glass beads, air-Therminol-glass beads, and air-C ₉ C ₁₁ -FT catalyst, 0.30 m/s, 9.1% vol., 1.0 MPa.....	92
3-26.	Effects of the solids loading on gas holdup radial profiles, method (I), air-C ₉ C ₁₁ -FT catalyst, 0.20 m/s, 1.0 MPa.....	96
3-27.	Effects of the solids loading on gas holdup radial profiles, method (I), air-C ₉ C ₁₁ -FT catalyst, 0.30 m/s, 1.0 MPa.....	96
3-28.	Effects of the solids loading on gas holdup radial profiles, method (I), air-C ₉ C ₁₁ -FT catalyst, 0.20 m/s, 0.1 MPa.....	96

3-29.	Effects of the solids loading on gas holdup radial profiles, method (I), air-C ₉ C ₁₁ -FT catalyst, 0.30 m/s, 0.1 MPa.....	97
3-30.	Effect of the solids loading on the holdup radial profiles, method (I), air-Therminol-FT catalyst, 0.30 m/s, 1.0 MPa.....	97
4-1.	Facilities of the gaseous tracer technique.....	102
4-2.	Schematic diagram of the gaseous tracer technique and the reactor setup.....	102
4-3.	Diagram of the convolution and model fits of the response curves.....	105
4-4.	Dynamic gas tracer concentration at the distributor with CSTR model fit.....	107
4-5.	Gas tracer response curves at the outlet with ADM fit (Bubbly flow).....	109
4-6.	Gas tracer response curves at the outlet with ADM fit (Churn-turbulent flow).....	109
4-7.	Effects of the superficial gas velocity and solids loading on the gas phase axial dispersion coefficient and Peclet number.....	111
4-8.	Effects of the operating pressure on the gas dispersion coefficient and Peclet number.....	114
4-9.	Schematic diagram of the injection/sampling levels (in the application to the ADM) and the extracted tracer response curves.....	118
4-10.	Virtual tracer response curves of liquid flow fitted with the ADM.....	120
4-11.	Schematic diagram of the RCFD model with its parameters.....	122
4-12.	Schematic diagram of the virtual tracer injection and sampling positions in the RCFD model.....	123
4-13.	Iteration process for the three-parameter fitting.....	124
4-14.	Virtual tracer response curves of liquid fitted with the RCFD model.....	125
4-15.	Virtual tracer response curves of solids flow fitted with the transient SDM.....	128
5-1.	Experimental setup of the optical oxygen probe in the SBCR.....	133
5-2.	Optical oxygen probe system (Ocean Optics, Inc.).....	134
5-3.	Working mechanism of the optical oxygen probe.....	135
5-4.	Schematic diagram of the optical oxygen probe calibration	136
5-5.	Optical oxygen probe calibration curve fitted by Equation 5-2.....	137
5-6.	Comparisons of the CSTR model, ADM, RCFD model in k_{a} measurements.....	144

5-7.	Effects of the superficial gas velocity and solids loading on oxygen k_{1a} ...	145
5-8.	Effects of the operating pressure on oxygen k_{1a}	146
5-9.	Response curves of various tracer gases.....	149
5-10.	Plots of the k_{1a} values estimated using Equation 5-14 vs. k_{1a} data.....	151
5-11.	Predicted k_{1a} values using the correlation vs. experimental data.....	154
5-12.	Predictions of H_2 k_{1a} in the mimicked FT SBCR using the correlation developed based on the Higbie penetration theory.....	155
5-13.	Predictions of CO k_{1a} in the mimicked FT SBCR using the correlation developed based on the Higbie penetration theory.....	156
A-1.	u_g effects on the phase holdups, air- C_9C_{11} , 0.1 MPa, 0.20 m/s vs. 0.30 m/s, method (I).....	164
A-2.	u_g effects on the phase holdups, air- C_9C_{11} , 1.0 MPa, 0.20 m/s vs. 0.30 m/s, method (I).....	164
A-3.	u_g effects on the phase holdups, air-Therminol, 0.1 MPa, 0.20 m/s vs. 0.30 m/s, method (I).....	165
A-4.	u_g effects on the phase holdups, air-Therminol, 1.0 MPa, 0.20 m/s vs. 0.30 m/s, method (I).....	165
A-5.	u_g effects on the phase holdups, air- C_9C_{11} -FT catalyst, 9.1% vol., 0.1 MPa, 0.20 m/s vs. 0.30 m/s, method (I).....	166
A-6.	u_g effects on the phase holdups, air- C_9C_{11} -FT catalyst, 25% vol., 0.1 MPa, 0.20 m/s vs. 0.30 m/s, method (I).....	166
A-7.	u_g effects on the phase holdups, air- C_9C_{11} -FT catalyst, 9.1% vol., 1.0 MPa, 0.20 m/s vs. 0.30 m/s, method (I).....	167
A-8.	u_g effects on the phase holdups, air- C_9C_{11} -FT catalyst, 25% vol., 1.0 MPa, 0.20 m/s vs. 0.30 m/s, method (I).....	168
A-9.	u_g effects on the phase holdups, air-Therminol-FT catalyst, 25% vol., 1.0 MPa, 0.20 m/s vs. 0.30 m/s, method (I).....	168
A-10.	Pressure effects on the phase holdups, air- C_9C_{11} , 0.20 m/s, 0.1 MPa vs. 1.0 MPa, method (I).....	169
A-11.	Pressure effects on the phase holdups, air- C_9C_{11} , 0.30 m/s, 0.1 MPa vs. 1.0 MPa, method (I).....	170
A-12.	Pressure effects on the phase holdups, air-Therminol, 0.20 m/s, 0.1 MPa vs. 1.0 MPa, method (I).....	170
A-13.	Pressure effects on the phase holdups, air-Therminol, 0.30 m/s, 0.1 MPa vs. 1.0 MPa, method (I).....	170

A-14.	Pressure effects on the phase holdups, air-C ₉ C ₁₁ -FT catalyst, 9.1% vol., 0.20 m/s, 0.1 MPa vs. 1.0 MPa, method (I).....	171
A-15.	Pressure effects on the phase holdups, air-C ₉ C ₁₁ -FT catalyst, 25% vol., 0.20 m/s, 0.1 MPa vs. 1.0 MPa, method (I).....	172
A-16.	Pressure effects on the phase holdups, air-C ₉ C ₁₁ -FT catalyst, 9.1% vol., 0.30 m/s, 0.1 MPa vs. 1.0 MPa, method (I).....	172
A-17.	Pressure effects on the phase holdups, air-C ₉ C ₁₁ -FT catalyst, 25% vol., 0.30 m/s, 0.1 MPa vs. 1.0 MPa, method (I).....	173
A-18.	Pressure effects on the phase holdups, air-Therminol-FT catalyst, 25% vol., 0.30 m/s, 0.1 MPa vs. 1.0 MPa, method (I).....	174
A-19.	u_g effects on the solids velocity and turbulence parameters, air-C ₉ C ₁₁ -FT Catalyst, 25% vol., 1.0 MPa, 0.20 m/s vs. 0.30 m/s.....	176
A-20.	u_g effects on the liquid velocity and turbulence parameters, air-C ₉ C ₁₁ , 1.0 MP, 0.20 m/s vs. 0.30 m/s.....	177
A-21.	Pressure effects on the solids velocity and turbulence parameters, air-C ₉ C ₁₁ -FT Catalyst, 0.30 m/s, 25% vol., 0.1 MPa vs. 1.0 MPa.....	180
A-22.	Pressure effects on the liquid velocity and turbulence parameters, air-C ₉ C ₁₁ , 0.30 m/s, 0.1 MPa vs. 1.0 MPa.....	181
C-1.	Axial distribution (gradient) of the solids occurrences by CARPT.....	190
C-2.	Asymptotic values of the six virtual tracer response curves.....	190
C-3.	Axial gradient of the solids concentration obtained from CARPT occurrences, with steady state SDM fit.....	192
C-4.	Axial gradient of the solids concentration calculated (with arbitrary adjustments) from the asymptotic values of the virtual tracer response curves, with steady state SDM fit.....	192
C-5.	Solids concentration axial gradients in the mimicked FT SBCR compared with the Rados (2003) Cs correlation.....	194
D-1.	Architecture of a neural network model with layers (Cloutier et al., 1996).....	199
D-2.	Plot of predictions by the ANN k_{ia} correlation vs. data	200
D-3.	Plot of predictions by the power law k_{ia} correlation vs. data.....	201

List of Abbreviations

AARD	Average absolute relative difference
AARE	Average absolute relative error
ADM	Axial dispersion model
BCR	Bubble column reactor
CARPT	Computer automated radioactive particle tracking
CFD	Computational fluid dynamics
CFMSR	Cross flow multistage stirred reactor
CREL	The chemical reaction engineering laboratory (Washington University)
CSTR	Continuous stirred tank reactor
CT	Computed tomography
DO	Dissolved oxygen
DWT	Discrete wavelet transformation
EIT	Electrical-impedance tomography
ECT	Electrical capacitance tomography
FT	Fischer-Tropsch
GDT	Gamma-densitometry tomography
LDA	Laser Doppler anemometry
LT-FT	Low temperature Fischer-Tropsch
MCM	Multi-cell model
MURR	University of Missouri Research Reactor
PDF	Probability density function
PEPT	Positron-emitting particle tracking
PIV	Particle image velocimetry
PMT	Photomultiplier tube
PPS	Perforated plate with small holes (sparger name)
PPL	Perforated plate with large holes (sparger name)
PPH	Perforated plate with huge holes (sparger name)
PPN	Perforated plate with non-evenly distributed holes (sparger name)

PVC	Polyvinyl chloride
PFR	Plug flow reactor
RCFD	Recirculation and cross flow with dispersion (the mechanistic model)
RPT	Radioactive particle tracking
RTD	Residence time distribution
SBCM	Single bubble class model
SBCR	Slurry bubble column reactor
SCFH	Standard cubic feet per hour
SDM	Sedimentation dispersion model
TBCM	Two bubble class model
TCD	Thermal conductivity detector
TKE	Turbulent kinetic energy
TLD	Trajectory length distribution
UCT	Ultrasonic computed tomography

Nomenclature

a	Specific surface area, m^2/m^3
c	Constant in the holdup radial profile correlations, dimensionless
C_D	Drag coefficient, dimensionless
C_g	Concentration of a specie in the gas phase, mol/m^3
C_{inj}	Gas tracer injection concentration, mol/m^3
C_l	Concentration of a specie in the liquid phase, mol/m^3
$C_{l,0}^*$	DO concentration in liquid saturated by air, mol/m^3
$C_{l,1}^*$	DO concentration in liquid saturated by the oxygen-enriched air, mol/m^3
C_s	Solids concentration in gas-free slurry (by volume), m^3/m^3
d_c	Column diameter, m
d_b	Bubble diameter, m
d_{b0}	Initial bubble size at sparger, m
d_{be}	Equilibrium bubble diameter, m
d_{bm}	Geometric mean bubble diameter, m
d_{bs}	Sauter mean bubble size, m
d_p	Particle diameter, m
D	Dispersion coefficient, m^2/s
D_{AB}	Gas diffusivity, m^2/s
g	Gravity, m/s^2
H	Henry's constant, dimensionless
k	Turbulent kinetic energy, m^2/s^2
k_l	Liquid side mass transfer coefficient, m/s
$k_{l\alpha}$	Volumetric gas-liquid mass transfer coefficient, 1/s
K_{sensor}	Sensor constant of the probe, 1/s
L	Length of reactor bed (dynamic height), m
n	Steepness factor of radial profiles, dimensionless
N_p	Particle occurrence density, counts/m^3
N_s	Solids particle occurrence, counts

P	Pressure, Pa
Pe	Peclet number, $Pe = u_g L / \varepsilon_g D_g$, dimensionless
P_s	Raw count of the solids tracer particle, counts
Q_g	Gas flow rate, m^3/s
r	Radial position, m
r'	Liquid velocity inversion point, m
r''	Gas velocity inversion point, m
R	Reactor radius, m
$R_{k,ij}$	Relative attenuation, dimensionless
t	Time, s
t_e	Exposure time in the Higbie penetration theory, s
t_∞	Asymptotic time in the virtual tracer response curves, s
T	Temperature, °C
u_b	Bubble rise velocity, m/s
u_{br}	Rise velocity of a swarm of bubbles, m/s
u_{bt}	Terminal bubble rise velocity, m/s
u_g	Superficial gas velocity, m/s
$u_{l,c}$	Liquid circulation velocity, m/s
$u_l(0)$	Liquid centerline velocity, m/s
$u_s(0)$	Solids centerline velocity, m/s
$u_{z,0}$	Axial velocity at the center, m/s
$u_{z,w}$	Axial velocity near the wall, m/s
u_{st}	Settling velocity of solids, m/s
V	Volume of a phase, m^3
z	Axial distance along the column, m

Greek Symbols

α	Constant of the d_{bm}/u_{bt} ratio, dimensionless
δ	Sparger hole diameter, m
ε	Phase holdup, m^3/m^3
θ	Azimuthal angle, °

μ	Viscosity, Pa·s
	Specific γ -ray attenuation coefficient, m ³ /kg
ϕ_p	Particle porosity, dimensionless
ϕ_s'	Volume fraction of the solid material in the packed space, dimensionless
ρ	Phase density, kg/m ³
σ	Surface tension, N/m
τ	Stress tensor/component, m ² /s ²
τ_0	Retention time in the CSTR model, s

Subscripts and Superscripts

a	Distributor zone (in the RCFD model)
b	Disengagement zone (in the RCFD model)
d	Downward-flowing zone (in the RCFD model)
D	Dynamic method
Exp	Experimental data
g	Gas phase
(i)~(iv)	Measurement in the gaseous tracer technique
in	Reactor inlet
l	Liquid phase
Mod	Model simulation
out	Reactor outlet
p	Particle
s	Solids phase
sensor	Signal with sensor delay
sl	Slurry (liquid + solids)
S	Steady state method
u	Upward-flowing zone (in the RCFD model)
w	Values at reactor wall
*	Convoluted parameters
	Equilibrium concentrations

Acknowledgements

I wish to express my deep gratitude to my advisor, Professor Muthanna Al-Dahhan, for his directions and advice on my research during these years. He has constantly supported new ideas and given encouragement with great enthusiasm in the chemical engineering field. His hard-working and energetic attitude always became a driving force for me, when I faced challenges.

I sincerely thank Professor Mike Duduković, Director of the CREL, for the useful suggestions and comments on my work. His supervision with high standards and profound insights drove this work towards higher quality in a catalytic manner. Also, I benefited much from the great opportunities he brought to me, from which I obtained valuable industrial exercises.

I appreciate the committee members, Professor P. A. Ramachandran, Professor Da-Ren Chen, Professor Guy Genin from Department of Mechanical & Aerospace Engineering, and Dr. Ralph Goodwin of ConocoPhillips for investing their time in examining this dissertation and providing useful comments.

I gratefully acknowledge the financial support by the members of the High Pressure Slurry Bubble Column (HPSBC) Consortium, which are ConocoPhillips (USA), EniTecnologie (Italy), Sasol (South Africa), and Statoil (Norway). This fund provided us financial capability to realize important research plans. I thank University of Missouri Research Reactor Center (MURR) and Matthew Sanford for their patient help in evaluating the feasibility and eventually irradiating the scandium tracer particles needed for CARPT, with special difficulties from the small particle size.

I would like to thank the secretaries of Department of Energy, Environmental, and Chemical Engineering. Their work and help often expedite necessary procedures. I also

thank Steve Picker for resolving technical problems during the experiments. I appreciate Professor James Ballard at the Engineering Technical Writing Center, who kindly spent time with me going through my publications and dissertation. Those many discussions with him for linguistic precision were helpful and enjoyable.

The CREL graduate students and researchers have offered help and ideas. I learned CT and CARPT from Ashfaq Shaikh and Huping Luo. And the CT/CARPT experiments were conducted with the help of Chengtian Wu, who went through frustrations with me during these tough experiments. Other CREL friends include Peng Chen, Junli Xue, Jing Guo, Shaibal Roy, Huping Luo, Satish Bhusarapu, R.C. Ramaswamy, Mehul Vesvikar, Rajneesh Verma, Debangshu Guha, Radmila Jevtic, Subramanya Nayak, Zeljko Kuzeljevic, Prashant Gunjal, Fadha Ahmed, and many others. I feel it was a privilege to work with this group of talented colleagues at the CREL.

I can not thank enough for the unconditional support and encouragement from my parents and sister, who never doubted me even at times that I doubted myself.

I owe my wife, Yang, for the gift of laughter during the years of my study, as well as her great support that is beyond spousal duty. If there is any, the secret of this doctoral work is within the numerous wonderful meals she made and often brought to the work for me.

Lu Han

Washington University

St. Louis, Missouri

May, 2007

Chapter 1

Introduction

While the world's proven petroleum reserves are being depleted, the total crude oil consumption rate is increasing each year. There is an urgent need to develop clean, alternative energy routes to ensure the nation's sustainable development and energy security. Among various sources of alternative energy, Fischer-Tropsch (FT) synthesis is a catalytic reaction that converts synthesis gas (syngas, a mixture of hydrogen and carbon monoxide) generated from natural gas, coal, or biomass into clean hydrocarbons and chemicals. Historically, industrial interest in FT processes for production of alternative fuels has experienced several surges since the joint invention of the basic process by Franz Fischer and Hans Tropsch in the 1920s. Due to the increasing cost of crude oil and increased energy needs, FT synthesis has again attracted great industrial attention as a means to produce transportable hydrocarbon fuels. The reactor choices for FT processes include fixed bed reactors, fluidized bed reactors, circulating fluidized bed reactors, and slurry bubble column reactors (SBCRs) (Steynberg, 2004). The SBCR is a promising reactor type for the low temperature

Fischer-Tropsch (LT-FT) (220~250C°) process to produce clean diesel or aviation fuel, which is the energy source for large vehicles and aircraft.

Slurry bubble column reactors are three-phase gas-liquid-solids systems in which the gas is sparged as bubbles via a distributor (sparger) into a liquid with suspended fine particles (solids). The gas phase typically contains soluble reactant components, while the liquid phase is usually the product and/or reactant (with inert components in some cases). The solids phase is typically catalyst particles, generally in sizes ranging between 5-150 μm (Krishna et al., 1997), whose presence distinguishes SBCRs from two-phase gas-liquid bubble column reactors (BCRs). SBCRs (and BCRs) are operated in either the semi-batch mode (zero slurry flow) or the continuous mode (co-current or counter-current with respect to the gas flow). In the continuous mode, the superficial slurry velocity is significantly (at least one order of magnitude) lower than the superficial gas velocity. Momentum is transferred from the fast rising gas phase to the slurry via interfacial forces, providing energy for the liquid and solids mixing. Depending on the operation and design parameters, SBCRs (and BCRs) can be operated in the bubbly (homogeneous) flow regime, churn-turbulent (heterogeneous) flow regime, or slug flow regime (which can occur in small diameter columns and is usually not desirable) (Figure 1-1). Flow regimes of SBCRs or BCRs are characterized by different bubble dynamics, which in turn determines different reactor behaviors in the phase mixing and transports.

Compared to other multiphase reactors (e.g., stirred tanks, packed beds, or trickle beds), SBCRs have various advantages, including excellent heat and mass transfer, simple construction, and ease of operation. Hence, SBCRs have been widely employed in the chemical, petroleum, and biochemical industries, including gas conversion processes such as Fischer-Tropsch synthesis of liquid hydrocarbons as mentioned earlier and liquid phase synthesis of methanol (Parkinson, 1997; Dudukovic et al., 1999; Krishna and Sie, 2000). One of the disadvantages of SBCRs is significant phase back-mixing due to global recirculation and local turbulent dispersion, which may cause lower

conversion and therefore lower volumetric productivity (Deckwer, 1991; Krishna et al., 1997; Dudukovic et al., 1999).

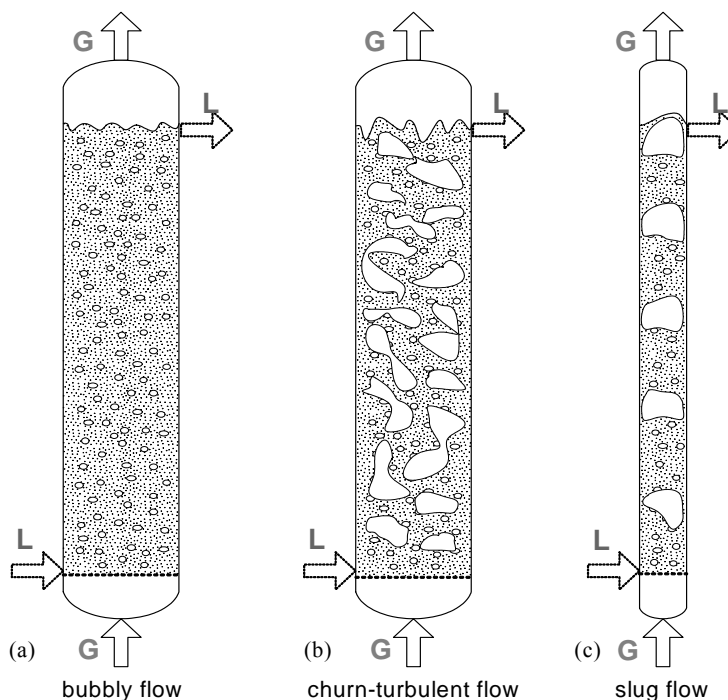


Figure 1-1. Slurry bubble columns in different flow regimes

In order to reduce the capital cost while pursuing high productivity, large SBCRs with diameters in 5~10 meters and high solids loading (typically 30~40% by volume) have been employed for FT processes. These reactors are operated at high pressure (typically 1~8 MPa) for increased reactant concentration. To achieve high throughput and to suspend the catalysts, FT SBCRs are usually operated at high superficial gas velocities (up to 0.50 m/s) in the churn-turbulent flow regime (Steynberg, 2004).

1.1. Motivation

Although the structure of SBCRs is simple, the design and scale-up of these reactors for FT processes are not. The hydrodynamics and phase mixing in the churn-turbulent

flow regime are much more complicated than those in the bubbly flow regime due to the intense phase interactions and turbulence (Xue, 2004). Since the reaction time in a SBCR is usually shorter than or comparable to the flow macro-mixing time, many processes are strongly affected by phase mixing. Reactor performance prediction of SBCRs requires thorough understanding of how the hydrodynamics, phase mixing, and transports in these reactors are affected by the reactor design (i.e., geometry), phase physical properties, and operating conditions. Experimentation is essential in obtaining and extending knowledge of SBCRs' behaviors with respect to different variables. Based on reproducible experimental evidence of the flow mixing and phase distribution, theoretical and mechanistic methods can be constructed for easier reactor performance prediction of SBCRs and for their successful design and scale-up.

The three-phase system in a real FT SBCR consists of syngas, hydrocarbon mixture liquid (FT wax), and FT catalyst fine particles. As mentioned earlier, a FT SBCR is operated at high pressure, high gas velocity, and high solids loading. However, the majority of the previous studies in SBCRs were limited to ambient conditions and materials that are relatively easier to obtain and to work with (typically air, water, and glass beads) instead of those that can mimic the actual process properties. Although some studies used systems of FT interest (Inga and Morsi, 1998; Behkish et al., 2000; Krishna and van Baten, 2003; etc.), their measurements were limited to overall parameters. In the last decade, the hydrodynamics in SBCRs has been investigated in more detail in a limited number of studies using tomography techniques, such as γ -ray computed tomography (CT) (Rados et al., 2005a; Rados, 2003; and Shaikh, 2007), and flow tracking techniques, such as the computer automated radioactive particle tracking (CARPT) (Rados et al., 2005b; Rados, 2003; and Shaikh, 2007). The hydrodynamics in an air-water-glass beads system was studied by Rados (2003), followed by studies in an air-Therminol-glass beads system used by Shaikh (2007), providing important measurements such as the solids flow field, turbulence parameters profiles, and phase holdup distribution. However, both of these two studies used 150 μm glass beads as the solids phase, which have different sizes, density, and shape characteristics than a

typical FT catalyst. Due to the lack of experimental evidence at industrial process conditions, there is a need for experimental studies in a system that closely mimics the physical properties in FT SBCRs. In particular, the differences in the hydrodynamics resulting from using the FT catalyst instead of glass beads need to be quantified. Such a detailed hydrodynamic study will not only provide insight into the physical behaviors of mimicked FT SBCRs via experimentation, but will also serve as a benchmark for future computational fluid dynamics (CFD) modeling. Since the multiphase turbulent models and interfacial closures heavily rely on empirical correlations, such data are essential in the evaluation, tuning, and validation of CFD models with FT interest.

Various reactor scale models have been used and reported for performance prediction in SBCRs. In FT reactor modeling, the gas phase is generally simulated using the plug flow assumption, with dispersion (back-mixing) being neglected (Stern et al., 1983; van Vuuren and Heydenrych, 1985; Herbolzheimer and Iglesia, 1994; Hedrick and Chuang, 2003; Song et al., 2003; etc.). In several other studies which did consider the back-mixing of gas phase in SBCRs (Stern et al., 1985a and 1985b; Turner and Mills, 1990; Mills et al., 1996; Rados et al., 2003), the gas dispersion coefficient values were obtained either using liquid dispersion coefficient correlations or from two-phase BCR gas dispersion studies. By doing this, these studies assumed that the gas phase back-mixing is the same as the liquid phase and neglected the solids' effect on the gas phase dispersion coefficient. Since adding solids may significantly change the hydrodynamics and phase back-mixing in SBCRs, the poorly understood effect of solids loading on the gas phase back-mixing needs to be investigated.

For liquid phase mixing, the most frequently used reactor models include the continuous stirred tank reactor (CSTR) (van der Laan et al., 1999; Song et al., 2003; Wang et al., 2004; Ahon et al., 2005), plug flow reactor (PFR) (Hedrick and Chuang, 2003), axial dispersion model (ADM) (Mills et al., 1996; de Swart et al., 2002; Rados et al., 2003), and multi-cell model (tanks in series) (MCM) (Leib et al., 1995). However, the assumptions underlying these reactor models are not based on the

physics of SBCRs or on the observed macro-scale flow pattern in the columns, and therefore application of these models warrants caution. Myers (1986) and Myers et al. (1987) proposed a two-region phenomenological model, the slug and cell model, for the liquid mixing in churn-turbulent bubble columns. This model can describe essentially the same liquid mixing behavior as the ADM. Several parameters in this model were determined based on the physics, and one parameter, the exchange between the slugs and the cells, was estimated using mixing experiments. A mechanistic model, namely the recirculation and cross flow with dispersion (RCFD) model, was developed by Degaleesan et al. (1996) and Degaleesan et al. (1997) for the liquid phase, which was then improved and extended by Gupta et al. (2001) and Gupta et al. (2002) for both phases with a dual bubble classes assumption. In this RCFD model, the liquid (slurry) phase recirculates by flowing upwards in the cylindrical zone at the center and flowing downwards in the annular zone near the wall, and turning over in the two end zones, the distributor zone and the disengagement zone. This mechanistic model is based on the observed flow pattern and hydrodynamic parameters, and hence is expected to be more reliable in predicting the phase mixing in BCRs or SBCRs. However, the application of this model has been limited partially due to the absence of estimations of the axial and radial dispersion parameters. Therefore, there is a need to develop a methodology to estimate these parameters in the mechanistic model at operating conditions of industrial FT interest.

The gas-liquid mass transfer, in particular the liquid side gas-liquid mass transfer, is often the limiting step in the overall mass transfer for many industrial processes in BCRs or SBCRs. Although the mass transfer may not be controlling in some cases, volumetric gas-liquid mass transfer is reduced significantly in larger columns (Vandu and Krishna, 2004) and becomes a concern during reactor design and scale-up. A number of mass transfer studies have been conducted in SBCRs (Dewes et al., 1995; Yang et al., 2001; Han et al., 2003; Vandu and Krishna, 2003 and 2004; Ruthiya et al., 2006; etc.). However, the majority of the available data is at ambient conditions, using glass beads, and/or for oxygen only, and much less measurements have been conducted

for various species in a system that has similar physical properties to FT SBCRs (Miller et al., 1990; Behkish et al., 2000; Yang et al., 2001; etc.). More importantly, no mass transfer studies have been performed in a three-phase system with measured or known profiles of hydrodynamic parameters. It may be difficult to understand the underlying mass transfer phenomena in SBCRs without knowing the hydrodynamics, phase mixing, and holdup distribution. Therefore, to help understand the underlying phenomena of mass transfer between gas and liquid phases, it is of importance to perform mass transfer measurements at the same conditions (of FT interest), at which the profiles of hydrodynamic parameters are measured by other techniques.

1.2. Research Objectives

The overall objective of this work is to advance the understanding of the hydrodynamics, mixing of phases, and gas-liquid mass transfer in a high-pressure slurry bubble column that mimics the physical properties in FT SBCRs, using real FT catalyst particles and appropriate solvents at selected operating conditions. In order to achieve this overall objective, this work is divided into several related sections, including the investigations of reactor hydrodynamics, phase back-mixing, and gas-liquid mass transfer.

1) Investigation of the Hydrodynamics in the Mimicked FT SBCR

This section includes the following:

- Three phase systems need to be selected to mimic the physical properties in industrial FT SBCRs. The CARPT technique is to be extended to the mimicked FT systems, with a new challenge to manufacture and handle small tracer particles to track the small FT catalyst particles. The single-source CT will be applied to the three-phase mimicked FT SBCR using the CT/Overall gas holdup reconstruction method proposed by Rados (2003). As an alternative, a new CT reconstruction method using CARPT occurrence data at the same CT conditions is to be developed and presented.

- Due to the change of liquids from Therminol in Shaikh (2007) to C_9C_{11} in this work (physical properties of which both mimic the FT wax at FT conditions), differences in the hydrodynamics using the two liquids are to be examined. The impacts of using the FT catalyst instead of glass beads on the hydrodynamics in the mimicked FT SBCR are to be quantified. The effects of operating conditions (superficial gas velocity, operating pressure, and solids loading) on the hydrodynamics in the mimicked FT SBCR will be investigated and compared with those in the air-water-glass beads and air-Therminol-glass beads systems.

2) Investigation of the Back-Mixing of Phases in the Mimicked FT SBCR

This section of the work investigates the phase back-mixing using the developed techniques/methods with selected reactor scale models. The extents of phase back-mixing will be quantified by estimating the dispersion parameters in the involved reactor models for the mimicked FT SBCR.

- The effects of operating pressure, gas velocity, and solids loading on the back-mixing of the gas phase will be investigated at the mimicked FT conditions, using the developed gaseous tracer technique.
- A virtual tracer response method is to be developed to generate response curves from CARPT trajectory data. With designed injections and samplings, this method is to be used to quantify the axial and radial dispersion coefficients in different reactor models, including the mechanistic, compartmental RCFD model.

3) Investigation of the Gas-Liquid Mass Transfer in the Mimicked FT SBCR

This section includes mass transfer measurements of different species in the mimicked FT SBCR and the development of a k_a correlation with a theoretical basis, using the obtained data. The objectives are:

- The k_{1a} values of oxygen will be obtained using an oxygen-enriched air method at various conditions in the mimicked FT SBCR. For such measurements, an optical oxygen probe technique will be developed.
- Using the developed gaseous tracer technique and various moderately soluble tracer gases, the mass transfer of different species (CH_4 , CO_2 , and Ar) are to be measured at a selected number of conditions.
- Based on the mass transfer coefficient values of various gases (O_2 , CH_4 , CO_2 , and Ar) obtained in the mimicked FT SBCR, the $k_{1a} \sim D_{AB}$ relation is to be evaluated to predict the k_{1a} values of other species at the same conditions with the known k_{1a} data. Furthermore, a k_{1a} correlation will be developed based on the Higbie penetration theory and tuned with the obtained data.

This work investigates the hydrodynamics, phase back-mixing, and gas-liquid mass transfer in the mimicked FT SBCR. These topics are interrelated: they provide evidence for explanations, necessary data for further processing, or parameter values in needed reactor models. With the motivations and objectives stated above, the relation among various sections of this work is shown in Figure 1-2. The [investigation] level lists the work that was conducted to achieve the above objectives. Various reactor models and multiphase reactor techniques were utilized, which are shown in the two levels below. This schematic summary shows the different sections of the work are not isolated but dependent and related to each other.

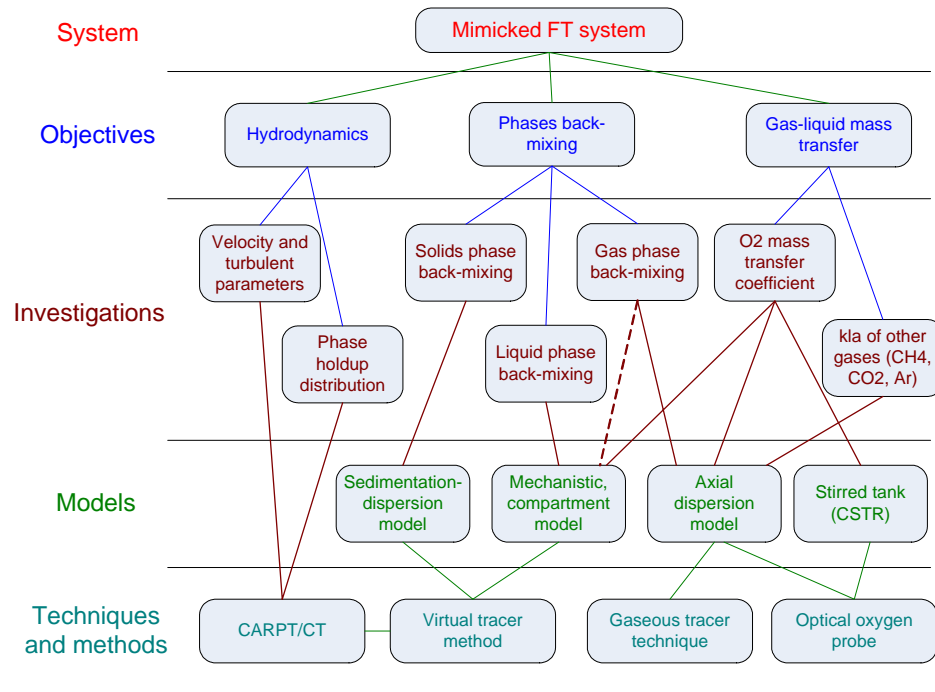


Figure 1-2. Schematic structure of the work

1.3. Structure of the Dissertation

The dissertation consists of six chapters and four appendixes as listed below:

- Chapter 1 outlines the research motivations and objectives.
- Chapter 2 provides a background review on the related topics.
- Chapter 3 investigates the hydrodynamics in the mimicked FT SBCR, and explains the selection of mimicked FT systems, experimental conditions, reactor setup, CT/CARPT techniques (with focuses on the differences and new developments), and the results and analysis.
- Chapter 4 is a study of the back-mixing of phases using various techniques/methods. This chapter quantifies the extent of phase back-mixing under the effects of various operating conditions. It provides estimated values of the dispersion parameters in reactor scale models that are needed in the mass transfer study in Chapter 5.

- In Chapter 5, the gas-liquid mass transfer of various species in the mimicked FT SBCR is measured, and the obtained k_{1a} data are used to develop a k_{1a} correlation based on the penetration theory with estimated bubble dynamic parameters.
- Chapter 6 summarizes the dissertation and makes recommendations for the future work.
- Appendix A lists the additional CT/CARPT data newly obtained in the mimicked FT SBCR that were mentioned but not shown in the main chapters.
- Appendix B includes the technical procedures and information of the two techniques developed for the gas mixing and mass transfer measurements, the optical probe technique, and the gaseous tracer technique.
- Appendix C shows a steady state method for estimating the solids axial dispersion coefficient, compared to the transient method in Chapter 4.
- Appendix D discusses the development of two empirical k_{1a} correlations using the artificial neural network method and the power law method, based on a collected database.

Chapter 2

Background

Slurry bubble column reactors have been widely employed in various industrial processes. However, these reactors' physical behavior in terms of hydrodynamics, phase mixing, and transports is still poorly understood despite a large amount of research. Experimental studies on the hydrodynamics in terms of the velocity field, turbulence parameters, and phase holdup distribution help explain the transfer of momentum, mass, and heat in a column and also provide benchmark data for the evaluation of CFD models. The back-mixing of phases and gas-liquid mass transfer are important factors in reactor performance which are closely affected by the phase interactions. This chapter summarizes the literature as a background to the present work. The current status and new findings on bubble column and slurry bubble column reactors are documented, with a particular focus on their application to Fischer-Tropsch processes. The background includes related topics of phase holdup profiles (tomography), velocity and turbulence parameters mapping, back-mixing of three phases, and gas-liquid mass transfer.

2.1. Phase Holdup Profiles Investigations

To understand the hydrodynamics in SBCRs, the effects of operating conditions and physical properties on the distribution of phase holdups must be experimentally investigated. The gas holdup dictates the local buoyancy, which drives the liquid/slurry into recirculation and turbulence. Measuring the gas holdup distribution has become the focus of many hydrodynamic studies in BCRs or SBCRs. Starting with BCRs, a number of tomography studies have been conducted in gas-liquid two phase systems, and recent references include Hervieu et al. (2002), Ong (2003), Veera et al. (2004), Hubers et al. (2005); Shaikh and Al-Dahhan (2005), etc. These studies measured the cross-sectional distribution of phase holdup, from which parabolic radial gas holdup profiles were obtained. Effects of superficial gas velocity, operating pressure, and reactor designs (e.g., gas distributors) have been investigated by these studies.

Nassos and Bankoff (1967) found a nearly constant ratio of the gas velocity to the mixture velocity, and proposed a correlation for gas holdup radial profiles based on their study in an air-water system, expressed as

$$\varepsilon_g(r) = \bar{\varepsilon}_g \left(\frac{n+2}{n} \right) \left[1 - (r/R)^n \right], \quad (2-1)$$

where $\bar{\varepsilon}_g$ is the cross-sectional average gas holdup, and n is a parameter representing the steepness of a parabolic radial profile. When n is larger, the steepness is lower, and vice versa. Ueyama and Miyauchi (1979) modified this correlation with an additional parameter, c , to make it possible to have a finite gas holdup value close to the wall, written as

$$\varepsilon_g(r) = \bar{\varepsilon}_g \left(\frac{n+2}{n} \right) \left[1 - c(r/R)^n \right]. \quad (2-2)$$

When c is equal to 1, the gas holdup has zero value at the wall; when c is equal to 0, the gas holdup is constant along the radial direction. Luo and Svendsen (1991) reported a similar expression with slight differences as

$$\varepsilon_g(r) = \bar{\varepsilon}_g \left(\frac{n+2}{n+2-2c} \right) \left[1 - c(r/R)^n \right]. \quad (2-3)$$

Based on the tomography data obtained in an air-water system (later published in Ong, 2003), Wu et al. (2001) developed a set of two correlations to predict the values of n and c , respectively, given as

$$n = 2.188 \cdot 10^3 \cdot \left(\frac{d_c u_g (\rho_l - \rho_g)}{\mu_l} \right)^{-0.598} \left(\frac{u_g^2}{g \cdot d_c} \right)^{0.146} \left(\frac{g \cdot \mu_l^4}{(\rho_l - \rho_g) \sigma^3} \right)^{-0.004} \quad (2-4)$$

$$c = 4.32 \cdot 10^{-2} \cdot \left(\frac{d_c u_g (\rho_l - \rho_g)}{\mu_l} \right)^{0.2492}. \quad (2-5)$$

These correlations predict gas holdup profiles with acceptable error for the data that were used for the correlation development. However, Wu et al. (2001) utilized only part of the data obtained in Ong (2003), and this correlation was proved by Ong (2003) to have apparently higher error at her other conditions.

For gas-liquid-solids three-phase systems, there are many fewer tomography studies which have measured the phase holdups distribution (Table 2-1). Hu et al. (1986) found parabolic radial gas holdup profiles in an air-water-glass beads system using a conductivity probe technique and an optical probe technique. They correlated the average gas holdup to the phase velocities and column diameter, and correlated the solids holdup radial profiles to the solids holdup values at the reactor center and at the wall. Using an ultrasonic computed tomography (UCT) technique, Warsito et al. (1997) measured the phase holdup in an air-water-glass beads system at low solids loadings (1~2% by volume) and low superficial gas velocities (< 0.03 m/s). They observed high solids concentration in the region between the central bubble stream and the vertical-spiral liquid flow and the region near, but not adjacent to, the wall. Warsito et al. (1999) and Utomo et al. (2001) used the UCT at conditions similar to their previous study and further described the macroscopic flow scheme and solids concentrating mechanism. Mitra-Majumdar and Farouk (1998) measured the gas holdup profiles using an electro-resistance probe technique. They observed parabolic gas holdup radial profiles and that

both the gas and solids holdups decreased with the reactor height. George et al. (2001) combined the electrical-impedance tomography (EIT) technique and the gamma-densitometry tomography (GDT) technique in their measurements of phase holdup distributions in an air-water-glass beads system and an air-water-polystyrene particles (PVC) system at high solids loadings. They found that the gas holdup distribution was insensitive to the solids loading, especially when using neutrally buoyant polystyrene particles. The electrolyte contaminants added into their systems had more apparent effects than the solids. Warsito and Fan (2003) measured the phase distribution in an air-paraffin-glass beads system using the electrical capacitance tomography (ECT) technique. Behling and Mewes (2004) reported their efforts in measuring the phase distributions in an air-water-PVC particles system using a dual-energy X-ray method. Recently, Warsito and Fan (2005) extended their ECT measurements with an improved reconstruction algorithm which enables real time 3-D imaging.

While all the previous tomography studies were performed at ambient pressure, Rados (2003) and Rados et al. (2005) measured the cross-sectional phase holdup distributions in an air-water-glass beads system at both low and high pressures, using a single-source γ -ray CT. The experimental conditions cover high superficial gas velocity (up to 0.45 m/s) and high pressure (1.0 MPa). However, all of his experiments were performed at a relatively low solids loading of 9.1% vol., except one at 17.8% vol. Rados (2003) found that the gas holdup profile correlation developed by Wu et al. (2001) was not capable to match his three-phase data, and suggested that using constant values of $n=2.5$ and $c=0.8$ yielded much closer predictions. Rados (2003) found linear axial profiles of the solids concentration (solids volume fraction in the gas-free slurry) rather than exponential profiles given by the conventional sedimentation dispersion model (SDM). The empirical linear relation was developed as

$$\frac{C_s}{\bar{C}_s} = 1.86 - \frac{1}{6.4} \frac{z}{d_c}. \quad (2-6)$$

This correlation considers that the axial profiles of the normalized solids concentration (C_s / \bar{C}_s) are dependent only on the relative axial position. Shaikh (2007) used the

same CT technique as Rados (2003) and measured the phase holdup distributions in an air-Therminol-glass beads system, with the Therminol liquid at room temperature mimicking typical FT wax at FT conditions. Shaikh (2007) also found the similar linear axial solids concentration profiles as Rados (2003). Using the same glass beads as Rados (2003), Shaikh (2007) quantified the differences between the two liquids (Therminol vs. water). Moreover, Shaikh (2007) used a higher solids loading (25% vol.) than Rados (2003) and found significant effects of solids loading on the phase distributions in the SBCR.

Table 2-1. Tomography studies in SBCRs

Study	d_c , m	Three-phase system	u_g , m/s	Pressure	Solids loading	Technique
Hu et al. (1986)	0.066-0.284	Air-water-glass beads	≤ 0.065	Ambient		Conductivity & optical probes
Lee et al. (1987)	0.2	Air-water-glass beads	≤ 0.02	Ambient		Optical sensor & pressure transducer
Warsito et al. (1997)	0.14	Air-water-glass beads	< 0.03	Ambient	$\leq 2\%$	UCT
Mitra-Majumdar and Farouk (1998)	0.15	Air-water-glass beads	0.05-0.10	Ambient		Electro-resistance probe & pressure transducer
Warsito et al. (1999)	0.14	Air-water-glass beads	≤ 0.02	Ambient	$\leq 2\%$	UCT
Utomo et al. (2001)	0.14	Air-water-TiO ₂ particles	< 0.04	Ambient	$\leq 2\%$	UCT
George et al. (2001)	0.19	Air-water-glass/polystyrene beads	0.03-0.3	Ambient	$\leq 30\%$	GDT and EIT
Warsito and Fan (2003)	0.1	Air-paraffin-glass beads	0.025-0.15	Ambient	40%	ECT
Behling and Mewes (2004)	0.244	Air-water-PVC particles (>2mm)	-	Ambient	-	dual source X-ray CT
Warsito and Fan (2005)	0.1	Air-paraffin-glass beads	0.02-0.20	Ambient	40%	ECT
Rados et al. (2005)	0.162	Air-water-glass beads	0.08-0.45	0.1 and 1.0 Mpa	$\leq 16\%$	γ -ray CT
Shaikh (2007)	0.162	Air-Therminol-glass beads	0.08-0.30	0.1 and 1.0 Mpa	$\leq 25\%$	γ -ray CT

The reviewed tomography studies greatly advanced the understanding of SBCRs' phase distribution pattern and the macroscopic flow structure. However, the majority of these studies focused more on the development/validation of techniques, and selected three-phase systems that could be easily acquired and handled. Almost all of these studies used glass beads as the solids phase, and many of them used water as the liquid phase. Although some SBCR tomography studies used organic liquids (Warsito and Fan, 2005; Shaikh, 2007), no tomography studies have been reported using FT catalyst, which has different sizes and density than the glass beads and has porous surface characteristics.

The techniques to measure gas holdup distribution have been based on different mechanisms, such as optical probes using normal light or laser; acoustic measurements using ultrasound; electrical techniques based on electrical resistance or capacitance; and nuclear-based techniques using γ -rays, X-rays, positrons, or neutrons. These sensing techniques have been recently developed and implemented into multiphase systems, and have led to great progress in understanding the dynamics in BCRs and SBCRs. Compared with other techniques, γ -ray (or X-ray) computed tomography has the advantage of non-invasiveness and the ability to be used in opaque systems (Chaouki et al., 1997; Dudukovic et al., 1999; Dudukovic, 2000). Details of γ -ray CT techniques and their application to multiphase reactors can be found in various studies, such as Ong (2003) and Hubers et al. (2005) (gas-liquid), Roy et al. (2005) (liquid-solid), Bhusarapu (2005) and Kai et al. (2005) (gas-solid), and Rados et al. (2005) (gas-liquid-solid).

As a single mode tomography, the single-source γ -ray CT technique does not allow straightforward reconstruction of holdup distributions in a dynamically moving three-phase system. Although the dual-source CT technique (Behling and Mewes, 2004; Gehrke and Wirth, 2005) is a direct solution of this issue, such a technique is more difficult to develop and not readily available. To overcome this problem, Rados (2003) and Rados et al. (2005) developed and used a CT/overall gas holdup methodology

based on two assumptions. The first assumption is axially invariant gas holdup, supported by Matsumoto et al. (1992), Bukur et al. (1996), and George et al. (2000). The second assumption is uniform cross-sectional solids concentration in the gas-free slurry, supported by Badgajar et al. (1986), Hu et al. (1986), and Limtarkul (1996). Making these two assumptions is equal to having an additional equation at each reconstruction pixel, which makes the reconstruction of three phases possible. Shaikh (2007) implemented the same CT/overall gas holdup method in a similar three phase tomography study.

2.2. Velocity Field and Turbulence Parameters Investigations

In recent years, the development and implementation of nuclear-based flow tracking techniques has greatly contributed to the better understanding of the flow characteristics in multiphase reactors (Chaouki et al., 1997; Dudukovic, 2000). A nuclear-based flow tracking technique usually uses a single radioactive particle containing a proper isotope (e.g., Sc^{46} or Co^{60}) made in the same density and size as a dispersed phase (e.g., solids tracking) or made buoyant in a continuous phase (e.g., liquid tracking). In such a technique, Lagrangian trajectories of the radioactive tracer particle in the reactor are reconstructed from the counts data received by an array of detectors around the reactor. From the long time Lagrangian trajectories, Lagrangian velocities of the tracer particle are calculated by space differentiation, from which ensemble averaged velocities and turbulence parameters can be obtained. The nuclear-based flow tracking techniques can be implemented in BCRs or SBCRs at almost any operating conditions, while other velocity mapping techniques, such as the optical probes, particle image velocimetry (PIV), or laser Doppler anemometry (LDA), have limitations in discrete phase holdups and high superficial gas velocities. More review of velocity mapping techniques and their comparisons is available in Chaouki et al. (1997) and Dudukovic (2000).

In the chemical reaction engineering laboratory (CREL) at Washington University, there has been a series of BCR and SBCR studies performed in a systematic manner using the CARPT technique. Devanathan et al. (1990) presented the first application of CARPT for liquid flow tracking in an air-water bubble column. In their study, a single recirculation cell of the liquid flow was observed rising along the column center and descending near the wall, although at gas velocities less than 0.05 m/s two recirculation cells were observed. The radial position for the axial liquid velocity transition (inversion point) was at $r/R=0.72$. The Reynolds stress radial profile peaks at a position close to that of a single phase flow through in a pipe. Moslemian et al. (1990 and 1992) presented the CARPT technique in more detail and provided evaluation of the technique. The operating principle and hardware development were discussed, and the reconstruction mechanism was introduced. Error analysis was performed by considering various factors such as the statistical nature of gamma photons, solids angle effects, and voidage fluctuation in multiphase systems. Yang et al. (1992) and Yang et al. (1993) investigated the liquid velocity field and turbulence parameters in a bubble column at more conditions, using the CARPT technique. Yang's studies applied the R/S analysis (presented by Hurst, 1956, and modified by Mandelbrot and Wallis, 1969) to the three components of the Lagrangian velocity to determine the mixing mechanisms in the three directions in the reactor. Such analysis of the velocity found that flow isotropy does not exist in the tested reactors.

Chen et al. (1999) investigated the velocity field and turbulence parameter profiles in an 18 inch (0.44 m) bubble column with and without internals using an air-drake oil system. Internals were used to simulate the heat exchangers in methanol synthesis SBCRs with 95% open area, and small effects of internals were found on the global liquid recirculation. Degaleesan (1997) and Degaleesan et al. (2001) used the CARPT technique in a similar 18 inch (0.44 m) bubble column with an air-water system. Based on the observed velocity field and turbulence parameter profiles, a mechanistic model, the recirculation and cross flow with dispersion (RCFD) model, was developed and presented for the liquid phase. In this mechanistic reactor model, liquid recirculates by

flowing upward in the center, flowing downward close to the wall, and turning over in the distributor zone and disengagement zone. There is axial dispersion in the up-flowing zone and the down-flowing zone, and radial dispersion between these two zones. The distributor zone and the disengagement zone are assumed perfectly mixed. Gupta et al. (2001) and Gupta (2002) extended this mechanistic RCFD model to the gas phase with gas-liquid mass transfer terms. The RCFD model for the gas phase was presented by Gupta in both a single bubble class model (SBCM) and a two bubble class model (TBCM) in which mass is exchanged between large bubbles and small bubbles. However, evaluation with gaseous tracer data indicated that the TBCM does not have additional advantages over the SBCM. Instead of lumping the phase mixing into one parameter as in the ADM, this mechanistic model separately accounts for the global recirculation and local dispersion within each compartment. Historically, because of the lack of a method to estimate the axial and radial dispersion coefficients in this reactor model, the axial and radial eddy diffusivities obtained by CARPT were used as substitutes in this model. The dispersion parameters in the RCFD model are yet to be estimated and need to be examined to determine whether they are close to the eddy diffusivities.

Ong (2003) performed CARPT measurements in a 6 inch stainless steel bubble column using an air-water system. The experimental conditions covered high superficial gas velocity (up to 0.45 m/s), high pressure (up to 1.0 MPa), and four different gas distributor designs. In addition to the previous hydrodynamics knowledge in gas-liquid systems, her study investigated the effects of high superficial gas velocity, operating pressure, and distributor designs on the velocity field and turbulence parameter profiles. It was found that deep into the churn-turbulent flow regime, the effect of distributor designs was insignificant, especially at low pressure. At high pressure, the axial liquid velocity increased while the liquid phase turbulence decreased. At high superficial gas velocities, the effect of operating pressure on the global circulation became smaller. Based on Zehner (1983), Ong (2003) developed a modified empirical relation to predict the centerline liquid velocity

$$u_1(0) = 0.737 \cdot g^{1/3} d_c^{1/3} u_g^{1/3} \left(\frac{\rho_g}{\rho_{g,atm}} \right)^{0.128} \quad (2-7)$$

An analysis on eddy diffusivities by Ong (2003), using the model of Ohnuki and Akimoto (2001), revealed that the bubble-induced turbulence is relatively small compared to the shear-induced turbulence at the tested conditions. More analysis of the turbulence parameter profiles can be found in Ong (2003).

Rados (2003) and Rados et al. (2005) greatly improved the CARPT hardware and implemented the technique in a 6 inch high pressure slurry bubble column using an air-water-glass beads (150 μm) system. Experiments were performed at high superficial gas velocities, high operating pressure, and moderately high solids loading, using three different distributor designs. Rados (2003) was the first solids tracking study performed in an SBCR at high pressure, which is of industrial interest. The effects of operating parameters and distributor designs on the hydrodynamics were investigated. The superficial gas velocity and operating pressure had strong effects on the global recirculation and turbulence, which is similar to observations in a gas-liquid two-phase system. The effects of increasing the solids loading from 9.1% vol. (20% wt.) to 17.8% vol. (35% wt.) were observed to be weak at atmosphere condition. The effects of the distributor design on the solids velocity and solids turbulence were also very small at high superficial gas velocity (0.30 m/s), which is an observation similar to that in the air-water system (Ong, 2003). Rados (2003) developed power-law correlations for solids axial velocity and shear stress radial profiles using the obtained data. The correlation for the radial profile of the axial solids velocity was based on Ueyama and Miyauchi (1979), and expressed as

$$\frac{u_z - u_{z,w}}{u_{z,0} - u_{z,w}} = \left[1 - (r/R)^2 \right]^{1.6} \quad (2-8)$$

The axial solids velocity at the center, $u_{z,0}$, and at the wall, $u_{z,w}$, can be estimated with the absolute values of the superficial gas velocity and pressure in the correlations shown below (Rados, 2003):

$$u_{z,0} = 1.50u_g P + 0.50u_g + 8.0P + 20.0 \quad (2-9)$$

$$-u_{z,w} = 0.525u_g P + 0.15u_g + 17P + 15.7. \quad (2-10)$$

In a continuation of SBCR hydrodynamic studies, Shaikh (2007) performed CARPT experiments in the 6 inch high pressure slurry bubble column using an air-Therminol-glass beads (150 μ m) system. By comparing results to the previous air-water-glass beads measurements (Rados, 2003), his study quantified the differences in the hydrodynamic parameters of Therminol and water. Shaikh (2007) also extended the solids loading from 9.1% vol. in Rados (2003) to 25% vol., and found that the solids loading increase yielded more apparent solids loading effects on the measured hydrodynamic parameters than the increase from 0 to 9.1% vol. Moreover, Shaikh (2007) presented new criteria for hydrodynamics similarity using the CT and CARPT data obtained in BCRs by his work and Ong (2003).

Besides the systematic BCR/SBCR studies in the CREL at Washington University, several other studies have implemented a similar technique, the radioactive particle tracking (RPT) technique, to various systems and conditions. Larachi et al. (1994 and 1995) presented the RPT technique and its application to a 0.10 m column using air-water-glass beads (0.9~5.5 mm) (or PVC solids in some cases). The RPT is similar in principle to the CARPT technique using a modified reconstruction method with a least-square 3-D inverse algorithm. Cassanello et al. (1996) performed RPT experiments in a 0.10 m SBCR using air-water-glass beads (1~5 mm) and air-water-PVC (5.5 mm) systems. A bubble-wake model was presented for the solids mixing, based on the classic two-phase model developed for fluidized beds (Kunii and Levenspiel, 1968). Godfroy et al. (1997) replaced the least-square search location algorithm used by Larachi et al. (1994 and 1995) with a three-layer neural network model. They proposed the potential of neural network models for quick reconstruction in real time flow visualization. In their study, various isotopes were tested, including Sc⁴⁶ (1005 keV), Mo⁹⁹ (140 keV), and Au¹⁹⁸ (412 keV). The Au¹⁹⁸ particle was found to have the best

spacial resolution, although it only has 2.7 days of half life. Kiared et al. (1997a, 1997b, and 1999) conducted a RPT study in a similar 0.10 m reactor, also using air-water-glass beads (1~5 mm) and air-water-PVC (5.5 mm) systems. Based on the obtained phase mixing information, they proposed a cross flow multistage stirred reactor (CFMSR) model. At University of Birmingham, a positron-emitting particle tracking (PEPT) technique using positron cameras was presented and extended to multiple particle tracking (Fan et al., 2006; Yang et al., 2006). They have implemented the PEPT technique in fluidized bed reactors.

These CARPT (RPT) studies in SBCRs provided remarkable understanding of the solids motion pattern which would have been difficult to achieve with other techniques. However, these previous SBCR studies mostly used water as the liquid (except Shaikh, 2007), and all of them used glass beads (or PVC solids in some cases) as the solids phase. The glass beads or PVC solids used in these previous studies were 150 μm or larger, while most industrial FT slurry reactors use catalysts with different physical properties and smaller sizes. Therefore, it is of industrial interest to perform detailed hydrodynamic studies using a real FT catalyst to investigate the effects of physical properties and operating conditions, although this may encounter difficulties of acquiring and handling smaller radioactive tracer particles.

2.3. Liquid and Solids Phase Back-Mixing Investigations

As mentioned earlier, the back-mixing of the liquid or solids phases may significantly affect the reactor performance in SBCRs. There have been a number of studies using tracer techniques to characterize the back-mixing of the liquid or solids at various conditions. The findings and techniques used in these studies are briefly reviewed below.

The liquid phase in SBCRs has been simulated using various models as discussed earlier. Despite the limitations of the ADM, which Levenspiel and Fitzgerald (1983)

warned about, this model has been widely used because of its simplicity and good fit to the residence time distribution. In liquid tracer studies that quantified the liquid phase back-mixing, the ADM was mostly used and the axial dispersion coefficient was estimated. Table 2-2 lists the correlations developed in the literature for the liquid axial dispersion coefficient. A simple calculation can reveal that there are great differences among their predictions. This is probably due to the effects-lumping nature of the ADM, which makes each correlation specific for the tested system and conditions. In addition, experimental errors in the tracer experiments may also contribute the deviations between these correlations.

Table 2-2. Correlations for the liquid axial dispersion coefficient in BCRs

Research	Correlations
Ohki et al., 1970	$D_1 = 0.30d_c^2 u_g^{1.2} + 170\delta$ (δ , hole diameter) bubble flow
	$D_1 = \frac{14d_c}{(1-\epsilon_g)^2}$ coalesced bubble-slug flow
Towel et al., 1972	$D_1 = 1.225d_c^{1.5} u_g^{0.5}$
Deckwer et al., 1974	$D_1 = 0.678d_c^{1.4} u_g^{0.3}$
Hikita et al., 1974	$D_1 = (0.065 + 0.3u_g^{0.77})d_c^{1.25} \mu_l^{-0.12}$
Baird et al., 1975	$D_1 = 0.35d_c^{4/3} g^{1/3} \cdot u_g^{1/3}$
Field et al., 1980	$D_1 = 0.44d_c^{1.33} [g(u_g - \epsilon_g u_s)]^{1/3}$ (us: slip velocity)
	$D_1 = 0.90d_c^{1.5} [L(u_g - 0.235\epsilon_g)]^{1/3}$
Joshi, 1980	$D_1 = 0.5g^{1/4} u_g^{1/2} d_c^{5/4}$
Miyauchi et al., 1981	$D_1 = 0.307d_c^{4/3} (g \cdot u_g)^{1/3}$
Kawase et al., 1986	$D_1 = 1.42d_c^{1.33} [u_g - \epsilon_g u_l / (1 - \epsilon_g)]^{0.73} / (1 - \epsilon_g)$
Kelkar et al, 1983	$D_1 = 0.31 \cdot u_l(0)D_c$ ($u_l(0)$: center-line liquid velocity)
Krishna et al., 1999 and 2000	$D_1 = 7.64 \times 10^{-3} L^{1.85} u_g^{0.28}$
Nedeltchev et al., 2005	$D_1 = 0.30d_c^2 u_g^{1.2} + 170\delta$ (δ , hole diameter) bubble flow
	$D_1 = \frac{14d_c}{(1-\epsilon_g)^2}$ coalesced bubble-slug flow

Various forms of tracer techniques were implemented to quantify the extent of liquid phase back-mixing, as listed in Table 2-3. These studies tracked the liquid flow by using electrolyte, dye, heat, or isotope tracers, which can be detected with conductivity sensors, spectrophotometers, thermocouples, or scintillation detectors, respectively. Tracer measurements were performed in the form of pulse injection, step change, or constant source. These methods are sometimes intrusive, and most importantly it is difficult to ideally distribute the tracer substance in time and space, as it is assumed to be in the reactor models. Significant experimental errors may result from the non-ideal injections and non-ideal sampling systems.

Table 2-3. Experimental studies of the liquid axial dispersion in BCRs

Research	Tracer	Injection	Measurement
Argo et al., 1965	KCl and NaCl solution	steady, at bottom	Ag-AgCl electrodes
Reith et al., 1968	NaCl solution	pulse at top surface	conductivity sensor
Ohki et al., 1970	KCl solution	instant pouring at top	conductivity sensor
Chen, 1972	Electrolyte solution	step change, at liquid inlet	conductivity sensor
Cova, 1974	Heat	steady, at top	thermocouples
Deckwer et al., 1974	Electrolyte, dye, heat	stationary and instationary	unspecified
Hikita et al., 1974	KCl solution	pulse at top surface	platinum electrode
Alexander, 1976	Sulfuric acid tracer	pulse at top surface	conductivity sensor
Field et al., 1980	Radioactive tracer Br ⁸²	pulse at liquid inlet, 5s	scintillation detectors
Khang et al., 1980	4% KCl solution	pulse at bottom, 0.5s	conductivity sensor
Mangartz et al, 1981	Heat	steady, near top surface	thermocouples
Chen et al., 1982	KCl solution	step change, at liquid inlet	conductivity sensor
Kelkar et al, 1983 and 1985	Heat	steady, at top	11 thermocouples
Devine et al., 1985	Heat	steady, at top	12 thermocouples
Tinge et al., 1986	KCl solution	pulse, 3cm above sparger	conductivity sensor
Rice et al., 1987	NaOH solution	step change, at inlet	observation of phenolphthalein
Baird et al., 1988	NaCl solution	pulse, <1s	conductivity sensor
Chen et al., 1989	Heat	steady, at liquid inlet	thermocouples
Rustemeyer et al., 1989	NaCl solution	-	conductivity sensor
Kago et al., 1989	KCl solution	pulse at liquid inlet	conductivity sensor
Asai et al., 1992	Oil red and methylene blue, KCl solution	pulse into column	spectrophotometer, conductivity sensor
Campos et al., 1992	Red color tracer, KCl	instant pouring at top	spectrophotometer, conductivity sensor

Yang et al., 1992	Radioactive particle	free moving reactor	CARPT technique
Wilkinson et al., 1993	NaCl solution	pulse at bottom, <0.3s	conductivity sensor
Syaiful et al., 1993	Oxygen gas	pulse at gas inlet	2 oxygen electrodes
Shah et al., 1995	NaCl solution	pulse at liquid inlet	conductivity sensor
Herbard et al., 1996	NaCl solution	pulse at bottom	conductivity sensor
Salvacion et al., 1996	NaCl solution	pulse spray at surface, <1s	conductivity sensor
Degaleesan et al., 1998	Radioactive particle	free moving in reactor	CARPT technique
Hidaka et al., 1998	KCl solution	pulse at top	conductivity sensor
Baird et al., 1998	NaCl solution, NaOH solution	pulse into column	conductivity sensor, observation of color
Tung et al., 1998	Hot water	pulse at top	two thermocouples
Krishna et al., 1999 and 2000	NaCl solution	pulse, at different locations	conductivity sensor
Camacho Rubio et al., 1999	Oxygen gas	step at gas inlet	oxygen electrode
Bin et al., 2001	KCl solution	pulse at bottom	3 conductivity sensor
Therning et al., 2001	H ₂ SO ₄ solution	instant pouring at top	conductivity sensor
Moustiri et al., 2001	NaCl solution	pulse at liquid inlet	conductivity sensor
Forret et al., 2003	KNO ₃ solution	pulse at top surface	conductivity sensor
Ahmad et al., 2003	KMnO ₄	pulse at top surface	time recording
Yang et al., 2003	Heat	steady, close to liquid outlet	thermocouples
Camacho Rubio et al., 2004	HCl solution	pulse at top surface	pH electrodes
Nedeltchev et al., 2005	CO ₂ gas	step change, at gas inlet	conductivity sensor

The FT catalysts suspended in the liquid are metal based and have apparent higher density than the liquid. Hence, there usually is a solids concentration axial gradient (higher near the bottom) as the result of equilibrium between two opposing effects, settling (sedimentation) and dispersion. Solids dispersion and distribution in the reactor play an important role in reactor performance, and they remain difficult to predict in reactor design and scale-up, due to the complicated interaction of phases. Estimation of the solids dispersion and distribution in SBCRs has been the focus of many studies over decades. Historically the sedimentation-dispersion model has been widely used to describe the axial solids distribution, and therefore the solids axial dispersion

coefficient became the target parameter. The reported methods of estimating the solids axial dispersion coefficient are mostly by measuring the steady solids concentration axial gradients. As a brief review, the previous studies of solids dispersion and distribution in SBCRs are listed in Table 2-4.

Table 2-4. Experimental studies of the solids axial dispersion

Research	Model	Measurement	$d_c \times L$	P	C_s	u_g , m/s
Cova, 1966	SDM	Withdraw	1.8 in x 4 ft	low		<0.08
Imafuku et al., 1968	SDM	Withdraw	5, 10, 20 cm	low	<3% vol.	<0.15
Farkas et al., 1969	SDM	Withdraw	1.5 in	low		≤ 0.015
Kato et al., 1972	SDM	Withdraw	6.6; 12.2; 21.4	low	<8% vol.	<0.20
Smith et al., 1984	SDM	Withdraw		low		<0.20
Smith et al., 1985	SDM	Withdraw	10.8 cm x 1.94 m	low		<0.20
Smith et al., 1986	SDM	Withdraw	7.62x1.54 10.8x1.94	low	10% wt.	<0.28 <0.20
O'Dowd et al., 1987	SDM	Withdraw	10.8 cmx.94 m	low	<12% vol.	<0.24
Matsumoto et al., 1989	SDM	Shutter plates	7 cm x 4.25 m	low	<30% vol.	0.01-0.3
Reilly et al., 1990	SDM	Withdraw	30 cmx5.28 m	low		< 0.30
Bukur et al., 1990	SDM	Withdraw	5 cm x 3 m	low	10, 20, 30% wt.	0.02 ~ 0.12
Matsumoto et al., 1992	SDM	Shutter plates	15 cm x 2.7 m	low		< 0.30
Sessieq et al., 1999	SDM	turbidity probe	0.15 m	low		
Nakao et al., 2000	SDM	Withdraw	7 cm x 1.0 m	low	5%-20% vol.	0.005-0.04
Zhang et al., 2002	SDM	Withdraw	4.2 cm x 1.4 m	low	<5% vol.	0.023 ~ 0.045
Zhang et al., 2002	SDM	Withdraw	4.2 cm x 1.4 m	low	<5% vol.	0.023 ~ 0.045
Cardoso et al., 2003	Mechanistic	Withdraw (stop gas)	3.2 cm x 7.5 m	low	10~30% vol.	
Knesebeck et al., 2004	Wake model	Withdraw	6 cm x 2.98 m	low	~10%	<0.0024

The majority of these studies measured the solids axial concentrations by withdrawing samples from ports (Bukur et al., 1990; Reilly et al., 1990; Nakao et al., 2000; Zhang et

al., 2002; etc.). Some measured by settling the solids onto several shutter plates (Matsumo et al., 1989 and 1992) or turbidity probes (Sessiecq et al., 1999). All of these procedures are greatly invasive.

Having reviewed the liquid and solids back-mixing studies, one can consider the feasibility of utilizing CARPT data to quantify the back-mixing extent. The CARPT technique provides long-time trajectory data by tracking the liquid phase using a buoyant tracer particle or tracking the solids phase using a tracer particle made in the same size and density of the solids. These trajectory data contain ample information about the phase mixing. However, besides the time-averaged velocity field, very limited work has been presented to extract more quantitative information about the extent of phase back-mixing. Villermaux (1996) proposed a method to generate the trajectory length distribution (TLD) from Lagrangian trajectories, which were later used by Kiared et al. (1997) and Bhusarapu (2005) for various systems. This method yields a length distribution of many trajectory sections between two zones in the reactor. Although the TLD obtained from trajectory data provide the variation of the trace of a fluid element or tracer particle and serves a similar purpose as a RTD, it is not suitable for estimating phase dispersion parameters in a transient reactor model. For loop systems such as a circulating fluidized bed (Bhusarapu, 2005), residence time distribution (RTD) between two open-open boundaries can be obtained from the trajectories obtained. However, CARPT (RPT) experiments in BCRs or SBCRs are usually performed in semi-batch mode due to technical limitations, and hence obtaining the RTD for the liquid or solids is out of the question. Cassanello et al. (1996) proposed a method based on the ergodic hypothesis to characterize the solids mixing in a slurry bubble column reactor. Pulses of particles were generated at different heights of the column, and the dynamic change of the centroids of these particles was used to characterize the mixing time scale in three different directions. Based on the idea of Cassanello et al. (1996), it is possible to generate virtual tracer response curves from CARPT data which can be fit to a transient reactor model. Compared to a conventional tracer technique, the virtual tracer response method, if successful, would

- Inherit the advantages of the CARPT technique, such as non-invasiveness in its application to multiphase reactors,
- Provide almost ideal tracer injection/sampling in terms of time and space, and
- Perform virtual tracer experiments in particularly designed patterns, which are needed for compartmental models but practically impossible with a traditional tracer technique.

By designing the virtual tracer injection and sampling in specific ways for multi-parameter regression, estimation of the dispersion coefficients in the mechanistic RCFD model will be possible. In the solids dispersion measurement, by using dynamic response curves instead of a steady solids concentration gradient, this method is expected to be less sensitive to the values of the solids settling velocity (as a parameter in the SDM), which are difficult to accurately measure or estimate. As a comparison, the traditional techniques shown above require a steady state method in which the axial dispersion coefficient measurements are dominantly affected by the estimated values of the solids settling velocity.

2.4. Gas Phase Back-Mixing Investigations

In SBCR simulations, the gas phase is generally modeled as a plug flow, with dispersion being neglected (Stern et al., 1983; van Vuuren and Heydenrych, 1985; Herbolzheimer and Iglesia, 1994; Hedrick and Chuang, 2003; Song et al., 2003; etc.). This assumption may not be correct, especially when a reactor has a small Peclet number (defined as $Pe = u_g L / \varepsilon_g D_g$, where u_g , L , ε_g , and D_g are the superficial gas velocity, height of the suspension, gas holdup, and gas axial dispersion coefficient, respectively). In several other studies which did consider axial dispersion of the gas phase for slurry bubble column modeling (Stern et al., 1985; Turner et al., 1990; Mills et al., 1996; Rados et al., 2003), the gas dispersion coefficient values were obtained from either liquid dispersion coefficients or two-phase BCR gas dispersion studies. In the open literature, almost no studies of gas phase dispersion in SBCR reactors were found, and only a very limited number of studies in BCRs (Table 2-5).

Table 2-5. Reported measurements of gas axial dispersion coefficient in BCRs

Research	System	$d_b, m / L, m$	$u_g, m/s$
Men'shchikov et al. (1967)	air-water	0.3 / 5.0	0.0076-0.096
Towell et al. (1972)	air-water	0.406 / 2.84 1.067 / 5.1	0.0162-0.131 0.0085-0.0344
Field et al. (1980)	air-water	3.2 / 18.9	0.045-0.055
Mangartz et al. (1981)	air, N ₂ -water, glycol, n-propanol	0.10 / 0.7, 1.7 0.14 / 0.6, 0.9	0.015-0.060 0.010-0.130
Joseph et al. (1984)	air-water	0.305 / 2.1	0.03-0.07
Kulkarni et al. (1984)	air-sulfite solution	0.075 / 2.65	0.001-0.013
Kago et al. (1989)	air-water	0.12 / 1.4, 2.14 0.19 / 0.97~2.49	0.01-0.14 0.01-0.06
Wachi et al. (1990)	air-water	0.2, 0.5 / 4.5	0.03-0.4
Shetty et al. (1992)	air-water	0.15, 0.25 / 2.7	0.01-0.16
Kantak et al. (1995)	air-water, alcohols	0.15, 0.25 / -	0.01-0.18

Until early 1980s, most of the measurements of the gas phase axial dispersion coefficient (D_g) in BCRs were performed within the low superficial gas velocity range (Men'shchikov et al., 1967; Towell et al., 1972; Field et al., 1980; Mangartz et al., 1981). A short review of the gas phase dispersion in BCs was given by Joshi et al. (1982). Thereafter, more BCR studies for gas phase dispersion using the ADM were conducted by Joseph et al. (1984); Kulkarni et al. (1984); Kago et al. (1989); Wachi et al. (1990); Shetty et al. (1992); and Kantak et al. (1995). Based on their measurements, various correlations were developed to predict the gas axial dispersion coefficient in two-phase BCRs (Table 2-6). As can be seen, these correlations have similar simple formats. According to these correlations, the gas axial dispersion coefficient is dependent only on the gas velocity and column diameter in most cases, and on gas holdup in some cases.

Table 2-6. Correlations for the gas axial dispersion coefficient

Research	D_g correlation
Men'shchikov and Aerov (1967)	$D_g = 1.47 \times u_g^{0.72}$
Towell and Ackermann (1972)	$D_g = 19.7 \times d_c^2 \times u_g$
Pilhofer et al. (1978)	$D_g = 2.64 \cdot u_{slip}^{3.56}$
Field and Davidson (1980)	$D_g = 56.4 \times d_c^{1.33} \times (u_g/\epsilon_g)^{3.56}$
Mangartz et al. (1981)	$D_g = 50 \times d_c^{3/2} \times (u_g/\epsilon_g)^3$
Joshi (1982)	$D_g = 110 \times d_c^2 \times (u_g^2/\epsilon_g)$
Wachi and Nojima (1990)	$D_g = 20 \times d_c^{3/2} \times u_g$

All of these gaseous tracer studies were performed in two-phase systems. The presence of solids and operation at high pressure cause significant differences in the hydrodynamics and phase mixing in SBCRs. It is of importance to investigate the gas phase back-mixing and gas axial dispersion at the mimicked FT conditions, which was the focus of this work.

2.5. Gas-Liquid Mass Transfer Investigations

As one of the key reactor design parameters, the volumetric gas-liquid mass transfer coefficient, $k_L a$, is directly affected by the hydrodynamics, phase mixing, and physical properties. In the ongoing effort to reduce uncertainty, there has been a large body of mass transfer research covering various specific topics (Yang et al., 2001; Behkish et al., 2000 and 2002; Han et al., 2003; Vandu and Krishna 2003 and 2004; etc.). These studies measured overall gas-liquid mass transfer parameters, including the volumetric gas-liquid mass transfer coefficient ($k_L a$), interfacial area (a), and liquid side mass transfer coefficient (k_l). This section briefly reviews the gas-liquid mass transfer studies in both BCRs and SBCRs as a background to the present mass transfer work performed in the mimicked FT SBCR.

As listed in Table 2-7, many correlations have been proposed for predictions of k_{1a} or k_1 in BCRs or SBCRs. These correlations were obtained using different database and optimization methods, and some of them have been frequently used in engineering designs. Among these studies, some correlated k_{1a} or k_1 to the superficial gas velocity along with only one or two other parameters (Deckwer, 1981; Nguyen-Tien et al., 1985; Patwari et al., 1986; Schumpe et al., 1987; Katnas et al., 1994; Jordan et al., 2002; Liu and Zheng, 2004). Apparently, these correlations would be suitable only in systems that are similar to those used in their measurements. Some other correlations used dimensionless groups in equations that are significantly different from each other (Calderbank and Moo-Young, 1961; Fair, 1967; Akita and Yoshida, 1973; Nakanoh and Yoshida, 1980; Hikita et al., 1981; Kawase et al., 1987; Ozturk et al., 1987; Chen and Yang, 1989; Lee et al., 1993; Sotelo et al., 1994; Yang et al., 2001a; Yang et al., 2001b; Behkish et al., 2002). The great difference between these correlations may be caused by the empirical nature of their development.

Table 2-7. Correlations for k_{1a} and k_1 in BCRs or SBCRs

Research	Correlations
Calderbank and Moo-Young, 1961	$k_1 = 0.31 \left(\frac{\Delta\rho\mu_1g}{\rho_1^2} \right)^{1/3} \left(\frac{\rho_1}{D_{AB}\mu_1} \right)^{-2/3}$ <p>For large Bubble with non-spherical shapes</p> $k_1 = 0.42 \left(\frac{\Delta\rho\mu_1g}{\rho_1^2} \right)^{1/3} \left(\frac{\rho_1}{D_{AB}\mu_1} \right)^{-1/2}$
Fair, 1967 a and b	$k_1a = 3.31 \frac{D_{AB}\epsilon_g}{d_b^2} \left(\frac{\rho_1}{D_{AB}\mu_1} \right)^{1/3} \left(\frac{d_b u_b \mu_1}{\rho_1} \right)^{1/2}$
Akita and Yoshida, 1973	$\frac{k_1a \cdot d_c^2}{D_{AB}} = 0.6 \left(\frac{\rho_1}{D_{AB}\mu_1} \right)^{0.5} \left(\frac{g \cdot d_c^2 \cdot \rho_1}{\sigma} \right)^{0.62} \left(\frac{g \cdot d_c^3 \mu_1^2}{\rho_1^2} \right)^{0.31} \cdot \epsilon_g^{1.1}$
Nakanoh and Yoshida, 1980	$\frac{k_1a \cdot d_c^2}{D_{AB}} = 0.09 \left(\frac{\rho_1}{D_{AB}\mu_1} \right)^{0.5} \left(\frac{gd_c^2\rho_1}{\sigma} \right)^{0.75} \left(\frac{gd_c^3\mu_1^2}{\rho_1^2} \right)^{0.39} \left(\frac{u_g}{\sqrt{gd_c}} \right) \left\{ 1 + C \left(\frac{u_{bzc}\lambda}{d_{vs}} \right) \right\}^{m-1}$ <p>$C = 0.13, m = 0.55$</p>
Deckwer, 1981	$k_1a = 0.00315 u_g^{0.59} \mu_{eff}^{-0.84}$

Hikita et al., 1981	$k_1 a = \frac{14.9 g f}{u_g} \left(\frac{u_g \mu_1}{\sigma} \right)^{1.76} \left(\frac{\mu_1 g}{\rho_l \sigma^3} \right)^{-0.248} \left(\frac{\mu_g}{\mu_l} \right)^{0.243} \left(\frac{\mu_1}{\rho_l D_{AB}} \right)^{-0.604}$ $f = \begin{cases} 1.0 & \text{for nonelectrolytes} \\ 10^{0.068 I} & I < 1.0 \text{ kg ion m}^{-3} \\ 1.114(10^{0.021}) & I > 1.0 \text{ kg ion m}^{-3} \end{cases}$
Nguyen-Tien et al., 1985	$k_1 a = 0.39 \left(1 - \frac{\phi_s}{0.58} \right) u_g^{-0.67}$ <p>where $\phi_s = \varepsilon_s / (1 - \varepsilon_g)$</p>
Patwari et al., 1986	$k_1 a = 0.0168 \cdot u_g^{-0.36} \mu_l^{-1.30} D_{AB}^{0.5}$
Kawase et al., 1987	$\frac{k_1 a \cdot d_c^2}{D_{AB}} = \frac{12}{\sqrt{\pi}} B \sqrt{1.07} \left(\frac{v_l}{D_{AB}} \right)^{1/2} \left(\frac{u_g d_c}{v_l} \right)^{3/4} \left(\frac{u_g^2}{g d_c} \right)^{7/60} \left(\frac{g d_c^2 \rho_l}{\sigma} \right)^{3/5}$ $B = 0.0645$
Ozturk et al., 1987	$\frac{k_1 a \cdot d_b^2}{D_{AB}} = 0.62 \left(\frac{\rho_l}{D_{AB} \mu_l} \right)^{0.5} \left(\frac{g d_b^2 \rho_l}{\sigma} \right)^{0.33} \left(\frac{g \rho_l^2 d_b^3}{\mu_l^2} \right)^{0.29} \left(\frac{u_g}{\sqrt{g d_b}} \right)^{0.68} \left(\frac{\rho_g}{\rho_l} \right)^{0.04}$
Schumpe et al., 1987	$k_1 a = K \cdot u_g^{0.82} \mu_{\text{eff}}^{-0.39}$ <p>K=0.042 for salt-free systems; K=0.063 for salt solutions.</p>
Chen and Yang, 1989	$\frac{k_1 \cdot d_b}{D_{AB}} = 1.13 \cdot 10^{-4} \cdot \left(\frac{d_b V_s \rho_l}{\mu_l} \right)^{1.75} \left(\frac{\mu_l}{\rho_l D_{AB}} \right)^{0.5} \left(\frac{d_c u_l \rho_l}{\mu_l} \right)^{0.285}$
Schumpe and Deckwer, 1989	$k_1 a = 2988 \cdot D_{AB}^{0.5} u_g^{0.44} u_l^{0.42} \mu_{\text{eff}}^{-0.34} u_T^{0.71}$
Kim and Kim, 1990	$k_1 a = 0.73 \cdot u_g^{0.87} u_l^{0.45} d_p^{0.71} \left[\begin{array}{l} 1 + 0.036 \cdot (V_f / V_s)^{1.11} \\ -1.348 \cdot 10^{-3} (V_f / V_s)^{2.09} \end{array} \right]$
Kang et al., 1991	$k_1 a = 4.47 \cdot 10^{-2} \cdot u_g^{0.782} u_l^{0.160} \mu_{\text{eff}}^{-0.407} (1 + \varepsilon_s)^{3.640}$
Lee et al., 1993	<p>In the bubble disintegrating regimes :</p> $k_1 a = 2.36 \cdot 10^{-5} \cdot u_g^{0.686} u_l^{0.469} d_p^{0.788} \sigma^{-1.532} \mu_{\text{eff}}^{-0.548}$ <p>or $\frac{k_1 a \cdot d_p^2}{D_{AB}} = 4.51 \cdot 10^{-5} \left(\frac{\mu_l}{D_{AB} \rho_l} \right)^{0.5} \left(\frac{P_v d_p^4 \rho_l^3}{\mu_l^3} \right)^{0.507} \left(\frac{u_l^2 \rho_l d_p}{\sigma} \right)^{0.457}$</p> <p>In the bubble coalescing or slug flow regimes :</p> $k_1 a = 1.10 \cdot 10^{-6} \cdot u_g^{0.940} u_l^{0.381} d_p^{0.790} \sigma^{-2.273} \mu_{\text{eff}}^{-0.671}$ <p>or $\frac{k_1 a \cdot d_p^2}{D_{AB}} = 4.19 \cdot 10^{-5} \left(\frac{\mu_l}{D_{AB} \rho_l} \right)^{0.5} \left(\frac{P_v d_p^4 \rho_l^3}{\mu_l^3} \right)^{0.483} \left(\frac{u_l^2 \rho_l d_p}{\sigma} \right)^{0.436}$</p>
Miyahara et al. (1993)	$k_1 a = 0.467 \cdot u_g^{0.82}$

Katnas et al., 1994	$k_1 a = 2.42 \cdot u_1^{0.69} u_g^{0.45}$ $k_1 = 0.002 \cdot u_1^{0.14} u_g^{-0.45}$ $a = 121 \cdot u_1^{0.55} u_g^{0.90}$
Sotelo et al., 1994	$\frac{k_1 a \cdot u_g}{g} = 16.9 \left(\frac{u_g \mu_1}{\sigma} \right)^{2.14} \left(\frac{\mu_1^4 g}{\rho_1 \sigma^3} \right)^{-0.518} \left(\frac{\mu_d}{\mu_1} \right)^{0.074} \left(\frac{\rho_1}{D_{AB} \mu_1} \right)^{-0.038} \left(\frac{d_o}{d_c} \right)^{0.908}$
Zheng et al., 1995	$k_1 a = a_1 u_g^{a_2} u_1^{a_3} d_p^{a_4} (1 - \varepsilon_s)^{a_5} (1 + a_6 \sqrt{h} + a_7 h)$ <p>Values of $a_1 \sim a_7$ are given depending on flow regimes</p>
Kang et al., 1999	$k_1 a = 10^{-3.08} d_c \left(\frac{d_c u_g \rho_g}{\mu_1} \right)^{0.254}$
Letzel et al., 1999	$\frac{k_1 a}{\varepsilon_g} = 0.5$
Yang et al., 2001a	$H_2: \frac{k_1 \cdot d_c}{D_{AB}} = 1.546 \cdot 10^2 \cdot \left(\frac{P}{\rho_{sl} u_g^2} \right)^{0.052} \left(\frac{d_c \rho_{sl} u_g}{\mu_{eff}} \right)^{0.073} \left(\frac{\mu_{eff}}{\rho_{sl} D_{AB}} \right)^{-0.231}$ $CO: \frac{k_1 \cdot d_c}{D_{AB}} = 8.748 \cdot 10^2 \cdot \left(\frac{P}{\rho_{sl} u_g^2} \right)^{-0.012} \left(\frac{d_c \rho_{sl} u_g}{\mu_{eff}} \right)^{0.024} \left(\frac{\mu_{eff}}{\rho_{sl} D_{AB}} \right)^{-0.133}$
Yang et al., 2001b	$H_2: \frac{k_1 \cdot d_c}{D_{AB}} = 1.802 \cdot 10^{-4} \cdot \left(\frac{P}{\rho_{sl} u_g^2} \right)^{0.374} \left(\frac{d_c \rho_{sl} u_g}{\mu_{eff}} \right)^{1.077} \left(\frac{\mu_{eff}}{\rho_{sl} D_{AB}} \right)^{0.868}$ $CO: \frac{k_1 \cdot d_c}{D_{AB}} = 9.246 \cdot 10^{-4} \cdot \left(\frac{P}{\rho_{sl} u_g^2} \right)^{0.299} \left(\frac{d_c \rho_{sl} u_g}{\mu_{eff}} \right)^{1.023} \left(\frac{\mu_{eff}}{\rho_{sl} D_{AB}} \right)^{0.960}$
Behkish et al., 2002	$k_1 a = 0.18 \cdot \left(\frac{\rho_1}{D_{AB} \mu_1} \right)^{-0.6} \left(\frac{\rho_1 u_g}{M_1} \right)^{-2.84} (\rho_g \cdot u_g)^{0.49} e^{-2.66 C_V}$ <p>C_V: volumetric solids concentration. $C_V = 0$ for BCRs.</p>
Jordan et al., 2002	$k_1 a = (1 - \varepsilon_g) \cdot C \cdot u_g^{0.91} \rho_g^{0.24}$ <p>$C = 0.99$ for water, 1.14 for ethanol (96%), 0.83 for 1-butanol, 1.49 for toluene.</p>
Liu and Zheng, 2004	$k_1 a = 0.018 \cdot u_g^{0.713} u_1^{0.076} G_s^{-0.301}$ <p>G_s: particle recirculating rate ($\text{kg}/(\text{m}^2 \cdot \text{s})$)</p>

In comparison with these fully empirical correlations, some studies developed k_1 correlations for BCRs starting from a theoretical basis. Lewis and Whitman (1924) proposed the famous film theory as a mathematical description of the rate at which a gas is absorbed into a liquid, which then became the basis of later research on gas-liquid transport in multiphase systems. The film theory assumes a gas film and a liquid

film at the interface, each in laminar flow and acting as a different transport resistance in series. Lewis and Whitman (1924) found that for a gas with solubility lower than sulfur dioxide, the liquid side interface is saturated at the partial pressure of the gas, which means only the resistance in the liquid film needs to be considered.

Based on Fick's second law of unsteady diffusion, Higbie (1935) proposed the penetration theory for unsteady mass transfer at the gas-liquid interface, considering only the liquid film resistance. For systems with discrete gas phase (bubbles) such as BCRs, the penetration theory assumes an average exposure time, t_e , for the liquid surface. With a given t_e , the liquid side mass transfer coefficient is calculated by the unsteady Fick's law as

$$k_l = 2 \sqrt{\frac{D_{AB}}{\pi \cdot t_e}} \quad (2-11)$$

Higbie validated the model with experiments using bench apparatuses including an absorption tube and a bubble controlling mechanism. As an extension to the penetration theory, Danckwerts (1951) proposed the surface renewal theory, which is based on a concept of renewing liquid at the surface instead of a stagnant film. He proposed that the age-distribution for the surface is

$$\Psi(t) = s \cdot e^{-s \cdot t}, \quad (2-12)$$

where s is the rate of the surface renewal. The liquid side mass transfer coefficient, k_l , is calculated as

$$k_l = \sqrt{D_{AB} \cdot s} \quad (2-13)$$

For gas absorption without chemical reactions, which is the case of this work, the penetration theory and surface renewal theory have the similar expression for k_l , both proportional to the square root of D_{AB} . The exposure time t_e in the penetration theory for BCRs has been calculated as

$$t_e = \frac{\text{bubble surface}}{\text{surface formation rate}} = \frac{\text{length of bubble}}{\text{relative velocity}} = \frac{d_b}{u_{\text{slip}}} \quad (2-14)$$

Therefore, the exposure time can be directly estimated either by the bubble surface and its formation rate or approximately by the bubble size and bubble slip velocity, which can be measured or predicted. The reported $k_L a$ correlations in BCRs using the bubble surface/formation rate method or the bubble size/velocity method are reviewed below.

Nakao et al. (1983) found relations of the bubble size and slip velocity with the superficial gas velocity as $d_b \propto u_g^{1/5}$ and $u_{slip} \propto u_g^{2/5}$. Hence the liquid side mass transfer coefficient is calculated as

$$k_L = 2 \sqrt{\frac{D_{AB}}{\pi \cdot t_e}} \propto \left(\frac{1}{t_e}\right)^{1/2} = \left(\frac{u_{slip}}{d_b}\right)^{1/2} \propto u_g^{1/10}. \quad (2-15)$$

In the churn-turbulent flow regime, there is much more intense bubble interaction, and the bubbles' shape is no longer spherical. Assuming isotropic turbulence, Kastanek (1977) and Kastanek et al. (1993) used a different expression for the exposure time as

$$t_e = \frac{d_{be}}{u_{br}}, \quad (2-16)$$

where d_{be} is the equilibrium (stable) bubble diameter based on the isotropic turbulence assumption, and u_{br} is the average rise velocity of a swarm of bubbles.

Nedeltchev (2002) proposed an expression similar to the one by Kastanek, with methods to determine the values of d_{bm} and u_{br} in the expression of t_e

$$t_e = \frac{d_{bm}}{u_{bt}}, \quad (2-17)$$

where d_{bm} is the geometric mean bubble diameter, and u_{bt} is the terminal bubble rise velocity. The geometric mean bubble diameter is calculated according to Miller (1974) as

$$d_{bm} = \sqrt{d_{b0} d_{be}}, \quad (2-18)$$

where d_{b0} is the initial bubble size formed at the gas distributor orifices, estimated as

$$d_{b0} = 2.05 \left(\frac{Q_g}{P_{abs} N} \right)^{0.4} \left(\frac{3C_D}{4g} \right)^{0.2}. \quad (2-19)$$

The equilibrium bubble diameter (d_{be}) is calculated by

$$d_{be} = 3.48 \cdot C_D^{0.6} \left(\frac{\sigma^{0.6}}{(g \cdot u_g)^{0.4} \rho_l^{0.2}} \right), \quad (2-20)$$

and the terminal bubble rise velocity is predicted by Mendelson (1967) as

$$u_{bt} = \sqrt{\frac{2\sigma}{\rho_l d_{bm}} + \frac{g \cdot d_{bm}}{2}}. \quad (2-21)$$

Sardeing et al. (2006) and Nedeltchev et al. (2006) presented the idea of calculating mass transfer coefficients using Higbie's penetration theory through the total bubble surface, S_b , and the rate of surface formation, R_{sf} , as

$$t_e = \frac{S_b}{R_{sf}}, \quad (2-22)$$

while S_b and R_{sf} are calculated by assuming ellipsoidal bubbles, as

$$S_b = \pi \frac{l_b^2}{2} \left[1 + \left(\frac{h_b}{l_b} \right)^2 \frac{1}{2e} \ln \frac{(1+e)}{(1-e)} \right], \quad (2-23)$$

$$\text{and } R_{sf} = \pi \sqrt{\frac{l_b^2 + h_b^2}{2} - \frac{(l_b - h_b)^2}{8}} u_b, \quad (2-24)$$

where e is the eccentricity calculated as

$$e = \sqrt{1 - \left(\frac{h_b}{l_b} \right)^2}, \quad (2-25)$$

and l_b and h_b are the length and height of the ellipsoidal bubbles, which both can be predicted using empirical correlations developed by Terasaka et al. (2004). Plus, the volumetric interfacial area is estimated as

$$a = \frac{4f_b S_b}{\pi d_c^2 \cdot u_b}, \quad (2-26)$$

where f_b is the bubble formation frequency, obtained by $f_b = Q_g / u_b$. Hence, Nedeltchev et al. (2006) obtained the correlation for the volumetric gas-liquid mass transfer coefficient as

$$k_{1a} = 8 \cdot f_c \sqrt{\frac{D_{AB} R_{sf}}{\pi S_b}} \cdot \frac{f_b S_b}{\pi d_c^2 \cdot u_b}. \quad (2-27)$$

As shown above, the development of k_{1a} correlations for BCRs based on the Higbie penetration theory usually involves estimation of the bubble dynamic parameters. Despite their theoretical basis, these k_{1a} correlations are still partially empirical with the estimation of the bubble dynamic parameters, and may not be suitable for all systems and conditions. Hence, the application of the penetration theory for a k_{1a} correlation is to be evaluated in SBCRs with solids and at high pressure. If such a method is validated using the data obtained in this work, a k_{1a} correlation can be developed which is expected to be more reliable than a fully empirical one in a three-phase system with physical properties close to a FT SBCR.

Chapter 3

Hydrodynamics in the Mimicked FT SBCR

3.1. Scope

The previous hydrodynamic studies in SBCRs at the CREL (Rados, 2003 and Shaikh, 2007) both used glass beads as the solids phase. FT catalyst particles differ from the glass beads in size, density, and porosity. Thus, their impact on SBCR hydrodynamics needs to be quantified. This work selected an air-C₉C₁₁-FT catalyst system that consists of high pressure air (mimicking syngas density), a C₉C₁₁ hydrocarbon mixture (at room temperature, mimicking the physical properties of FT wax at FT conditions), and FT catalyst carrier (with the same physical properties as active FT catalyst). Additionally, an air-Therminol-FT catalyst system was also selected for limited conditions in order to separately show the effects of two mimicking liquids and different solids by comparisons with the previous hydrodynamic studies in SBCRs. Rados (2003) studied the hydrodynamics of an air-water-glass beads system at high superficial gas velocity (up to 0.45 m/s), high pressure (up to 1.0 MPa), and solids loading of 9.1% vol. for most of the conditions. Shaikh (2007) conducted a hydrodynamic study in an air-Therminol-glass beads system at high solids loading (25% vol.), and similar high

superficial gas velocities and high pressure. Shaikh (2007) used Therminol at room temperature to mimic the physical properties of FT wax at real FT conditions, and quantified the differences with Rados (2003)'s air-water-glass beads system. Shaikh (2007) also investigated the solids loading effects on the hydrodynamics at higher (25% vol.) solids loading. However, Shaikh (2007) used the same 150 μ m glass beads as Rados (2003) due to the difficulties in manufacturing, irradiation, and handling of smaller radioactive tracer particles. These technical difficulties were overcome in this work, which made it possible to conduct CARPT experiments using FT catalyst.

The hydrodynamics in the mimicked FT SBCR was investigated by conducting CT/CARPT experiments which involve three-phase systems, reactor setups, CT/CARPT procedures, and experimental conditions. Since this work used reactor setups and techniques that were developed and used by several previous studies (Ong, 2003; Rados, 2003; Shaikh, 2007), the common information is briefly shown and referred to these studies. Details are provided on the new information, which includes the three phase systems, three phase reconstruction equations for porous solids modified from Rados (2003), smaller radioactive tracer particles for CARPT, and a new and alternative three-phase CT reconstruction method. The new three-phase reconstruction algorithm combines CARPT occurrences and single-source CT scans, which makes only one ergodicity assumption instead of the two assumptions made by Rados (2003) for his method. The phase holdup profiles obtained using the two reconstruction methods are compared and commented.

The C₉C₁₁ and Therminol liquids were found to yield similar hydrodynamics in both two-phase and three-phase systems. The mimicked FT SBCR used FT catalyst rather than glass beads, and the resulting differences in the hydrodynamic parameters were quantified and analyzed. Some observed differences in the effects of operating parameters compared with the previous air-water-glass beads system (Rados, 2003) and air-Therminol-glass beads system (Shaikh, 2007) are shown as well. This hydrodynamic study used both materials and conditions of industrial interest and

obtained flow visualization data which can be used as benchmarks for evaluation, validation, and tuning of CFD models. Based on the CARPT data, the macro-mixing of liquid/solids phases is interpreted using various reactor scale models to quantify the back-mixing extent in Chapter 4.

3.2. Selection of Three-Phase Systems

The following sections discuss the selection of the air-C₉C₁₁-FT catalyst and air-C₉C₁₁-FT catalyst systems, with each phase having the same or similar physical properties at room temperature as the corresponding phase in a syngas-FT wax-FT catalyst system at typical LT-FT conditions (about 200~240 °C, 1~4 MPa). The SBCR that mimics the FT physical properties is referred to as the mimicked FT SBCR in this work. The hydrodynamics (Chapter 3), phase back-mixing (Chapter 4), and mass transfer (Chapter 5) studies were mostly conducted in the air-C₉C₁₁-FT catalyst system, with a few hydrodynamic measurements conducted in the air-Therminol-FT catalyst system for comparison.

3.2.1. Gas Phase Selection

The syngas in an industrial FT SBCR mainly consists of carbon monoxide and hydrogen at various ratios, along with some carbon dioxide, water, etc. Table 3-1 shows that the density of high-pressure air (at 1.0 MPa) is similar to that of syngas at typical FT conditions. Therefore, high pressure air was selected as the gas phase, and operating pressure of 1.0 MPa was selected for some of the conditions. A low pressure of 0.1 MPa was also used at some conditions to investigate pressure effects.

Table 3-1. Gas phase densities.

	Syngas in a FT SBCR (~240 °C, ~3 MPa)	High pressure air (Room temperature, 1.0 MPa)
Composition	CO, H ₂ , CO ₂ , H ₂ O	N ₂ , O ₂
Density, kg/m ³	7~14	11.8

3.2.2. Liquid Phase Selection

The liquid phase in a FT SBCR is typically a mixture of various paraffins, olefins, and alcohols at high temperature. In order to match the liquid density, viscosity, and surface tension, a hydrocarbon mixture (C₉~C₁₁) supplied by Sasol was selected, which mostly consists of C₉, C₁₀, and C₁₁ normal paraffins, referred to as C₉C₁₁ in this work. Table 3-2 shows the physical properties of typical FT wax at FT conditions, and other liquids at room temperature, including C₉C₁₁, Therminol (used in Shaikh, 2007), and water (used in Rados, 2003). It can be seen that C₉C₁₁ and Therminol are both within the range of FT wax properties, while water has obviously higher surface tension and density. However, Therminol is an aromatic chemical and historically has caused health and safety concerns during previous experiments, which motivated the selection of the relatively environmentally benign liquid, C₉C₁₁, in this work. Because of this liquid change, this work also used Therminol for a limited number of conditions. The differences in the hydrodynamics using these two liquids were examined with and without FT catalyst. The results obtained in the air-Therminol-FT catalyst system can be compared to Shaikh (2007)'s air-Therminol-glass beads system to quantify the differences of using FT catalyst and glass beads.

Table 3-2. Physical properties of various liquids

	Typical FT wax	Sasol wax	C ₉ C ₁₁	Therminol	Water
T, °C	200~250	240	25	25	25
P, MPa	3~5	3.1	0.1	0.1	0.1
ρ _L , kg/m ³	650-900	691	728	866	998
μ _L , Pa·s	0.0005-0.0010	0.00081	0.00084	0.00088	0.00090
σ, N/m	0.015-0.030	0.0166	0.0232	0.017	0.072

3.2.3. Solids Phase Selection

Due to the difficulties involved with smaller radioactive tracer particles, most of the reported SBCR hydrodynamic studies used 150 μm or larger glass beads, which are larger than FT catalyst particles. The technical issues related to smaller radioactive

particles were recently resolved, and hence real FT catalyst carriers were used as the solids phase to quantify the solids effects in the mimicked FT SBCR. FT catalyst carrier particles are inert, porous, alumina based catalyst skeletons, with the same physical properties (size, density, and porosity) as the active catalyst. As measured by the providing company, the mean size (by volume) of these particles is about 75 μm , significantly smaller than the glass beads (150 μm) used in Rados (2003) and Shaikh (2007). As another difference from the glass beads, these FT catalyst carriers have certain porosity. The inert FT catalyst carrier is referred to as FT catalyst, since this work focused on cold-flow experiments without reactions involved.

3.3. Reactor Setup

This hydrodynamic study was conducted in two SBCRs, which were similarly configured, with only some design differences in the column for different measurements. Figure 3-1 schematically shows the experimental setup, which can represent both reactor units. Two compressors in parallel provide high pressure air at 200 psig (intake flow is 158 SCFM for each compressor), filtered and regulated before entering the rotameters. Four rotameters with different scales were connected in parallel for a wide range of flow rate indication (10 to 10000 SCFH). The operating pressure of the reactor was determined by adjusting the back pressure regulator and was guaranteed within a safe operation range by the safety release valve. Liquid and solids were loaded from the top for semi-batch operation and unloaded from the drain valve near the bottom.

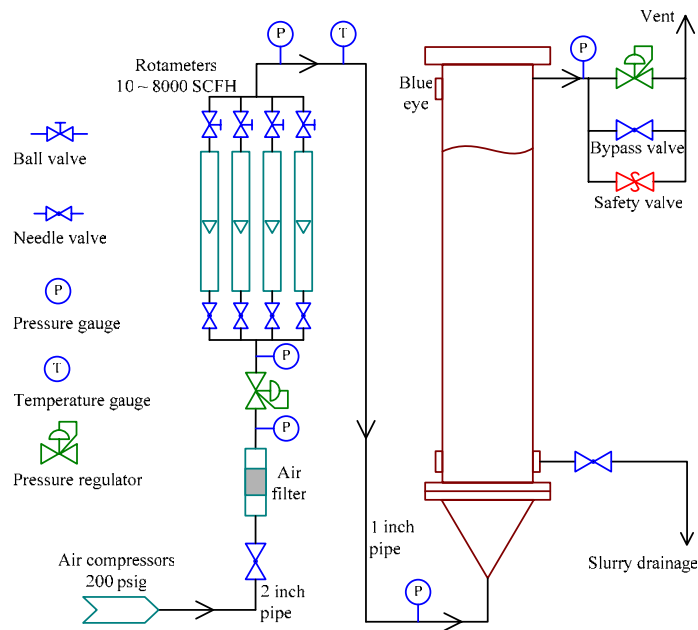


Figure 3-1. Schematic diagram of the reactor setup

The reactors in the two units have mostly identical geometry except for the ports and eye windows. They were first designed for Ong (2003) and Rados (2003), and then used in Shaikh (2007) and this work. Figures 3-2(a) and 3-2(b) show the two reactors. The SBCR (I) (Figure 3-2a) has a plain design without any ports or connections on the reactor wall. This plain design is suitable for conducting CT and CARPT experiments since non-symmetric metal parts complicate γ -ray attenuation and the data reconstruction. The SBCR (II) (Figure 3-2b) has threaded ports for implementing probes or sensor techniques, and has transparent ports for observing the bed expansion in overall gas holdup measurements. The inner diameter of these SBCRs is 6-3/8 inches (0.162 m) and the total height is 2.52 m. Stainless steel perforated plates of the same design were used as the gas distributors (spargers), with 163 holes of 1.32 mm diameter arranged in a triangular pattern and a total open area of 1.09% (Figure 3-3). Ong (2003) and Rados (2003) investigated the sparger effects on the hydrodynamics in two-phase and three phase systems, respectively. They found the sparger effects negligible or small at conditions deep in the churn-turbulent flow regime. Since this

study was focused on high superficial gas velocity conditions, one gas sparger design was used for all the studied conditions. The selected sparger was named PPH (perforated plate with huge holes) in Ong (2003) and Rados (2003). The large hole size and open area in the selected gas distributor are necessary for high gas throughput with a pressure drop that is sustainable by the compressor capacity.

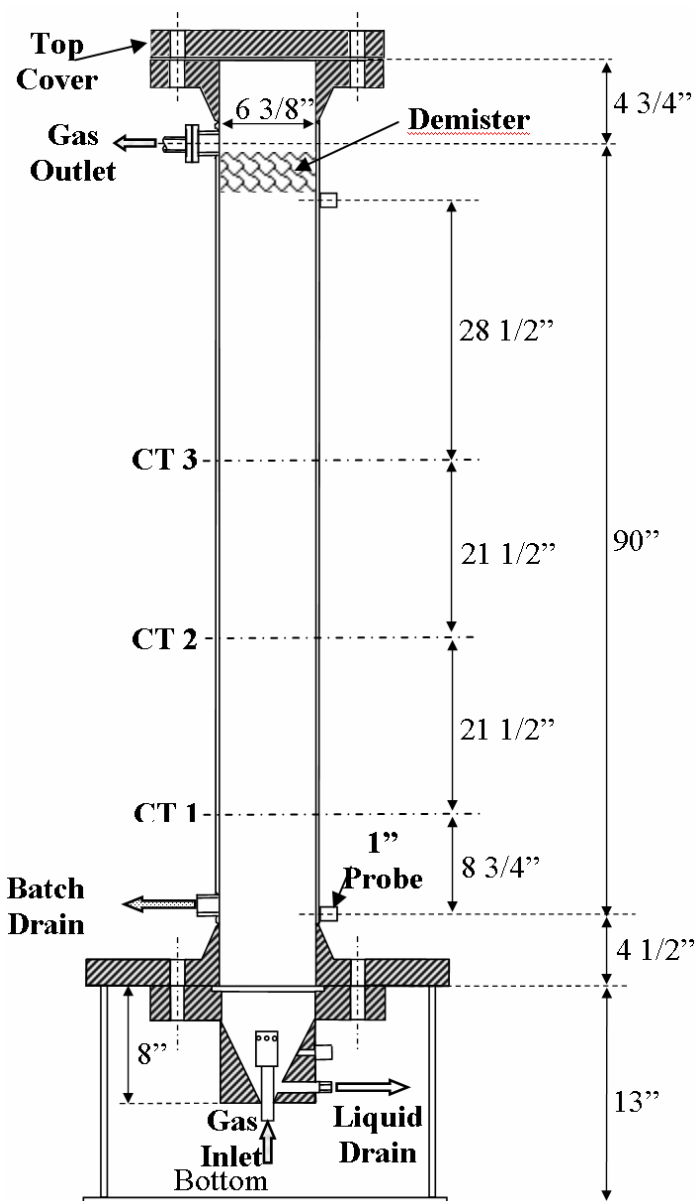


Figure 3-2 (a). SBCR (I): 6-inch stainless steel slurry bubble column reactor (plain design)

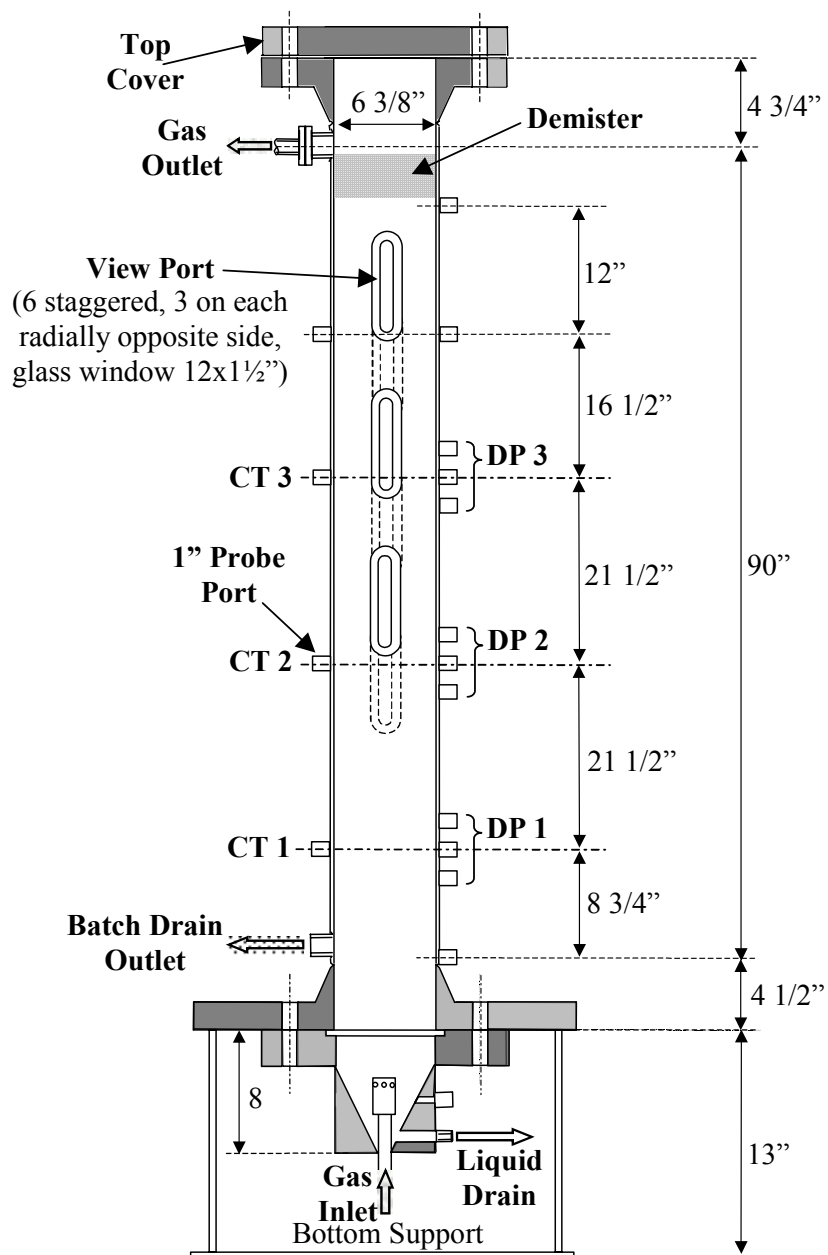


Figure 3-2 (b). SBCR (II): 6-inch stainless steel slurry bubble column reactor (with ports)

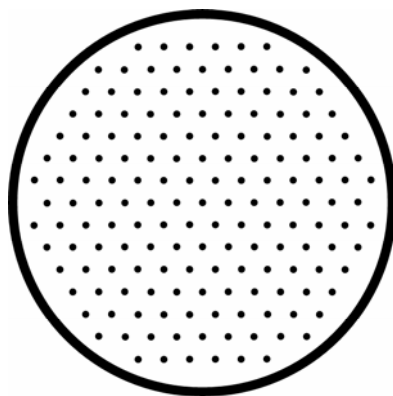


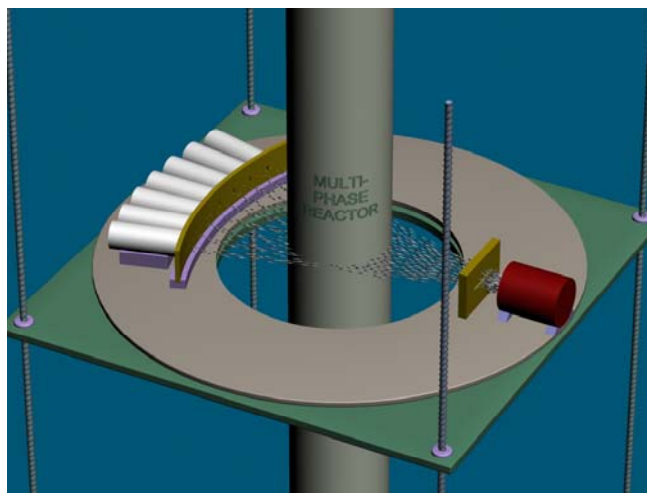
Figure 3-3. Schematic diagram of the gas distributor (holes shown not to scale)

3.4. CT Experiments

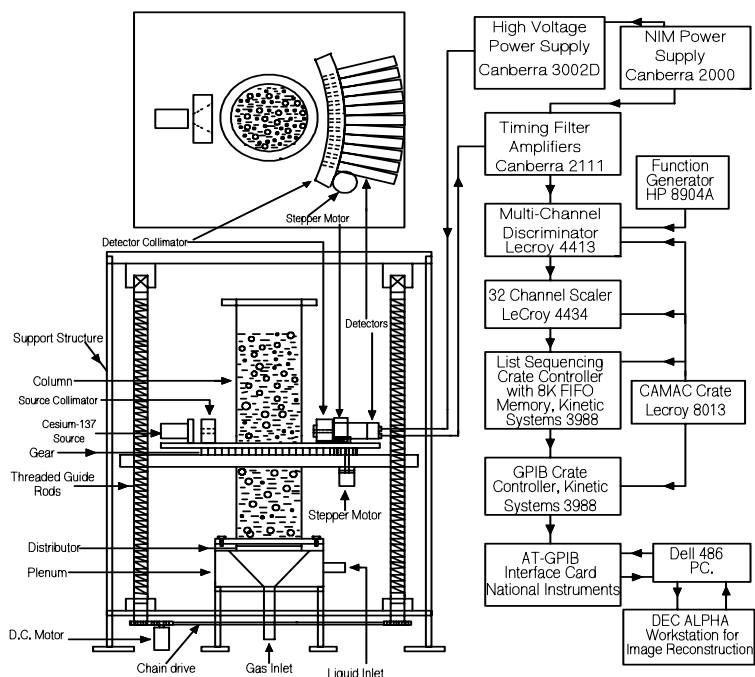
3.4.1. CT Setup

In the CREL, the single-source γ -ray CT technique has been implemented in various multiphase reactors using gas-liquid, gas-solids, liquid-liquid, and gas-liquid-solids systems. Details of the CT technique and its mechanism have been presented in Kumar (1994) and other following studies. Figure 3-4 schematically shows the single-source CT unit used in this study, which was also used in Ong (2003), Rados (2003), and Shaikh (2007) for BCRs and SBCRs. This CT setup consists of a single γ -ray source and an array of 5 NaI scintillation detectors. At the time of the experiments, the encapsulated Cesium (C^{137}) source (nominally 100 μCi) had an approximate activity of 85 μCi . Cs^{137} is one of the 30 plus Cesium isotopes and has a half life of 30.23 years. It decays by pure β -decay, producing Barium-137, which creates all the γ -ray emissions with an energy of 662 KeV. The source is collimated to provide a fan shape γ -ray beam. Each of the detectors contains a cylindrical 2X2 inch fluor crystal of NaI, a photomultiplier, and electronics. The NaI scintillator absorbs γ -ray or X-ray and emits photons at a characteristic wavelength to release the absorbed energy, which can be easily detected by a photomultiplier tube (PMT). The detector collimator can move in the azimuthal direction (with the Cs^{137} source as the center) to create 7 projections on each detector. The source assembly and detector assembly are mounted on a plate

which rotates around the reactor, providing 99 views in each scan. Also, the plate can be moved in the vertical direction by the step motor and gears for measurements at different axial locations.



a) 3-D demonstration of the CT setup for the 6" SBCR



b) CT movement mechanism and data acquisition (Kumar, 1994)

Figure 3-4. Schematic diagram of the single source CT technique

The CT scan sampling rate was selected as one set of samples (114 samples) at 20 Hz, which took approximately 7 seconds to finish a projection and 1.5 hours to finish a complete scan. Counts received at the five detectors were recorded by the PC. In the reconstruction process for three-phase systems, single-source CT scans alone are not sufficient. As a solution to this problem, the CT/overall gas holdup method was developed by Rados (2003) and used by Shaikh (2007), as discussed in section 3.4.3. In addition, a new CT/CARPT occurrence method is presented by this work in section 3.6.

3.4.2. CT Experimental Conditions

CT experiments were carried out in the 6-inch (0.162 m) stainless steel SBCR (I) introduced above. During the operation, the dynamic bed height was kept at 1.80 m for all the conditions by proportionally adjusting the liquid and solids loaded. Keeping the same dynamic bed height, instead of the same static slurry height, at different conditions allows fair comparisons of the maps of various hydrodynamic parameters and keeps the relative axial positions of probes in the bed the same. Since the L/d_c ratio is large, the distributor zone and disengagement zone at the two ends of the reactor occupy a small portion of the bed (Degaleesan, 1997). Hence, this study focuses on the fully developed region by conducting CT scans at three axial levels, including 0.33 m ($2.0 d_c$), 0.89 m ($5.5 d_c$), and 1.45 m ($9.0 d_c$). The experimental conditions were selected to cover different operating parameters that are consistent with the previous studies in different systems (Table 3-3).

Unlike the previous studies using glass beads, the catalyst particles in this work are porous, and the definition of the solids loading needs to be clarified here. The porous particles (catalyst skeletons) with liquid filling in the pores are counted together as the solids in calculating the solids loading. The liquid in the pores exchanges with the bulk at a rate much slower than the turbulent movement of the bulk liquid and therefore can be considered as part of the porous particles. Hence, to have comparable results with previous glass beads studies, the solids loading is defined as

$$C_s = \frac{\text{volume of solids (soaked with liquid)}}{\text{total volume of slurry (gas free)}} \quad (3-1)$$

It is noted that the total volume of the slurry is equal to the sum of the liquid volume and the dry solid material (skeleton) volume. In other words, the total slurry volume is equal to the sum of the volume of the free liquid in the reactor and the volume of the soaked solids, provided that the porous catalyst is fully wetted with almost no unfilled pores.

A different volume fraction, which is based on the catalyst skeleton (excluding the pores' volume), had to be used in the CT reconstruction process due to the density mechanism of CT. However, the final results of solids loading or solids holdup are always converted and presented using the definition of Equation 3-1.

Table 3-3. List of the CT experimental conditions

System	u_g , m/s	Pressure, MPa	Solids loading	Axial level
Air-Therminol	0.30	1.0	0	5.5 d _c
	0.20	1.0	0	5.5 d _c
	0.30	0.1	0	5.5 d _c
	0.20	0.1	0	5.5 d _c
Air-Therminol-FT Catalyst	0.30	1.0	25% vol.	2.0/5.5/9.0 d _c
	0.20	1.0	25% vol.	2.0/5.5/9.0 d _c
	0.30	0.1	25% vol.	2.0/5.5/9.0 d _c
	0.30	1.0	9.1% vol.	2.0/5.5/9.0 d _c
Air-C ₉ C ₁₁	0.30	1.0	0	2.0/5.5/9.0 d _c
	0.20	1.0	0	2.0/5.5/9.0 d _c
	0.30	0.1	0	2.0/5.5/9.0 d _c
	0.20	0.1	0	2.0/5.5/9.0 d _c
Air-C ₉ C ₁₁ -FT Catalyst	0.30	1.0	25% vol.	2.0/5.5/9.0 d _c
	0.30	0.1	25% vol.	2.0/5.5/9.0 d _c
	0.20	1.0	25% vol.	2.0/5.5/9.0 d _c
	0.20	0.1	25% vol.	2.0/5.5/9.0 d _c
	0.30	1.0	9.1% vol.	2.0/5.5/9.0 d _c
	0.30	0.1	9.1% vol.	2.0/5.5/9.0 d _c
	0.20	1.0	9.1% vol.	2.0/5.5/9.0 d _c
	0.20	0.1	9.1% vol.	2.0/5.5/9.0 d _c

3.4.3. CT Reconstruction Algorithms

This work conducted CT experiments in both two-phase and three-phase conditions, and therefore involves reconstruction algorithms for both two-phase and three-phase systems. The two phase reconstruction is only briefly mentioned here, because it is straightforward and has been presented by Kumar (1994). The CT/overall gas holdup algorithm presented by Rados (2003) for three phases with single-source CT scans was slightly modified for the porous solids in this work, as presented below. After introducing the CARPT experiments in section 3.6, a new CT reconstruction algorithm for three phases with single-source CT scans, the CT/CARPT occurrence method, is presented in detail as an alternative algorithm to Rados' CT/overall gas holdup method.

CT Reconstruction Algorithm for Two Phase Systems

The reconstruction algorithm of Kumar (1994) was used for the two-phase CT conditions in this work that were selected to study the solids loading effects. The holdup reconstruction was performed in a right angle coordinate system with the center of the column cross-section as the origin of the coordinate. The cross-section is covered by a 2-D square divided into a 32 x 32 evenly distributed mesh, which decides the resolution of the tomography results. The Estimation-Minimization (E-M) algorithm (Dempster et al., 1977; Kumar, 1994; Rados; 2003) was used for the reconstruction of the cross-sectional distribution of relative attenuation. The two-phase reconstruction procedures have been described extensively in Kumar (1994) and used in Chen et al. (1999) and Ong (2003). Hence, their details are not discussed here.

CT/Overall Gas Holdup Reconstruction Algorithm with Porous Solids

As mentioned earlier, the single CT scans can not independently determine the holdup distributions in a three-phase system. Rados (2003) developed the CT/overall gas holdup method solve this problem, which was later used by Shaikh (2007). The difference between this work and Rados (2003) and Shaikh (2007) is that the solids were porous and soaked with liquid in the SBCR. The CT/overall gas holdup method

needs to be slightly modified to be implemented for the FT catalyst. Due to the mechanism of the tomography, only the volume of the solid material (catalyst skeletons) is considered as the solids phase during the reconstruction. Then the obtained solids phase holdup, ε_s' , was converted into the holdup of whole porous catalyst particles, ε_s , for the final result by

$$\varepsilon_s = \varepsilon_s' / (1 - \phi_p), \quad (3-2)$$

where ϕ_p is the catalyst particle porosity, defined as the volume fraction of the voidage (pores) in the spherical particles.

According to Rados (2003)'s reconstruction algorithm, equations of relative attenuation are obtained from the set of four gamma-ray scans

$$R_{K,ij} = (\rho\mu)_{K,ij} - (\rho\mu)_{g,ij}, \quad (3-3)$$

where $K=l, gs, \text{ or } gls$, and i and j are the index numbers of the cells in the x and y directions, respectively. Therefore, three equations are obtained from the reconstruction of the relative attenuation for each cell in the reconstruction mesh. The attenuation of multiphase mixtures are linear combinations of that of each phase, expressed as

$$(\rho\mu)_{gs,ij} = (1 - \phi_s') \cdot (\rho\mu)_{g,ij} + \phi_s' \cdot (\rho\mu)_{s,ij} \quad (3-4)$$

$$(\rho\mu)_{gls,ij} = \varepsilon_{g,ij} \cdot (\rho\mu)_{g,ij} + (1 - \varepsilon_{g,ij} - \varepsilon_{s,ij}') \cdot (\rho\mu)_{l,ij} + \varepsilon_{s,ij}' \cdot (\rho\mu)_{s,ij}, \quad (3-5)$$

where ϕ_s' is the volume fraction of the solid material in the space where solids are statically packed in air, measured in a dry column. The three equations of the reconstructed relative attenuation (Equation 3-3) can be written as

$$R_{l,ij} = (\rho\mu)_{l,ij} - (\rho\mu)_{g,ij}, \quad (3-6)$$

$$R_{gs,ij} = \phi_s' [(\rho\mu)_{s,ij} - (\rho\mu)_{g,ij}], \text{ and} \quad (3-7)$$

$$R_{gls,ij} = \varepsilon_{g,ij} [(\rho\mu)_{g,ij} - (\rho\mu)_{l,ij}] + \varepsilon_{s,ij}' [(\rho\mu)_{s,ij} - (\rho\mu)_{l,ij}] + [(\rho\mu)_{l,ij} - (\rho\mu)_{g,ij}]. \quad (3-8)$$

Combining Equations 3-6 ~ 3-8 yields an expression of the gas holdup

$$\varepsilon_{g,ij} = \frac{\varepsilon_{s,ij}' \frac{R_{gs,ij}}{\phi_s'} + (1 - \varepsilon_{s,ij}') R_{l,ij} - R_{gls,ij}}{R_{l,ij}} \quad (3-9)$$

There are two unknowns in Equation 3-9 because there is always one more degree of freedom than the attenuation equations when a single-source γ -ray CT is applied to a dynamically moving three-phase system. As a solution, Rados (2003) made two assumptions based on previous experimental evidence:

- 1) The cross-sectional average gas holdup is axially invariant, and is approximately equal to the overall gas holdup. This assumption is supported by several other experimental studies for the fully developed regime at a certain range of conditions (Matsumoto et al., 1992; Bukur et al., 1996; George et al., 2001).
- 2) The solids loading (solids volume concentration in the gas-free slurry, i.e., liquid and solids only) is uniform within a cross-section, which was previously reported for the fully developed regime in a certain range of conditions (Badgujar et al., 1986; Hu et al., 1986; Warsito et al., 2003).

From the second assumption, the solids holdup becomes dependent on the gas holdup in each reconstruction pixel. Hence, an equation is obtained, written as

$$\varepsilon_{s,ij}' = \bar{C}_s(z) \cdot (1 - \varepsilon_{g,ij}), \quad (3-10)$$

where $\bar{C}_s(z)$ is the cross-sectional average solids concentration. Substituting Equation 3-10 into Equation 3-9 yields

$$\varepsilon_{g,ij} = 1 - \frac{R_{gls,ij}}{\frac{\bar{C}_s(z)}{\phi_s'} R_{gs,ij} + (1 - \bar{C}_s(z)) R_{l,ij}} \quad (3-11)$$

There is still one unknown parameter, $\bar{C}_s(z)$, in Equation 3-11, which can be determined with the help of the first assumption. For each given $\bar{C}_s(z)$ value, the cross-sectional distribution of the gas holdup, $\varepsilon_{g,ij}$, and therefore, the cross-sectional average, $\bar{\varepsilon}_g$, can be calculated. The $\bar{C}_s(z)$ value for each cross-section is determined by the minimum square error fit between the calculated cross-sectional average gas

holdup, $\bar{\epsilon}_g$, and the measured overall gas holdup $\bar{\epsilon}_{g,0}$. The solids phase (skeleton material) holdup is then obtained by Equation 3-10, and converted into the holdup of liquid-filled catalyst particles according to Equation 3-2.

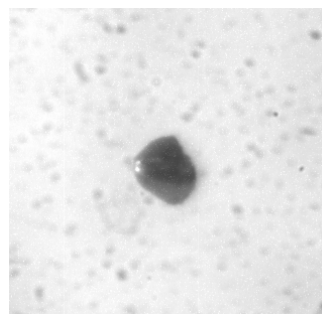
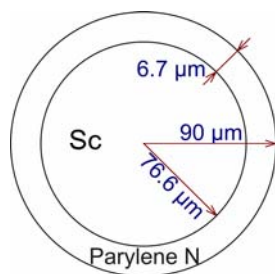
3.5. CARPT Experiments

3.5.1. Radioactive Tracer Particles

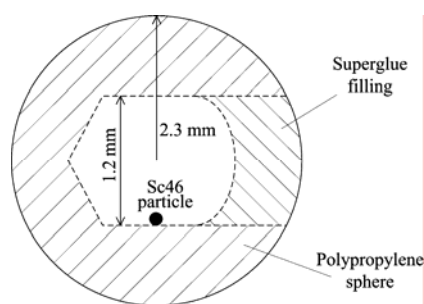
The CARPT technique requires a radioactive tracer particle that can track the flow in a multiphase reactor. Sc^{46} has been used as the isotope tracer material in the CREL (Degaleesan, 1997; Chen et al., 1999; Ong, 2003; Rados, 2003). It was selected out of several candidate isotopes, including Co^{60} and Au^{198} . The half-life of Sc^{46} is 83.8 days, which is sufficient to conduct a series of experiments, while not too long to cause additional safety issues. Sc^{46} β -decays into Ti^{46} , which then emits soft γ -ray at 889 KeV and 1120 KeV. A γ -ray at this energy has good attenuation in its path through the slurry and stainless steel reactor wall. Parylene N was used as the material to coat the particles to match the solids' density and size, and also to protect the Sc^{46} particle with improved thermal stability, mechanical strength, and chemical stability.

The previous CARPT studies in the CREL all used 150 μm or larger tracer particles (Ong, 2003; Rados, 2003; Bhusarapu, 2005; Luo, 2005; and Shaikh, 2007). In this work, the catalyst particles were much smaller, with a mean size of $\sim 75 \mu\text{m}$, which caused additional difficulties in irradiating and handling Sc^{46} tracer particles. The tracer particles must contain sufficient scandium mass to be irradiated to the desired activity within an acceptable time length, and they also need to equal or be reasonably close to the small size of the FT catalyst. Balancing between these two factors, the outer diameter of the coated tracer particles was determined as 90 μm . Although this size is not exactly the mean size of the solids, catalyst particles larger than 90 μm constitute 40-45% of the whole size distribution, according to the providing company. With the diameter of the whole (coated) particle determined, the diameter of the Sc metal sphere is also fixed to match both the size and apparent density of the FT catalyst.

As shown in Figure 3-5(a), the calculated diameter of the naked Sc metal spheres is 76.7 μm , which means the Sc mass contained in each particle is 0.7 μg . The desired thickness of the Parylene N coating is 6.7 μm according to the calculation. Based on the Sc mass in each particle, the irradiation time was 42 days (1000 hours) at a flux of thermal neutrons of $8.0 \times 10^{13} \text{ n/cm}^2\text{-s}$ to achieve radioactivity of 150 μCi per particle, as calculated by the University of Missouri Research Reactor Center (MURR). Before the actual irradiation, a lengthy and costly technical evaluation process was conducted and special safety procedures were established by MURR to handle such small tracer particles with this long irradiation time.



a) Schematic of the Sc particle dimensions b) Microscopic picture of a Sc particle



c) Schematic of a polypropylene ball d) Picture of a polypropylene ball

Figure 3-5. Parylene N coated Sc particle and polypropylene ball with dimensions

The Sc particles were manufactured by Arris International Corporation from the material provided by them. The metal has a purity of 99.9+%, and other radio-nuclides are negligible. The naked Sc metal particles were received in inert helium gas in a

sealed container to prevent oxidation. The Sc particles were then coated with Parylene N by vaporization of Parylene N dimmer at Para Tech Coating, Inc. Two coated particles were selected under a microscope by visually evaluating their size, shape, and quality of coating. Figure 3-5(b) shows one of the coated particles under the microscope. The selected two particles were then separated from any fragments, put into a quartz vial (3 inches long), sealed with inert helium gas, and sent to MURR for irradiation. The irradiated Sc⁴⁶ particles were examined under the microscope again for any possible damage before being used in the CARPT experiments.

For liquid tracking, one of the irradiated Sc particles was put into a hollow polypropylene ball with a 2.3 mm outer diameter. The first attempts used a smaller polypropylene ball (0.8 mm). However due to the influence of the organic liquid on the sealing and density adjusting materials, it was difficult to match the density of the composite ball to that of the liquid. The 2.3 mm polypropylene ball, holding more sealing material, was found to keep the desired density better and longer than the smaller 0.8 mm ball. As shown in Figures 3-5(c) and (d), the polypropylene ball was drilled with an 1.2 mm hole. The active Sc⁴⁶ particle was put into the hole, which was then sealed with a plug and superglue. Some air was kept in the polypropylene ball to adjust its overall density. Fine adjustment was made by slightly filing off some polypropylene to reach the density of the C₉C₁₁ liquid, which is 728 kg/m³. The apparent density of this composite ball was checked by measuring its terminal settling velocity in the C₉C₁₁ liquid in a long measuring cylinder. The final terminal settling velocity was less than 0.5 cm/s, from which the ball density was calculated to be within a 0.2% difference from the liquid by

$$\rho_p = \rho_l + \frac{u_s 18\mu_l}{d_p^2 g}, \quad (3-12)$$

which is derived from Stoke's equation

$$u_s = \frac{d_p^2 (\rho_p - \rho_l) g}{18\mu_l}, \quad (3-13)$$

where u_s = velocity of sedimentation; d_p = diameter of the particle; ρ_p = density of the particle; ρ_l = density of the liquid; g = acceleration of gravity; μ_l = viscosity of the liquid.

3.5.2. CARPT Setup and Procedures

The CARPT setup for high pressure applications used in this work was developed by Rados (2003), and used by (Ong, 2003) and Shaikh (2007). This CARPT setup includes an automatic calibration device, a controlling mechanism for the motors, and a signal processing and data acquisition system. As shown in Figure 3-6, thirty NaI scintillation detectors, which are same as those used in CT, were arranged in 8 vertical columns at equally distributed angles around the reactor. Each pair of axis-symmetrical opposite-facing detectors were at the same height (axial distance), and a total of 15 axial levels covered the whole fully developed region of the SBCR. The distance of the detectors to the reactor wall was adjusted while moving the Sc^{46} particle in the reactor so that good attenuation was obtained at various particle-detector distances. The determined detector coordinates, listed in Table 3-4, were used as the input in the reconstruction. The radial distance was defined as the shortest length from the reactor axis to the center of the scintillator in a detector. The γ -ray emitted by the tracer particle in the reactor was detected by the 30 detectors, and the signal was recorded as photon counts at a 50Hz sampling rate. Details of the signal processing and data acquisition have been covered in previous CARPT works in the CREL, including Kumar et al. (1997), Ong (2003), and Rados (2003).

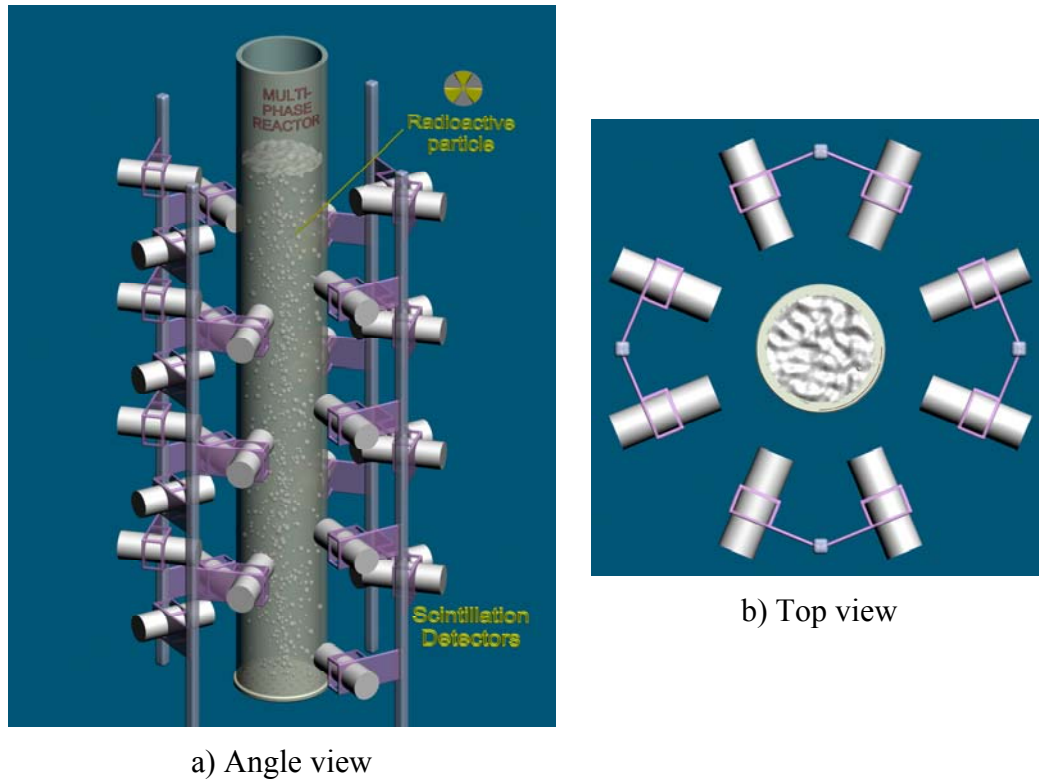


Figure 3-6. 3-D demonstration of the CARPT setup for the 6'' SBCR

Table 3-4. Coordinates of the CARPT detectors

Detector	z, cm	r, cm	θ , °	Detector	z, cm	r, cm	θ , °
1	30	17	0	16	30	17	180
2	47	17	45	17	47	17	225
3	64	17	0	18	64	17	180
4	81	17	45	19	81	17	225
5	98	17	0	20	98	17	180
6	115	17	45	21	115	17	225
7	132	17	0	22	132	17	180
8	149	17	45	23	149	17	225
9	140.5	17	90	24	140.5	17	270
10	123.5	17	135	25	123.5	17	315
11	106.5	17	90	26	106.5	17	270
12	89.5	17	135	27	89.5	17	315
13	72.5	17	90	28	72.5	17	270
14	55.5	17	135	29	55.5	17	315
15	38.5	17	90	30	38.5	17	270

A CARPT experiment consists of two parts: the calibration with known positions of the tracer particle to obtain the count-distance relation at each detector, and the experiment with a freely moving tracer particle to track the phase flow. In the calibration process, the counts were measured while the particle was positioned at 49 points at each of the 54 axial levels with an axial increment of 2.54 cm. Therefore, calibration data at a total of 2646 positions were obtained. The calibration was performed at the same operating conditions as the subsequent experiment (in-situ). In the experiment, the Sc^{46} tracer particle was released into the aerated suspension of slurry (or liquid) in the reactor. The tracer particle then followed the flow of the tracked phase, while the 30 detectors recorded the photo counts in a time series for over 20 hours. The obtained experimental data were then used for the particle location reconstruction and further processing.

3.5.3. CARPT Experimental Conditions

The CARPT experimental conditions were selected to be consistent with the previous SBCR studies (Rados, 2003; Shaikh, 2007) to quantify the differences caused by the FT catalyst. Compared with CT, CARPT must overcome more technical difficulties caused by the high pressure and the fine, porous catalyst particles. The CARPT experimental conditions were selected at a limited number of conditions (Table 3-5), which covered different superficial gas velocities, pressures, solids loadings, and liquid physical properties in the BCR or SBCR. The definition of solids loading of the porous catalyst is consistent with that defined in the CT (Equation 3-1).

Table 3-5. List of the CARPT experimental conditions

System	u_g , m/s	P, MPa	C_s , % vol.
Air-C ₉ C ₁₁	0.30	1.0	0
	0.20	1.0	0
	0.30	0.1	0
Air-C ₉ C ₁₁ -FT Catalyst	0.30	1.0	25
	0.30	0.1	25
	0.20	1.0	25
	0.30	1.0	9.1
Air-Therminol-FT Catalyst	0.30	1.0	25

3.5.4. CARPT Reconstruction Algorithm

In the CARPT reconstruction process, the particle position at each instance was reconstructed using the count-distance relation built from the calibration data. This work used the reconstruction algorithm of Degaleesan (1997), which is also shown in detail in Rados (2003). A discrete wavelet transformation (DWT) threshold filtration method developed by Degaleesan (1997) was used to remove the background noise in the Lagrangian trajectories. The threshold (st coefficient) for the filtration was selected at 0.85, consistent with Degaleesan (1997), Rados (2003), and Shaikh (2007). Different filtration thresholds (st coefficients) were employed to evaluate the influence of the threshold on the reconstruction results. It was found that the axial velocities were not affected by the st values, while the turbulent kinetic energy was significantly affected. Therefore, it is important to use a consistent st value for comparisons with the previous data. With properly filtered particle trajectory data, the turbulence parameters were then calculated according to Degaleesan (1997) and Rados (2003).

3.6. CT/CARPT Occurrence Reconstruction Method

Moslemian et al. (1992) proposed the idea of using long-time single solids tracer particle occurrence data to estimate the solids holdup in multiphase reactors, but also warned that such a method does not work in a system with solids dead zones. The SBCR in this work was operated in the churn-turbulent flow regime without any internals. Hence it is reasonable to expect no stagnant zones that are inaccessible to the solids tracer particle. Rados (2003) attempted a CT/DP/CARPT method for three-phase CT reconstruction by using pressure drop measurements around the CT planes (cross-sections), along with CARPT occurrence data within each cross-section. He found that this CT/DP/CARPT method failed because of its high sensitivity to the pressure drop measurements. However, it should be noted that if the solids tracer particle occurrence is already used and assumed to proportionally represent the solids holdup, it is sufficient in itself to assist the three-phase reconstruction without pressure drop

measurements needed. This section presents a method of using only the CARPT occurrence data to assist three-phase reconstruction from single-source CT scans.

Instead of the two assumptions made in the CT/overall gas holdup method, one different assumption is needed for this CT/CARPT occurrence method, which is that the long-time occurrences of a solids tracer particle in a compartment are proportional to the time-averaged solids holdup in the same cell, based on the idea of Moslemian et al. (1992). Therefore, the solids holdup in a reconstruction pixel, ij , within a cross-section can be calculated as

$$\varepsilon_{s,ij} = N_{p,ij} \frac{\bar{\varepsilon}_s}{\bar{N}_p}, \quad (3-14)$$

where $N_{p,ij}$ is the local occurrence density (by volume) calculated for each pixel within a thin cylinder in the cross-section and a small depth Δz , and \bar{N}_p is the overall occurrence density (by volume) in the reactor calculated by dividing the counted total occurrences by the whole dynamic bed volume. The overall averaged solids holdup $\bar{\varepsilon}_s$ is calculated from the known total solids volume loaded, V_s , and total dynamic bed volume, V_{gls}

$$\bar{\varepsilon}_s = \frac{V_s}{V_{gls}}. \quad (3-15)$$

Combining Equations 3-2 and 3-14, the volume fraction of the solid material can be calculated accordingly as

$$\varepsilon_{s,ij}' = \varepsilon_{s,ij} (1 - \phi_p) = (1 - \phi_p) N_{p,ij} \frac{\bar{\varepsilon}_s}{\bar{N}_p}. \quad (3-16)$$

With $\varepsilon_{s,ij}'$ obtained from the occurrence data, the gas holdup distribution can then be reconstructed using Equation 3-9. The results obtained using this reconstruction method are presented in the next section and compared with those obtained with the Rados (2003) method at the same example condition.

Although the CT/CARPT occurrence method is presented, this work mainly used the CT/overall gas holdup algorithm which was developed by Rados (2003) and also used by Shaikh (2007). The present work is in continuation with these two previous studies, and fair comparisons with their results are necessary to investigate the impact of FT catalyst.

3.7. Hydrodynamic Parameters at the Main Mimicked FT Condition

The CT/CARPT experimental conditions in this work were selected in line with those of Rados (2003) and Shaikh (2007). In comparison with their air-water-glass beads and air-Therminol-glass beads systems, the present work used air-C₉C₁₁-FT catalyst and obtained new hydrodynamics data at the mimicked FT conditions. Among all the selected CT and CARPT conditions, the one using high superficial gas velocity (0.30 m/s), high pressure (1.0 MPa), and high solids loading (25% vol.) was the primary condition to mimic the physical properties of a FT SBCR. Profiles of the measured parameters at this condition are shown below as an example. The CT and CARPT data beyond those shown in this chapter are provided in Appendix A.

3.7.1. Phase Holdup Distribution using Two Reconstruction Algorithms

Three-phase holdup distributions were obtained using the two reconstruction methods for three phases with single-source CT scans, which are

- Method (I) - CT/overall gas holdup method (Rados, 2003), and
- Method (II) - CT/CARPT occurrence method (presented by this work).

Figures 3-7(a) and 3-7(b) are the cross-sectional phase distributions obtained using methods (I) and (II), respectively. The color gradient in the gas holdup maps suggests that the gas holdup was lowest near the wall and increased toward the center. Axial symmetry was observed in the cross-section, similar to findings in other three-phase systems (Rados, 2003 and Shaikh, 2007). For method (I), the solids holdup was larger near the wall and decreased toward the center, in an opposite trend to the gas holdup; for method (II), the solids holdup was more uniform in the cross-section. Due to the

axial symmetry, the cross-sectional gas and solids holdup distributions can be described by their radial profiles by azimuthally averaging.

Figures 3-8 and 3-9 show the radial profiles of the phase holdups using reconstruction methods (I) and (II), respectively. For method (I), the exactly identical cross-sectional average gas holdups at the three axial levels are likely a result of the first assumption in the CT/Overall gas holdup method (axially invariant gas holdup), as also seen in Rados (2003) and Shaikh (2007). For method (II), some magnitude differences in gas holdup between the three axial levels were observed. Using reconstruction method (II), the gas holdup appears to decrease slightly along the axial distance at all the three-phase conditions. It was found that at the two-phase conditions, the gas holdup increased along the axial distance in the air-C₉C₁₁ system. In the air-water BCR, Ong (2003) obtained two different trends: the gas holdup increased with the axial distance at the majority of her CT conditions (the same as the two-phase conditions in this work), while the gas holdup decreased with the axial distance at a few of her CT conditions, including Sparger PPS, 0.14 m/s, 0.1 MPa; Sparger PPL, 0.14 m/s, 0.1 MPa; Sparger PPL, 0.45 m/s, 0.4 MPa; Sparger PPN, 0.14 m/s, 0.1 MPa. It is unknown whether the different axial trends of gas holdup in the CT results are from measurement errors or other sources. Using a four-point probe technique developed by Xue et al., 2003, Xue (2004) observed no gas holdup change along the axial distance at low pressure in the air-water system, and increasing gas holdup with axial distance at high pressure (opposite trend to this study). Xue (2004) explained this finding by measurements of small and large bubble numbers. At high pressure in the air-water system, the bubble frequency was higher near the top than near the bottom, indicating accumulation of bubbles in the upper section of the column. Without investigation of the bubble dynamics in the mimicked FT SBCR, it is difficult to explain the axial gas holdup trend observed using reconstruction method (II). A possible reason for the axial trend in Figure 3-9(a) is that the some small bubbles still keep coalescing slowly in the fully developed zone under the effect of the large amount of solids, further generating larger bubbles which rise faster and reduce the gas holdup slightly along the column.

Regarding the solids holdup, apparent differences were observed between the results using the two reconstruction methods, as shown in Figures 3-8(b) and 3-9(b). The solids holdup (and therefore solids concentration) has a larger axial gradient in the method (II) results than in the method (I) results. The difference is likely caused by the fact that the magnitude of the solids holdup obtained using method (I) is affected by arbitrarily adjusting the cross-sectional average gas holdup to satisfy the first assumption in this reconstruction method. Therefore, a difference between the real cross-sectional average gas holdup and the measured overall gas holdup, more or less, will result in errors in the reconstructed solids holdup magnitude. The axial dispersion of the FT catalyst in the mimicked FT SBCR was quantified using the SDM in Chapter 4. In the radial profiles reconstructed by method (I), the solids holdup is apparently higher near the wall than at the center. Because of the second assumption in method (I) (constant solids concentration in the cross-section), the relative (normalized) shape of the solids holdup radial profiles is completely dependent on the gas holdup radial profiles at corresponding levels. For method (II), the solids holdup was determined independently and shows only small radial differences. The solids holdup profiles from method (II) indicate that the solids concentration (defined in Equation 3-1) in the slurry is higher in the center than near the wall, as confirmed by a simple calculation (Figure 3-10). In contrast, the solids concentration obtained with method (I) is arbitrarily constant in cross-section. The radial differences in the solids concentration (higher in the center) obtained by method (II) can be explained by global recirculation of the slurry and the axial solids concentration gradient. Due to the solids sedimentation, there is an apparent axial gradient in the solids concentration along the reactor height. The upward flow in the reactor center brings up higher concentration slurry from the bottom, while the downward flow near the wall brings down lower concentration slurry from the reactor top. In comparison to the constant solids concentration assumption in method (I), it is more reasonable to have higher solids concentration at the center than near the wall in the fully developed region.

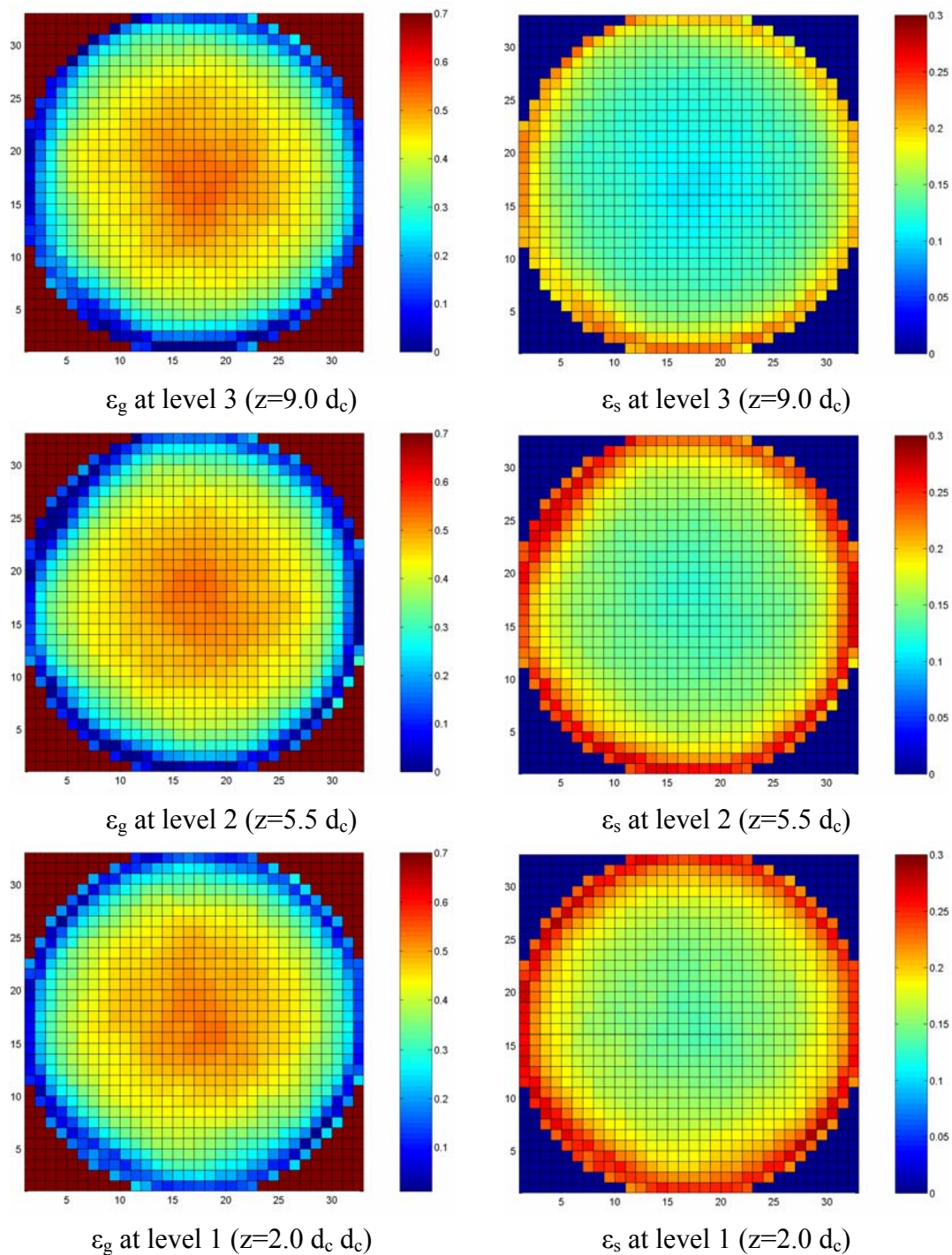


Figure 3-7 (a). Cross-sectional distributions of the gas and solids holdups using reconstruction method (I) – the CT/overall gas holdup method, air-C₉C₁₁-FT catalyst, 25% vol., 0.30 m/s, 1.0 MPa

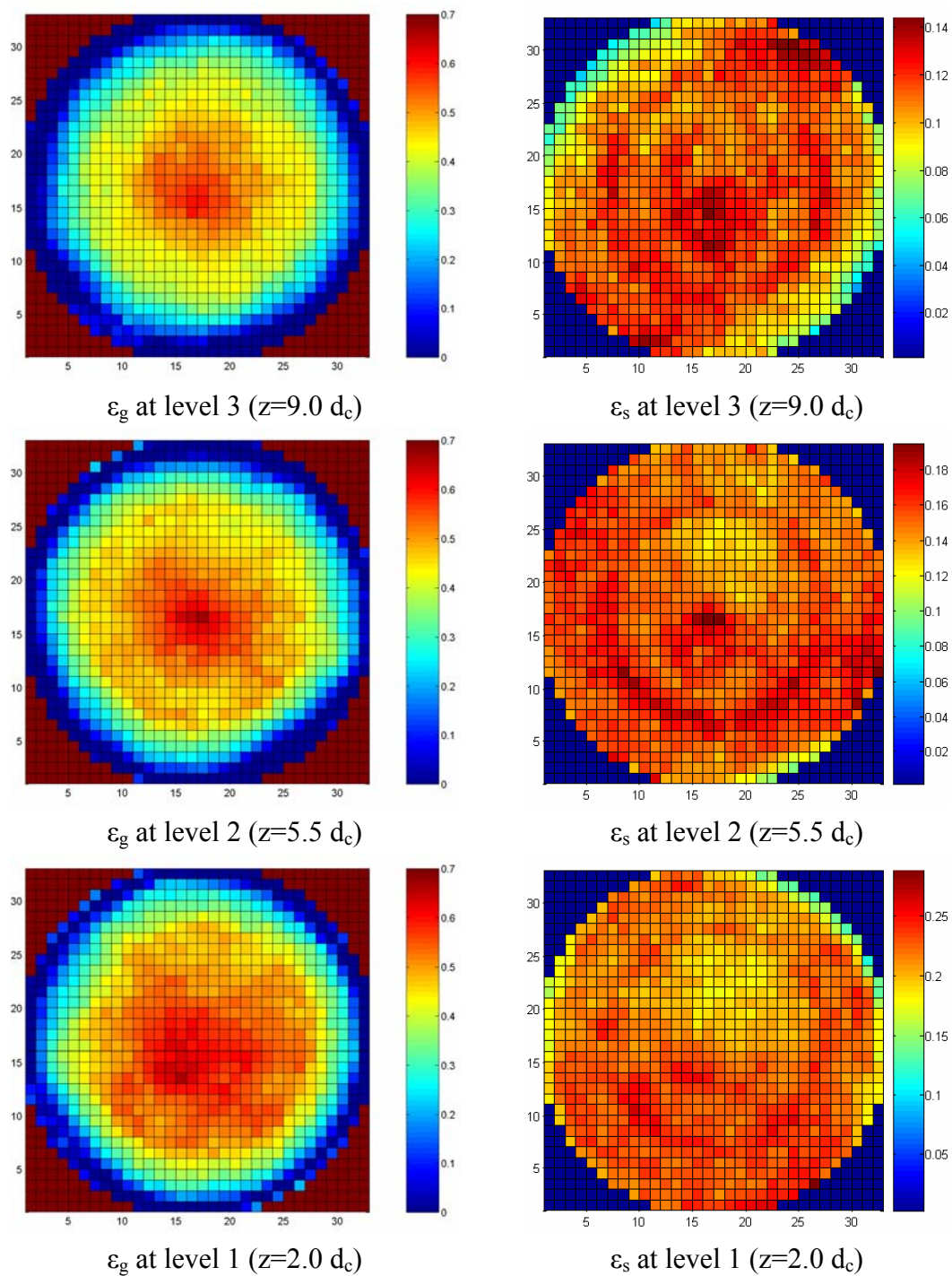
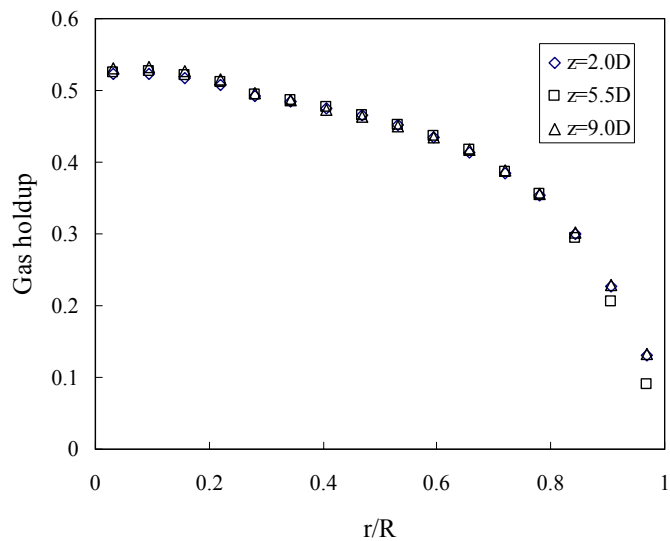
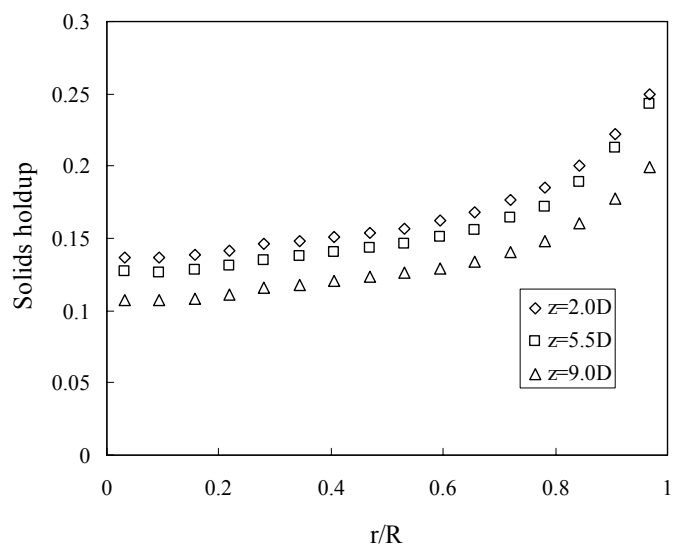


Figure 3-7 (b). Cross-sectional distributions of the gas and solids holdups using reconstruction method (II) – the CT/CARPT occurrence method, air-C₉C₁₁-FT catalyst, 25% vol., 0.30 m/s, 1.0 MPa

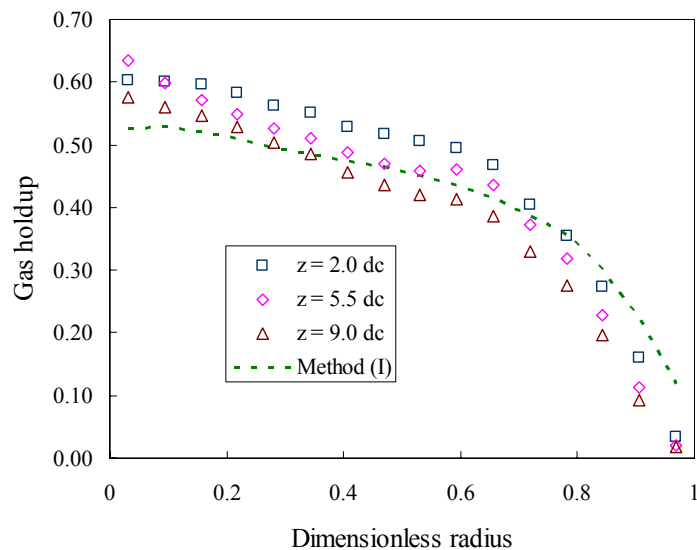


a) Gas holdups radial profiles – method (I)

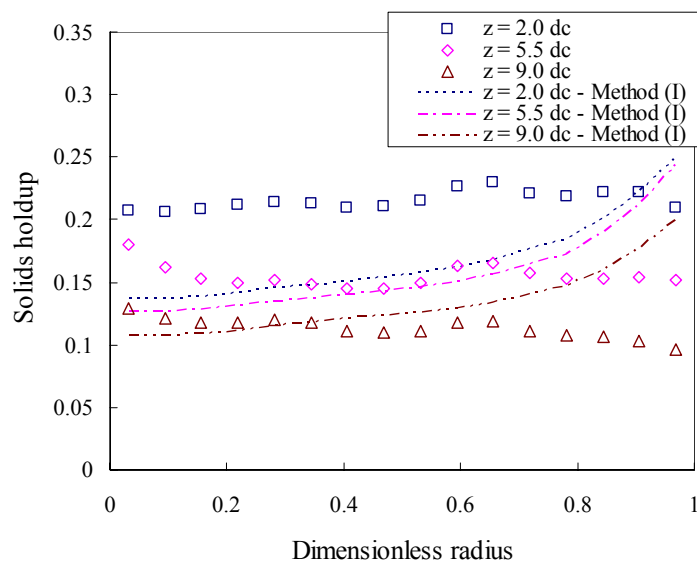


b) Solids holdups radial profiles – method (I)

Figure 3-8. Radial profiles of the gas and solids holdups using reconstruction method (I) – the CT/overall gas holdup method, air-C₉C₁₁-FT catalyst, 25% vol., 0.30 m/s, 1.0 MPa



(a) Gas holdup radial profiles – method (II)



(b) Solids holdup radial profiles – method (II)

Figure 3-9. Radial profiles of the gas and solids holdups using reconstruction method (II) – the CT/CARPT occurrence method, compared with results of method (I), air-C₉C₁₁-FT catalyst, 0.30 m/s, 1.0 MPa, 25% vol.

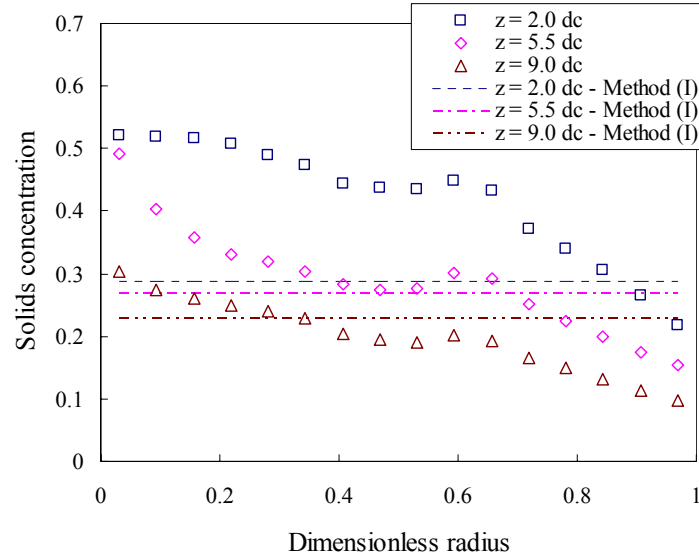


Figure 3-10. Radial profiles of the solids concentration in slurry using reconstruction method (II) – the CT/CARPT occurrence method, compared with results of method (I), air-C₉C₁₁-FT catalyst, 0.30 m/s, 1.0 MPa, 25% vol.

The radial gradient in the gas holdup magnitude drives the global slurry recirculation due to the density difference it dictates. This effect can be quantified by calculating the steepness of the gas holdup radial profile by fitting the curve with models introduced in Chapter 2. The correlation reported by Luo and Svendsen (1991) (Equation 2-3, also shown below) was used on the obtained gas holdup profiles, and two parameters, n and c , were fitted.

$$\varepsilon_g(r) = \bar{\varepsilon}_g \left(\frac{n+2}{n+2-2c} \right) \left[1 - c(r/R)^n \right].$$

This expression gives radial profiles similar to a parabolic curve ($n=2$) and such shape is called parabolic for brevity. From the expression above, it can be understood that the smaller the n value, the steeper the radial profile, and vice versa. According to the assumptions made in reconstruction method (I), solids holdup profiles obtained with this method are essentially dependent on the gas holdup radial profiles with a first order linear relation. Therefore, the steepness of solids holdup profiles using the CT/overall gas holdup method was not calculated. The solids profiles obtained using

reconstruction method (II) are not parabolic and hence not fitted, either. The n values obtained for the gas holdup radial profiles obtained using method (I) at the center level ($z/d_c=5.5$) are listed in Table 3-6 for further discussion in the following sections. The radial gas holdup profiles at the three axial levels have similar shapes and n values. At 0.30 m/s, 1.0 MPa, and 25% vol. in the air-C₉C₁₁-FT catalyst system, for instance, the n values at the three levels are 3.49, 3.96, and 3.34, respectively. Therefore, the n value at the center level is representative of the gas holdup profile steepness in the fully developed region.

Table 3-6. Values of the steepness factor n obtained at CT conditions

System	u_g , m/s	Pressure, MPa	Solids loading	n (method I)
Air-Therminol	0.30	1.0	0	4.38
	0.20	1.0	0	5.01
	0.30	0.1	0	2.50
	0.20	0.1	0	2.60
Air-Therminol- FT Catalyst	0.30	1.0	25% vol.	3.90
	0.20	1.0	25% vol.	4.23
	0.30	0.1	25% vol.	2.87
	0.30	1.0	9.1% vol.	4.00
Air-C ₉ C ₁₁	0.30	1.0	0	4.59
	0.20	1.0	0	4.96
	0.30	0.1	0	3.06
	0.20	0.1	0	3.06
Air-C ₉ C ₁₁ -FT Catalyst	0.30	1.0	25% vol.	3.96
	0.30	0.1	25% vol.	4.16
	0.20	1.0	25% vol.	2.53
	0.20	0.1	25% vol.	2.18
	0.30	1.0	9.1% vol.	4.72
	0.30	0.1	9.1% vol.	4.48
	0.20	1.0	9.1% vol.	2.64
	0.20	0.1	9.1% vol.	2.63

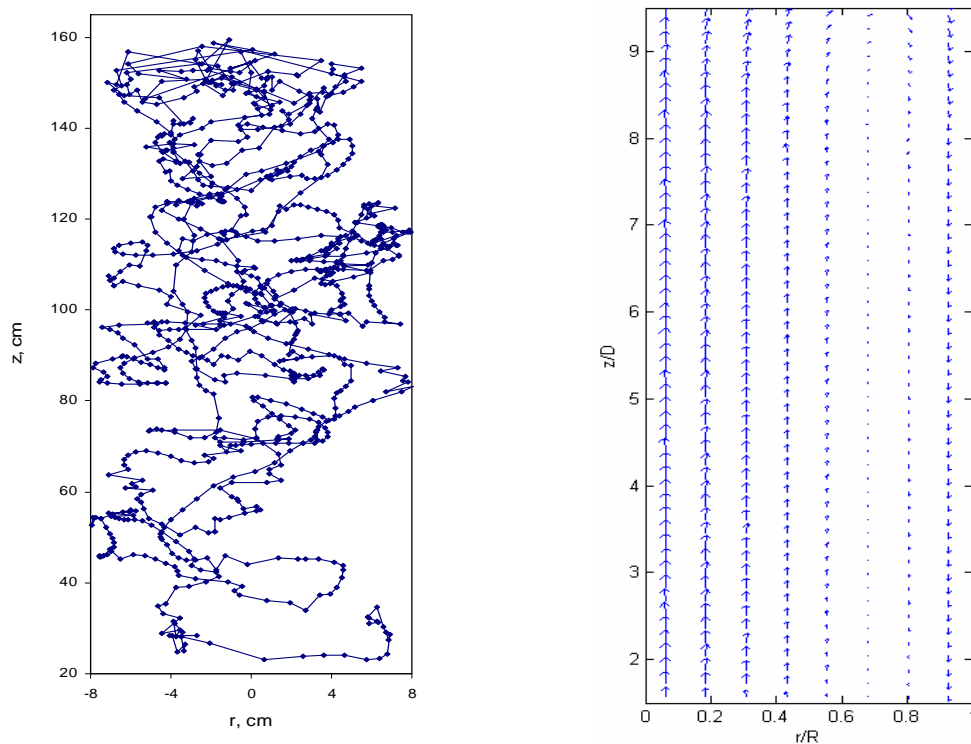
The CT/CARPT occurrence method avoids using the two assumptions made in Rados (2003), and obtains independent holdups of gas and solids. Although both methods eventually need to be evaluated by the dual-source CT being developed in the CREL,

the CT/CARPT occurrence method uses a much less problematic assumption, as long as the ergodic hypothesis holds. However, in the comparisons with previous CT results shown in the following sections, Rados' reconstruction method was still used for consistency. Besides, the CARPT occurrence data were available at only a few conditions, limiting the use of the alternative reconstruction method.

3.7.2. Trajectories and Velocity Field

Figure 3-11(a) is a short section of the particle Lagrangian trajectories plotted in 2-D, which appear as random motions in the reactor. From the Lagrangian trajectories, Lagrangian velocities and time-averaged velocity field were then obtained according to Degaleesan (1997). Because of the time-averaged flow axis-symmetry in the cylindrical reactor, the velocity field was azimuthally averaged, yielding 2-D u_z - u_r velocity vector maps as shown in Figure 3-11(b). From the 2-D time-averaged velocity vector map, a one-cell recirculation pattern was observed for the solids, which is similar to the previous two SBCR studies. The axial differences in the velocity vector are small through the fully developed region (between $z=2 d_c$ and $z=9 d_c$). Therefore, the mapping results are demonstrated with radial profiles which are axially averaged in the fully developed region. Figures 3-12(a~c) show the radial profiles of axial, radial, and azimuthal velocities of the solids. The plotted error bars are the standard deviations along the axial direction in the fully developed section. The radial profiles of the solids axial velocity have similar qualitative characteristics to those observed in Rados (2003) and Shaikh (2007). The radial inversion point of the velocity profile is about $r/R=0.7$, which is the cylindrical boundary of the azimuthally and time-averaged upward flow and downward flow regions. The centerline solids velocity (at $r/R=0$) is about 0.65 m/s at the example condition, more than twice as much as the superficial gas velocity. The time-averaged solids radial velocities have insignificant magnitudes, which are close to zero within the error range; the time-averaged azimuthal velocities have even smaller magnitudes, which are also close to zero within the error range. This is due to the axis-symmetry and vertical construction of the slurry bubble column. Therefore, further

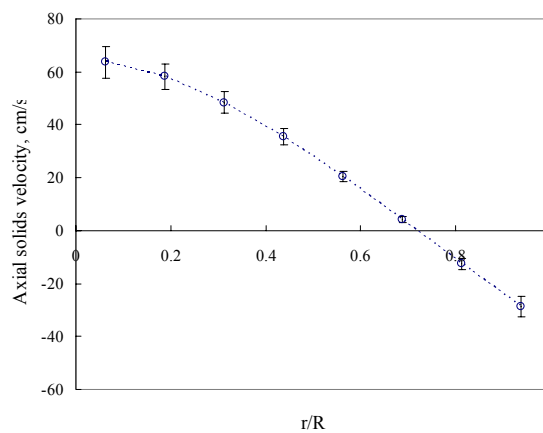
discussion is focused on the axial velocity profiles, since they represent the global recirculation in the slurry bubble column in the fully developed region.



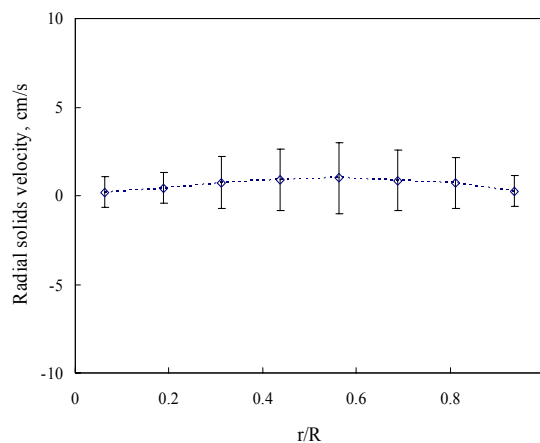
a) A section of the Lagrangian trajectories

b) u_z - u_r velocity vector map

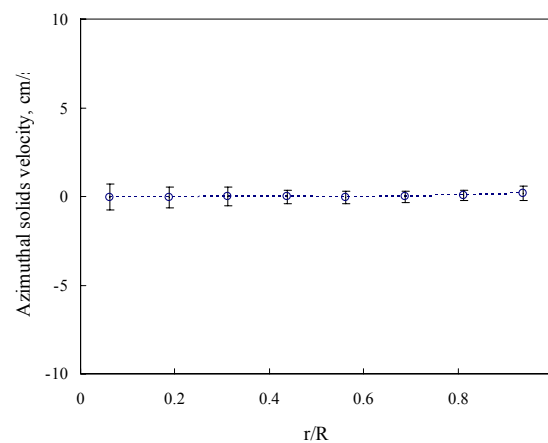
Figure 3-11. Lagrangian trajectories and a 2-D velocity vector map, air- C_9C_{11} -FT Catalyst, 0.30 m/s, 25% vol., 1.0 MPa



a). Radial profile of the axial solids velocity



b). Radial profile of the radial solids velocity



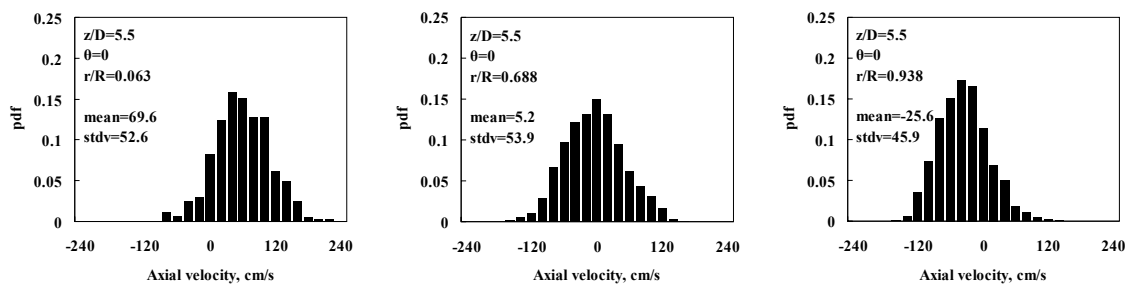
c). Radial profile of the azimuthal solids velocity

Figure 3-12. Radial profiles of the solids velocities in three directions, air-C₉C₁₁-FT Catalyst, 0.30 m/s, 25% vol., 1.0 MPa

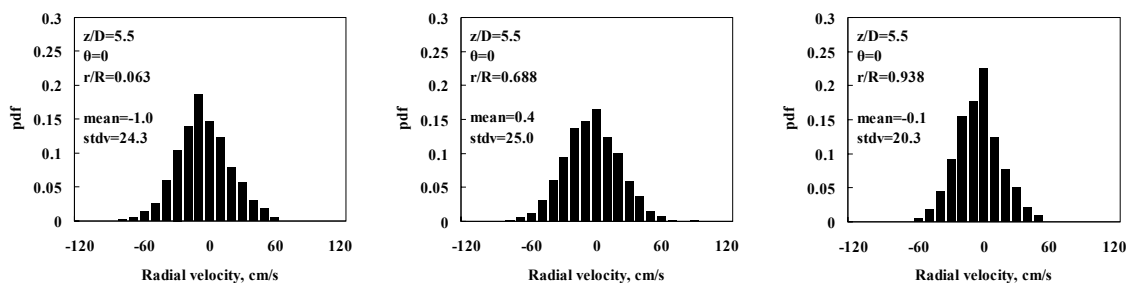
3.7.3. Velocity Probability Density Functions

In addition to the time-averaged velocity field, fluctuation characteristics of the velocities can be characterized by probability density functions (PDF). PDFs were obtained from the instantaneous velocities at axial length $z/d_c=5.5$ and azimuthal position $\theta=0^\circ$, which can typically represent the characteristics of other axial and azimuthal locations in the fully developed region. Figures 3-13(a~c) show the PDFs of

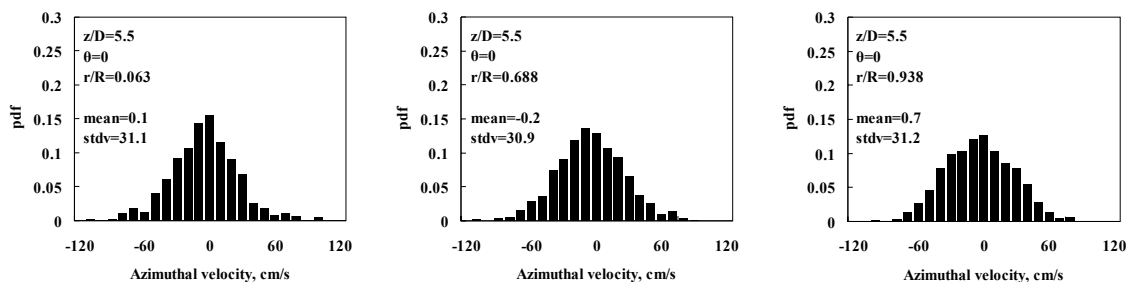
the three velocity vectors obtained at three different radial locations, which are near the center ($r/R=0.063$), approximately at the axial velocity inversion point ($r/R=0.688$), and close to the wall ($r/R=0.938$), respectively. The means and standard deviations of the instantaneous velocities are also shown in each PDF figure. All the PDFs appear close to normal distributions, which shows the random nature of the flow turbulence. In the axial velocity PDFs, the distribution centroid apparently moves from positive to negative along the radius. While the mean of each PDF is close to the overall averaged axial velocity at the corresponding radial position, the axial velocity PDFs have standard deviations of about 0.50 m/s. As in Rados (2003) and Shaikh (2007), it was found that a small part of the axial velocities at $r/R=0.063$ are negative, as a result of some downward moving bubbles (observed in an air-water system by Xue, 2004). At the radial position of $r/R=0.938$, the negative axial velocities become dominant, indicating the solids are mainly moving downward in this region. The radial and azimuthal velocity PDFs have means close to zero at all the three radial locations, but with significant standard deviation. The spreading of each PDF indicates the intensity of the turbulence at that direction. The standard deviations of the PDFs follow similar trends with corresponding normal stresses.



a) PDFs of the axial solids velocity



b) PDFs of the radial solids velocity



c) PDFs of the azimuthal solids velocity

Figure 3-13. PDFs of instantaneous solids velocities in three directions, air-C₉C₁₁-FT Catalyst, 0.30 m/s, 25% vol., 1.0 MPa

3.7.4. Turbulence of the FT Catalyst Particles

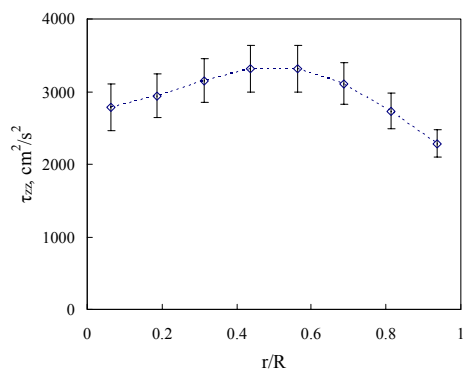
The high gas throughput in many industrial processes, including FT processes, often results in high turbulence which usually dominates other flow phenomena in affecting the mixing and transports. Flow turbulence has been one of the difficult factors in reactor simulations, especially in a multiphase system. The instantaneous fluctuations of the velocity field are random and highly transient in a BCR or a SBCR, which is usually modeled with ensemble parameters using second order (or higher) correlations of the fluctuations. The second order velocity fluctuation, $\overline{u_i u_j}$, represents the turbulent momentum transport in the i^{th} direction due to the instantaneous flow in the j^{th} direction (Degaleesan, 1997). The stress tensor defined in cylindrical coordinates is shown as the following symmetric matrix

$$\tau = \rho_s \begin{pmatrix} \overline{u_r' u_r'} & \overline{u_r' u_\theta'} & \overline{u_r' u_z'} \\ \overline{u_\theta' u_r'} & \overline{u_\theta' u_\theta'} & \overline{u_\theta' u_z'} \\ \overline{u_z' u_r'} & \overline{u_z' u_\theta'} & \overline{u_z' u_z'} \end{pmatrix}, \quad (3-17)$$

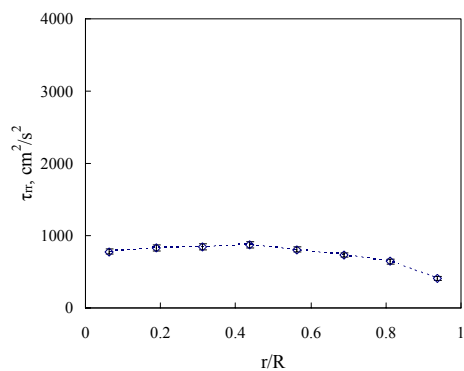
where $\overline{u_i' u_j'} = \overline{u_j' u_i'}$. The stress tensor consists of normal stresses in three directions ($\rho_s \overline{u_z' u_z'}$, $\rho_s \overline{u_r' u_r'}$, and $\rho_s \overline{u_\theta' u_\theta'}$) and shear stresses ($\rho_s \overline{u_r' u_z'}$, $\rho_s \overline{u_r' u_\theta'}$, and $\rho_s \overline{u_\theta' u_z'}$). The solids turbulent kinetic energy (TKE) (based on per unit mass) is calculated from the normal stresses as

$$k = \frac{1}{2} [\overline{u_r'^2} + \overline{u_\theta'^2} + \overline{u_z'^2}]. \quad (3-18)$$

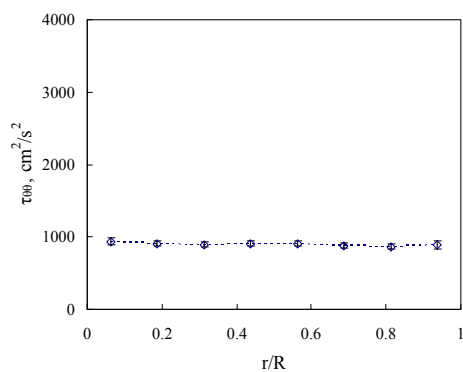
The stress tensors and the TKE have been visualized in various two-phase and three-phase systems by Degaleesan (1997), Ong (2003), Rados (2003), and Shaikh (2007). Using the similar method, this work obtained the six turbulent stresses in the mimicked FT SBCR. Figure 3-14 shows the radial profiles of the solids shear stresses and normal stresses at 0.30 m/s, 1.0 MPa, and 25% vol. The axial normal stress, τ_{zz} , is significantly higher than the radial normal stress, τ_{rr} , and the azimuthal normal stresses, $\tau_{\theta\theta}$. This indicates the anisotropic nature of the solids turbulence at the mimicked FT condition, which was also found in the air-water-150 μm glass beads system (Rados, 2003) and the air-Therminol-150 μm glass beads system (Shaikh, 2007). The anisotropic turbulence is likely caused by the limitation of the reactor diameter, as compared with the height in the length scale. Also shown in Figure 3-14 is the radial profile of Reynolds shear stress, τ_{rz} , which is lower than the normal stresses. As expected from the radial profile of time-averaged axial velocity, the maximum of Reynolds shear stress is at the inversion point ($r/R \sim 0.7$). The following two findings suggest time-averaged axial symmetry of the turbulence in the mimicked FT SBCR: the shear stress is close to zero when the radial profile is extrapolated to $r/R=0$, and the shear stresses in the r - θ and z - θ directions are negligible. The TKE was calculated according to Degaleesan (1997) (Equation 3-18), and its radial profile is shown in Figure 3-15. Basically, the TKE is the result of the three normal stresses, especially the axial normal stress (because of the non-isotropic turbulence in the reactor).



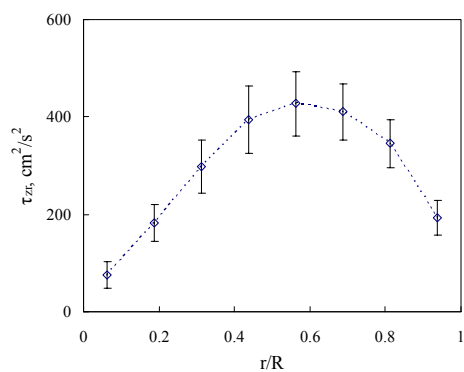
a) Axial normal stress



b) Radial normal stress



c) Azimuthal normal stress



d) z-r (Reynolds) shear stress

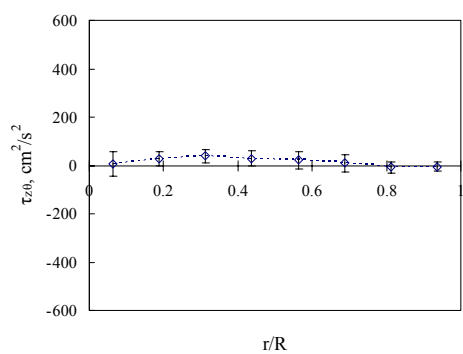
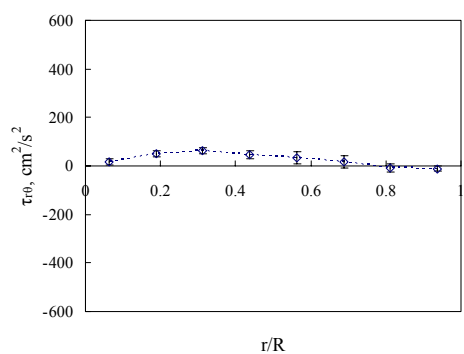
e) z- θ shear stressf) r- θ shear stress

Figure 3-14. Radial profiles of the stresses,
air-C₉C₁₁-FT Catalyst, 0.30 m/s, 25% vol., 1.0 MPa

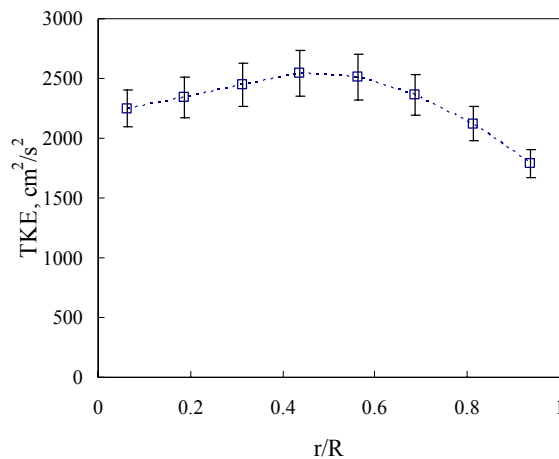
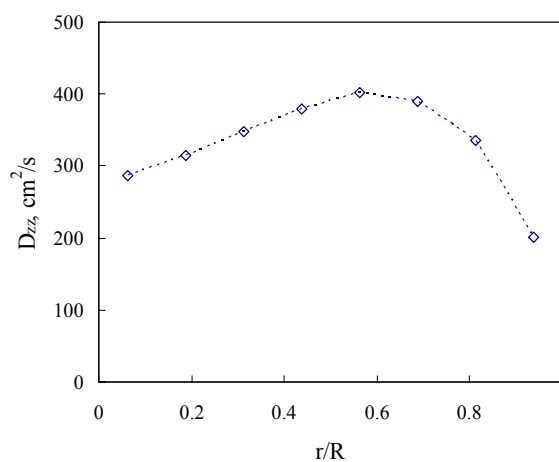
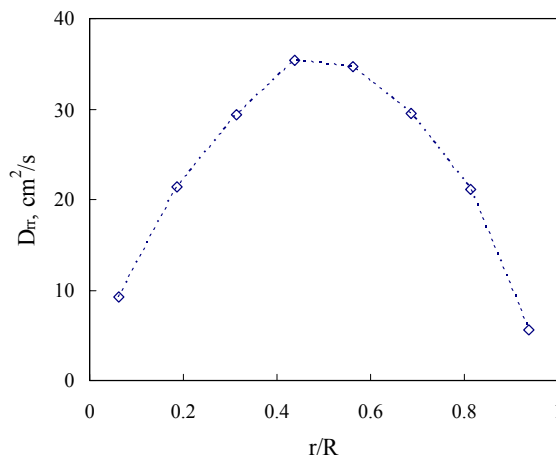


Figure 3-15. Radial profiles of the TKE, air-C₉C₁₁-FT Catalyst, 0.30 m/s, 25% vol., 1.0 MPa

The axial and radial eddy diffusivities were calculated from the auto- or cross-correlation coefficients using the Lagrangian velocities (Degaleesan, 1997), and their radial profiles are shown in Figures 3-16(a, b). The axial eddy diffusivity peaks near the inversion point, and has a minimum value close to the wall. The radial eddy diffusivity has a peak value at about the middle of the radius ($r/R \sim 0.5$), showing the radial position that has the maximum radial turbulence diffusion.



a) Axial eddy diffusivity



b) Radial eddy diffusivity

Figure 3-16. Radial profiles of the eddy diffusivities, air-C₉C₁₁-FT Catalyst, 0.30 m/s, 25% vol., 1.0 MPa

3.8. Evaluation of Two FT Mimicking Liquids (Therminol vs. C₉C₁₁)

At room temperature, both Therminol and C₉C₁₁ mimic the physical properties of FT wax at FT conditions (Table 3-2). Shaikh (2007) used Therminol, while this work selected C₉C₁₁ to avoid the aromatic Therminol's environmental and health concerns. The differences in the hydrodynamics of these two liquids were evaluated in the mimicked FT SBCR. The majority of the CT and CARPT experiments in this work were conducted in the air-C₉C₁₁-FT catalyst system, while a limited number of CT conditions and one CARPT condition were selected for the air-Therminol-FT catalyst system.

Figures 3-17, 3-18, and 3-19 show the two liquids' comparative phase distributions at various two-phase and three-phase conditions. At all the tested conditions, it was found that the gas holdup and its radial profiles were close. The average absolute relative differences (AARDs) (defined in Equation 3-19) between each set of profiles in Figures 3-17, 3-18, and 3-19 are between 1% ~ 7%.

$$\text{AARD} = \frac{1}{n_r} \sum_{i=1}^{n_r} \frac{|X_{1,i} - X_{2,i}|}{(X_{1,i} + X_{2,i})/2} \quad (\text{i, radial position number; } n_r=16). \quad (3-19)$$

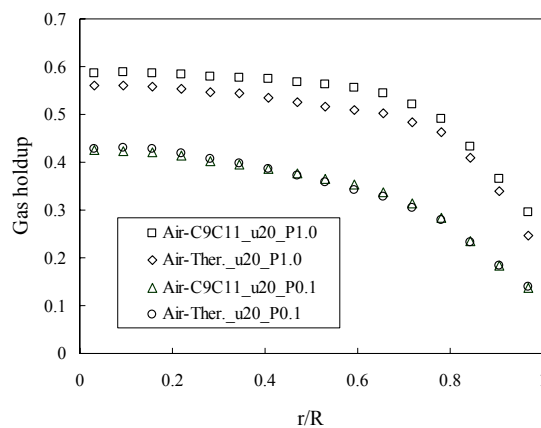


Figure 3-17. Effects of the two liquids on the gas holdup radial profiles, air-Therminol vs. air-C₉C₁₁, 0.20 m/s, AARD=1% at 0.1 MPa, AARD=7% at 1.0 MPa

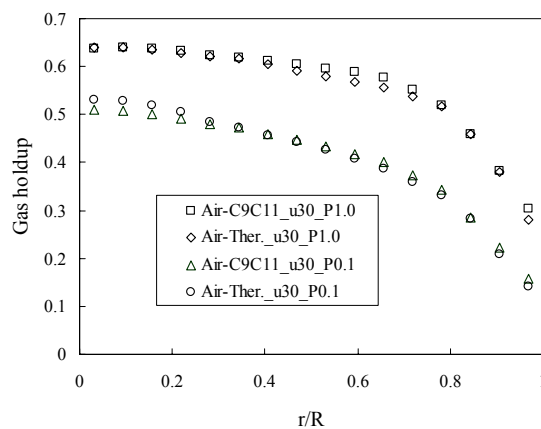


Figure 3-18. Effects of the two liquids on gas holdup radial profiles, method (I), air-Therminol vs. air-C₉C₁₁, 0.30 m/s, AARD=3% at 0.1 MPa, AARD=2% at 1.0 MPa

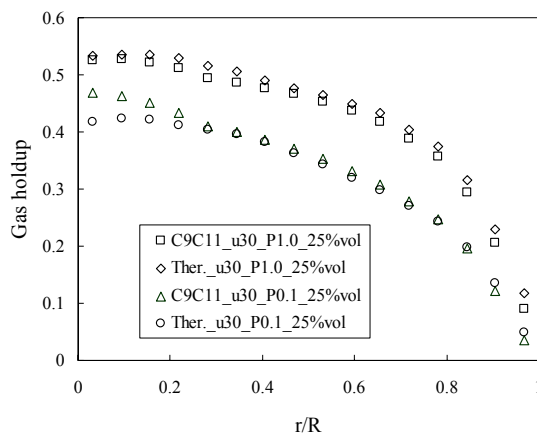
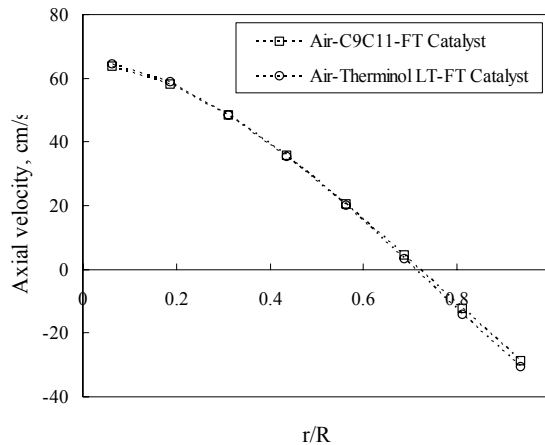
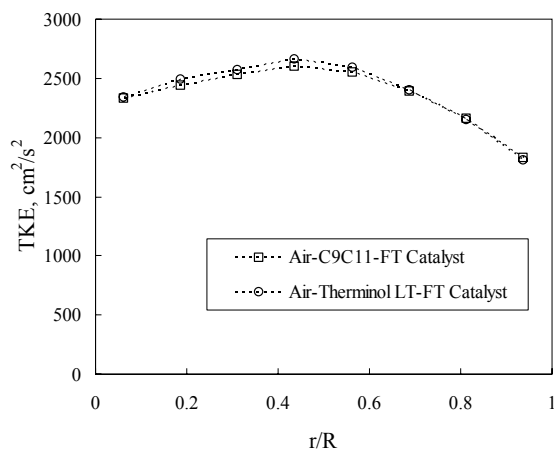


Figure 3-19. Effects of the two liquids on gas holdup radial profile, method (I), air-Therminol-FT catalyst vs. air-C₉C₁₁-FT catalyst, 0.30 m/s, 25% vol., AARD=6% at 0.1 MPa, AARD=5% at 1.0 MPa

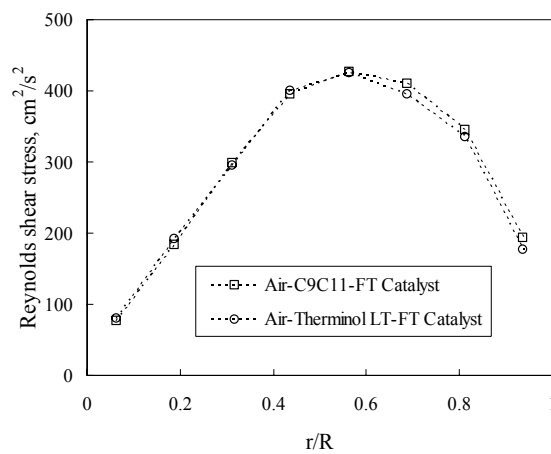
CARPT experiments using the air-C₉C₁₁-FT catalyst system and the air-Therminol-FT catalyst system were performed at high superficial gas velocity (0.30 m/s), high pressure (1.0 MPa), and high solids loading (25% vol.). The two systems yield similar solids axial velocity, TKE, and other turbulence parameters (Figures 3-20 a~f). As noted in the figures, the AARDs are all below 5%, indicating similar macro-mixing and turbulence in these two three-phase systems.



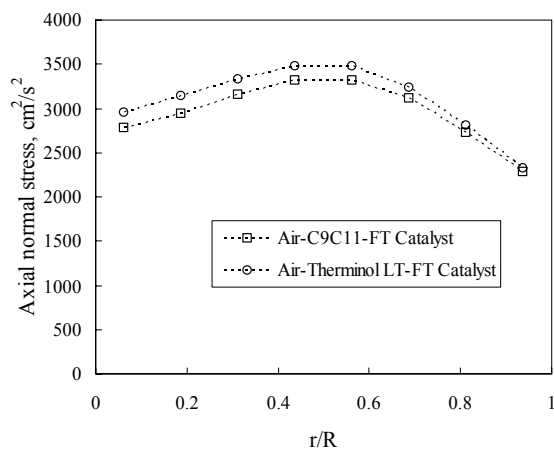
a) Solids axial velocities (AARD=2%)



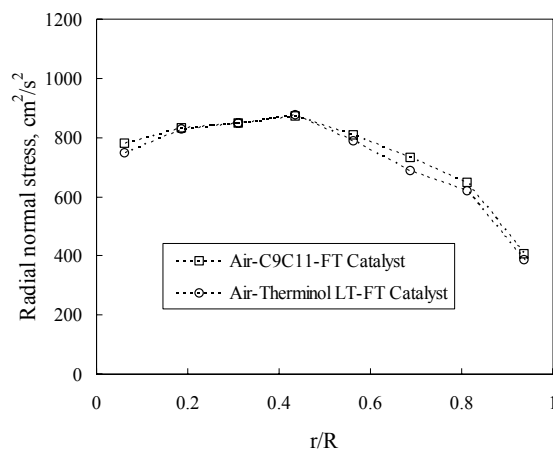
b) Solids TKEs (AARD=1%)



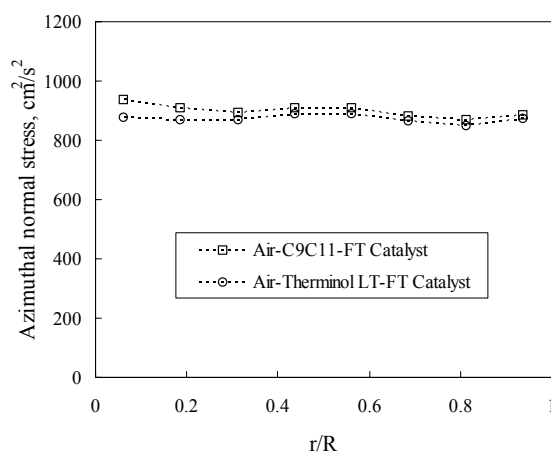
c) Solids Reynolds stresses (AARD=4%)



d) Solids axial normal stresses (AARD=5%)



e) Solids radial normal stresses (AARD=3%)



f) Solids azimuthal normal stresses (AARD=3%)

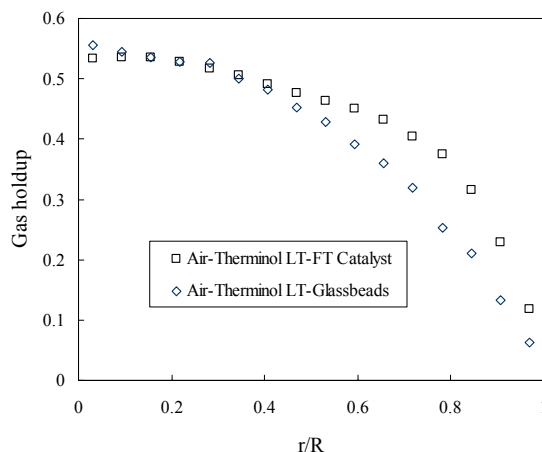
Figure 3-20. Effects of the two liquids on solids velocity and turbulence parameters, air- C_9C_{11} -FT Catalyst vs. air-Therminol-FT Catalyst, 0.30 m/s, 25% vol., 1.0 MPa

3.9. Differences in Hydrodynamics using FT Catalyst and Glass Beads

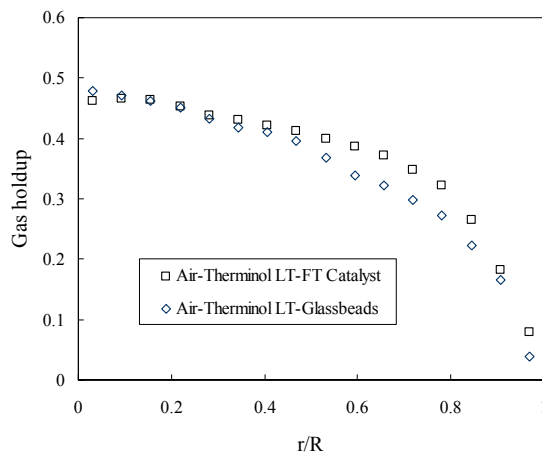
While the previous tomography and particle tracking studies used glass beads (Rados, 2003; Shaikh, 2007), this study selected FT catalyst (carrier) as the solids phase. In order to quantify the differences between these two solids under exactly the same other variables, this work performed CT/CARPT experiments using the air-Therminol-FT

catalyst system at selected conditions for comparison with the previous study using air-Therminol-glass beads (Shaikh, 2007).

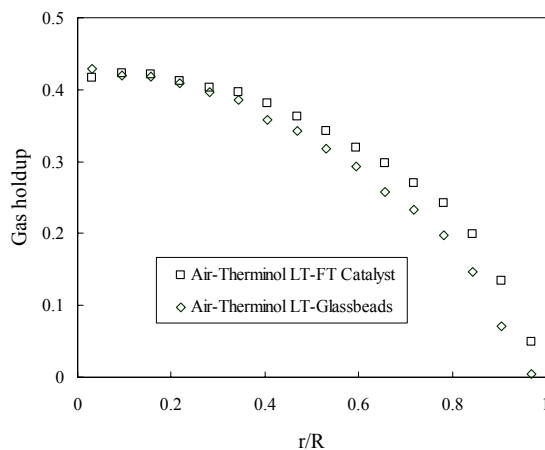
Figures 3-21 (a~c) show the gas holdup profiles of the two different solids with the same gas and liquid at the high solids loading (25% vol.) and various other operating conditions. Significant differences in the overall gas holdup and profile steepness were observed in the two systems, especially at the 1.0 MPa pressure. The air-C₉C₁₁-FT catalyst system yielded higher overall gas holdup with less steep radial profiles (higher *n* values) than the air-Therminol-glass beads system. The gas holdup values in the two systems are similar near the center (*r/R*<0.4), while most of the differences are near the wall (*r/R*>0.4).



a) $u_g=0.30$ m/s, $P=1.0$ MPa, $C_s=25\%$ vol.
 Air-Therminol-FT catalyst: $\bar{\epsilon}_g=0.372$, $n=3.90$
 Air-Therminol-glass beads: $\bar{\epsilon}_g=0.309$, $n=2.36$



b) $u_g=0.20$ m/s, $P=0.1$ MPa, $C_s=25\%$ vol.
 Air-Therminol-FT catalyst: $\bar{\epsilon}_g=0.318$, $n=4.23$
 Air-Therminol-glass beads: $\bar{\epsilon}_g=0.282$, $n=2.71$

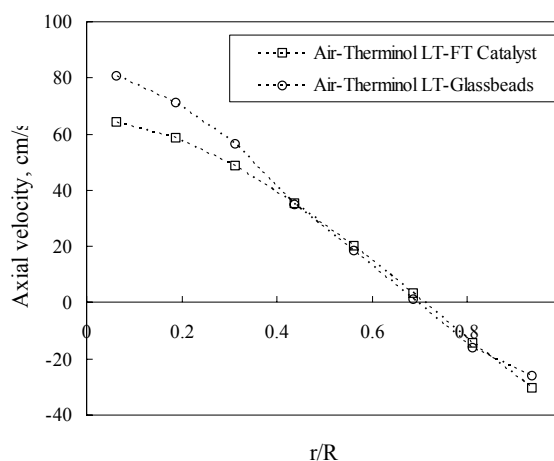


c) $u_g=0.30$ m/s, $P=0.1$ MPa, $C_s=25\%$ vol.
 Air-Therminol-FT catalyst: $\bar{\epsilon}_g=0.259$, $n=2.87$
 Air-Therminol-glass beads: $\bar{\epsilon}_g=0.223$, $n=2.23$

Figure 3-21. Gas holdup radial profiles using FT catalyst and glass beads, method (I)

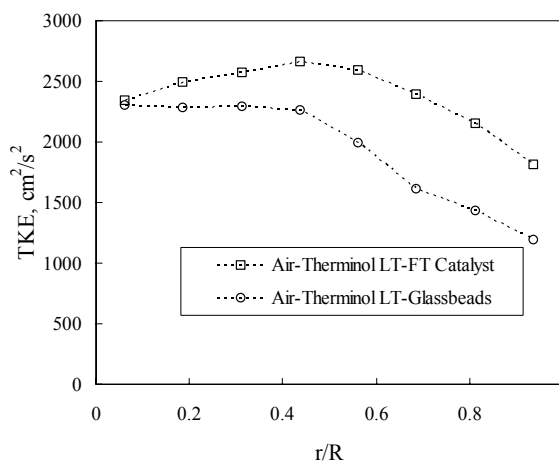
Radial profiles of the solids velocity and turbulence parameters were obtained using CARPT in the two three-phase systems at 0.30 m/s, 1.0 MPa, and 25% vol. Figures 3-22(a~d) show the effects of the two different solids, FT catalyst and glass beads, on the solids axial velocity and turbulence parameters. In the radial range of $r/R>0.4$, the two

radial profiles of the solids axial velocity are similar. Near the center of the column ($r/R < 0.4$), the axial velocity of the glass beads is about 25% higher than that of the FT catalyst. Combined with the gas holdup radial profiles at the same condition (Figure 3-21a), the recirculating rates of the pseudo-slurry were calculated and indicated below 3-21 (a). It was found that using the FT catalyst results in a slower global slurry recirculation than using the glass beads. The radial profiles of TKE, Reynolds stress, and axial normal stress have similar values at the center, while having larger differences close to the wall.

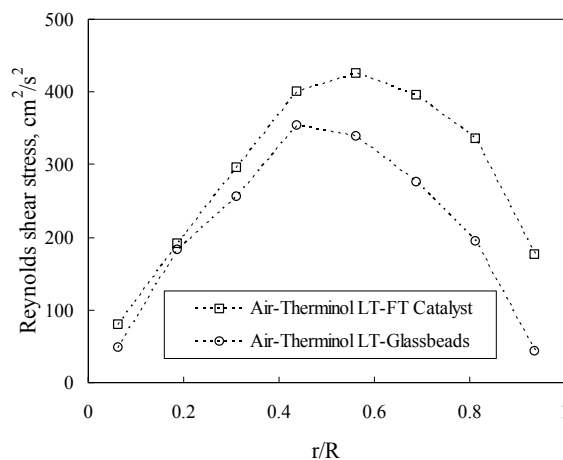


a) Solids axial velocities

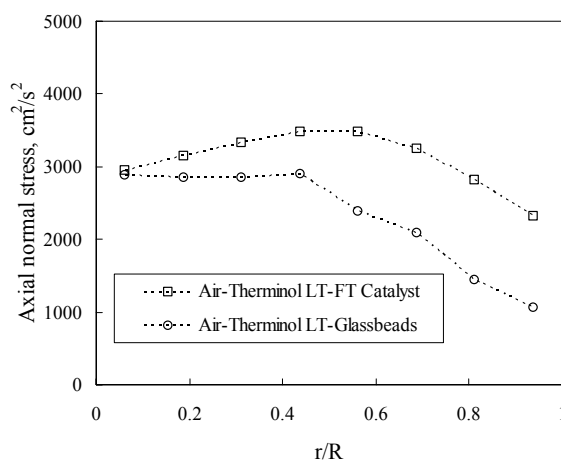
FT catalyst slurry: $1510 \text{ cm}^3/\text{s}$ up and $1550 \text{ cm}^3/\text{s}$ down
 Glass beads slurry: $1620 \text{ cm}^3/\text{s}$ up and $1650 \text{ cm}^3/\text{s}$ down.



b) Solids TKEs



c) Solids Reynolds stresses



d) Solids axial normal stresses

Figure 3-22. Differences of FT catalyst and glass beads in the resulting solids velocities and turbulence parameters, air-Therminol-FT Catalyst vs. air-Therminol-glass beads, 0.30 m/s, 25% vol., 1.0 MPa

As shown above, the differences in the hydrodynamic parameter profiles using the two solids were for the first time observed with the assistance of CT and CARPT techniques. These solids effects may be caused directly or indirectly by the differences in the solids physical properties, such as the particle size and density, or by the FT catalyst's porous surface, which may cause different liquid-solids drag. The FT catalyst

particles are smaller and lighter (in apparent density) than the 150 μm glass beads, and therefore have lower settling velocity in the SBCR. With a lower settling velocity, the FT catalyst yields a smaller solids concentration axial gradient than the glass beads, i.e., lower solids concentration at the bottom of the reactor, which has been proved by the solids holdup measured in these two systems. The lower solids concentration of FT catalyst near the reactor bottom imposes less bubble size increasing effect of the solids near the sparger, which may cause lower gas holdup and less steep gas holdup profiles. In comparison, the glass beads have a higher solids concentration near the reactor bottom, and impose an earlier and stronger solids effect of increasing the bubble sizes from the beginning of the gas passage. The higher value and flatter radial profiles of gas holdup using FT catalyst support this mechanism, as a result of smaller bubbles explained above. Another explanation of the different gas holdup profiles is based on the different turbulence measured by the CARPT technique (Figure 3-22b). The FT catalyst yielded higher values of TKE, which may have more effect of breaking bubbles into smaller ones, which then cause the observed differences in the gas holdup. Both explanations involve bubble sizes at the mimicked FT conditions, which are yet to be investigated. Measuring the radial and axial differences in the bubble dynamic parameters is critical to understanding the effects of different solids on the hydrodynamics observed in the mimicked FT SBCR.

It should be noted that the higher solids TKE of the FT catalyst does not necessarily mean an also higher liquid turbulence in the FT catalyst SBCR. FT catalyst particles are smaller and therefore follow the liquid more closely, while the larger glass beads may not follow the liquid velocity fluctuations as closely. The porous surface of the FT catalyst may be another factor increasing the liquid-solids drag, and therefore cause the same effect of closer liquid following. Hence, which system has the higher liquid TKE is unknown from this study, since the liquids may actually have more velocity fluctuations that the solids do not follow exactly. This may be evaluated by using a liquid form of tracer technique in the SBCR to estimate the liquid phase dispersion, which is not part of this study.

3.10. Comparison of Three Different Systems (Air-Water-Glass Beads, Air-Therminol-Glass Beads, and Air-C₉C₁₁-FT Catalyst)

In continuation with the previous SBCR hydrodynamic studies, some of the results in this work using air-C₉C₁₁-FT catalyst were compared with the air-water-glass beads system (Rados, 2003) and the air-Therminol-glass beads system (Shaikh, 2007). Conditions at low solids loading (9.1% vol.) only are common among these three studies, because Rados (2003) did not use 25% vol. solids loading. Figures 3-23 and 3-24 show the results in these three systems at high pressure (1.0 MPa) and low pressure (0.1 MPa), respectively. At high pressure (Figure 3-23), the air-C₉C₁₁-glass beads system and the air-Therminol-FT catalyst system have similar gas holdup, which are both higher than the air-water-glass beads system. However, at low pressure (Figure 3-24), the three systems yield similar gas holdup magnitudes and profiles with small differences. Both FT mimicking liquids have lower surface tension and lower viscosity than water. The lower surface tension encourages bubble break-up, resulting in formation of more small bubbles and increased gas holdup. The lower viscosity also favors smaller bubbles due to lower bubble stability and therefore higher gas holdup. However, since the viscosity difference between the mimicked FT liquids and water is small, the gas holdup difference is most likely caused by the surface tension differences.

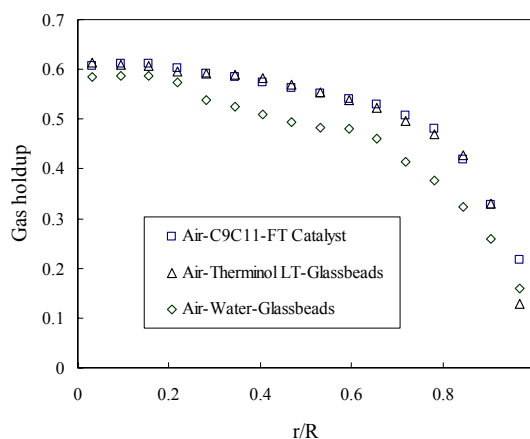


Figure 3-23. Comparison of the gas holdup in three systems (method I) - air-water-glass beads, air-Therminol-glass beads, and air-C₉C₁₁-FT catalyst, 0.30 m/s, 1.0 MPa, 9.1% vol.

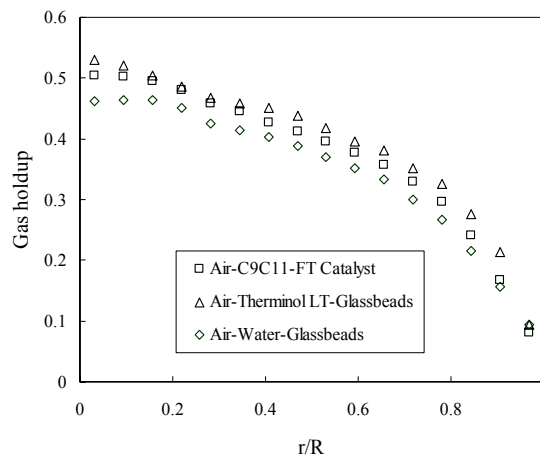
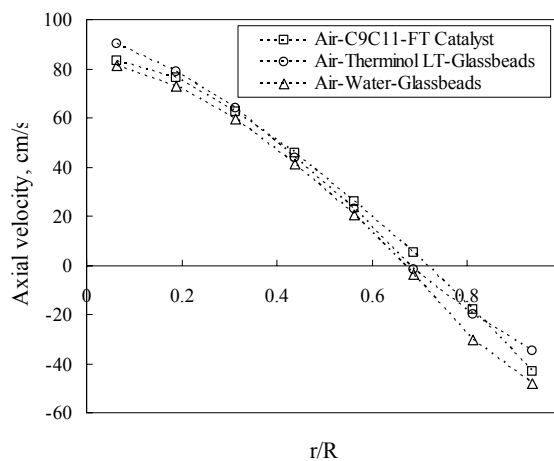
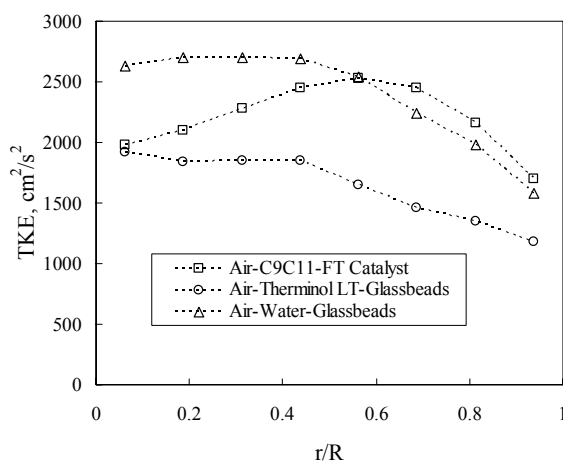


Figure 3-24. Comparison of the gas holdup in three systems (method I) - air-water-glass beads, air-Therminol-glass beads, and air-C₉C₁₁-FT catalyst, 0.30 m/s, 0.1 MPa, 9.1% vol.

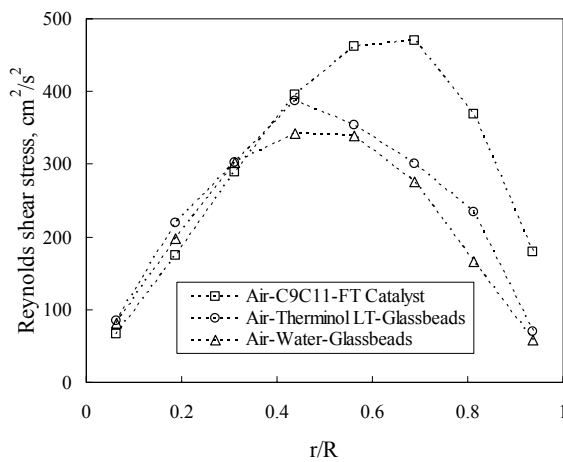
The CARPT results at low solids loading (9.1% vol.) in the three systems are plotted in Figure 3-25. At this condition, the solids axial velocity of the air-C₉C₁₁-FT catalyst system has an AARD of 13% from that of the air-water-glass beads system, and has an AARD of 8% from that of the air-Therminol-glass beads system. The differences in the solids axial velocities of the three systems are relatively larger near the wall ($r/R > 0.5$). The shear stresses have an apparent difference between the air-C₉C₁₁-FT catalyst and the other two systems at $r/R > 0.4$. Differences in the shear stresses are similar to those shown in the earlier comparisons between using FT catalyst and glass beads (Figure 3-22c). This indicates that the difference of the shear stresses in Figure 3-25(c) is likely caused mainly by the FT catalyst solids. The differences in the TKE and axial normal stress between air-Therminol-glass beads and air-C₉C₁₁-FT catalyst are similar to that shown in the solids comparisons above. This further validates that the hydrodynamic differences between the two three-phase systems using different mimicking liquids are mainly caused by the different solids instead of the two FT-mimicking liquids.



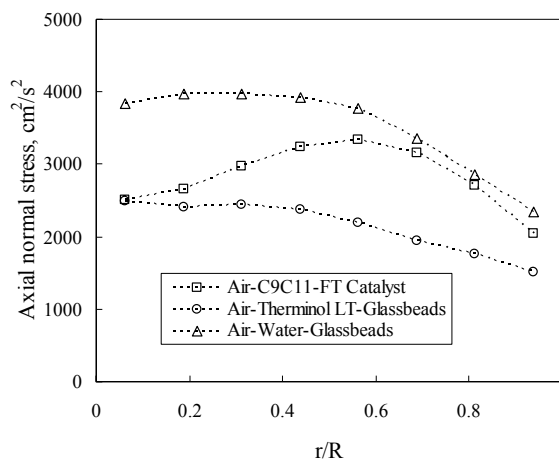
a) Solids axial velocities



b) Solids TKEs



c) Solids Reynolds stresses



d) Solids axial normal stresses

Figure 3-25. Comparison of the velocity and turbulence parameters in three different systems - air-water-glass beads, air-Therminol-glass beads, and air-C₉C₁₁-FT catalyst, 0.30 m/s, 9.1% vol., 1.0 MPa

The apparent physical properties of the slurry phases (assuming pseudo-homogeneous slurry) were also checked in explaining the hydrodynamic differences observed in the three systems (Table 3-7). The apparent viscosities, μ_{sl} , of these three slurries are very close. However, when the surface tension, σ_{sl} , increased, the turbulence was found to increase. The increase of surface tension favors formation of larger bubbles due to better bubble stability. As analyzed in the CT section, larger bubbles rise faster and reduce the gas holdup, causing lower gas holdup in the air-water-glass beads system as shown in the CT results. Therefore, the differences in the turbulence parameters between air-water-glass beads and the other systems are mainly due to the different surface tensions (Walter and Blanch, 1986).

Table 3-7. Apparent physical properties of the pseudo- slurries

Slurry (9.1% vol.)	ρ_{sl} , kg/m ³	μ_{sl} , Pa·s	σ_{sl} , dyne/cm
Water-150 μ m glass beads	1.13	0.00114	0.072
Therminol-150 μ m glass beads	1.01	0.00111	0.017
C ₉ C ₁₁ -FT catalyst	0.86	0.00107	0.023

3.11. Comparison of the Effects of Operating Parameters on the Hydrodynamics

The effects of the superficial gas velocity (up to 0.45 m/s at low pressure and 0.30 m/s at high pressure) and pressure (up to 1.0 MPa) on the SBCR hydrodynamics in an air-water-glass beads system have been investigated by Rados (2003). Moreover, Rados (2003) studied the solids loading effects at two solids loadings, zero and 9.1% vol. Shaikh (2007) extended the solids loading to 25% vol. in an air-Therminol-glass beads system. In the present work, the effects of operating parameters in the mimicked FT SBCR were examined using 20 CT conditions (Table 3-3) and 8 CARPT conditions (Table 3-5). Among the observed effects of operating parameters in the air-C₉C₁₁-FT catalyst system, those similar to the previously used systems are only briefly described here (Detailed data are included in Appendix A), and some differences in the observed solids loading effects are shown and discussed.

3.11.1. Effects of the Superficial Gas Velocity

Similar effects of the superficial gas velocity were found in the mimicked FT SBCR as in the air-water system (Ong, 2003), air-water-glass beads system (Rados), and air-Therminol-glass beads system (Shaikh, 2007). At higher superficial gas velocity, the gas holdup magnitude increases and its radial profiles become steeper (n becomes smaller, Table 3-6) as a result of additional large bubbles. Accordingly, the solids gas holdup has lower magnitude and also steeper radial profiles at higher superficial gas velocity. The superficial gas velocity also results in higher axial velocity and turbulence of the liquid or solids phase.

3.11.2. Effects of the Operating Pressure

This study investigated the effects of operating pressure on the hydrodynamics in the mimicked FT SBCR, and obtained results that are in line with the previous BCR and SBCR studies. An elevated operating pressure reduces the stability of bubbles and results in a smaller maximum stable bubble size (Wilkinson, 1991; Lin et al., 1998).

Smaller mean bubble size and narrower bubble size distribution at 1.0 MPa were observed in an air-water BCR by Xue (2004) using the four-point probe technique (Xue et al., 2003). Small bubbles have lower rise velocity and reside longer in the reactor, yielding higher gas holdup, as proved in various systems by Xue (2004), Ong (2003), Shaikh (2007), and the present study. The changes in the hydrodynamic parameters from 0.1 MPa and 1.0 MPa in the mimicked FT SBCR are listed below, with detailed explanations provided in Xue (2004), Ong (2003), and Rados (2003).

- 1) The gas holdup magnitude was larger, and the radial profiles of gas holdup became less steep (higher n values) at the elevated pressure.
- 2) The axial velocity of the liquid phase (in BCRs) or solids phase (in SBCRs) became higher since the smaller bubbles formed have higher drag and are more efficient in driving the liquid/slurry into higher recirculation.
- 3) Turbulence parameters (TKE, stresses, and eddy diffusivities) became smaller because of the reduced bubble sizes and less bubble interactions.

3.11.3. Effects of the Solids Loading

Adding solids (increasing solids loading) may greatly change the hydrodynamics in a SBCR. This study investigated the effects of solids loading on the hydrodynamics in the mimicked FT SBCR and obtained profile trends similar to those in the air-water-glass beads system (Rados, 2003) and the air-Therminol-glass beads system (Shaikh, 2007). However, some small differences were observed.

The solids loading effects that are in common with the previous studies include:

- 1) The gas holdup magnitude became lower, while its radial profiles were steeper because of the increases bubble sizes as a result of enhanced bubble coalescence by the solids.
- 2) The solids axial velocity decreased with the reduced gas holdup.
- 3) The TKE increased with the solids loading, showing a higher turbulence especially near the column center, because of the larger increase of the axial normal stress near

the center in particular. Eddy diffusivities also increased with the solids loading because of the enhanced turbulence.

Rados (2003) and Shaikh (2007) both reported a weak decrease in gas holdup from zero solids loading to the low solids loading (9.1% vol.). Rados (2003) observed a relatively more apparent gas holdup decrease with the solids loading from 9.1% vol. to 17.8% vol.; and Shaikh (2007) also observed a more apparent effect of the solids loading from 9.1% vol. to 25% vol. In the present work, however, the gas holdup apparently decreased when the solids loading changed from zero to 9.1% vol. as well as from 9.1% vol. to 25% vol. (Figures 3-26 ~ 3-30). In other words, the solids effects on the gas holdup are already apparent at 9.1% vol., while in the previous two systems the solids did not have apparent effects until it was increased beyond 9.1% vol. Considering the observed similarity between air-water-glass beads (Rados, 2003) and air-Therminol-glass beads (Shaikh, 2007) in this regard, the difference in the low solids loading range may be attributed to the solids' differences. Although the same volumetric solids loadings were used, the smaller FT catalyst particles ($\sim 75 \mu\text{m}$) have more particles per unit slurry volume than the glass beads ($\sim 150 \mu\text{m}$), and are mixed with the liquid phase on a smaller scale than the glass beads. Besides, the smaller FT catalyst particles have a porous surface, which possibly increases the liquid-solids drag, so they may follow the liquid better. Therefore, the more apparent solids effects at the low solids loading using the FT catalyst than using the glass beads are likely due to the more uniform mixture of the FT catalyst- C_9C_{11} slurry. This explanation does not have direct evidence but may be evaluated by comparing the bubble dynamics in the three systems when four-point probe measurements are available in the mimicked FT SBCR in the future.

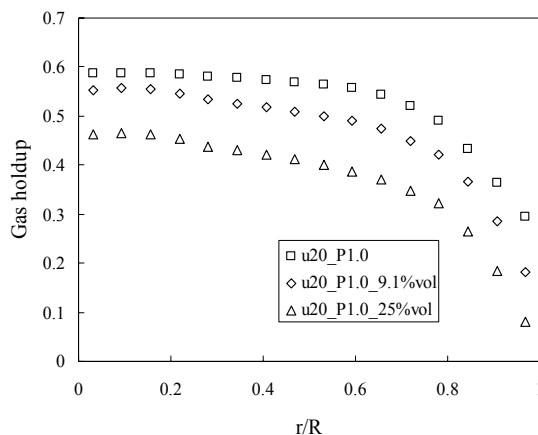


Figure 3-26. Effects of the solids loading on gas holdup radial profiles, method (I), air-C₉C₁₁-FT catalyst, 0.20 m/s, 1.0 MPa

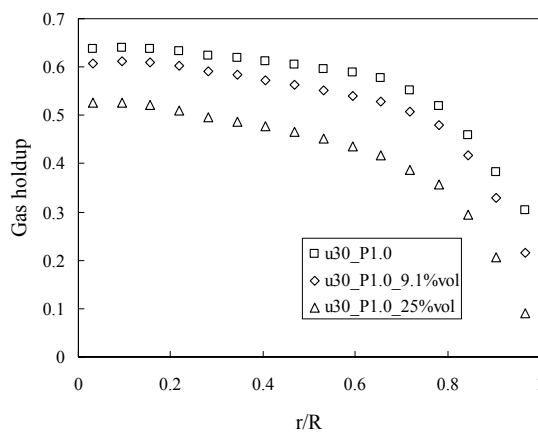


Figure 3-27. Effects of the solids loading on gas holdup radial profiles, method (I), air-C₉C₁₁-FT catalyst, 0.30 m/s, 1.0 MPa

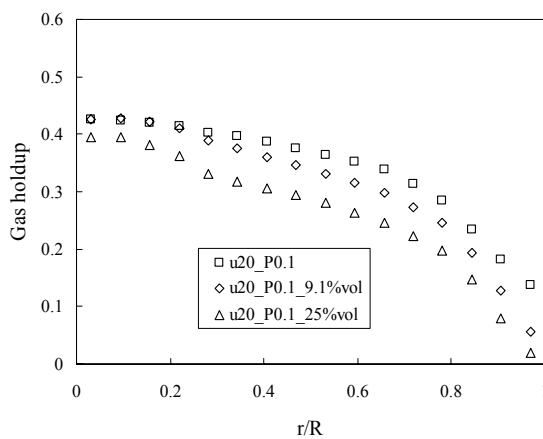


Figure 3-28. Effects of the solids loading on gas holdup radial profiles, method (I), air-C₉C₁₁-FT catalyst, 0.20 m/s, 0.1 MPa

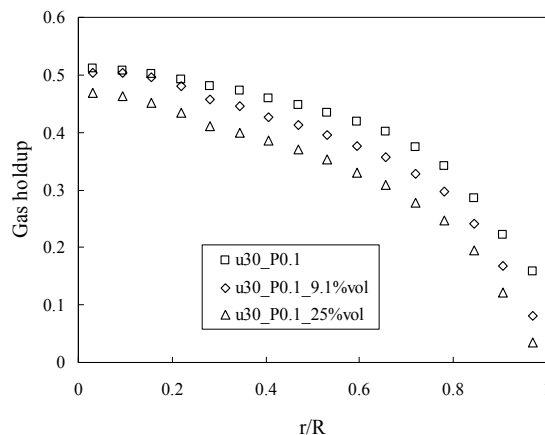


Figure 3-29. Effects of the solids loading on gas holdup radial profiles, method (I), air-C₉C₁₁-FT catalyst, 0.30 m/s, 0.1 MPa

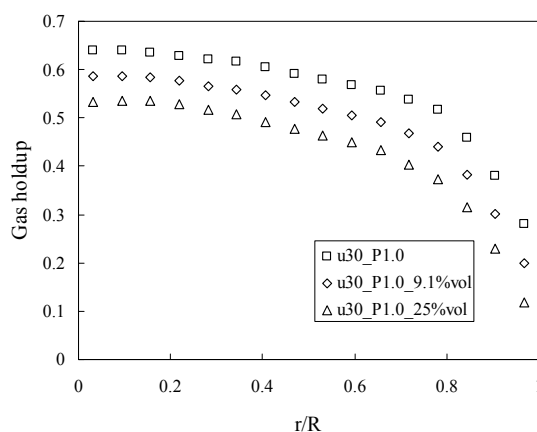


Figure 3-30. Effect of the solids loading on the holdup radial profiles, method (I), air-Therminol-FT catalyst, 0.30 m/s, 1.0 MPa

3.12. Summary

In this chapter, an air-C₉C₁₁-FT catalyst system and an air-Therminol-FT catalyst system were selected to mimic the physical properties of the three phases in a typical FT SBCR. The hydrodynamics in the mimicked FT SBCR was investigated in terms of phase holdup distribution, liquid/solids velocity field, and turbulence parameters using CT and CARPT techniques. Once technical difficulties were overcome, 90 μm tracer particles were used, which made it possible to track the small FT catalyst. A

CT/CARPT occurrence reconstruction method was presented and tested, which independently estimates the three-phase holdup distributions using single-course γ -ray CT scans, avoiding the two assumptions made in the previous CT/overall gas holdup method (Rados, 2003). The two reconstruction methods were compared at the same conditions, which showed some differences in the gas holdup and apparent differences in the solids holdup. With closely similar physical properties, the two liquids, C₉C₁₁ and Therminol, resulted in similar profiles of the measured hydrodynamic parameters. The FT catalyst was found to exhibit significant differences from the 150 μm glass beads in profiles of gas holdup, solids velocity, and turbulence parameters. Apparent solids loading effects on the hydrodynamics were found at 9.1% vol. which were observed to a lesser degree by Rados (2003) and Shaikh (2007) in other systems. The effects of solids types may be caused by different particle sizes, different apparent densities, or the porous surface of FT catalyst. Further study is needed in order to separately investigate these factors for the main reason that causes the FT catalyst/glass beads differences in the hydrodynamic parameters.

Chapter 4

Back-Mixing of Phases

4.1. Scope

Back-mixing of phases in BCRs or SBCRs can negatively affect reactor performance, and has been the focus of a number of tracer studies. Despite considerable effort to investigate the back-mixing extent of gas, liquid, and solids phases, the dispersion parameters predicted by the reported empirical correlations are in great deviation, because of the complicated effects of different variables (reactor geometry, physical properties, and operating parameters). Prediction of the phase back-mixing, especially in a mimicked or real FT SBCR, remains a difficulty due to the lack of experimental data in systems at conditions of FT interest. This part of the work investigates the back-mixing of the three phases in the mimicked FT SBCR via tracer techniques. A gaseous tracer technique was developed to estimate the gas phase back-mixing using a helium tracer. The particle tracking data obtained in Chapter 3 were interpreted using a virtual tracer response method to quantify the liquid or solids phase back-mixing. The obtained response curves were fitted with axial dispersion models or a mechanistic model, and the extent of phase back-mixing was quantified by estimating the

dispersion parameters. The dispersion parameters measured in this chapter provide necessary inputs for the reactor models used in the mass transfer study in Chapter 5.

4.2. Gas Phase Back-Mixing

As mentioned previously, there exist almost no gas tracer studies in SBCRs, and only very limited measurements in BCRs using air and water at ambient pressure. Both adding FT catalyst to a system at high solids loadings and operating at high pressures are expected to have significant impacts on the bubble dynamics, which may result in different back-mixing of the gas phase in the mimicked FT SBCR. Hence, it is of importance to quantify the gas phase back-mixing in the mimicked FT SBCR. For the developed gaseous tracer technique, procedures were designed to remove extra dispersions caused in the distributor plenum zone and the sampling/analytical system for accurate measurements. For quantification, an axial dispersion model was used to fit the response curves of the tested SBCR (with a large L/d_c ratio), and the gas phase axial dispersion coefficient values were obtained. Effects of the catalyst solids loading and operating pressure on the gas phase back-mixing were investigated. The obtained axial dispersion coefficient values can also be used as needed model inputs in the mass transfer measurements of various gases, using the developed gaseous tracer technique.

4.2.1. Reactor Setup and Experimental Conditions

The gas tracer experiments were conducted in the 0.162 m stainless steel SBCR (II) that was used for the overall gas holdup measurements in the CT/overall gas holdup method (Figure 3-2b). Details of the reactor setup and its operation have been reported in the hydrodynamics chapter, hence they are not discussed here.

To quantify the effects of FT catalyst and high pressure on the gas phase back-mixing, experimental conditions were selected with superficial gas velocities ranging up to 0.30 m/s, operating pressure at 0.1 MPa and 1.0 MPa, and solids loading at 0, 9.1% vol., and 25% vol. in the air-C₉C₁₁-FT catalyst system (Table 4-1).

Table 4-1. List of gas back-mixing experimental conditions (helium tracer)

System	Superficial gas velocity u_g , m/s	Pressure, MPa	Solids loading
	0.03, 0.05, 0.08, 0.14, 0.20, 0.30	1.0	0
	0.03, 0.05, 0.08, 0.14, 0.20, 0.30	0.1	0
Air-C ₉ C ₁₁ -FT	0.03, 0.05, 0.08, 0.14, 0.20, 0.30	1.0	9.1% vol.
Catalyst	0.03, 0.05, 0.08, 0.14, 0.20, 0.30	0.1	9.1% vol.
	0.03, 0.05, 0.08, 0.14, 0.20, 0.30	1.0	25% vol.
	0.03, 0.05, 0.08, 0.14, 0.20, 0.30	0.1	25% vol.

4.2.2. The Developed Gaseous Tracer Technique

As shown in Figure 4-1, the gaseous tracer unit consists of a gas-liquid/slurry separator, gas analyzer, gas pump, and PC with data acquisition software. The gas analyzer is a GOW-MAC 20 series binary analyzer which contains a flowing reference thermal conductivity detector (TCD). A GOW-MAC 59-300 pump was used to draw the gas sample out of the reactor, through the gas-liquid/slurry separator, and past the TCD. For proper operation of the gas analyzer, the gas-liquid/slurry separator is necessary to remove the liquid or solids mixed in the gas sample. The response from the TCD was amplified, converted to digital signals, and recorded as time-series data at a sampling frequency of 10 Hz. A schematic diagram of the gaseous tracer technique configuration with the reactor setup is shown in Figure 4-2. Operating procedures and technical information of the gaseous tracer technique are provided in Appendix B.

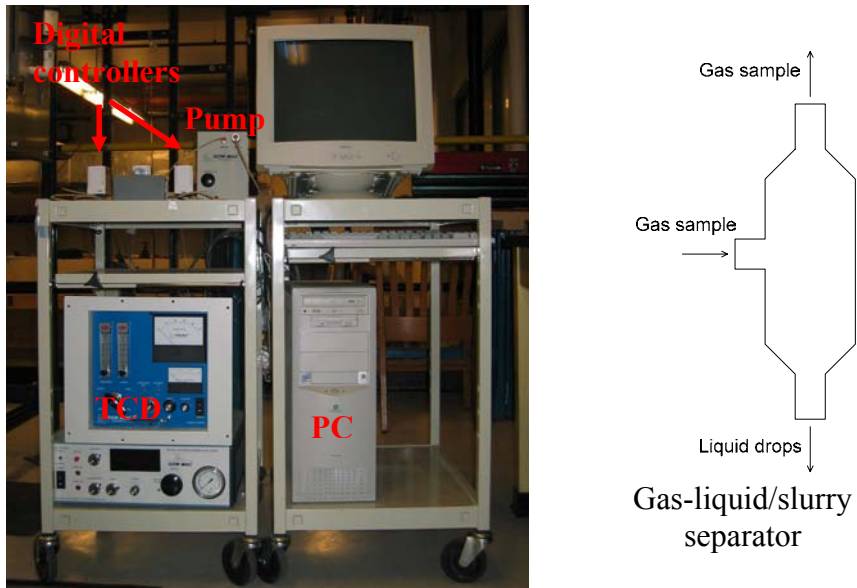


Figure 4-1. Facilities of the gaseous tracer technique

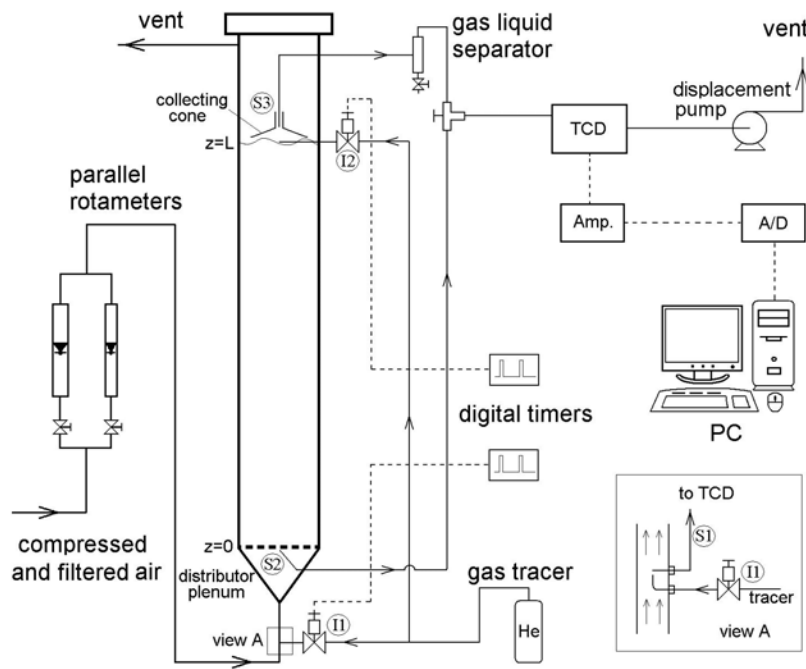


Figure 4-2. Schematic diagram of the gaseous tracer technique and the reactor setup

Common difficulties involved in a gaseous tracer technique are non-ideal injections and extra dispersion in the sampling and analysis system, which may cause significant measurement errors if they are not accounted for. When the tracer impulse injection is made at the gas inlet, the dynamic tracer concentration at the gas distributor, which is the input of the reactor model, does not make a delta function (or an ideal step in the step change method). The gas phase undergoes mixing in the distributor plenum. Similarly, due to the extra dispersion caused by the sampling and analytical components, responses measured by the gas analyzer do not exactly represent the actual tracer response at the reactor disengagement level. To take account of the extra dispersion effects in the distributor plenum zone and the sampling/analytical system, a convolution or deconvolution method needs to be applied (Levenspiel, 1972). These two methods both yield a fair comparison between experimental measurements and reactor model predictions, either by adding the extra dispersion to the model predictions (convolution) or by removing the extra dispersion from the measurements of the whole system (deconvolution). However, due to its numerical instability, the deconvolution method is difficult to apply and is not widely used in chemical engineering research (Mills et al., 1989). Therefore, it is not discussed here. The convolution method had not been employed in gas dispersion studies of BCRs until 1990 (Wachi et al., 1990; Shetty et al., 1992; and Kantak et al., 1995). Before then, the systems were generally assumed to have ideal tracer input and an ideal sampling/analytical system, which are not the actual cases. However, even in the above mentioned three BCR studies, only the dispersion in the sampling/analytical system was measured and accounted for with the convolution method, while the mixing in the distributor plenum was still neglected. The necessity of considering the mixing in the distributor plenum was evaluated and is shown below.

To estimate extra mixings in the distributor plenum and the sampling/analytical system, different ports for injection and sampling were designed. As shown in Figure 4-2, two injection ports were used separately for injections: one in the center of the inlet gas line

(port I1), and one at the center of the gas-liquid disengagement surface (port I2). The three sampling ports are:

- S1, a thin tube placed in the gas inlet, close to the injection port I1 (shown in view A in Figure 4-2).
- S2, a thin tube placed very close to one of the pores of the gas distributor.
- S3, a thin tube placed in the neck area of the collecting cone above the disengagement surface.

The collecting cone for S3 was designed to be open at its top to keep the mass gas flow passing quickly through it, in order to avoid gas back-mixing in the gas phase and to have a quick response. Using solenoid valves controlled by digital timers, the injecting time was set to be 0.05 s, and the pulses were precisely started at the set time. Gas samples were continuously withdrawn to the gas analyzer through thin nylon tubes (1/16" inner diameter), under vacuum generated by the pump connected at the exit of the analytical instrument. Using the designed injection and sampling ports, four measurements (i~iv) were designed and conducted at each experimental condition. As shown in Table 4-2, different ports of tracer injection and gas sampling were used for the four measurements. The gas dispersion effects measured in each measurement are also listed in Table 4-2. The obtained response curves were normalized by the maximum value in each curve. As discussed in detail in the next two sections, two model fits using the convolution method were conducted (Figure 4-3) to accurately estimate the gas phase axial dispersion.

Table 4-2. The designed four measurements for the gaseous tracer technique

Measure-ment	Tracer injection	Sampling location	Dispersion zones measured
(i)	I1	S1	Sampling/analytical system from S1 (S2)
(ii)	I1	S2	Plenum zone + sampling/analytical system from S2
(iii)	I2	S3	Sampling/analytical system from S3
(iv)	I1	S3	Plenum zone + reactor zone + sampling/analytical system from S3

I1, I2 – Injection ports; S1, S2, S3 – Sampling ports. Locations of all ports are indicated in Figure 4-2

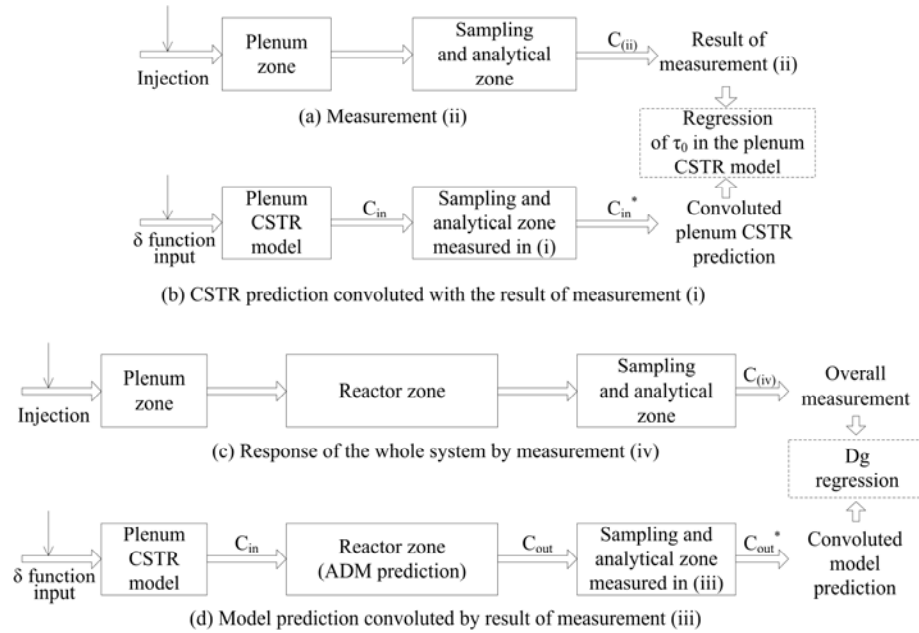


Figure 4-3. Diagram of the convolution and model fits of the response curves

4.2.3. Estimation of the Gas Mixing in the Distributor Plenum

The distributor plenum of a SBCR usually causes significant back-mixing before the gas tracer reaches the distributor. In this work, gas mixing in the distributor plenum is assumed to be a continuous stirred tank reactor (CSTR), which was validated and then used to provide the input for the reactor model (ADM). The equation for the pulse injection in the plenum is expressed as

$$\frac{dC}{dt} = -\frac{1}{\tau_0} C, \quad (4-1)$$

where τ_0 is the retention time of the CSTR. The initial condition is given as $C=C_{inj}$ at $t=0$, where C_{inj} is the tracer concentration in the plenum immediately after the injection. The solution of Equation 4-1 gives the output of the plenum at the gas distributor

$$C = C_{inj} \cdot e^{-t/\tau_0}. \quad (4-2)$$

The plenum output in a dimensionless form (C/C_{inj}) was used as the input of the reactor model (Figure 4-3) and is therefore defined as C_{in} , which gives

$$C_{in} = e^{-t/\tau_0}. \quad (4-3)$$

The τ_0 was estimated by a regression as shown in Figure 4-3 (a) and (b). Measurements (i) and (ii), respectively, represent the dispersion in the sampling/analytical system and the dispersion in the plenum section plus the sampling/analytical system (Table 4-2). In measurement (i), the gaseous tracer input profile can be considered as an ideal pulse, because the sampling tube of port S1 was placed very close to the injection nozzle and the mass flow of air removes the gas tracer around the nozzle almost instantly. As seen in Figure 4-4, the response of measurement (i), $C_{(i)}$, has apparent spreading, suggesting dispersion in the sampling/analytical system. The sampling lines from S1 and S2 were designed with the same length and inner diameter, therefore, the dispersion from S1 and that from S2 can be considered as identical, and $C_{(i)}$ was used to convolute the plenum CSTR predictions, C_{in} . Therefore, C_{in} , calculated from Equation 4-3 was convoluted by $C_{(i)}$, per Levenspiel (1972)

$$C_{in}^*(t) = \int_0^t C_{in}(t') \cdot C_{(i)}(t-t') \cdot dt'. \quad (4-4)$$

The convoluted plenum CSTR prediction, C_{in}^* , was then compared against the response of the measurement (ii), $C_{(ii)}$, and τ_0 was optimized by minimizing the averaged squared error in the time domain, defined as

$$\text{Error} = \frac{1}{n} \sum_{j=1}^n [C_{in}^*(t_j) - C_{(ii)}(t_j)]^2. \quad (4-5)$$

As also shown in Figure 4-4 (where $u_g=0.03$ m/s), the good fit between $C_{(ii)}$ and C_{in}^* indicates that the gas mixing in the distributor plenum can be modeled with a CSTR. In this work, instead of a delta function (i.e., no plenum back-mixing), C_{in} calculated from the plenum CSTR model with a fitted τ_0 was used as the input tracer profile at the gas distributor (i.e., the input profile to the reactor model) for the reactor dispersion parameter regression.

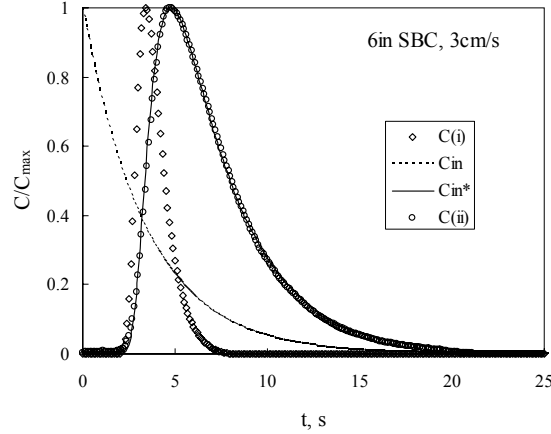


Figure 4-4. Dynamic gas tracer concentration at the distributor with CSTR model fit. $C_{(i)}$ - measured dispersion in the sampling/analytical system from S1 (S2); C_{in} - plenum CSTR prediction at the gas distributor; C_{in}^* - C_{in} convoluted by $C_{(i)}$; $C_{(ii)}$ – response measured at the gas distributor

4.2.4. Estimation of the Gas Axial Dispersion in the Reactor

An 1-D ADM was used for the gas phase axial dispersion in this work, expressed as

$$\frac{\partial C_g}{\partial t} = D_g \frac{\partial^2 C_g}{\partial z^2} - \frac{u_g}{\epsilon_g} \frac{\partial C_g}{\partial z}. \quad (4-6)$$

Danckwerts boundary conditions were used for the closed-closed boundaries, because at the inlet there was sufficient pressure drop across the gas distributor, and at the outlet the cone covers most of the reactor cross-section and the flow rate through the neck of the cone was large due to the open design.

$$z = 0, \quad u_g \cdot C_{in} = u_g \cdot C_g|_{z=0} - D_g \frac{\partial C_g}{\partial z}|_{z=0}$$

$$z = L, \quad \frac{\partial C_g}{\partial z}|_{z=L} = 0,$$

where C_{in} was calculated by Equation 4-3 with a fitted τ_0 as discussed earlier. The initial condition is given by

$$t = 0, \quad C_g = 0.$$

The superficial gas velocity u_g in the reactor model is known from the pre-set flow rate. The regression of the reactor dispersion parameter is schematically illustrated in Figure 4-3 (c) and (d). First, the dispersion in the sampling/analytical system from port S3 was obtained by measurement (iii) (Table 4-2), providing $C_{(iii)}$ to convolute the reactor and plenum models' prediction. Then, the response of a pulse injection through the whole system was obtained by measurement (iv) (Table 4-2). Using C_{in} from Equation 4-3 (CSTR model of the plenum) as the input tracer profile, the reactor model yields an output profile $C_{out}(t)$ at the disengagement level, which is then convoluted by $C_{(iii)}$ per Levenspiel (1972)

$$C_{out}^*(t) = \int_0^t C_{out}(t') \cdot C_{(iii)}(t-t') \cdot dt' \quad (4-7)$$

The convoluted reactor model prediction, C_{out}^* , was compared against the measured dispersion of the whole system, $C_{(iv)}$, for parameter fitting, by minimizing the averaged squared error in the time domain, defined as

$$\text{Error} = \frac{1}{n} \sum_{j=1}^n [C_{out}^*(t_j) - C_{(iv)}(t_j)]^2 \quad (4-8)$$

The gas holdup ε_g was considered as another fitted parameter along with D_g , although it could be measured separately by observing the dynamic bed expansion. This is because there usually is some error in the measured overall ε_g , which yields imprecise time lag in the model predicted curves, and therefore, inaccurate fitted D_g values. With the ε_g - D_g two-parameter fitting, the model better matches both the time lag and the dispersion (spreading) of the response curves. The fitted gas holdup values and those from independent overall gas holdup measurements were found to have less than 5% average absolute relative errors. Figures 4-5 and 4-6 show good model fits of C_{out}^* and $C_{(iv)}$ in both the bubbly flow regime (0.02 m/s) and the churn-turbulent flow regime (0.20 m/s), respectively. Similar good fits were also observed at other operating conditions. The averaged squared error calculated by Equation 4-8 is in the range of $0.1 \cdot 10^{-3} \sim 0.3 \cdot 10^{-3}$. The helium tracer has a small solubility in the liquid, which was assumed negligible in the D_g measurements. To evaluate the error caused by the helium

solubility, D_g fittings using Equation 4-6 with a mass transfer term and a correlation predicted k_1a value were tested. It was found that considering the small solubility of helium or not caused only less than 1% of relative error in the fitted D_g values.

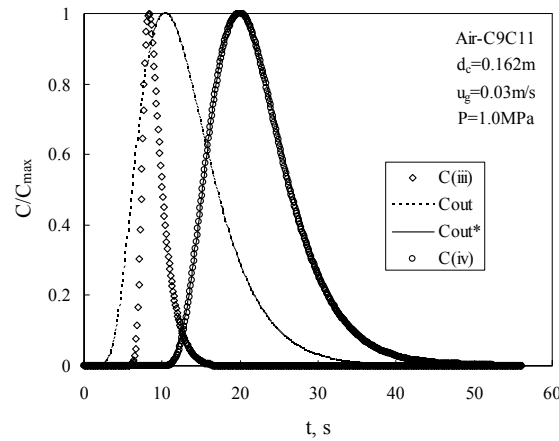


Figure 4-5. Gas tracer response curves at the outlet with ADM fit (Bubbly flow). $C_{(iii)}$ - measured dispersion in sampling/analytical system; C_{out} - reactor outlet tracer response predicted by the ADM; C_{out}^* - C_{out} convoluted by $C_{(iii)}$; $C_{(iv)}$ - measured reactor outlet response

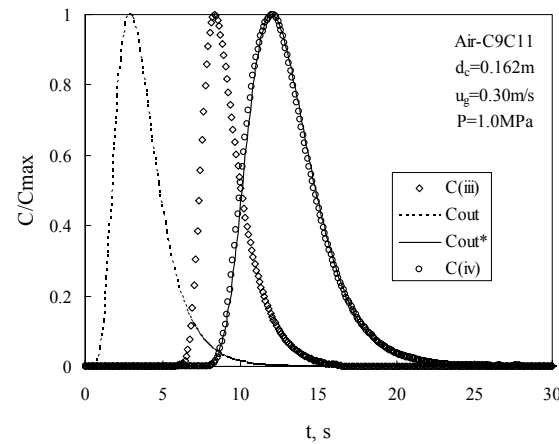


Figure 4-6. Gas tracer response curves at the outlet with ADM fit (Churn-turbulent flow). $C_{(iii)}$ - measured dispersion in sampling/analytical system; C_{out} - reactor outlet tracer response predicted by the ADM; C_{out}^* - C_{out} convoluted by $C_{(iii)}$; $C_{(iv)}$ - measured reactor outlet response

In order to prove it is necessary to use C_{in} as the input of the reactor model, similar parameter fitting was conducted using a delta function to replace C_{in} . It was found that

the obtained D_g values using a delta function input were about double those obtained using C_{in} . This suggests that not accounting for the mixing in the distributor plenum causes about 100% error in the final D_g results, because the extra mixing in the plenum is lumped into the axial dispersion coefficient and makes its estimated value larger. Such consideration of the plenum mixing was not part of the previous investigations in the literature.

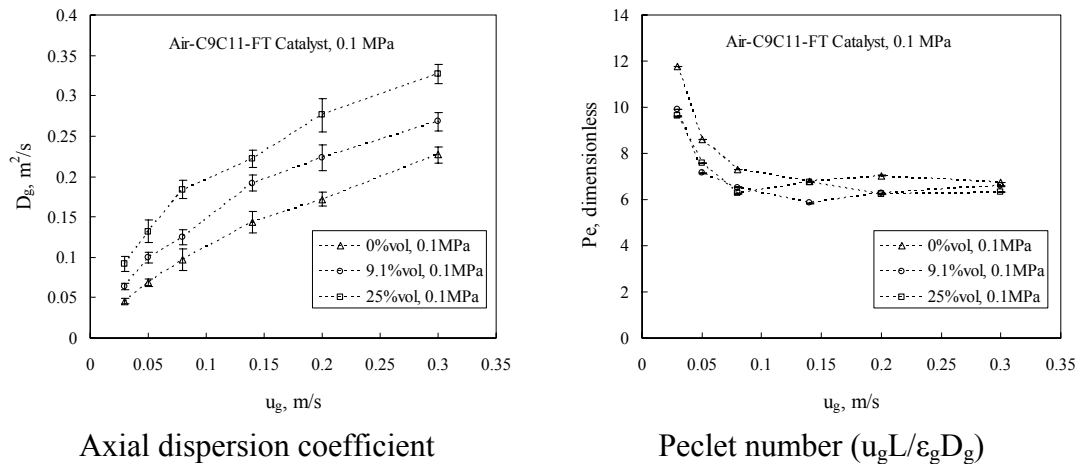
4.2.5. Investigation of the Effects of Operating Parameters on Gas Phase Back-Mixing

Gaseous tracer measurements are scarce in the literature for three-phase SBCRs, especially in mimicked FT conditions. The effects of various operating parameters on the gas axial dispersion in the mimicked FT SBCR were investigated in this work.

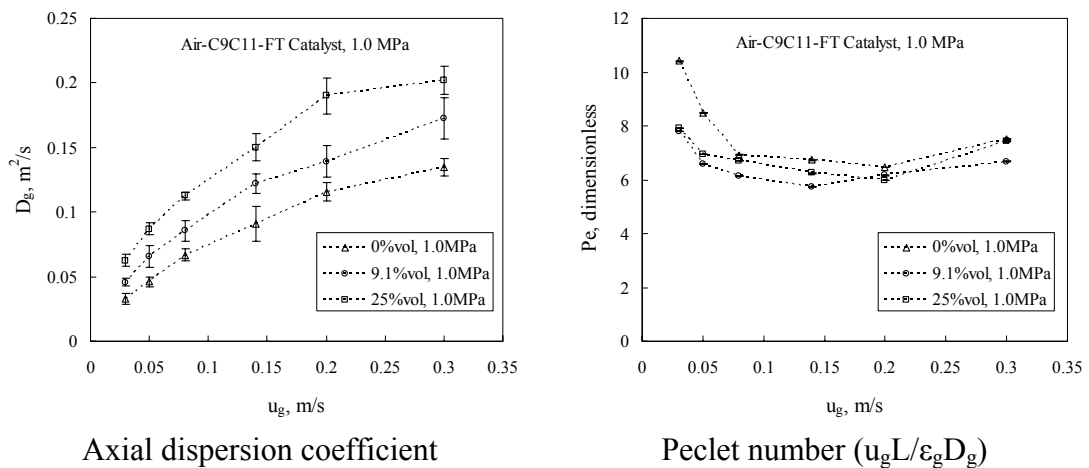
a) Effects of the Superficial Gas Velocity on the Gas Axial Dispersion

As shown in Figures 4-7 (a, b), D_g values increased with the superficial gas velocity up to 0.30 m/s at all the tested pressures and solids loadings. This effect is due to the wider bubble size distribution and increased bubble frequency at higher gas throughput (as found in an air-water system by Xue, 2004). A similar effect of superficial gas velocity in two-phase BCRs has been reported by Joseph et al. (1984), Kulkarni et al. (1984), Kago et al. (1989), Wachi et al. (1990), Shetty et al. (1992), and Kantak et al. (1995), and is also reflected in all the reported D_g correlations (Table 2-6). Besides, the Peclet number ($Pe = u_g L / \varepsilon_g D_g$, a ratio of convection to dispersion) was calculated and also plotted (Figures 4-7 a, b) to show the extent of gas back-mixing. The Pe values decrease apparently with the superficial gas velocity at $u_g < 0.10$ m/s, indicating a quick increase of gas back-mixing in this u_g range. However, the Pe - u_g curves reach plateaus at $u_g > 0.10$ m/s, showing little further increase. The Pe values even increase slightly (i.e., gas back-mixing reduces slightly) at high superficial gas velocities, especially at 1.0 MPa. Xue (2004) found in an air-water system that deep in the churn-turbulent flow regime the number of smaller bubbles increased faster than larger bubbles with

the superficial gas velocity. Xue (2004) also found that the mean bubble chord length first increased with the superficial gas velocity and then decreased when the superficial gas velocity became higher ($u_g > 0.30$ m/s). Similar trends of the bubble dynamic parameters possibly also exist in the mimicked FT SBCR, which may have contributed to the trend of the measured Pe number to increase with the superficial gas velocity. The bubble dynamics in the mimicked FT SBCR is yet to be investigated.



a) Air-C₉C₁₁-FT catalyst, 0.1 MPa



b) Air-C₉C₁₁-FT catalyst, 1.0 MPa

Figure 4-7. Effects of the superficial gas velocity and solids loading on the gas phase axial dispersion coefficient and Peclet number

b) Effect of the Solids Loading on the Gas Axial Dispersion

The gas axial dispersion was measured at three solids loadings: zero, 9.1% vol., and 25% vol. Effects of the solids loading on the gas axial dispersion can be seen in Figures 4-7 (a, b). Adding solids significantly enhanced D_g at both low and high pressures. Such an effect of solids loading has not been reported in the open literature to the best of the author's knowledge. This effect may be caused by the formation of a wider bubble size distribution and more large bubbles, which increase the turbulence (as proved by the CARPT measurements). The higher and non-isotropic turbulence enhances gas dispersion (especially in the axial direction) and therefore increases the axial dispersion coefficient. On the other hand, the D_g increase may be also attributed to the radial differences in the axial gas convection. The bubbles in a wider size distribution carry the tracer gas at more non-uniform rise velocities, causing more spreading of the response, which is interpreted with a D_g value by the ADM.

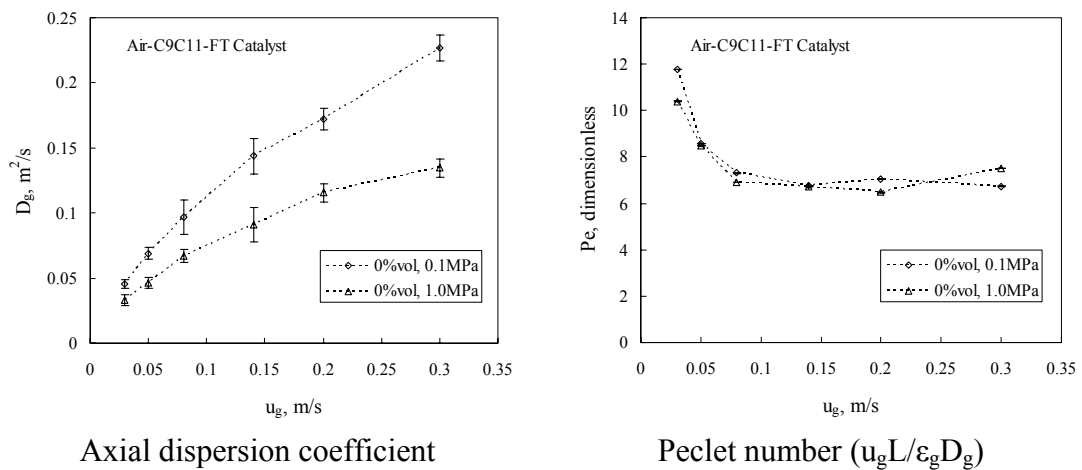
In contrast to the behavior of D_g , the differences in the calculated Pe values between different solids loadings are smaller than those in the D_g values. This suggests that although adding solids significantly increased the axial dispersion coefficient, the total back-mixing extent was increased only slightly or moderately. This is because the gas holdup is reduced by adding solids (observed by CT), yielding a shorter gas phase residence time for the back-mixing to happen. Therefore, a shorter residence time and a higher D_g value have opposite effects on the resulting total gas phase back-mixing.

c) Effect of the operating pressure on the gas axial dispersion

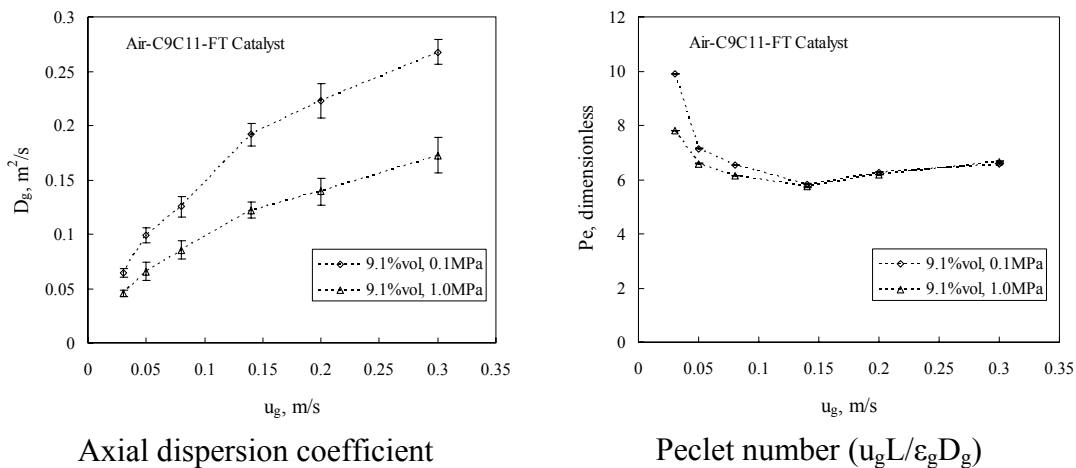
Effects of the operating pressure on the gas axial dispersion have not been investigated and reported in the open literature, either. This study investigated the pressure effect at 0.1 MPa and 1.0 MPa using various superficial gas velocities and solids loadings. As shown in Figures 4-8 (a, b, and c), the elevated pressure decreased the D_g values at the tested conditions. The smaller bubble sizes and lower turbulence parameters at high pressure decrease the gas phase dispersion. Compared with the liquid phase back-

mixing study described later in this chapter, the pressure effect on the gas phase axial dispersion is opposite to that on the liquid phase axial dispersion, which increased with the pressure. Both eddy diffusivities and global recirculation contribute to the axial dispersion of liquid or solids phase in bubble/slurry bubble columns. (Degaleesan et al., 1998). The operating pressure increases the liquid back-mixing by a faster global liquid recirculation (as proved and discussed in the CARPT section). However, due to the nature of BCRs and SBCRs, the bubbles' recirculation is much smaller than that of the liquid or slurry (Xue, 2004). Therefore, the high pressure mainly has the effect of decreasing the gas axial dispersion coefficient through lowering the turbulence and eddy diffusivities.

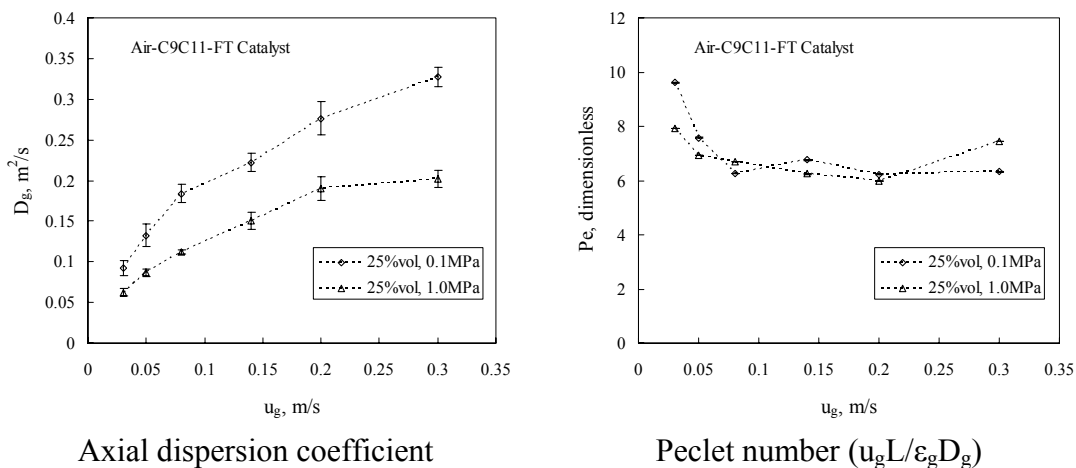
As also shown in Figures 4-8, the Pe values have little differences between 0.1 MPa and 1.0 MPa at $u_g > 0.10$ m/s. The reason is similar to that which explains the solids effect on the Peclet number, but in the other direction. The gas holdup increases at high pressure, causing the gas phase to stay longer in the column and have more back-mixing. Therefore, the total gas phase back-mixing in terms of Peclet number is similar at 0.1 MPa and 1.0 MPa as a combined result of two competing factors, axial dispersion coefficient and mean residence time.



a) Zero solids loading



b) 9.1% vol. solids loading



c) 25% vol. solids loading

Figure 4-8. Effects of the operating pressure on the gas dispersion coefficient and Peclet number

4.2.6. Summary of the Gas Phase Back-Mixing Investigation

Gaseous tracer experiments were conducted for the first time in the mimicked FT system (air-C₉C₁₁-FT catalyst) at superficial gas velocities up to 0.30 m/s; solids loading of zero, 9.1% vol., and 25% vol.; and pressures of 0.1 MPa and 1.0 MPa. The gas axial dispersion coefficient and the Peclet number, therefore the extent of gas phase

back-mixing, have been measured and discussed. The findings and conclusions are summarized as follows:

- The mixing in the distributor plenum and sampling/analytical system is significant and causes D_g measurement errors. By using four experiments and the convolution method, the extra dispersion was removed from the measured axial dispersion in the reactor bed.
- The FT catalyst significantly enhances the axial dispersion coefficient of the gas phase in the SBCR, which may be caused by the wider bubble size distribution and higher turbulence resulted from adding solids.
- At high pressure, the measured D_g values become smaller, which is opposite to the pressure effects on the liquid or slurry phases. This is because the gas phase does not have as much recirculation, and the high pressure generates smaller bubbles and lower turbulence.
- Despite the obvious effects of the solids loading and operating pressure on the axial dispersion coefficient, their effects on the total gas back-mixing in terms of Peclet number are small, especially at $u_g > 0.10$ m/s. Affected by the operating parameters through the gas holdup, the mean residence time added an opposite effect on the Peclet number than the axial dispersion coefficient. In other words, the shorter mean residence time reduces or even cancels the effects of the higher axial dispersion coefficient values on the calculated Peclet numbers.

4.3. Liquid Phase Back-Mixing using a Virtual Tracer Response

Method

The liquid phase back-mixing was investigated by estimating different dispersion parameters in both an ADM and a mechanistic model. With conventional liquid tracer techniques, it is practically impossible to distribute the liquid tracer perfectly in a specific spatial pattern within a short instance. Measurements of the liquid tracer concentration usually involve sensors which are intrusive and have a certain extent of response delay. The virtual tracer response method developed in this work can provide

almost perfect injection and sampling using the trajectory data obtained by CARPT. The sections below introduce the virtual tracer method and its application in different reactor scale models. Since a buoyant tracer particle for liquid-tracking CARPT experiments is highly affected by the high concentration solids, the liquid phase tracking was conducted only under two-phase conditions, and therefore the liquid phase back-mixing was investigated only under the two-phase CARPT conditions.

4.3.1. The Developed Virtual Tracer Method

This section shows a developed virtual tracer response method to obtain response curves from the CARPT Lagrangian trajectories, which can be considered as the result of a virtual tracer batch injection. Essentially this method estimates the behavior of a batch of tracer particles using long-time traces of a single particle, invoking the ergodic hypothesis. The idea to obtain various types of information from the single particle tracking data was used in several previous studies (Villermaux, 1996; Cassanello et al., 1996; Kiared et al., 1997; Bhusarapu, 2005). The information obtained in these previous studies includes trajectory length distribution, residence time distribution, and dynamic change of the tracer centroids. Response curves resulting from a virtual tracer injection have not been reported in the literature, and can be useful in quantification of dispersion parameters in reactor models.

Procedures of the method are given below. First, an injection position and several sampling positions are defined in the reactor. These positions can be selected in any shape (points, lines, surfaces, or volumes) depending on the needs of a reactor model. Figure 4-9 schematically shows the injection/sampling positions and the response curves for an ADM application. One axial injection level was selected at z_0 , and several axial sampling levels were selected at z_i ($i=1, 2, 3\dots$). Then, a counting process generates raw count tracer response curves ($P_s(z_i, t)$, $i=1, 2, 3\dots$) at the sampling levels z_i ($i = 1, 2, 3\dots$) using the developed computer program. Such a counting process is described as follows. Each time when the tracer particle passes the injection level z_0 , a counting thread starts from $t = 0$ and ends at $t = t_\infty$. The value of t_∞ was set as 100

seconds, which was found sufficient at the tested conditions for the dynamic response curves to reach asymptotic values (Figures 4-9 and 4-10). The physical meaning of t_∞ is that, after this time, the position of the tracer particle becomes independent of its original position at $t=0$ (the injection level) and is located randomly with the flow. Within each t_∞ -long counting thread, at any time $t = t_j$ when the particle passes a sampling level z_i , one count is added to the curve of $P_s(z_i, t)$ at time t_j . It should be noted that very likely the tracer particle passes the injection level again during a current counting thread. At this time, a new counting thread with its own clock starts from $t = 0$, in addition to the existing counting threads. This means that multiple counting threads could exist in parallel with their counting clocks running differently. Although these counting threads overlap in time, each one of them represents an independent section of the tracer particle motion at the operating conditions. After about 40,000 counting threads were completed using the 20-hour trajectory data, each raw count curve $P_s(z_i, t)$ accumulated many counts. The curves obtained from these 40,000 counting threads of a single tracer particle can be considered as the responses of releasing that many tracer particles simultaneously and uniformly at the injection level. Hence, the obtained curves represent the responses of an almost perfect virtual injection of a batch of tracer in the cross-section of the injection level. According to the same assumption made in the CT/CARPT occurrence reconstruction method (Chapter 3), the obtained raw counts $P_s(z_i, t)$ are proportional to the virtual liquid tracer concentration based on the reactor volume. However, the reactor model for the liquid phase uses the liquid tracer concentration in gas-free liquid $C_l(z_i, t)$, and therefore needs the same type of data for model fit. Although the liquid concentrations $C_l(z_i, t)$ are proportional to the raw counts $P_s(z_i, t)$, the liquid volume-based $C_l(z_i, t)$ can not be calculated from the reactor volume-based $P_s(z_i, t)$ without knowing the gas holdup. Fortunately, only dimensionless response curves are sufficient for fitting the parameters, which can be obtained by normalizing $P_s(z_i, t)$ curves. The obtained raw count response curves $P(z_i, t)$ were normalized by the asymptotic values of the curves to yield the dimensionless liquid tracer concentration $C'(z_i, t)$.

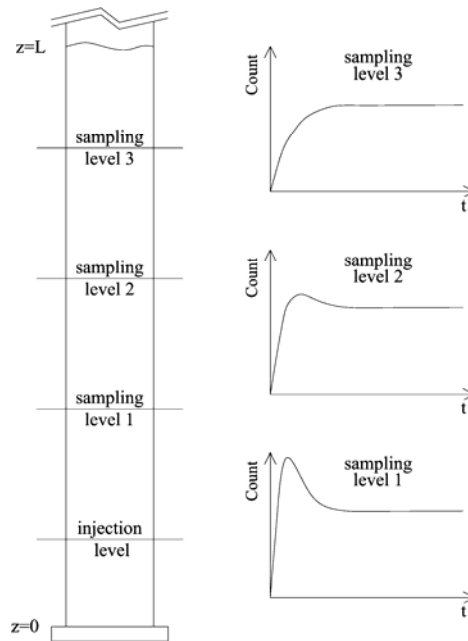


Figure 4-9. Schematic diagram of the injection/sampling levels (in the application to the ADM) and the extracted tracer response curves

4.3.2. Parameter Estimation for the Axial Dispersion Model

ADMs have been widely used for the liquid phase in modeling BCRs or SBCRs. Applications for FT processes include Mills et al. (1996), de Swart et al. (2002), Rados et al. (2003), etc. The axial dispersion coefficient is lumped with the effects of both global recirculation and local turbulent diffusions, and remains difficult to predict at unknown conditions. This section obtains data of the liquid axial dispersion coefficient in the air-C₉C₁₁ system.

For the ADM, the injection level was made at $z_0=2 d_c$, and additional six sampling levels were evenly distributed between $3 d_c$ and $8 d_c$ (i.e. $z_2=3 d_c$, $z_2=4 d_c$, $z_3=5 d_c$, $z_4=6 d_c$, $z_5=7 d_c$, and $z_6=8 d_c$). These axial levels were all selected within the CARPT calibrated zone ($1.5 d_c \sim 9.5 d_c$) for better data confidence. The obtained dimensionless liquid tracer concentration curves at 0.30 m/s and 1.0 MPa are shown in Figure 4-10.

Equations for the transient 1-D ADM are shown below, with boundary conditions and initial conditions written in the way that the virtual tracer response curves were obtained.

$$\frac{\partial C_1}{\partial t} = D_1 \frac{\partial^2 C_1}{\partial z^2} \quad (4-9)$$

$$\text{Boundary conditions: } z=0, \frac{\partial C_1}{\partial z} = 0 ; z=L, \frac{\partial C_1}{\partial z} = 0$$

$$\text{Initial conditions: } t=0, C(z,0)=0 \text{ at } z \neq 2 d_c, \text{ and } C(z_0,0) = \infty \text{ at } z_0 = 2 d_c$$

The optimum D_1 values were obtained by fitting the model predictions to the tracer response curves at all of the six sampling levels simultaneously, using the minimum squared error defined as

$$\text{error} = \sum_{i=1}^{n_{z,D}} \sum_{j=1}^{n_t} [C_1^{\text{Exp-D}}(z_i, t_j) - C_1^{\text{Mod-D}}(z_i, t_j)]^2 \quad (4-10)$$

Figure 4-10 shows the virtual tracer response curves fitted with the model predictions. Besides the “simultaneous fitting” method described above, an “individual fitting” method was used as a check of the axial consistency of the model fit. The “individual fitting” method obtains a set of D_1 values by fitting the model to each response curve individually, with a minimum squared error defined as

$$\text{error} = \sum_{j=1}^{n_t} [C_1^{\text{Exp-D}}(z_i, t_j) - C_1^{\text{Mod-D}}(z_i, t_j)]^2 \quad (4-11)$$

The relative difference in the D_1 results obtained by the two fitting methods is less than 5%, and the standard deviation of the fitted D_1 values at different axial levels using the “individual fitting” method is about 10%. This suggests that the fitting results are consistent in the fully developed region for the tested column. The obtained D_1 values for the three two-phase CARPT conditions are shown in Table 4-3, along with the values of the centerline liquid velocity, $u_l(0)$, and the cross-sectional time-averaged axial liquid eddy diffusivity, D_{zz} , measured by CARPT.

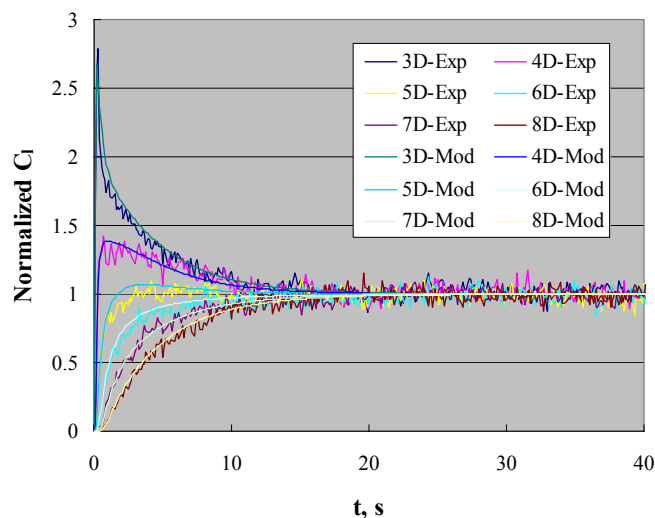


Figure 4-10. Virtual tracer response curves of liquid flow fitted with the ADM

Table 4-3. Obtained values of the liquid axial dispersion coefficient

Conditions	$D_1, 10^{-4} \text{ m}^2/\text{s}$	$u_1(0), \text{ m/s}$	$D_{zz}, 10^{-4} \text{ m}^2/\text{s}$
Air-C ₉ C ₁₁ , 0.30 m/s, 0.1 MPa	475	0.58	253
Air-C ₉ C ₁₁ , 0.30 m/s, 1.0 MPa	764	0.87	172
Air-C ₉ C ₁₁ , 0.20 m/s, 1.0 MPa	482	0.71	156

The $u_1(0)$ and D_{zz} values show the extent of global liquid recirculation and local turbulent diffusion, which both contribute to the axial dispersion coefficient (Degaleesan et al., 1998). At 0.30 m/s, the D_1 value at 1.0 MPa is higher than that at 0.10 MPa, although the eddy diffusivity is lower at the high pressure. This suggests that the larger recirculation rate at high pressure, as shown by the centerline liquid velocity, plays a major role in the measured axial dispersion coefficient. A higher superficial gas velocity at 1.0 MPa increased the values of $u_1(0)$ and D_{zz} , which both contribute to a higher D_1 value. Because the superficial liquid velocity is zero in the semi-batch system, the Peclet number for the liquid phase was not calculated.

4.3.3. Parameter Estimation for a Mechanistic Model

Based on the flow mapping studies in BCRs at the CREL, the mechanistic recirculation and cross flow with dispersion (RCFD) model was first developed for the liquid phase by Degaleesan et al. (1996) and Degaleesan (1997), and then extended to both gas and liquid phases by Gupta et al. (2001 a and b) and Gupta (2002). Later, the RCFD model was used to match the tracer response curves, using parameters estimated by correlations (Chen et al., 2006). With its phenomenological basis, the mechanistic RCFD model is expected to reduce the difficulties of predicting the phase mixing in reactor modeling. Figure 4-11 schematically shows the RCFD model with its compartments and the involved parameters. The holdups, velocities, and inversion point were obtained by CT and CARPT measurements. The length ratios of the sparger compartment and the disengagement compartment to the reactor diameter were assumed to be 1.0, based on the velocity field observed in the CARPT measurements. Gupta (2002) found that changing these two ratios between 0.5 and 2.0 does not make a significant difference in the model predictions. Besides these parameters, this mechanistic model has three dispersion parameters: the axial dispersion coefficient in the up-flowing zone, $D_{x,u}$; the axial dispersion coefficient in the down flowing zone, $D_{x,d}$; and the radial dispersion (between the two zones) coefficient, D_r . As mentioned earlier, these three dispersion parameters had not been estimated directly from experimental measurements. Historically, eddy diffusivities measured by CARPT were used for the RCFD model due to the lack of dispersion parameter values. The axial eddy diffusivities averaged in the up-flowing and down-flowing zones and the radial eddy diffusivity at the inversion point were used as substitutes for $D_{x,u}$, $D_{x,d}$, and D_r in the model, respectively. This work presents a method to estimate the values of these dispersion parameters using the virtual tracer method and the CARPT data obtained in Chapter 3.

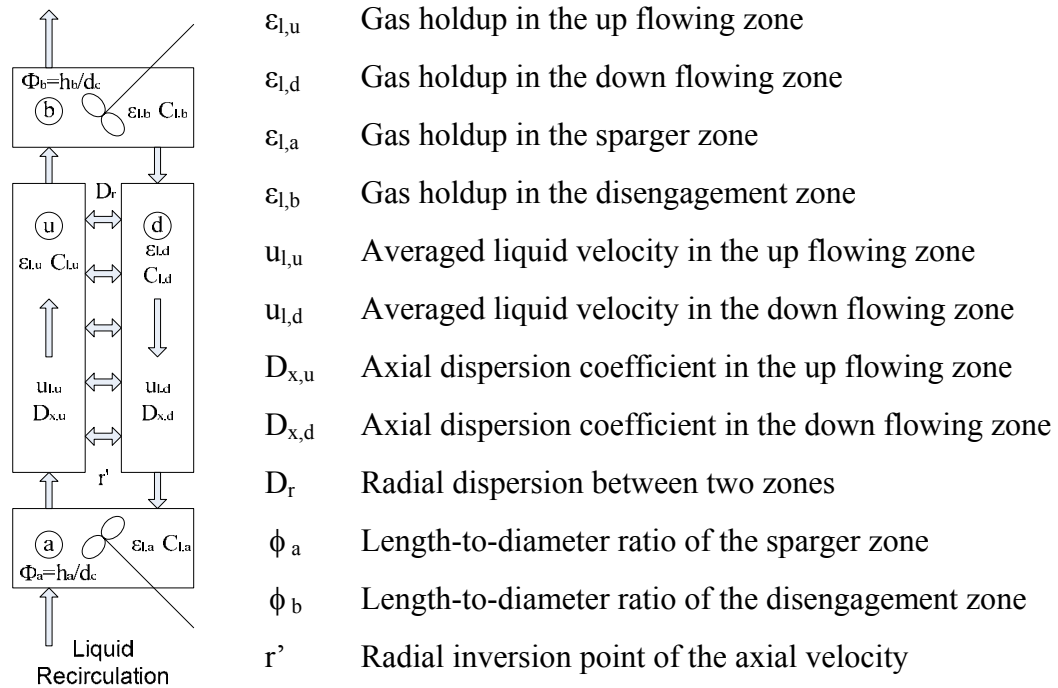


Figure 4-11. Schematic diagram of the RCFD model with its parameters

In order to fit the three dispersion coefficients using virtual tracer response curves, the injection and sampling positions need to be defined properly. It was found that two virtual tracer injections in different zones were necessary for the three-parameter fit. For each injection, two response curves were obtained at different locations. As shown in the schematic diagram of Figure 4-12, the selected injection and sampling positions are:

Injection (1): up zone $z/d_c=5.5$
 Sampling (1-1): up zone $z/d_c=7.0$
 Sampling (1-2): down zone $z/d_c=5.5$

Injection (2): down zone $z/d_c=5.5$
 Sampling (2-1): down zone $z/d_c=4.0$
 Sampling (2-2): up zone $z/d_c=5.5$

Using the virtual tracer method introduced earlier and the CARPT data obtained in this work, four response curves were obtained for each operating condition, as shown in Figure 4-14 for an example condition (air-C₉C₁₁, 0.30 m/s, 0.1 MPa).

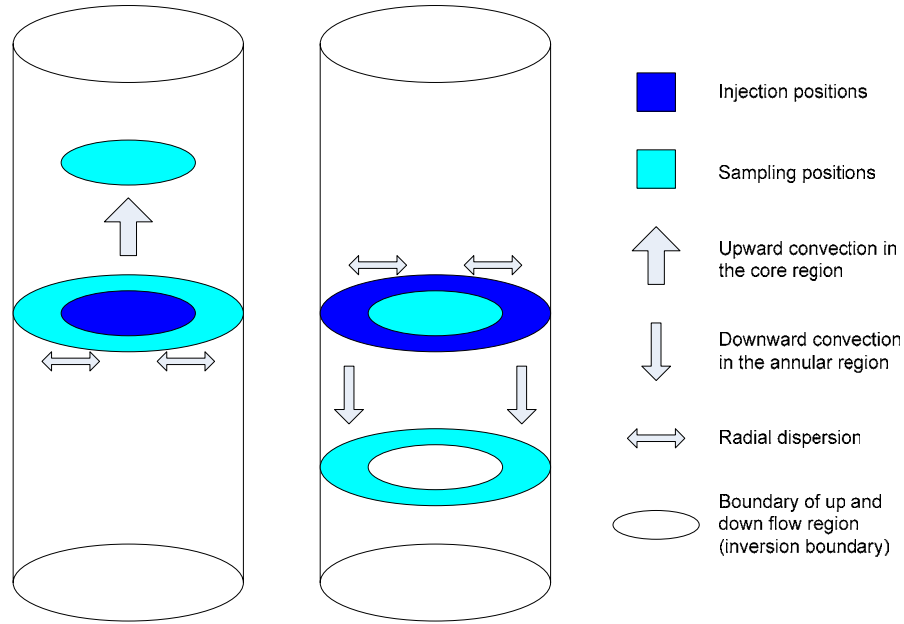


Figure 4-12. Schematic diagram of the virtual tracer injection and sampling positions in the RCFD model

The RCFD model for the liquid phase was used with the dispersion and convection terms, written as below.

1) Liquid moving upwards ($0 \sim r'$):

$$\frac{\partial C_{1,u}}{\partial t} = D_{x,u} \frac{\partial^2 C_{1,u}}{\partial z^2} - u_{1,u} \frac{\partial C_{1,u}}{\partial z} - \frac{4(D_r \varepsilon_l)_{r=r'}}{r' R \varepsilon_{1,u}} (C_{1,u} - C_{1,d}) \quad (4-12)$$

2) Liquid moving downwards ($r' \sim R$):

$$\frac{\partial C_{1,d}}{\partial t} = D_{x,d} \frac{\partial^2 C_{1,d}}{\partial z^2} + u_{1,d} \frac{\partial C_{1,d}}{\partial z} + \frac{4r'/R}{R^2 - r'^2} \cdot \frac{(D_r \varepsilon_l)_{r=r'}}{\varepsilon_{1,d}} (C_{1,u} - C_{1,d}) \quad (4-13)$$

3) Liquid in distributor zone (a):

$$\frac{dC_{1,a}}{dt} = \frac{\varepsilon_{1,d} u_{1,d}}{\varepsilon_1 \phi_a d_C} \cdot \frac{(R^2 - r'^2)}{R^2} C_{1,d} \Big|_{x=0} - \frac{\varepsilon_{1,u} u_{1,u}}{\varepsilon_1 \phi_a d_C} \cdot \frac{r'^2}{R^2} C_{1,a} \quad (4-14)$$

4) Liquid in disengagement zone (b):

$$\frac{dC_{1,b}}{dt} = \frac{\varepsilon_{1,u} u_{1,u}}{\varepsilon_1 \phi_b d_C} \cdot \frac{r'^2}{R^2} C_{1,u} \Big|_{x=L} - \frac{\varepsilon_{1,d} u_{1,d}}{\varepsilon_1 \phi_b d_C} \cdot \frac{(R^2 - r'^2)}{R^2} C_{1,b} \quad (4-15)$$

Boundary conditions:

$$z = 0, C_{1,u} \Big|_{z=0} = C_{1,a}, C_{1,d} \Big|_{z=0} = C_{1,a}$$

$$z = L, C_{1,u} \Big|_{z=L} = C_{1,b}, C_{1,d} \Big|_{z=L} = C_{1,b}$$

Initial conditions:

$$t = 0, C_{1,a} = C_{1,b} = C_{1,u} = C_{1,d} = 0$$

$$t \rightarrow 0+, C_{1,u} \Big|_{z=5.5d_c} = \infty \text{ at } z=5.5 d_c \text{ for injection (1)}$$

$$t \rightarrow 0+, C_{1,d} \Big|_{z=5.5d_c} = \infty \text{ at } z=5.5 d_c \text{ for injection (2)}$$

An iteration process was used for the three-parameter regression. Each dispersion parameter was fitted individually using old values of other dispersion parameters. The parameter value was updated after its individual fit, and such a procedure was repeated for three parameters until iteration convergence criteria (tolerances) were met (Figure 4-13).

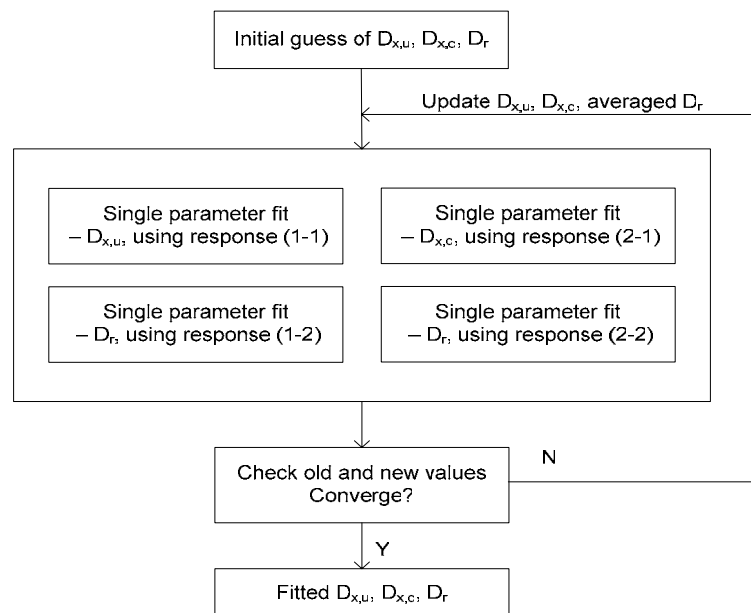


Figure 4-13. Iteration process for the three-parameter fitting

The generated virtual tracer response curves with RCFD model fits are shown in Figures 4-14 (a~d) at the example condition (air-C₉C₁₁, 0.30 m/s, 0.1 MPa). The estimated parameter values for the three two-phase CARPT conditions are listed in Table 4-4, along with the values of other parameters obtained by CARPT.

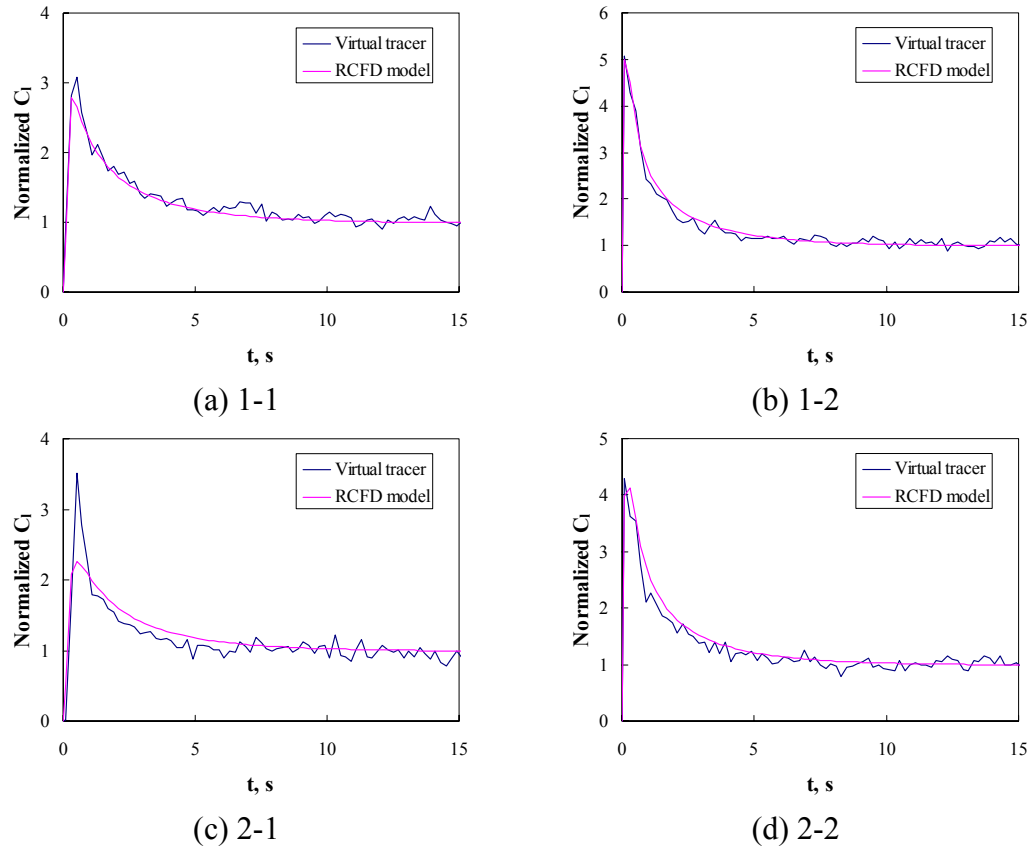


Figure 4-14. Virtual tracer response curves of liquid fitted with the RCFD model

Table 4-4. Obtained values of the RCFD dispersion coefficients

Conditions	Estimated RCFD dispersion coefficients			Eddy diffusivities by CARPT		
	$D_{x,u}$	$D_{x,d}$	D_r	D_{zz} zone 1	D_{zz} zone 2	D_{rr} at r'
	$10^{-4} \text{ m}^2/\text{s}$	$10^{-4} \text{ m}^2/\text{s}$	$10^{-4} \text{ m}^2/\text{s}$	$10^{-4} \text{ m}^2/\text{s}$	$10^{-4} \text{ m}^2/\text{s}$	$10^{-4} \text{ m}^2/\text{s}$
0.30 m/s, 0.1 MPa	358	413	39	262	244	24
0.30 m/s, 1.0 MPa	275	319	41	193	151	18
0.20 m/s, 1.0 MPa	242	303	32	170	143	17

The values of the dispersion coefficients in the RCFD model were found to be greater than the eddy diffusivities obtained by CARPT. This is because the axial dispersion parameters in the RCFD model are contributed by the eddy diffusivity and the mixing within each compartment. As a compartment model, instead of a 2-D model, this RCFD model uses an axial dispersion coefficient to describe the back-mixing in each of the two compartments. The radial non-uniformity of the axial convection also contributes to the axial dispersion coefficients in the compartments. On the other hand, the axial dispersion parameters in the RCFD model are apparently reduced from the axial dispersion coefficient in the ADM. The RCFD model was built by separating the global recirculation from the dispersions within each compartment, which are completely lumped into one axial dispersion coefficient in the ADM.

4.3.4. Summary of the Liquid Phase Back-Mixing Investigation

A virtual tracer response method was presented which obtained response curves using the CARPT trajectory data. With the virtual tracer response method, back-mixing of the liquid phase at two-phase conditions was investigated using an ADM and a mechanistic RCFD model. Dispersion parameters of the liquid phase in these two reactor models were estimated at the CARPT conditions. At the tested conditions, the axial dispersion coefficient in the ADM was larger than the axial dispersion coefficients in the RCFD model, and the dispersion coefficients in the RCFD model were larger than the eddy diffusivities obtained by CARPT. This can be explained by a Taylor-type analysis of a 2-D convection-dispersion model and the axial dispersion model (Degaleesan et al., 1996), which separates the contributions of global recirculation and local eddy diffusivities to the axial dispersion coefficient in the ADM. The effects of operating pressure on the various dispersion parameters were found and discussed.

4.4. Solids Phase Back-Mixing using the Virtual Tracer Response

Method

The solids concentration axial gradient in a SBCR is a result of particle settling and solids dispersion, as described by the sedimentation-dispersion model (SDM) used in many 1-D modeling studies (from Cova, 1966 and Imafuku et al., 1968 to Nakao et al., 2000 and Zhang et al., 2002). This section presents a transient method to estimate the solids axial dispersion coefficient in the SDM, using the virtual tracer response method. The SDM was selected to describe the solids back-mixing in the mimicked FT SBCR because this tested reactor has a large length-to-diameter ratio. However, for a short and shallow (low L/d_c ratio) SBCR, the SDM may not be suitable for describing the solids phase mixing and needs further evaluation, which is not the focus of this work.

4.4.1. Solids Virtual Tracer Response Curves for the Transient Method

Virtual tracer response curves were obtained from the CARPT trajectories using the virtual tracer response method presented in the liquid back-mixing section. Similarly, one injection level ($z_0=2 d_c$) and six sampling levels ($z_1=3 d_c$, $z_2=4 d_c$, $z_3=5 d_c$, $z_4=6 d_c$, $z_5=7 d_c$, and $z_6=8 d_c$) were selected for the SBCR. Virtual tracer response curves were obtained at five of the three-phase CARPT conditions included in Table 3-5.

4.4.2. Sedimentation-Dispersion Model and its Parameter Fitting

For semi-batch SBCRs, a transient SDM is written in Equation 4-16, along with the boundary and initial conditions. The initial conditions were determined according to how the injection and sampling levels were defined.

$$\frac{\partial C_s}{\partial t} = D_s \frac{\partial^2 C_s}{\partial z^2} + u_{st} \frac{\partial C_s}{\partial z}, \quad (4-16)$$

where u_{st} is the settling velocity of the FT catalyst.

$$\text{Boundary conditions: } z=0, D_s \frac{\partial C_s}{\partial z} + u_{st} C_s = 0; z=L, D_s \frac{\partial C_s}{\partial z} + u_{st} C_s = 0$$

$$\text{Initial conditions: } t=0, C_s(z,0)=0 \text{ at } z \neq 2 d_c, \text{ and } C_s(z,0)=\infty \text{ at } z=2.0 d_c$$

The values of u_{st} at different conditions were estimated using the correlation presented by Matsumoto et al. (1989), which uses phase physical properties and considers the three-phase correction. The model's sensitivity on the u_{st} estimation was analyzed and is reported in Appendix C. For a given D_s value, solving Equation 4-16 yields solids concentration profiles at the sampling levels, and $C_s^{Mod-D}(z_i, t)$ can be obtained from normalization by the asymptotic values of the model predicted curves. The optimum D_s values were obtained by fitting the model predictions to the tracer response curves at all six sampling levels simultaneously, with the minimum squared error method defined as

$$\text{error} = \sum_{i=1}^{n_{z,D}} \sum_{j=1}^{n_t} [C_s^{Exp-D}(z_i, t_j) - C_s^{Mod-D}(z_i, t_j)]^2. \quad (4-17)$$

Besides the “simultaneous fitting” method, the “individual fitting” method was also used to evaluate the axial consistency of the model fit. Similar to the findings in the liquid back-mixing section, the two fitting methods have small differences, indicating that the results are consistent in the fully developed region. Figure 4-15 shows the response curves and SDM fits at an example condition.

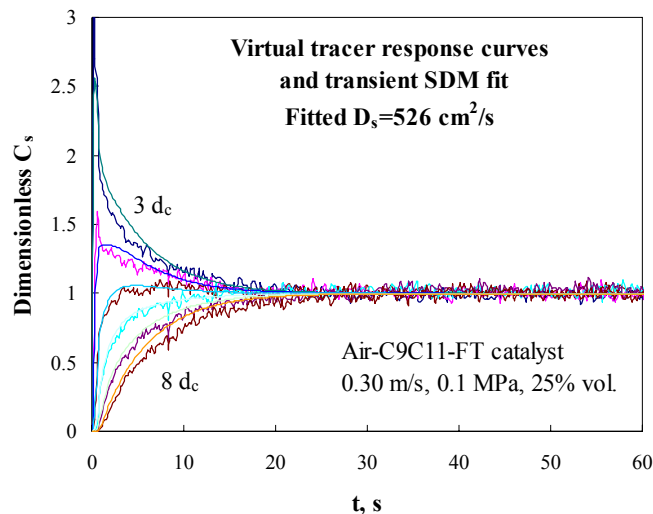


Figure 4-15. Virtual tracer response curves of solids flow fitted with the transient SDM

A steady state method is presented in Appendix C, which estimates the solids axial dispersion coefficient using the solids concentration axial gradient obtained from both the CARPT occurrence and the asymptotic values of the response curves. Compared to the steady state method, the transient method was found to be much less sensitive to the estimated solids settling velocity. Therefore, the transient method was used for all of the tested conditions, and the results are presented below.

4.4.3. Solids Phase Axial Dispersion in the Mimicked FT SBCR

Values of fitted D_s , estimated u_{st} , and measured ε_g are listed in Table 4-5. Also listed in this table are the centerline solids axial velocity and axial eddy diffusivity obtained by CARPT. The solids axial dispersion coefficient increased with the superficial gas velocity, which is consistent with the previous studies (Matsumoto et al., 1992; Nakao et al., 2000; Zhang et al., 2002; etc.). The higher solids recirculation and solids axial eddy diffusivity observed by CARPT both contribute to the higher D_s value at higher superficial gas velocity. The D_s value is higher at 1.0 MPa than that at the ambient pressure. This is caused by the enhanced solids recirculation at high pressure, as shown by the larger $u_s(0)$ value. At high pressure, the resulting higher gas holdup and reduced bubble sizes (Wilkinson, 1991; Lin et al., 1998; Xue, 2004) lift the slurry more efficiently and cause faster solids recirculation. On the other hand, the smaller bubble sizes at high pressure result in lower turbulence, and therefore lower eddy diffusivities, as found in the CARPT data. Similar to the liquid flow, solids global recirculation and eddy diffusivities both contribute to the axial dispersion coefficient (Degaleesan and Dudukovic, 1998). Although the axial eddy diffusivity is lower at high pressure, the increase of the global solids circulation dominates the pressure effect on the solids axial dispersion coefficient.

At the common condition (0.30 m/s, 1.0 MPa, and 25% vol.) of the air-C9C11-FT catalyst and air-Therminol-FT catalyst systems, the D_s values are close, as a result of the similar hydrodynamics as proved by CT and CARPT.

Table 4-5. Obtained values of the solids axial dispersion coefficient

System	u_g , m/s	P, MPa	C_s , % vol.	D_s , cm^2/s	$u_s(0)$, m/s	D_{zz} , cm^2/s
Air-C ₉ C ₁₁ -FT Catalyst	0.30	1.0	25	868	0.65	327
	0.30	0.1	25	526	0.44	290
	0.20	1.0	25	578	0.55	248
	0.30	1.0	9.1	797	0.86	256
Air-Therminol-FT Catalyst	0.30	1.0	25	879	0.66	331

4.4.4. Summary of the Solids Phase Back-Mixing Investigation

The solids phase axial dispersion was investigated at the three-phase CARPT conditions, which cover different superficial gas velocities, operating pressures, and solids loadings. Values of D_s were estimated using the virtual tracer response method and a transient SDM. The solids axial dispersion coefficient increased with the superficial gas velocity, due to the enhanced solids recirculation and solids axial eddy diffusivity. Elevated operating pressure yielded a higher solids axial dispersion coefficient as a result of the significantly enhanced solids global recirculation, despite the lower solids axial eddy diffusivity due to the reduced turbulence observed at high pressure.

Chapter 5

Gas-Liquid Mass Transfer

5.1. Scope

For FT processes which involve absorption of various gases into the liquid phase, the liquid-side gas-liquid mass transfer is usually the controlling mass transfer step in SBCRs. The volumetric gas-liquid mass transfer coefficient, k_{1a} , is one of the important design parameters for SBCRs. Despite the large amount of k_{1a} data and correlations reported in the literature, none is available at FT conditions or mimicked FT conditions using real FT catalyst. The gas-liquid mass transfer in a SBCR is greatly affected by the hydrodynamics and mixing, which are yet to be fully understood. This work has investigated the hydrodynamics and phase back-mixing using selected three phase systems. If the gas-liquid mass transfer is studied at the same conditions, the obtained knowledge may greatly help understand the gas-liquid mass transfer in systems that mimic FT physical properties. The phase dispersion parameters that were estimated from other parts of this work provide necessary inputs to estimate k_{1a} values using the selected reactor models.

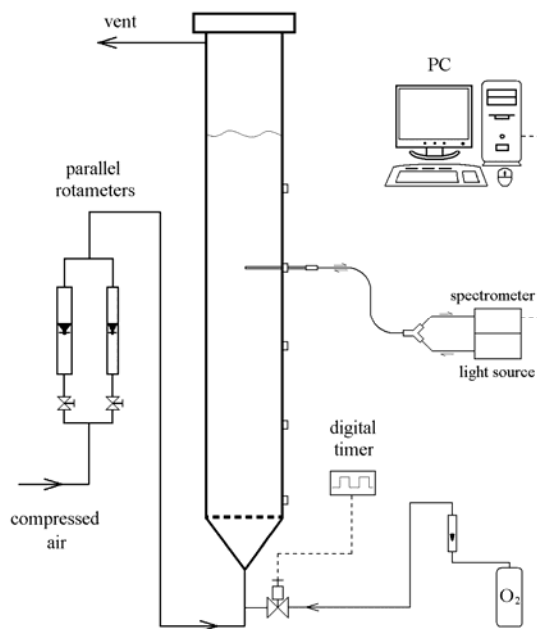
The k_{1a} values in a mimicked FT SBCR would be significantly different from those in a real FT SBCR, due to the obvious differences in gas diffusivities or the presence of chemical reactions. However, mass transfer measurements in a real FT SBCR are practically impossible due to the rigorous conditions. This work investigated the gas-liquid mass transfer of various gas species in the selected FT mimicking system using the developed gaseous tracer technique and optical oxygen probe technique. The objective was to obtain k_{1a} data in the mimicked FT SBCR, and to develop a k_{1a} correlation with a theoretical basis for predictions of other species. The following sections discuss the developed techniques, improved measurement methods, involved reactor models, results and analysis, and the development of a relation/correlation.

5.2. Gas-Liquid Mass Transfer of Oxygen

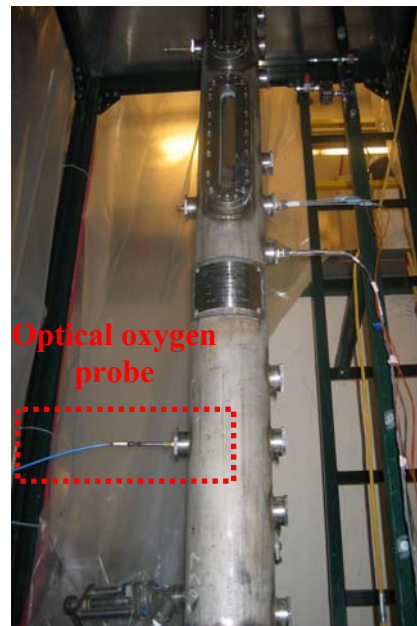
The k_{1a} values of oxygen were measured using the optical oxygen probe technique and an oxygen-enriched air dynamic method. The experimental details, reactor models used, and results are shown below.

5.2.1. Reactor Setup and Experimental Conditions

Mass transfer experiments were conducted in SBCR (II) (Figure 3-2b), which was designed with ports and windows. The gas distributor was the same as in the hydrodynamic study (PPH). Various ports in the column were used for mounting the optical oxygen probe for local measurements at different axial locations (Figure 5-1). The radial position of the probe was selected at the center ($r/R=0$) for the axial dispersion model (ADM) and at both $r/R=0$ and $r/R=0.85$ for the mechanistic, compartmental model.



a) Schematic diagram of the setup



b) Picture of the probe in column

Figure 5-1. Experimental setup of the optical oxygen probe in the SBCR

The air-C₉C₁₁-FT catalyst system was used for all the mass transfer measurements. To quantify the effects of operating parameters and provide a k_{1a} database in the mimicked FT SBCR, experimental conditions for the oxygen mass transfer measurements cover various superficial gas velocities, solids loadings, and operating pressures (Table 5-1).

Table 5-1. Experimental conditions of oxygen mass transfer measurements

System	u_g , m/s	Pressure, MPa	Solids loading
Air-C ₉ C ₁₁	0.03, 0.05, 0.08, 0.14, 0.20, 0.30	1.0	0
	0.03, 0.05, 0.08, 0.14, 0.20, 0.30	0.1	0
Air-C ₉ C ₁₁ -FT Catalyst	0.03, 0.05, 0.08, 0.14, 0.20, 0.30	1.0	9.1% vol.
	0.03, 0.05, 0.08, 0.14, 0.20, 0.30	0.1	9.1% vol.
	0.03, 0.05, 0.08, 0.14, 0.20, 0.30	1.0	25% vol.
	0.03, 0.05, 0.08, 0.14, 0.20, 0.30	0.1	25% vol.

5.2.2. Optical Oxygen Probe Technique

The dissolved oxygen (DO) concentration was measured using the optical oxygen probe, a fluorescence-type sensor first developed at the TU-Hannover, Germany (Comte et al., 1995). Due to their fast response, stability, and long life, optical oxygen probes have been recently used in BCR mass transfer studies (Terasaka et al., 1998; Jordan and Schumpe, 2001; Lau et al., 2004). This type of probe was further developed and commercialized by Ocean Optics, Inc. and has been acquired for this work. The technique (Figure 5-2) consists of an optical probe (model T1000), optic fiber, light source, spectrometer, USB A/D converter, PC, and software. As shown in Figure 5-3, when irradiated at 470 nm by the light source, a thin film coated on the probe tip emits fluorescence at about 600 nm. Increase of the DO concentration quenches the 600-nm fluorescence linearly. Therefore, DO concentration data are obtained by measuring the fluorescence intensity with the spectrometer.



Figure 5-2. Optical oxygen probe system (Ocean Optics, Inc.)
1. Optical oxygen probe; 2. Optical fiber; 3. Light source; 4. Spectrometer; 5. Integrated A/D converter and USB interface; 6. PC and software

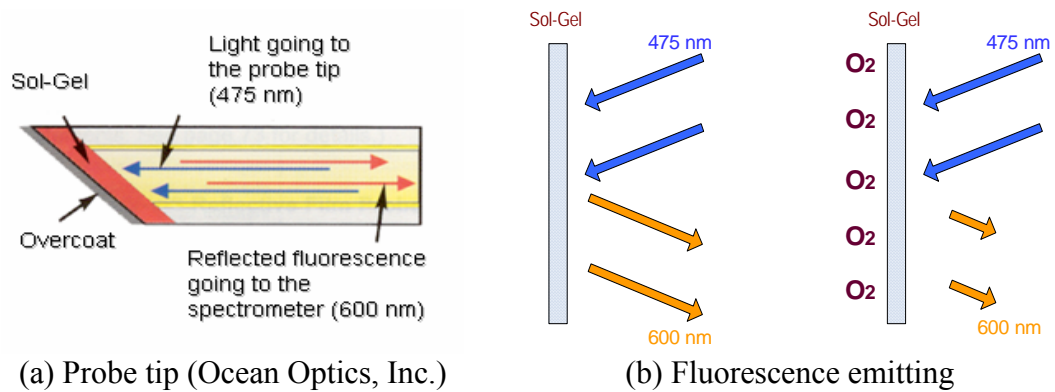


Figure 5-3. Working mechanism of the optical oxygen probe

Due to the sensor delay, the measured DO response $C_{\text{sensor}}(t)$ does not exactly represent the actual DO concentration, $C_1(t)$, and needs to be deconvoluted. As illustrated in Figure 5-4, the sensor response constant, K_{sensor} , was estimated by a two-point calibration process using liquid (A), stripped of oxygen by a nitrogen flow, and liquid (B), saturated with the oxygen in the air flow. By quickly switching the probe from liquid (A) to liquid (B), a step change in the DO concentration was created which yielded a response, $C_{\text{sensor}}(t)$, at the probe signal. As shown in Equation 5-1, the measured response follows the actual DO concentration with a certain delay determined by the probe constant (K_{sensor}).

$$\frac{dC_{\text{sensor}}(t)}{dt} = K_{\text{sensor}}[C_1(t) - C_{\text{sensor}}(t)]. \quad (5-1)$$

$C_{\text{sensor}}=0$ at $t=0$, and $C_1=C_{1,0}^*$ at $t>0$, where $C_{1,0}^*$ is the DO concentration saturated by the oxygen in the air.

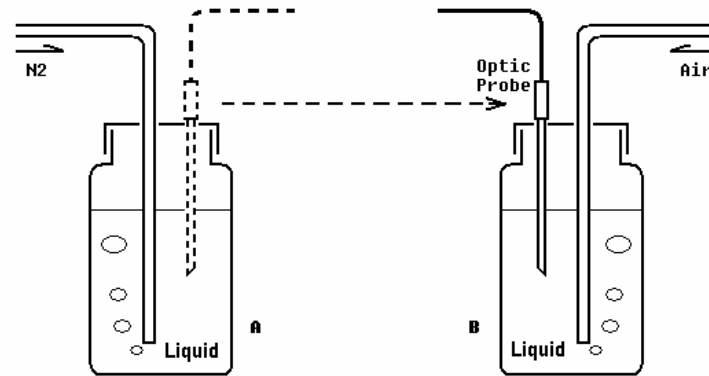


Figure 5-4. Schematic diagram of the optical oxygen probe calibration

Equation 5-1 and its initial condition yield the sensor response as

$$C_{\text{sensor}}(t) = C_{1,0}^* (1 - e^{-K_{\text{sensor}} \cdot t}). \quad (5-2)$$

By fitting Equation 5-2 to the measured calibration curves (Figure 5-5), the value of K_{sensor} was found to be approximately 1.1 s^{-1} , varying slightly with each individual probe. This sensor constant is about one magnitude larger than a typical k_{la} value, indicating that the time scale of the probe delay is small enough for k_{la} measurements. Using Equation 5-1, the probe responses obtained in experiments were deconvoluted to obtain the actual DO concentration profiles by

$$C_1(t) = C_{\text{sensor}}(t) + \frac{1}{K_{\text{sensor}}} \frac{dC_{\text{sensor}}(t)}{dt}. \quad (5-3)$$

The deconvoluted $C_1(t)$ responses were then used for the model fits.

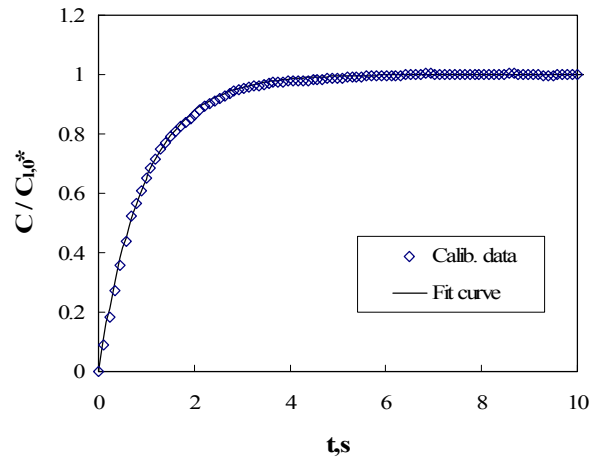


Figure 5-5. Optical oxygen probe calibration curve fitted by Equation 5-2

5.2.3. Oxygen-Enriched Air Dynamic Method

For gas-liquid mass transfer measurements in BCRs or SBCRs, the needed transport driving force is usually generated by a concentration change in the gas or liquid input (pulse or step), by pressurizing the gas phase, or by the presence of chemical reactions. Ever since it was first used in fermentation reactors (Bartholomew et al., 1950, Bandyopadhyay et al., 1967), the dynamic gas absorption or desorption method has been popularly used in BCRs due to its simplicity and reliability. The application of the method is typically based on switching the gas flow between air and nitrogen (or between air and oxygen for some rare cases). However, this creates difficulties and flow disturbance in a reactor at high operating pressure and high gas velocity. First, the nitrogen consumption rate can be inconveniently large. For instance, 500 kg/hour nitrogen is needed to operate a 0.162 m SBCR at $u_g=0.30$ m/s and $P=1.0$ MPa. Secondly, instantly stopping one flow and starting another at high gas flow rate causes significant flow fluctuation and disturbance, which disturb the hydrodynamics and mixing. In many studies (Godbole et al., 1983, Grund et al., 1992, Letzel et al., 1999, Ellenberger and Krishna, 2002, Vandu and Krishna, 2003, Bhatia et al., 2004), before switching to the air flow at the desired operating conditions, the nitrogen flow was stopped or maintained only at a minimum level. Accordingly, these studies had to

assume instantaneous build-up of steady hydrodynamics, which is probably not the case. As a solution, an oxygen-enriched-air method was implemented to overcome these difficulties, which is also called the gas-in or gas-out method. While maintaining the main air flow, a small oxygen flow can be added to achieve a switch between air and oxygen-enriched air. This modified dynamic method was first introduced in fermentation systems by Chang et al. (1989). Then Linek et al. (1991) validated its application on coalescent liquid systems such as an air-water system.

For the reasons discussed above, the dynamic method with oxygen-enriched air was implemented for the optical oxygen probe measurements. The oxygen concentration in the main gas flow was raised by a small oxygen flow, measured as 3% of the overall flow rate, started and stopped by a solenoid valve and a digital timer. The desired mass air flow rate was maintained during the whole process, which kept the hydrodynamics steady. Using a smaller oxygen concentration step (3%) instead of air-nitrogen (21%), the influence of probe noise to the final results becomes larger due to a smaller probe signal span. Such a problem with the oxygen-enriching air method was overcome by performing the same measurements multiple times. Controlled by the digital timer that was synchronized with the PC, the oxygen gas-in and gas-out process was repeated with time precision. The obtained curves can be considered as responses of identical gas dynamic changes, except with random noises. By taking average of these curves, a smoother response curve with less noise can be obtained. The oxygen absorption data (starting the small oxygen flow) was used for the dynamic method of $k_L a$ measurements. The relative oxygen saturation, $C_1'(t)$, is accordingly given by

$$C_1'(t) = \frac{C_1(t) - C_{1,0}^*}{C_{1,1}^* - C_{1,0}^*}, \quad (5-4)$$

where $C_{1,0}^*$ is the DO concentration saturated by air, and $C_{1,1}^*$ is the DO concentration saturated by oxygen-enriched air.

5.2.4. Reactor Models

In the dynamic method, the measured transient responses contain information of not only the extent of gas-liquid mass transfer but also the phase mixing. Hence, a reactor model is needed to describe the phase mixing when estimating the k_{1a} values. The continuous stirred tank reactor (CSTR) model has been used in most of the reported k_{1a} measurements, and assumes perfect mixing (complete back-mixing) for all phases and constant gas concentration in the gas phase (zero gas consumption). A few other studies (Deckwer et al., 1983; Lau et al., 2004) have used the ADM and found apparent differences in the estimated k_{1a} values from those obtained using the CSTR model. However, the CSTR remains prevalent in estimating mass transfer coefficients in BCRs with the dynamic method. Since the phase mixing in bubble columns with large L/d_c ratios could be significantly deviant from perfect mixing, the selection of reactor models and sampling locations may result in significant differences in the k_{1a} results. This work compared the CSTR, ADM, and RCFD models in the k_{1a} estimations. Based on the model comparison, a reactor model and sampling location were selected for all the experimental conditions.

a) CSTR Model

With the CSTR assumptions, only one equation for the liquid phase is needed for the absorption method with oxygen-enriched air, which is

$$\frac{dC_1(t)}{dt} = \frac{k_{1a}}{\varepsilon_1} [C_{1,1}^* - C_1(t)], \quad (5-5)$$

with the initial condition as $t = 0, C_1(t) = C_{1,0}^*$. Equation (5-5) gives a solution in the normalized (relative) form as

$$C_1'(t) = 1 - e^{-\frac{k_{1a}}{\varepsilon_1} t}. \quad (5-6)$$

The unknown term k_{1a}/ε_1 is determined by a minimum squared error fit between Equation 5-6 and the DO data. Provided ε_1 is known from the overall phase holdup measurements, the value of k_{1a} can then be obtained.

b) Axial Dispersion Model

For mass transfer measurements, the 1-D ADM is written as Equations 5-7 and 5-8 for the liquid phase and gas phase, respectively.

$$\frac{\partial C_1}{\partial t} = D_1 \frac{\partial^2 C_1}{\partial z^2} + \frac{k_1 a}{\epsilon_1} (HC_g - C_1) \quad (5-7)$$

$$\frac{\partial C_g}{\partial t} = D_g \frac{\partial^2 C_g}{\partial z^2} - u_g \frac{\partial C_g}{\partial z} - \frac{k_1 a}{\epsilon_g} (HC_g - C_1). \quad (5-8)$$

Danckwerts boundary conditions are used to guarantee mass preservation

$$z = 0, \quad \frac{\partial C_1}{\partial z} \Big|_{z=0} = 0 \quad \text{and} \quad u_g C_{g,\text{in}} = u_g C_g \Big|_{z=0} - D_g \frac{\partial C_g}{\partial z} \Big|_{z=0}$$

$$z = L, \quad \frac{\partial C_1}{\partial z} \Big|_{z=L} = 0 \quad \text{and} \quad \frac{\partial C_g}{\partial z} \Big|_{z=L} = 0,$$

where $C_{g,\text{in}} = 1$ at $t > 0$.

Initial conditions are given as $t = 0, C_1 = C_g = 0$.

The local gas holdup was assumed to be equal to the overall gas holdup, ϵ_g , which was measured by observation of the bed expansion. Although the local gas holdup may vary with the axial distance, the z-derivative term of the holdup in the fully developed region was neglected by assuming constant axial gas holdup. Such an assumption would be reasonable with small error, since the bubble column used is long (large L/d_c), and its fully developed flow region is much larger than the sparger and disengagement zones. The values of D_g were obtained experimentally at the same conditions using the gaseous tracer technique (Chapter 4). The values of D_1 at the two-phase CARPT conditions were obtained using the virtual tracer method (Chapter 4). At the three-phase CARPT conditions, only values of the solids axial dispersion coefficient, D_s , are available, which were used as the D_1 values by assuming pseudo-homogeneous slurry. Han and Al-Dahhan (2007) found in an air-water system that the final $k_1 a$ results were not sensitive to the D_1 values when varying D_1 in a $\pm 50\%$ range from the correlation predictions they used.

c) Mechanistic Model

In addition to the ADM, the mechanistic RCFD model (Figure 4-11) was also used for mass transfer measurements to evaluate the model differences. Due to the lack of gas phase parameters in the RCFD model, the RCFD model was used only for the liquid phase in the k_{ja} measurements. The gas phase has much less recirculation than the liquid, and therefore the ADM was used. Therefore, Equation 5-8 and the corresponding boundary and initial conditions were used again for gas phase in this case. The RCFD model equations for the liquid phase with mass transfer terms are expressed below, with slight differences from Gupta (2002).

1) Liquid moving upwards ($0 \sim r'$):

$$\frac{\partial C_{1,u}}{\partial t} = D_{x,u} \frac{\partial^2 C_{1,u}}{\partial z^2} - u_{1,u} \frac{\partial C_{1,u}}{\partial z} - \frac{4(D_r \varepsilon_1)_{r=r'}}{r' R \varepsilon_{1,u}} (C_{1,u} - C_{1,d}) + \frac{k_{gulu} a_{gulu}}{\varepsilon_{1,u}} (HC_g - C_{1,u}) \quad (5-9)$$

2) Liquid moving downwards ($r' \sim R$):

$$\frac{\partial C_{1,d}}{\partial t} = D_{x,d} \frac{\partial^2 C_{1,d}}{\partial z^2} + u_{1,d} \frac{\partial C_{1,d}}{\partial z} + \frac{4r'/R}{R^2 - r'^2} \cdot \frac{(D_r \varepsilon_1)_{r=r'}}{\varepsilon_{1,d}} (C_{1,u} - C_{1,d}) + \left(\frac{r'^2 - r^2}{R^2 - r'^2} \right) \frac{k_{guld} a_{guld}}{\varepsilon_{1,d}} (HC_g - C_{1,d}) + \left(\frac{R^2 - r'^2}{R^2 - r'^2} \right) \frac{k_{gdld} a_{gdld}}{\varepsilon_{1,d}} (HC_g - C_{1,d}) \quad (5-10)$$

3) Liquid in distributor zone (a):

$$\frac{dC_{1,a}}{dt} = \frac{\varepsilon_{1,d} u_{1,d}}{\varepsilon_1 \phi_a d_C} \cdot \frac{(R^2 - r'^2)}{R^2} C_{1,d} \Big|_{z=0} - \frac{\varepsilon_{1,u} u_{1,u}}{\varepsilon_1 \phi_a d_C} \cdot \frac{r'^2}{R^2} C_{1,a} + \frac{k_{CST} a_{CST}}{\varepsilon_1} (HC_g - C_{1,a}) \quad (5-11)$$

4) Liquid in disengagement zone (b):

$$\frac{dC_{1,b}}{dt} = \frac{\varepsilon_{1,u} u_{1,u}}{\varepsilon_1 \phi_b d_C} \cdot \frac{r'^2}{R^2} C_{1,u} \Big|_{z=L} - \frac{\varepsilon_{1,d} u_{1,d}}{\varepsilon_1 \phi_b d_C} \cdot \frac{(R^2 - r'^2)}{R^2} C_{1,b} + \frac{k_{CST} a_{CST}}{\varepsilon_1} (HC_g - C_{1,b}) \quad (5-12)$$

Boundary conditions:

$$z = 0, C_{1,u} \Big|_{z=0} = C_{1,a}, C_{1,d} \Big|_{z=0} = C_{1,a}; \quad z = L, C_{1,u} \Big|_{z=L} = C_{1,b}, C_{1,d} \Big|_{z=L} = C_{1,b}$$

Initial conditions:

$$t = 0, C_{1,a} = C_{1,b} = C_{1,u} = C_{1,d} = 0.$$

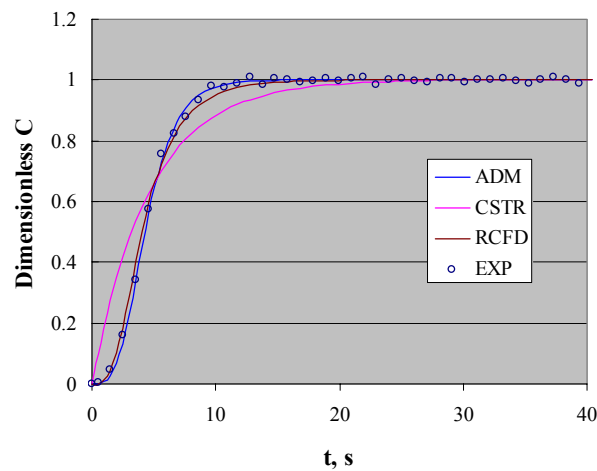
As shown in Figure 4-11, the phase holdups and liquid velocities in different compartments were obtained from the CT and CARPT data. The three dispersion parameters were estimated using the virtual tracer method and CARPT data. The DO responses measured by the optical probe in the upward-flowing zone ($r/R=0$ and various axial positions) and in the downward-flowing zone ($r/R=0.85$ and various axial positions) were fitted with $C_{1,u}(z,t)$ and $C_{1,d}(z,t)$, respectively. The k_{1a} values in four compartments were assumed to be equal, because the measurement accuracy did not support fitting different k_{1a} values for the compartments.

d) Selection of Reactor Model and Sampling Position

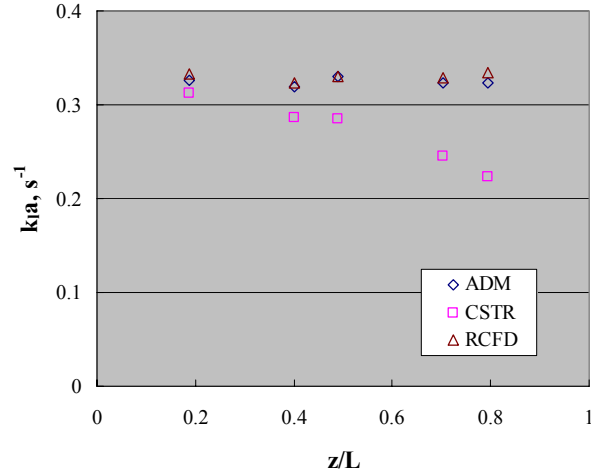
Figure 5-6(a) shows fitting of the three reactor models to the experimental data obtained at an axial position close to the reactor top ($z/L=0.8$). The ADM and RCFD model yielded similar results and have better fitting with the DO profile. The CSTR model can not account for the convection delay and shows poor fitting. The k_{1a} value obtained using the CSTR model is 28% less than that using the ADM or RCFD model at the example conditions. Such model differences are mainly attributed to the CSTR model not being able to correctly account for the convection and dispersion of phases. At the example conditions, the k_{1a} results obtained using different axial sampling positions are shown in Figure 5-6 (b). Compared to the ADM and RCFD model, results using the CSTR model are much more dependent on the axial sampling locations. Since k_{1a} represents the overall mass transfer coefficient in the reactor models, it was expected that same k_{1a} values would be obtained regardless of where the sampling position is. However the CSTR does not count for the convection effect and obtains different k_{1a} values with axial variance. It was noticed that the sampling locations were generally not reported in the literature mass transfer studies that used the CSTR model. In this study, the k_{1a} values at different axial sampling positions vary up to 30% using the CSTR model, while using the ADM or RCFD model yielded less than 5%

differences. The findings in the model comparison are due to the high length-to-diameter ratio ($L/d_c=11.2$) of the reactor used in this study.

Unfortunately, in this study, the radioactive particle tracking data from which needed dispersion parameters were estimated were available for only a limited number of conditions. From the results shown above, the model differences are small ($\sim 5\%$) when measurements are made close to the inlet. However, the sampling position should not be too close to the inlet (into the sparger zone) where the gas holdup may be significantly different than the overall gas holdup (Han and Al-Dahhan, 2007). Based on the model comparisons, it was found that at $z/d_c=2.0$ the three reactor models yielded the smallest differences in the results ($\sim 5\%$), i.e. this position for the tested reactor results in the smallest model dependence. To make measurements at much more conditions than the CARPT conditions (where dispersion parameters were estimated), the CSTR model was used for the oxygen k_a measurements, and the axial sampling position was selected at $z/d_c=2.0$.



a) DO response fitted by three reactor models at $z/L=0.8$



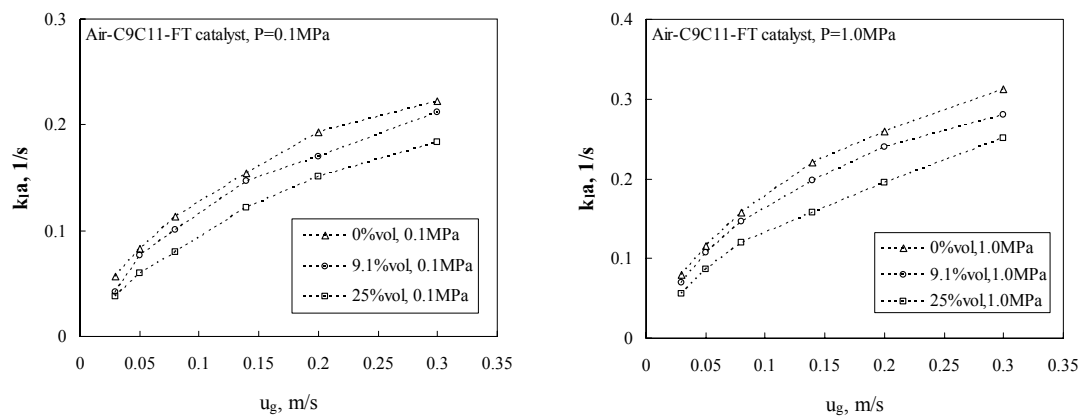
b) Fitted k_{1a} using the three reactor models at different axial positions

Figure 5-6. Comparisons of the CSTR model, ADM, RCFD model in k_{1a} measurements

5.2.5. Results and Analysis

The k_{1a} values of oxygen in the mimicked FT system were obtained using the discussed optical oxygen probe technique, the oxygen-enriched air method, the CSTR model, and local measurements made at $z/d_c=2.0$. The k_{1a} results at different superficial gas velocities and solids loadings are shown in Figures 5-7 (a) and (b). The volumetric mass transfer increased with the superficial gas velocity, but the increasing trend was reduced at high gas velocities. Adding solids significantly decreased the mass transfer coefficient at both low pressure (0.1 MPa) and high pressure (1.0 MPa) in most of the u_g range. Such solids effect on the k_{1a} values was not clear at low gas velocities ($u_g=0.03$ m/s and 0.05 m/s) between 9.1% vol. and 25% vol. at 0.1 MPa and between 0% vol. and 9.1% vol. at 1.0 MPa. This may be due to the measurement errors. Figures 5-8 (a~c) show that the operating pressure increases the k_{1a} values significantly. These observed effects of solids loading and operating pressure are qualitatively similar to those observed in previous reports (Letzel et al., 1999; Jordan et al., 2002; Vandu et al., 2003; Lemoine et al., 2004; etc).

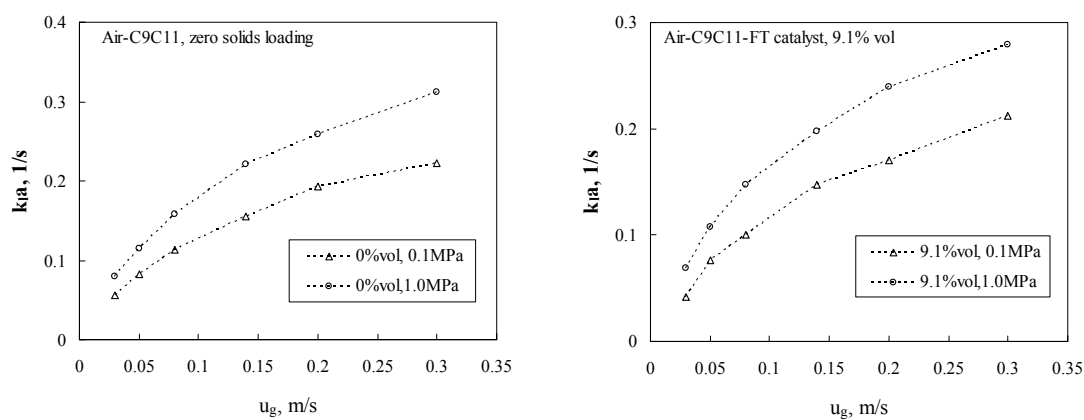
More importantly, these oxygen k_{1a} data cover various operating conditions in the mimicked FT SBCR. Such data are used in the development of a relation or correlation for k_{1a} predictions of various gas species at conditions of FT interest.



a) $P=0.1$ MPa, AARDs between 0% vol. and 25% vol. are in the range of 19% ~ 41%

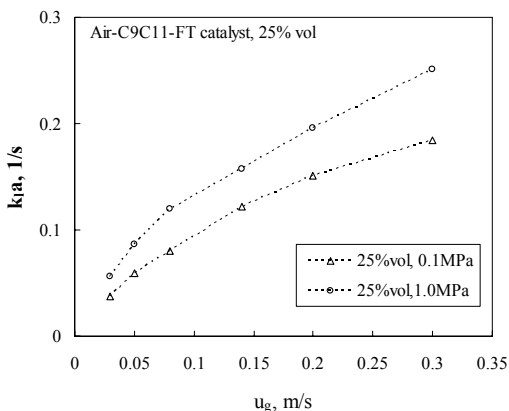
b) $P=1.0$ MPa, AARDs between 0% vol. and 25% vol. are in the range of 22% ~ 34%

Figure 5-7. Effects of the superficial gas velocity and solids loading on oxygen k_{1a}



a) zero solids loading
AARDs between 0.1 MPa and 1.0 MPa
are in the range of 29% ~ 38%

b) 9.1% vol. solids loading
AARDs between 0.1 MPa and 1.0 MPa
are in the range of 27% ~ 49%



c) 25% vol. solids loading
AARDs between 0.1 MPa and 1.0 MPa are in the range of 26% ~ 41%

Figure 5-8. Effects of the operating pressure on oxygen k_{1a}

5.3. Gas-Liquid Mass Transfer of Various Species

The k_{1a} values of three selected gases (CH_4 , CO_2 and Ar) were measured in the same mimicked FT SBCR, using the gaseous tracer technique discussed in Chapter 4. Experimental details and the obtained results are shown in the following sections.

5.3.1. Gaseous Tracer Technique for Mass Transfer Measurements

The gaseous tracer technique used for the mass transfer study is basically the same as used in the gas back-mixing study (Chapter 4). The difference here is using moderately soluble gases instead of the practically insoluble helium. In this case, the response curves have delayed tails as a result of mass transfer between gas and liquid phases. A similar method has been used by Breman et al. (1996) for mass transfer measurements in multiphase reactors. Using a reactor model and dispersion parameters measured at the same conditions, the k_{1a} of the soluble tracer gas can be estimated. The selection of tracer gases for the k_{1a} measurements was based on two requirements of this method: 1) they should have moderate solubility to obtain a proper extent of response delay due to the gas-liquid exchange; 2) they should have enough differences in thermal

conductivity from the mass gas flow (air) to be detected by the TCD. Table 5-2 lists all the involved gases and their solubility and thermal conductivity data. As shown by these numbers, the solubility of hydrogen is too low for measuring its mass transfer rate. The thermal conductivity of carbon monoxide is very close to that of the air, which makes it difficult to detect the concentration using the TCD. According to these standards, CH₄, CO₂, and Ar were selected for the k_{1a} measurements using the gaseous tracer technique. Although the k_{1a} values of H₂ and CO (the main components of syngas) are of FT interest, they could not be measured using the techniques available in this work. The k_{1a} values of H₂ and CO at the same conditions are predicted using the k_{1a} data of other species and the developed relation/correlation.

Table 5-2. Properties of various tracer gases (P=101.325 kPa, T=298.2 K)

Gas	Solubility $X_2, \cdot 10^4$	Diffusivity, $\cdot 10^9 \text{ m}^2/\text{s}$	Thermal conductivity, W/m·K
He	2.4 ^[1]		156.0 ^[3]
H ₂	6.7 ^[2]	7.49 ^[4]	185.8 ^[3]
CO	16.6 ^[1]	4.59 ^[4]	25.0 ^[3]
Ar	24.4 ^[1]	4.74 ^[4]	17.8 ^[3]
CH ₄	52.6 ^[1]	4.03 ^[4]	33.9 ^[3]
CO ₂	125.8 ^[1]	4.05 ^[4]	16.7 ^[3]
O ₂		5.16 ^[4]	
Air	-		26.0 ^[3]

[1] – Wilcock et al., 1978.

[2] – Brunner 1985.

[3] – CRC Handbook of chemistry and physics, Edition 82.

[4] – Diaz et al., 1987.

5.3.2. Experimental Conditions

Due to the limited availability of dispersion parameters estimated by the virtual tracer response method, the experimental conditions were selected at the CARPT conditions (Table 5-3). These experimental conditions cover different superficial gas velocities, solids loadings, and pressures.

Table 5-3. Experimental conditions of mass transfer measurements (gas tracer)

System	u_g , m/s	Pressure, MPa	Solids loading
Air-C ₉ C ₁₁	0.30	1.0	0
	0.30	0.1	0
	0.20	1.0	0
Air-C ₉ C ₁₁ -FT Catalyst	0.30	1.0	25% vol.
	0.30	0.1	25% vol.
	0.30	1.0	9.1% vol.
	0.20	1.0	25% vol.

5.3.3. The Reactor Scale Model and k_{1a} Fitting

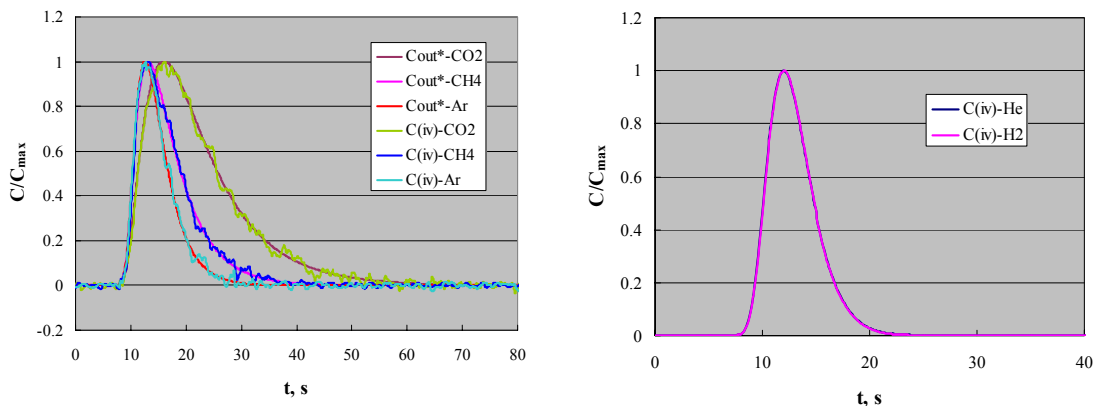
In this work, the ADM was found to fit the gas response curves well, and the axial dispersion coefficients were measured already. Therefore, the ADM was selected for the k_{1a} measurements using the gaseous tracer technique. The ADM equations used here are the same as given in Equations 5-7 and 5-8 for the optical oxygen probe measurements. The boundary and initial conditions are also the same except that the inlet concentration of the tracer gas is given by

$$C_{g,in} = C_{in} \text{ at } t = 0^+,$$

where C_{in} is calculated according to Equation 4-3 as discussed in the gaseous tracer technique in Chapter 4. At the selected operating conditions, the phase holdups and axial dispersion coefficients are known, as listed in Table 5-4 along with the results below. Therefore, k_{1a} is the only unknown parameter left, and was fitted using the minimum squared error method. The response curves of CH₄, CO₂, and Ar with ADM fitting are shown in Figure 5-9 (a). Due to their different magnitudes of solubility, these gases have various extents of delay in their response curves. As listed in Table 5-2, the solubility of hydrogen is of the same order of magnitude as helium. Figure 5-9 (b) shows that the response curves of using helium and hydrogen are almost identical, both giving only the residence time distribution due to the phase mixing.

Compared to the background gas (air), CH₄, CO₂, and Ar have relatively smaller thermal conductivity differences than He and H₂ do. Hence, the noise in the response

curves coming from the flow fluctuation in the sampling is more apparent for CH₄, CO₂, and Ar. In order to reduce the random fluctuations in the signal, multiple (10~20) runs were conducted using the digital timers, and the means of the k_{1a} numbers are shown. The standard deviations in the results were calculated to be less than 10%.



a). Response curves of CH₄, CO₂, and Ar with ADM fits

b). Response curves of helium vs. hydrogen.

Figure 5-9. Response curves of various tracer gases

5.3.4. Results and Analysis

Mass transfer coefficients of CH₄, CO₂, and Ar were measured using the gaseous tracer technique introduced earlier (Table 5-4). At the selected conditions, it can be seen that the mass transfer coefficients of different gases have the same trend under the effects of superficial gas velocity, operating pressure, and solids loading as those observed for the oxygen (section 5.2.5). At each condition, the bubble dynamics (including the specific interfacial area) are the same when small amounts of different tracer gases are used, and the only factor that causes different mass transfer rates is the different diffusivities of the tracer gases. Hence, a power relation of k_{1a}/D_{AB}^n for different tracer gases was evaluated with the data obtained in the mimicked FT SBCR. By optimum fits, the value of n was found to be 0.7 (AARE=7%). However, it was also noticed that when n is equal to 0.6 or 0.5, the fitting errors (AARE<8%) are only slightly larger

than $n=0.7$. This n value range (0.5~0.7) indicates that Higbie's penetration theory can describe the effect of diffusivity on the obtained k_{1a} data with a relation of

$$k_1 \propto \sqrt{D_{AB}}. \quad (5-13)$$

Using k_{1a} data obtained for one species (such as O_2), the relation above can then be used to predict k_{1a} values of different other species, such as H_2 and CO at the same conditions (same a), using the expression

$$k_{1a} = k_{1a}^0 \left(\frac{D_{AB}}{D_{AB}^0} \right)^{1/2}. \quad (5-14)$$

As a further validation of this relation, the k_{1a} values of CH_4 , CO_2 , and Ar were estimated using Equation 5-14 and the oxygen data at the same conditions. Such estimated k_{1a} values of the three gases and those measured in this section were compared and are shown in Figure 5-10. The average absolute relative error between predictions and measurements is less than 10%. With this validation, the mass transfer coefficients of H_2 and CO , which could not be measured in this work, can be predicted at the tested conditions using the obtained oxygen k_{1a} data, diffusivity numbers (Table 5-2), and Equation 5-14. Except the different magnitudes (proportional to the square root of D_{AB}), the predicted k_{1a} values of H_2 and CO have similar curves to those shown in Figures 5-7 and 5-8, and hence are omitted here.

Table 5-4. Measured k_{1a} values of CH_4 , CO_2 , and Ar with used model parameters

Condition	$D_g, \text{cm}^2/\text{s}$	$D_l, \text{cm}^2/\text{s}$	ε_g	$k_{1a}, \text{s}^{-1} \text{CH}_4$	$k_{1a}, \text{s}^{-1} \text{CO}_2$	$k_{1a}, \text{s}^{-1} \text{Ar}$
u30, P1.0	764	1350	0.523	0.273	0.258	0.299
u20, P1.0	482	1160	0.494	0.230	0.221	0.238
u30, P0.1	475	2270	0.353	0.157	0.194	0.200
u30, P1.0, 25%vol	868	2020	0.359	0.183	0.197	0.224
u20, P1.0, 25%vol	578	1900	0.317	0.131	0.180	0.198
u30, P0.1, 25%vol	526	3270	0.265	0.159	0.153	0.157
u30, P1.0, 9.1%vol	797	1730	0.469	0.247	0.243	0.236

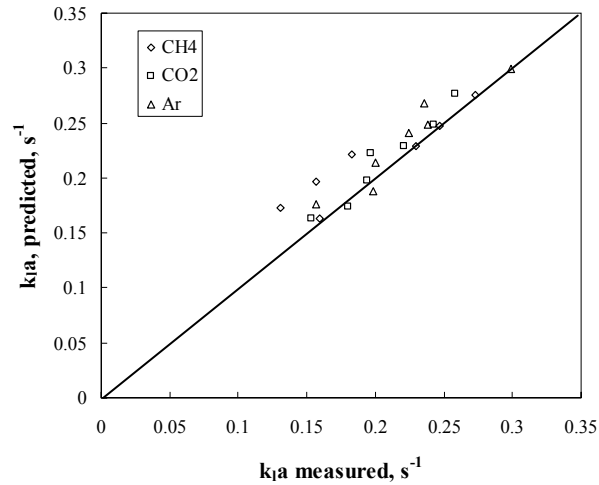


Figure 5-10. Plots of the k_{1a} values estimated using Equation 5-14 vs. k_{1a} data

The evaluated $k_{1a} \sim D_{AB}$ relation is for k_{1a} predictions of different species at the same conditions, with known k_{1a} data of at least one species. A further effort was made in developing a k_{1a} correlation using Higbie's penetration theory, as discussed in the next section.

5.4. A k_{1a} Correlation using the Higbie Penetration Theory

As reviewed in Chapter 2 (Table 2-7), a number of k_{1a} correlations for BCRs or SBCRs have been presented on an empirical basis. It was found that these correlations do not give close predictions to the k_{1a} data in the mimicked FT SBCR. As shown in Appendix D, two new empirical k_{1a} correlations were developed by the author of this work, using the literature data in BCRs and SBCRs collected from 43 studies, published during 1965 ~ 2004. Both an artificial neural network method and a power law method were used, each yielding a different k_{1a} correlation. Both of the two developed correlations gave good fits to the used data. However, their predictions have apparent deviations with the data at the mimicked FT conditions, which are out of the condition ranges of the collected database.

The square root $k_{lA} \sim D_{AB}$ relation found in last section indicates that Higbie's penetration theory may be used to develop a k_{lA} correlation for the mimicked FT conditions. As introduced in Chapter 2, the liquid side mass transfer coefficient k_l is estimated by Higbie as

$$k_l = 2 \sqrt{\frac{D_{AB}}{\pi \cdot t_e}} \quad (5-15)$$

In Higbie's penetration theory, the exposure time of the fresh liquid film is crucial in predicting the gas liquid mass transfer. In a BCR or SBCR, the exposure time can be estimated by the averaged diameter and rise velocity of bubbles according to

$$t_e \propto \frac{d_{bm}}{u_{bt}}, \quad (5-16)$$

where d_{bm} is the geometric mean bubble diameter, and u_{bt} is the terminal bubble rise velocity (assuming all bubbles moving upward). Due to the lack of bubble dynamics measurements in the mimicked FT SBCR, the mean bubble size and terminal bubble rise velocity need to be estimated in the exposure time calculation.

Mendelson (1967) presented a correlation to predict terminal (stable) bubble rise velocities using wave theory, expressed as

$$u_{bt} = \sqrt{\frac{2 \cdot \sigma}{\rho_l d_b} + \frac{g \cdot d_b}{2}} \quad (5-17)$$

The Mendelson (1967) correlation has been widely used in various systems with modifications by Lehrer (1976), Clift et al. (1978), Jamialahmadi et al. (1994), and Luo et al. (1997 and 1999). Luo et al. (1997 and 1999) proposed Equation 5-18 for liquid-solids suspensions at high pressure which was selected to be used here.

$$u_{bt} = \sqrt{\frac{2.8 \cdot \sigma}{\rho_{sl} d_{bm}} + \frac{g \cdot d_{bm}}{2} \frac{\rho_{sl} - \rho_g}{\rho_{sl}}} \quad (5-18)$$

The specific interfacial area was calculated as below, using the geometric mean as the Sauter mean diameter, d_{bs} .

$$a = 6\varepsilon_g / d_{bs} \quad (5-19)$$

As shown above, the mean bubble size is the key parameter needed for calculating the exposure time (Equation 5-16), terminal bubble rise velocity (Equation 5-18), and specific interfacial area (Equation 5-19). The mean bubble size has not been measured in the mimicked FT SBCR, and its values were predicted using a correlation. In order to select a suitable correlation, the bubble dynamics data in an air-water system in the same high pressure column (Xue, 2004) were used as an evaluation standard. The predictions of various correlations were compared with the bubble sizes measured by Xue (2004) at 0.30 m/s and 1.0 MPa. It was found that the bubble size correlation of Akita et al. (1974) (Equation 5-20) yields a better match to the data.

$$\frac{d_{bm}}{d_c} \approx \frac{d_{bs}}{d_c} = 26 \cdot \left(\frac{g \cdot d_c^2 \rho_l}{\sigma} \right)^{-0.50} \cdot \left(\frac{g \cdot d_c^3 \rho_l^2}{\mu_l^2} \right)^{-0.12} \cdot \left(\frac{u_g}{\sqrt{g \cdot d_c}} \right)^{-0.12} \quad (5-20)$$

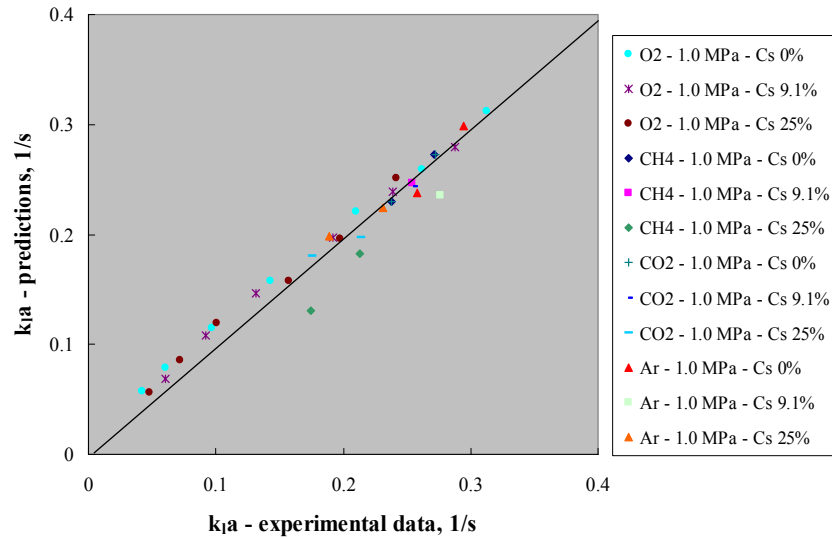
Therefore, at this stage, this correlation was used to calculate d_{bm} at the mimicked FT conditions, assuming the geometric mean is approximately same as the Sauter mean. Once d_{bm} and the exposure time are estimated, the liquid side mass transfer coefficient, k_l , can be calculated using the diffusivity, D_{AB} , by Equation 5-15. Then, the volumetric mass transfer coefficient, $k_{l,a}$, is obtained by multiplying the k_l and (a) numbers.

Some further tuning was made to mechanistically determine the ratio constant in Equation 5-16, because the exposure time may not be exactly equal the ratio of d_{bm} and u_{st} , but proportional to it with a ratio α . Therefore one can write

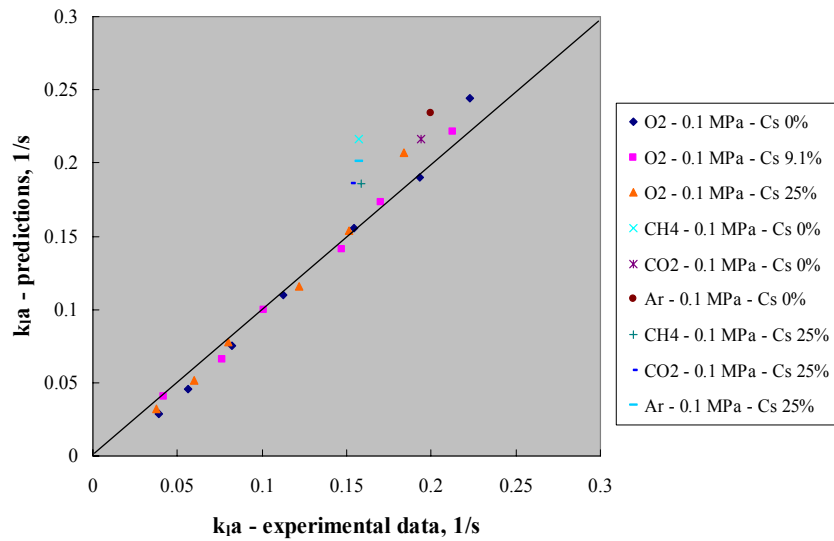
$$t_e = \alpha \frac{d_{bm}}{u_{bt}} \quad (5-21)$$

With the obtained $k_{l,a}$ data of four species, it was found that $\alpha=5.0$ for high pressure (1.0 MPa), while $\alpha=3.6$ for low pressure (0.1 MPa). The different α values at high and low pressures may result from the different surface refresh pattern at different pressures, and they may also come from errors in the correlations for d_{bm} and u_{bt} at the two pressures. Also, the optimized α values may be a combined result of the two factors. With arbitrary corrections to the correlation through α , good data fits were obtained for

the four species at the studied conditions. Comparisons of the predictions vs. data are shown in Figures 5-11 (a) and (b) for high pressure and low pressure, respectively.



a) At High pressure, 1.0 MPa, $\alpha=5.0$



b) At low pressure, 0.1 MPa, $\alpha=3.6$

Figure 5-11. Predicted k_{La} values using the correlation vs. experimental data

The average absolute relative error (AARE) defined as Equation 5-21 was calculated for the data in each figure.

$$\text{AARE} = \frac{1}{n_{\text{data}}} \sum_{i=1}^{n_{\text{data}}} \frac{|k_{1a}^{\text{pre}} - k_{1a}^{\text{data}}|}{k_{1a}^{\text{data}}} \quad (n_{\text{data}} \text{ is the data points number}). \quad (5-21)$$

The AAREs at high and low pressures are 9% and 12%, respectively. In a selected high u_g range ($u_g > 0.14$ m/s), the AARD for high and low pressures are even slightly lower, 6% and 11%, respectively. This correlation is based on the penetration theory, and tuned using the k_{1a} data obtained in the mimicked FT SBCR. Although the k_{1a} numbers in a real FT SBCR would be apparently higher than those in the mimicked FT SBCR, the difference is mainly due to the higher diffusivities at higher temperature. This correlation may work relatively better than others in a FT SBCR whose physical properties were mimicked by the SBCR in this work.

Using the correlation developed above, the k_{1a} values of H_2 and CO in the mimicked FT SBCR were predicted at various conditions (Figures 5-12 and 5-13). The effects of superficial gas velocities, operating pressures, and solids loadings were found to be in line with those observed and discussed in the oxygen k_{1a} measurements section.

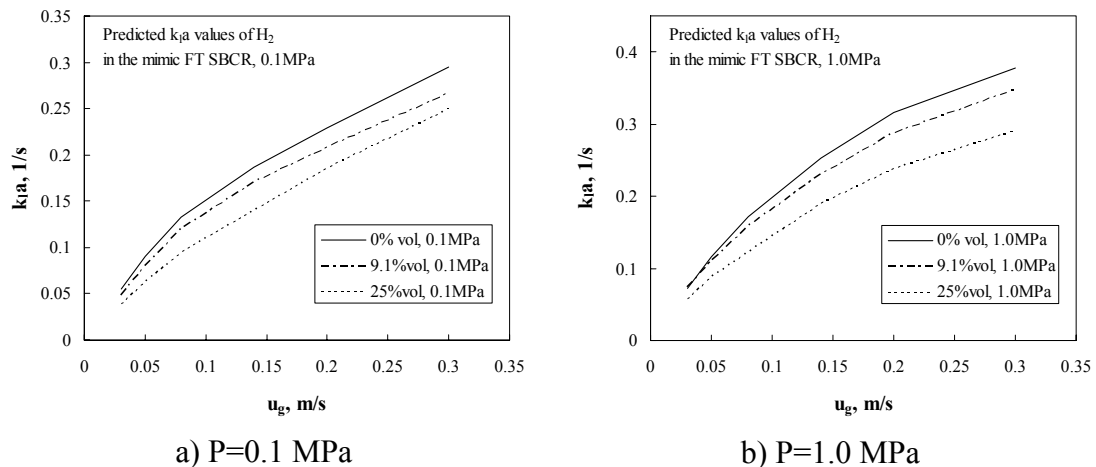


Figure 5-12. Predictions of H_2 k_{1a} in the mimicked FT SBCR using the correlation developed based on the Higbie penetration theory

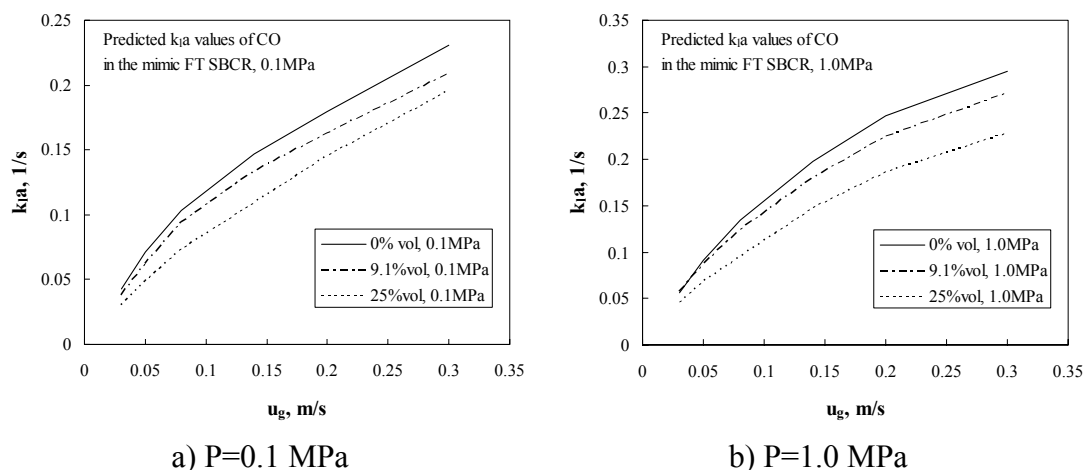


Figure 5-13. Predictions of CO k_{La} in the mimicked FT SBCR using the correlation developed based on the Higbie penetration theory

5.5. Summary

This study investigated the mass transfer in the mimicked FT SBCR. The k_{La} values of CH_4 , CO_2 , and Ar in the mimicked FT SBCR were obtained at limited conditions using the gaseous tracer technique, while the k_{La} values of O_2 were measured at more conditions using the optical oxygen probe technique. Although some of the measured components (O_2 and Ar) are not of interest in FT processes, these data were used to validate the square root relation between k_{La} and D_{AB} , with which the obtained O_2 k_{La} data at more conditions can be used for k_{La} predictions of different species at those mimicked FT conditions. Furthermore, the obtained k_{La} data were used in developing and validating a k_{La} correlation based on the Higbie penetration theory. With tuned constant values, this correlation agrees well with the k_{La} values of various species measured in the mimicked FT SBCR. With this developed correlation, the k_{La} values of H_2 and CO in the mimicked FT SBCR were predicted at various conditions.

Chapter 6

Conclusions and Recommendations

6.1. Summary of Conclusions

This work investigated the hydrodynamics, phase back-mixing, and gas-liquid mass transfer in an SBCR using three-phase systems that mimic the physical properties in real FT SBCRs. The proposed research objectives were accomplished by performing experimental investigations using various developed techniques/methods and selected reactor scale models. The accomplishments and conclusions are briefly summarized in the following sections.

6.1.1. Investigation of the Hydrodynamics in the Mimicked FT SBCR

An air-C₉C₁₁-FT catalyst system (at selected operating conditions) and an air-Therminol-FT catalyst system (at fewer conditions) were used to mimic the phase physical properties in a typical FT SBCR. The hydrodynamics in this mimicked FT SBCR were investigated in terms of phase holdup distribution, liquid/solids velocity field, and turbulence parameters using CT and CARPT techniques. Technical

difficulties were overcome to irradiate and handle 90 μm tracer particles, which made it possible to track the small FT catalyst. A CT/CARPT occurrence reconstruction method for CT images was presented and tested, which independently estimates holdup distributions of the three phases in a SBCR, avoiding the two assumptions made in the CT/overall gas holdup method (Rados, 2003). With close physical properties, the tested two liquids, C_9C_{11} and Therminol, exhibit similar profiles of the measured hydrodynamic parameters. In comparison with the 150 μm glass beads, the FT catalyst was found to cause significant differences at high solids loading in profiles of gas holdup, solids velocity, and turbulence parameters. The effects of the solids types may result from different particle sizes, different apparent densities, or the porous surface of FT catalyst. Further study is needed in order to separately investigate these factors.

Profiles of hydrodynamic parameters measured in a mimicked FT SBCR using real FT catalyst are not available in the literature. This work provides benchmark data which can be used for tuning and evaluation of closures in future CFD simulations.

6.1.2. Investigation of the Phase Back-Mixing in the Mimicked FT SBCR

The gas phase back-mixing was investigated using a gaseous tracer technique and an axial dispersion model. The effects of FT catalyst and high pressure on the gas phase back-mixing were investigated, providing dispersion coefficient values as input for the mass transfer measurements at the same conditions.

For the liquid/solids back-mixing study, a virtual tracer response method was developed to generate response curves from single particle Lagrangian trajectories obtained by CARPT. The virtual tracer response curves can be considered as the results of a batch tracer injection. Various reactor models were used to characterize the back-mixing of liquid and solids phases, respectively. Values of the dispersion parameters in the reactor models were estimated by fitting the model to the response curves. Among the tested reactor models, the mechanistic RCFD model developed at the CREL has three dispersion parameters, which were for the first time estimated. This part of the

study also provides dispersion parameter values for the following mass transfer measurements.

6.1.3. Investigation of the Mass Transfer in the Mimicked FT SBCR

The volumetric gas-liquid mass transfer coefficient, k_{1a} , of various species (O_2 , CH_4 , CO_2 , Ar) in the mimicked FT SBCR were evaluated using the developed optical oxygen probe technique and gaseous tracer technique. The effects of operating parameters on the mass transfer in the mimicked FT SBCR were quantified. A square root $k_{1a}-D_{AB}$ relation was substantiated at the tested conditions, which can be used to estimate k_{1a} values of other species at the same conditions, with known k_{1a} data of one species. The obtained k_{1a} data at the mimicked FT conditions were also used to develop a k_{1a} correlation based on Higbie's penetration theory, using estimated bubble dynamic parameters. With the tuned constant ratios, the correlation predictions agree well with the data of different species. The main advantage of this k_{1a} correlation compared with others is its theoretical basis and the fact that it was tuned using the data in the mimicked FT SBCR. The k_{1a} values of H_2 and CO were predicted at the mimicked FT conditions using the developed correlation.

6.2. Overall Presentation of the Effects of Different Variables

This work investigated the effects of superficial gas velocity, operating pressure, solids loading, and solids type on the hydrodynamic parameters, dispersion parameters, and mass transfer coefficient. The effects observed in the mimicked FT SBCR are summarized in the overall presentation below (Table 6-1).

Table 6-1. Overall presentation of the effects of various variables

Varying parameter	Resulting effects	Supporting data
$u_g \uparrow$	$\varepsilon_g \uparrow$	Figures A-1 ~ A-9
	$n \downarrow$	Table 3-6
	$u_l(0)$ or $u_s(0) \uparrow$	Figures A-19, A-20
	TKE \uparrow	Figures A-19, A-20
	$D_{zz} \uparrow$	Tables 4-3, 4-5
	$D_g \uparrow$	Figure 4-7
	$Pe_g \rightarrow$ at high u_g	Figure 4-7
	D_1 or D_s (ADM, SDM) \uparrow	Table 4-3, 4-5
	$D_{x,u}, D_{x,d}$ (RCFD) \uparrow	Table 4-4
	$k_{ja} \uparrow$	Figure 5-7, Table 5-4
$P \uparrow$	$\varepsilon_g \uparrow$	Figures A-10 ~ A-18
	$n \uparrow$	Table 3-6
	$u_l(0)$ or $u_s(0) \uparrow$	Figures A-21, A-22
	TKE of solids (25%vol.) \rightarrow	Figure A-21
	TKE of liquid \downarrow	Figure A-22
	$D_{zz} \downarrow$	Tables 4-3, 4-5
	$D_g \downarrow$	Figure 4-8
	$Pe_g \rightarrow$	Figure 4-8
	D_1 or D_s (ADM, SDM) \uparrow	Tables 4-3, 4-5
	$D_{x,u}, D_{x,d} \downarrow$	Table 4-4
$k_{ja} \uparrow$	Figure 5-8, Table 5-4	
$C_s \uparrow$	$\varepsilon_g \downarrow$	Figures 3-26 ~ 3-30
	$n \downarrow$	Table 3-6
	$u_s(0) \downarrow$	Table 4-5
	$D_{zz} \uparrow$	Table 4-5
	$D_g \uparrow$	Figure 4-7
	$Pe_g \rightarrow$	Figure 4-7
	D_s (SDM) \uparrow	Table 4-5
	$k_{ja} \downarrow$	Figure 5-7, Table 5-4
Glass beads \rightarrow FT catalyst	$\varepsilon_g \uparrow$	Figure 3-21
	$n \uparrow$	Figure 3-21
	$u_s(0) \downarrow$	Figure 3-22 (a)
	TKE of solids \uparrow	Figure 3-22 (b)

6.3. Recommendations for Future Work

Among the various but related topics studied in this work, the following recommendations for future work are made.

6.3.1. Effects of Different Solids

The differences in the hydrodynamic parameters between FT catalyst and glass beads come from a combination of several factors, including the particle sizes, apparent density, and the FT catalyst's porous surface. While the glass beads have been widely used in SBCR research to replace the catalyst particles, it is of importance to perform further tests to separately investigate the effects of these difference factors. For instance, glass beads with the same size of the FT catalyst may be used to evaluate the effect of the porous surface, which may cause different liquid-solids drag and therefore different solids/liquid dynamics.

6.3.2. Validation of the CT/CARPT Occurrence Reconstruction Method

Both the CT/overall gas holdup method developed by Rados (2003) and the CT/CARPT occurrence method presented by this work were used for the three phase holdup reconstruction. Significant differences were observed in the results of these two CT reconstruction methods, especially in solids holdup profiles. The CT/CARPT occurrence method is based on the assumed proportionality between the occurrences of the tracer particle and the local solids holdup. An evaluation can be performed using the dual-source CT being developed in the CREL to simultaneously measure the holdup distributions of all three phases in the mimicked FT SBCR.

6.3.3. Validation of the Bubble Dynamic Parameters Estimations

Although the $k_{\text{L}a}$ correlation developed in this work is based on Higbie's penetration theory, empirical information is still used, particularly in the bubble dynamic parameters' estimations. Due to the lack of bubble dynamics measurements, the stable bubble size and rise velocity in the $k_{\text{L}a}$ correlation were estimated using literature correlations. The exposure time calculation was corrected by arbitrarily adjusting the $d_{\text{bm}}/u_{\text{bt}}$ ratio α , which lumps the errors from both the empirical bubble dynamic parameters estimation and the approximate exposure time estimation. With the 4-point

probe technique developed at the CREL, bubble dynamics in the mimicked FT SBCR can be investigated, which will greatly help to improve the $k_L a$ correlations and to better understand the hydrodynamics and phase mixing as well.

Appendix A

Additional CT/CARPT Data in the Mimicked FT SBCR

This appendix provides additional CT/CARPT data obtained in the mimicked FT SBCR, which are not shown in the main chapters. As mentioned in Chapter 3, effects of the superficial gas velocity and operating pressure on the hydrodynamic parameters were investigated and found to be qualitatively similar to those in the air-water-glass beads system and air-Therminol-glass beads system. The sections below show such effects in parts of CT and CARPT, with brief discussion. The solids effects on the hydrodynamic parameters have been reported in Chapter 3 with figures, hence are not included here.

A.1. Profiles of Phase Holdup by CT

A.1.1. Effects of the Superficial Gas Velocity on the Phase Holdup Profiles

The superficial gas velocity u_g is a crucial operating variable in BCR or SBCR, which greatly affects the hydrodynamics and flow regimes. The u_g effects on the gas holdup and its radial profile in SBCRs has been reported in previous studies (e.g., Jackson et al., 1996; George et al., 2001; Rados, 2003; and Shaikh, 2007). This work quantified

the u_g effects on the gas holdup profiles in the mimicked FT SBCR (Figures A-1 ~ A-9). It can be seen that both the magnitude and steepness of the gas holdup increased with u_g , and the liquid (and solids) holdup had the opposite trend. The findings are in line with previous studies in other SBCRs.

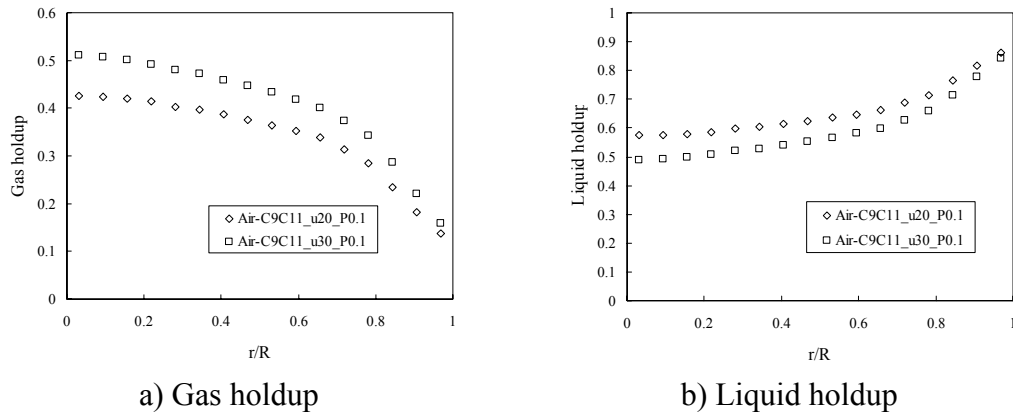


Figure A-1. u_g effects on the phase holdups, air-C₉C₁₁, 0.1 MPa, 0.20 m/s vs. 0.30 m/s, method (I)

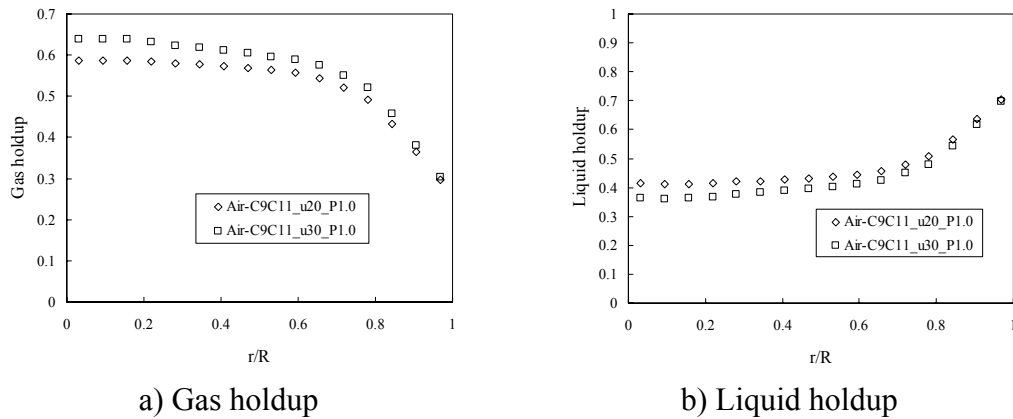
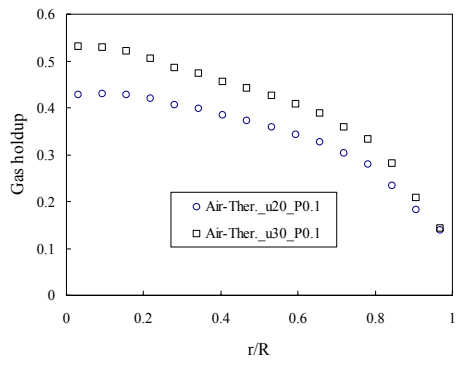
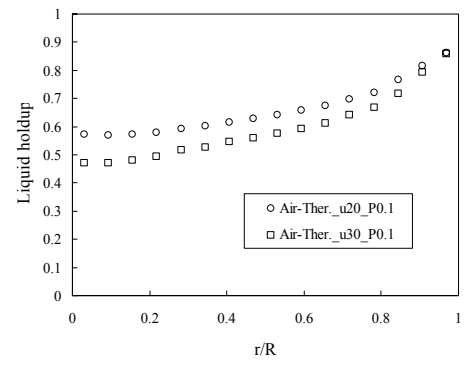


Figure A-2. u_g effects on the phase holdups, air-C₉C₁₁, 1.0 MPa, 0.20 m/s vs. 0.30 m/s, method (I)

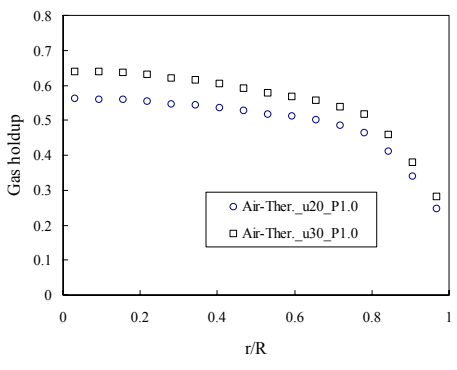


a) Gas holdup

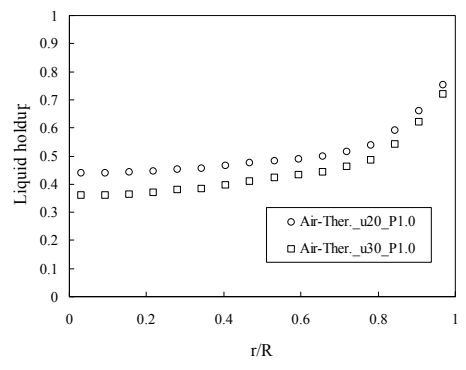


b) Liquid holdup

Figure A-3. u_g effects on the phase holdups, air-Therminol, 0.1 MPa, 0.20 m/s vs. 0.30 m/s, method (I)

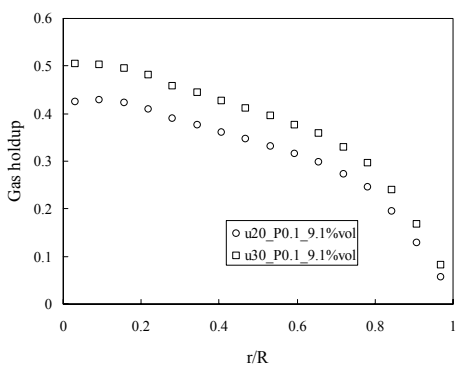


a) Gas holdup

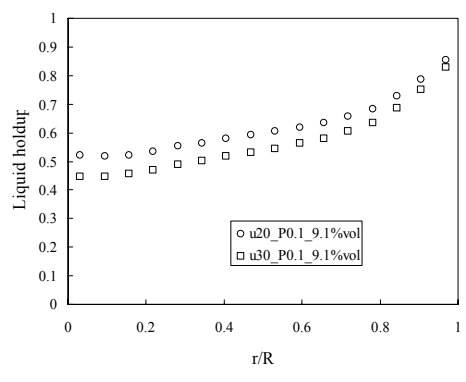


b) Liquid holdup

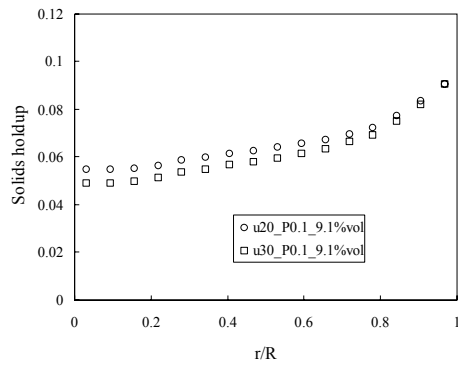
Figure A-4. u_g effects on the phase holdups, air-Therminol, 1.0 MPa, 0.20 m/s vs. 0.30 m/s, method (I)



a) Gas holdup

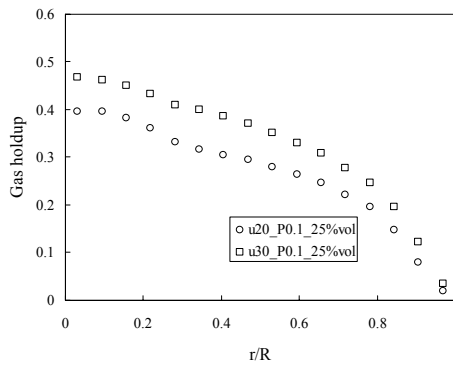


b) Liquid holdup

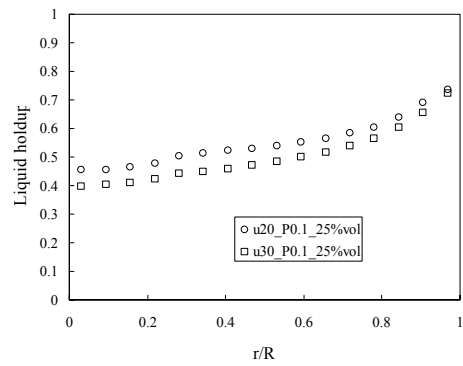


c) Solids holdup

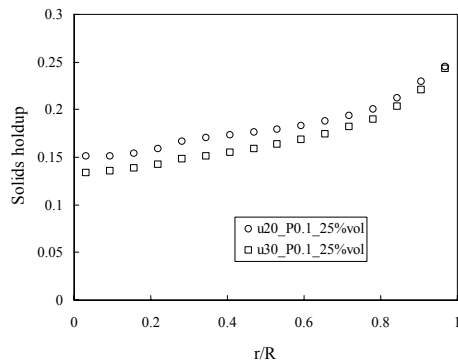
Figure A-5. u_g effects on the phase holdups, air- C_9C_{11} -FT catalyst, 9.1% vol., 0.1 MPa, 0.20 m/s vs. 0.30 m/s, method (I)



a) Gas holdup



b) Liquid holdup



c) Solids holdup

Figure A-6. u_g effects on the phase holdups, air- C_9C_{11} -FT catalyst, 25% vol., 0.1 MPa, 0.20 m/s vs. 0.30 m/s, method (I)

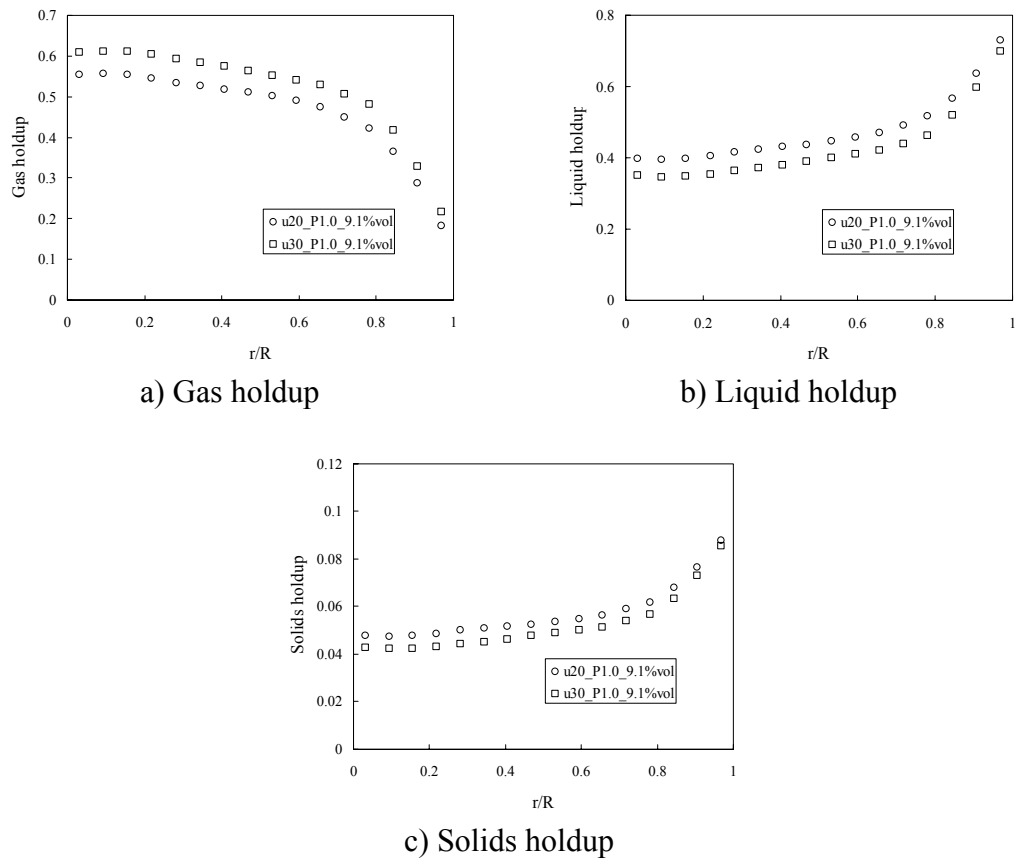
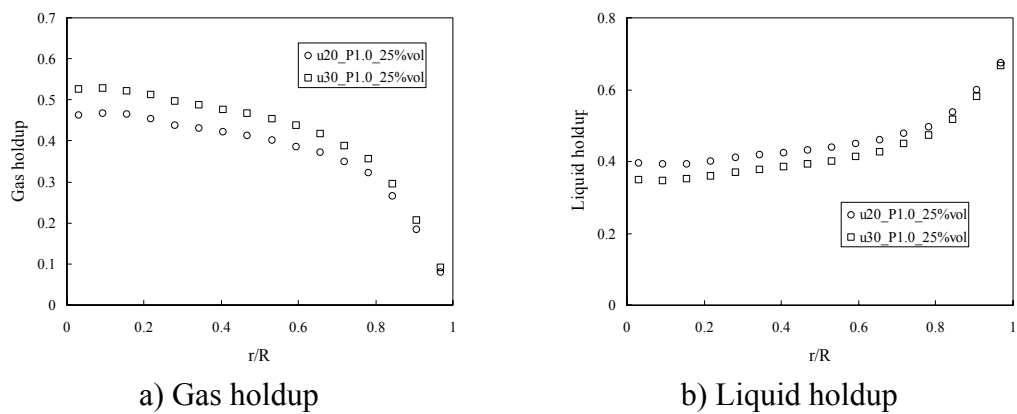
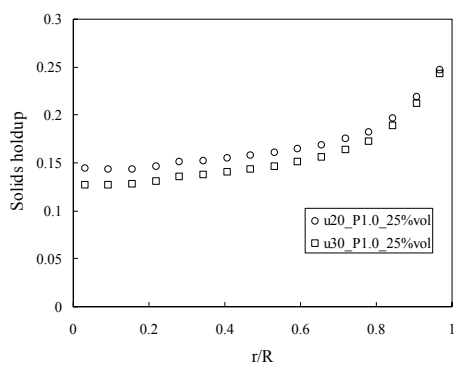


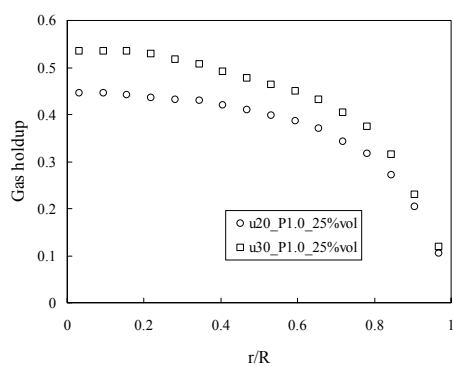
Figure A-7. u_g effects on the phase holdups, air- C_9C_{11} -FT catalyst, 9.1% vol., 1.0 MPa, 0.20 m/s vs. 0.30 m/s, method (I)



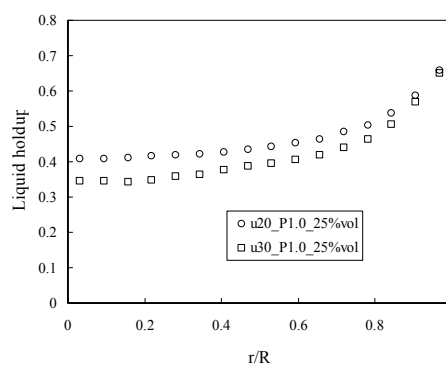


c) Solids holdup

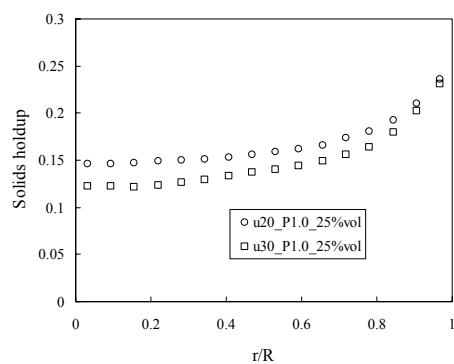
Figure A-8. u_g effects on the phase holdups,
air-C₉C₁₁-FT catalyst, 25% vol., 1.0 MPa, 0.20 m/s vs. 0.30 m/s, method (I)



a) Gas holdup



b) Liquid holdup



c) Solids holdup

Figure A-9. u_g effects on the phase holdups,
air-Therminol-FT catalyst, 25% vol., 1.0 MPa, 0.20 m/s vs. 0.30 m/s, method (I)

A.1.2. Effects of the Operating Pressure on the Phase Holdup Profiles

Operating pressure is one of the key factors affecting the hydrodynamics in SBCRs. An increase in the pressure results in smaller bubbles. As a result, the gas holdup increases because of the longer residence of the smaller bubbles in the reactor (Reid et al., 1987; Lin et al., 1998; Luo et al., 1999; Xue 2004). The pressure effects on the phase holdup profiles have been studied in an air-water BCR (Ong, 2003), an air-water-glass beads SBCR (Rados, 2003), and an air-Therminol-glass beads SBCR (Shaikh, 2007). This work quantified the pressure effects on the phase holdup profiles in the mimicked FT SBCR (Figures A-10 ~ A-18). The increase of pressure from 0.1 MPa to 1.0 MPa caused higher gas holdup and lower liquid (and solids) holdup. The steepness of the gas holdup radial profiles reduced significantly with the pressure, due to the pressure effects on the bubble dynamics as discussed above.

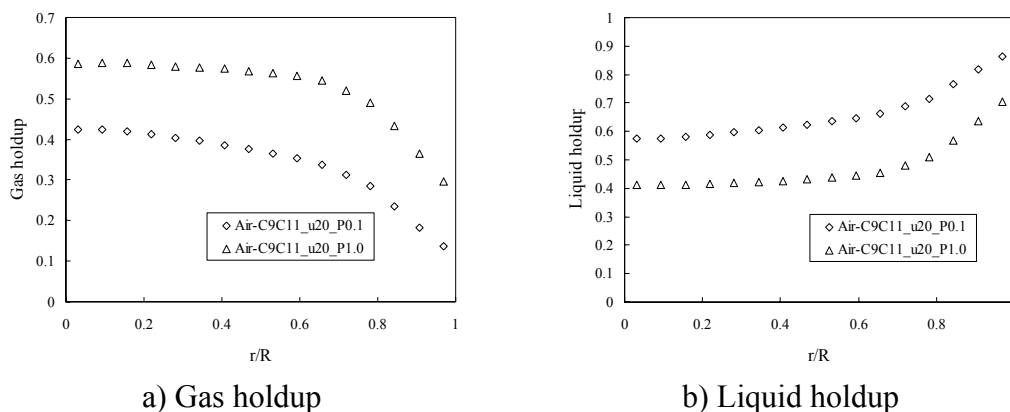
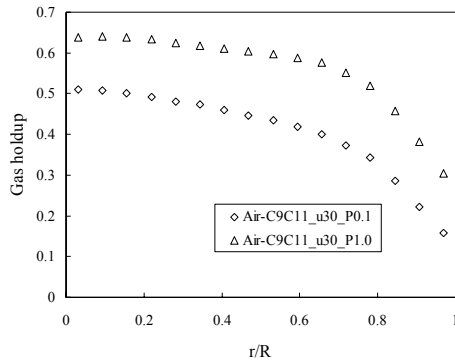
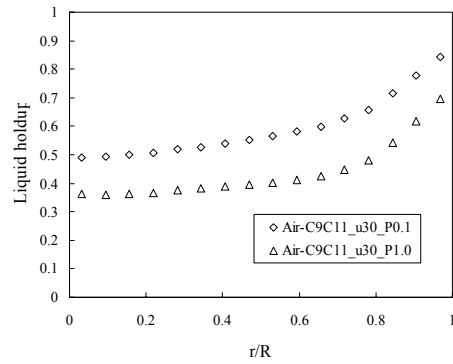


Figure A-10. Pressure effects on the phase holdups, air-C₉C₁₁, 0.20 m/s, 0.1 MPa vs. 1.0 MPa, method (I)

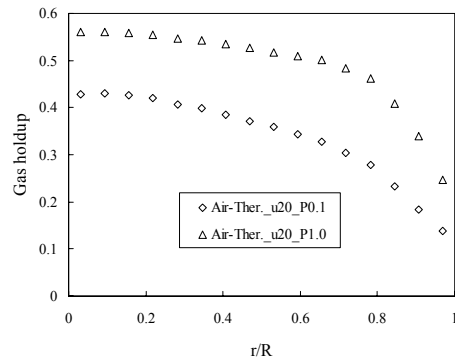


a) Gas holdup

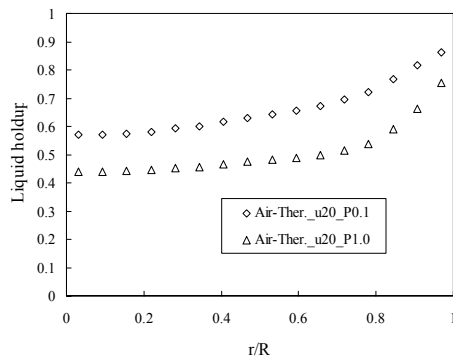


b) Liquid holdup

Figure A-11. Pressure effects on the phase holdups, air-C₉C₁₁, 0.30 m/s, 0.1 MPa vs. 1.0 MPa, method (I)

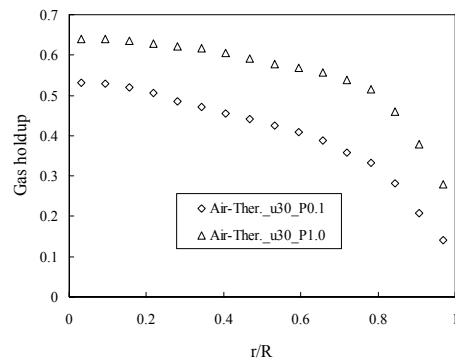


a) Gas holdup

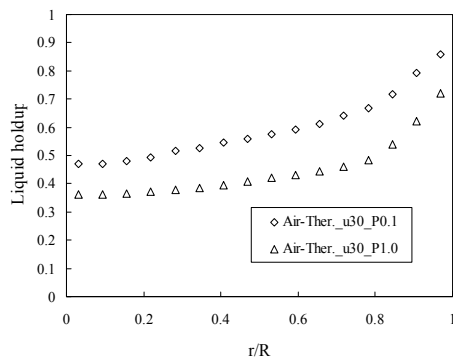


b) Liquid holdup

Figure A-12. Pressure effects on the phase holdups, air-Therminol, 0.20 m/s, 0.1 MPa vs. 1.0 MPa, method (I)



a) Gas holdup



b) Liquid holdup

Figure A-13. Pressure effects on the phase holdups, air-Therminol, 0.30 m/s, 0.1 MPa vs. 1.0 MPa, method (I)

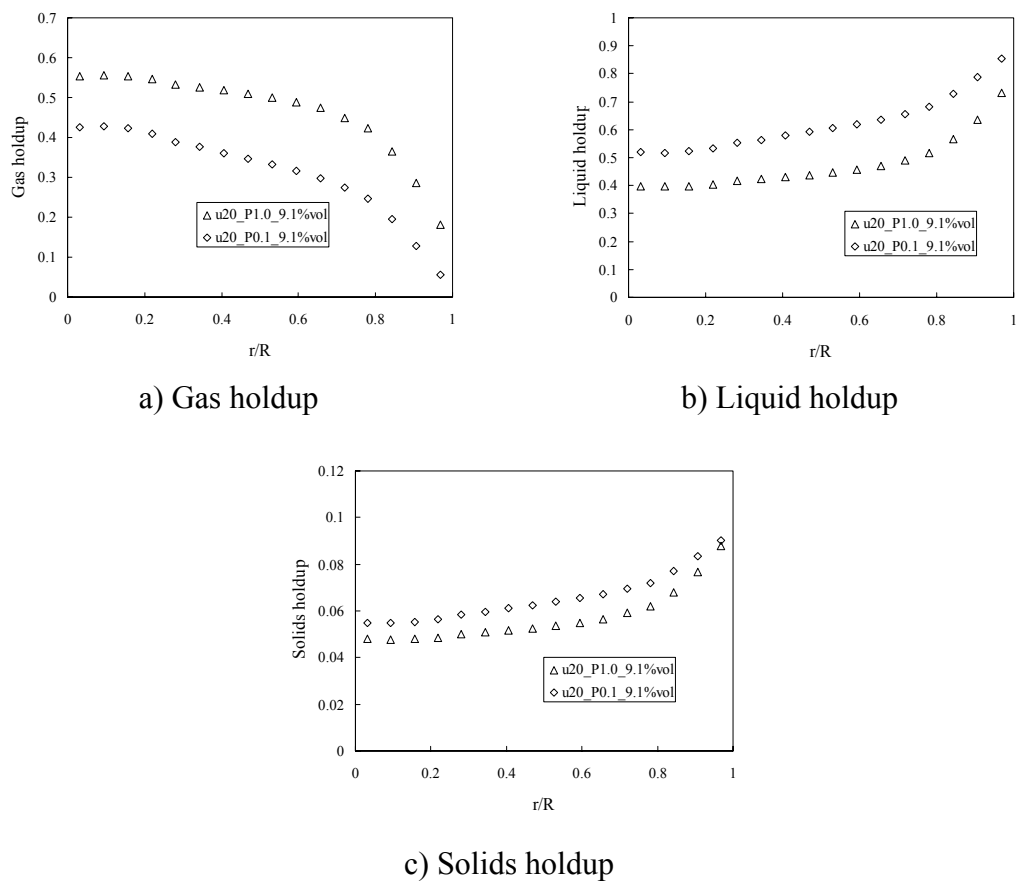
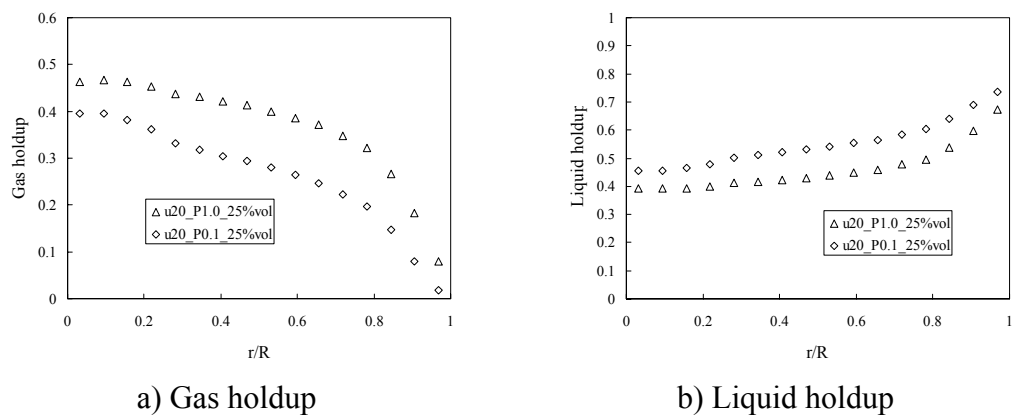
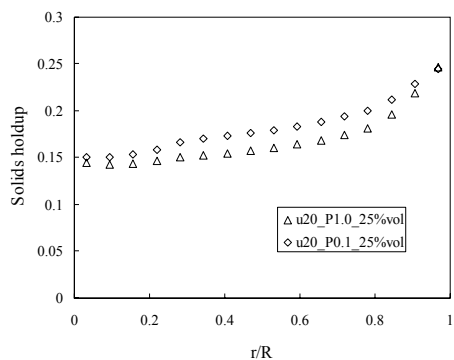


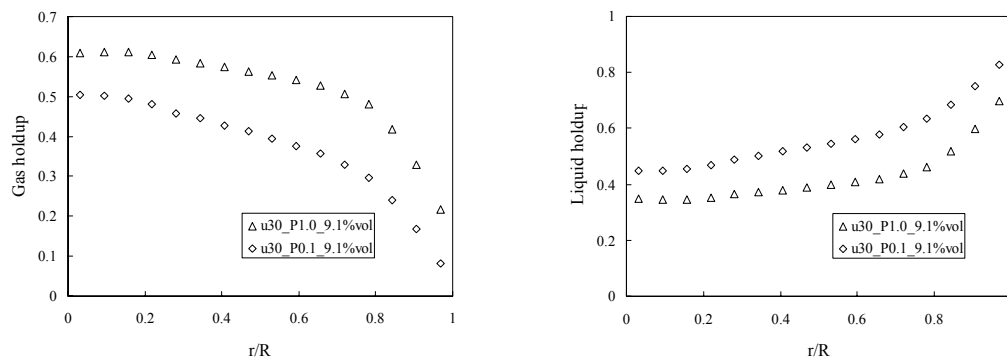
Figure A-14. Pressure effects on the phase holdups, air-C₉C₁₁-FT catalyst, 9.1% vol., 0.20 m/s, 0.1 MPa vs. 1.0 MPa, method (I)





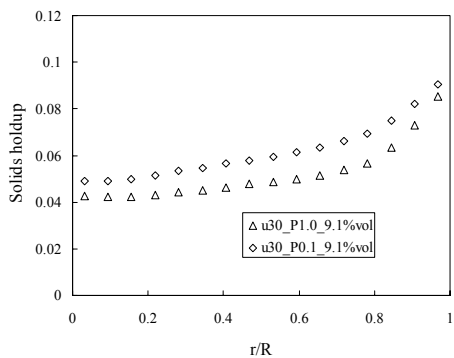
c) Solids holdup

Figure A-15. Pressure effects on the phase holdups, air-C₉C₁₁-FT catalyst, 25% vol., 0.20 m/s, 0.1 MPa vs. 1.0 MPa, method (I)



a) Gas holdup

b) Liquid holdup



c) Solids holdup

Figure A-16. Pressure effects on the phase holdups, air-C₉C₁₁-FT catalyst, 9.1% vol., 0.30 m/s, 0.1 MPa vs. 1.0 MPa, method (I)

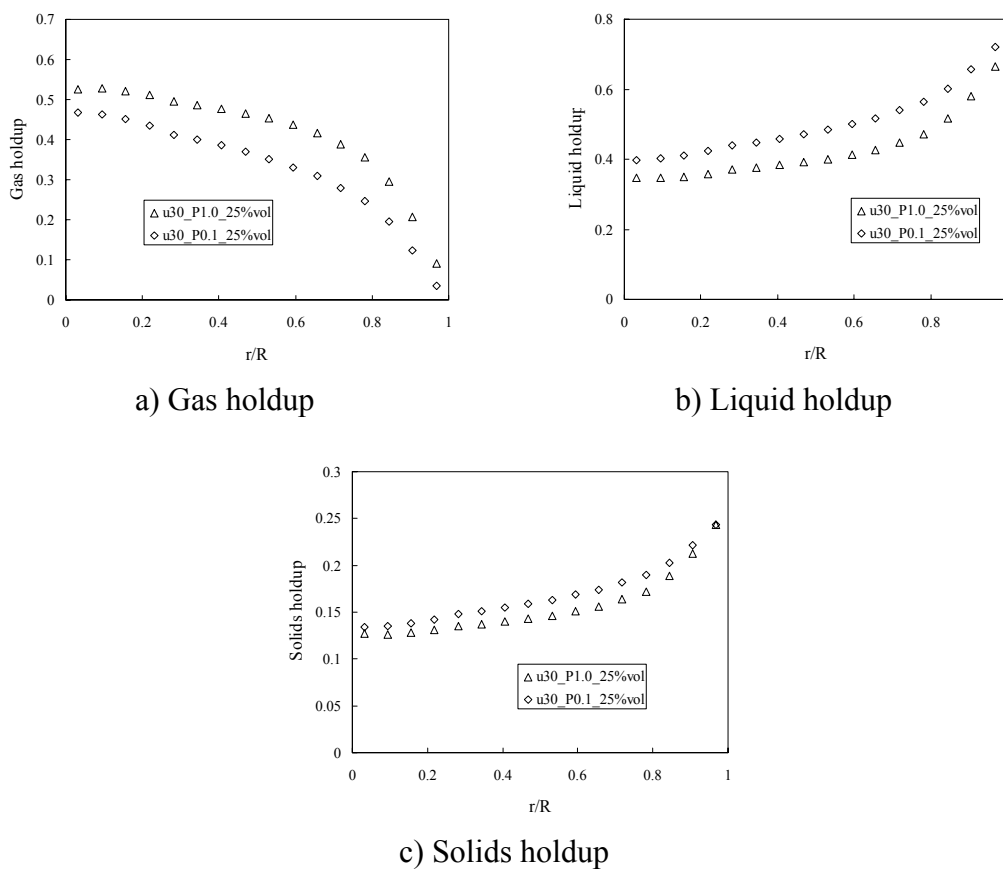
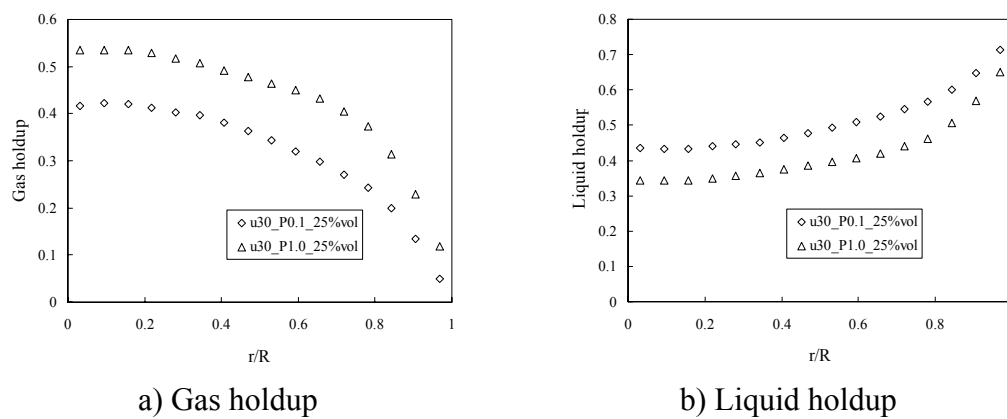
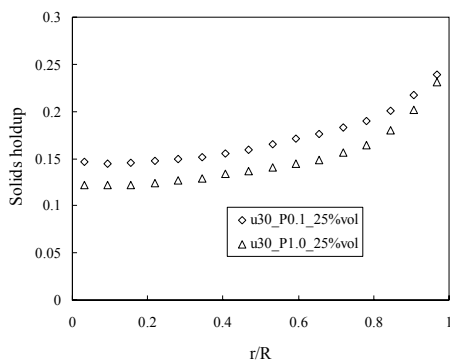


Figure A-17. Pressure effects on the phase holdups, air-C₉C₁₁-FT catalyst, 25% vol., 0.30 m/s, 0.1 MPa vs. 1.0 MPa, method (I)





c) Solids holdup

Figure A-18. Pressure effects on the phase holdups, air-Therminol-FT catalyst, 25% vol., 0.30 m/s, 0.1 MPa vs. 1.0 MPa, method (I)

A.2. Profiles of Velocity and Turbulence parameters by CARPT

A.2.1. Effects of the Superficial Gas Velocity on the Velocity and Turbulence parameter Profiles

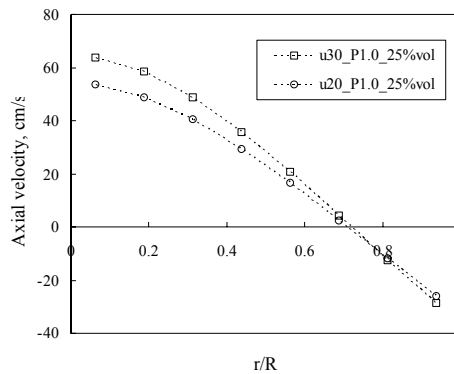
Based on the measurements in the mimicked FT SBCR, two sets of comparisons (Figures A-19 and A-20) show the u_g effects on the velocity and turbulence parameters at three-phase and two-phase conditions, respectively. The following u_g effects were found:

Time-averaged axial velocities increased with u_g , including both the positive velocity in the center region and the negative velocity in the wall region. This observation is in line with previous studies of Ong (2003), Rados (2003), and Shaikh (2007) in other systems. At the tested SBCR and BCR conditions, from 0.20 m/s to 0.30 m/s, the axial velocity magnitude increased approximately by 10~20% in average.

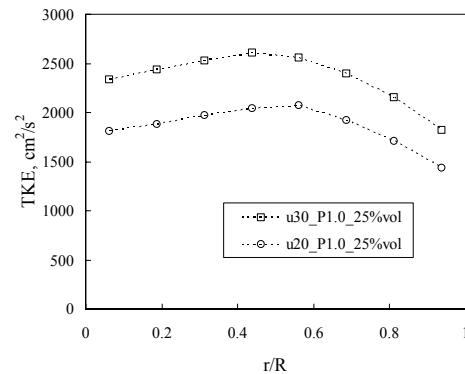
The TKEs were significantly increased by the superficial gas velocity. For the increase of u_g from 0.20 m/s to 0.30 m/s, the cross-sectional average TKE of the liquid flow in the BCR became 35% higher, while the TKE of the solids flow in the SBCR was 27%

higher. This is due to the more bubbles and energy introduced into the reactor at higher superficial gas velocity, which result in more bubble interactions (Xue, 2004) and higher turbulence (CARPT data).

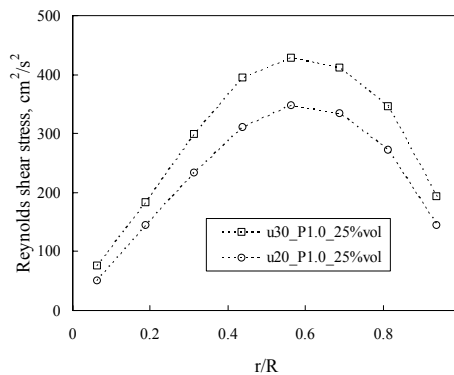
The other turbulence parameters also significantly increased with the superficial gas velocity. From 0.20 m/s to 0.30 m/s, the axial, radial, and azimuthal normal stresses of the liquid in the BCR were increased by 31%, 12%, and 16%, respectively. For the same u_g increase, the axial, radial, and azimuthal normal stresses of the solids in the SBCR were increased by 34%, 20%, and 14%, respectively. The increases of the three normal stresses directly contribute to higher TKEs. The increase of the Reynolds shear stress is in correspondence of the increase of axial velocity gradient at the high superficial gas velocity.



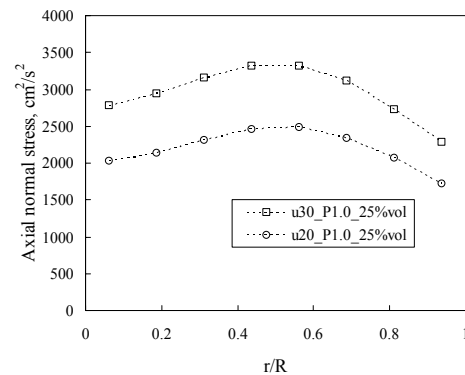
a) Solids axial velocity



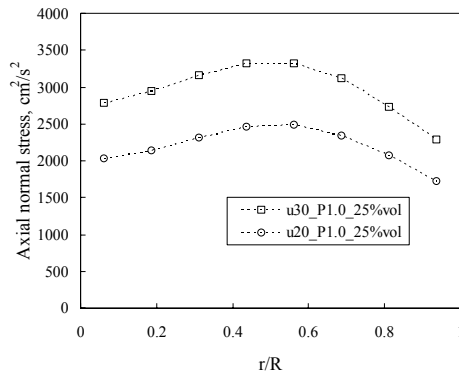
b) Solids TKE



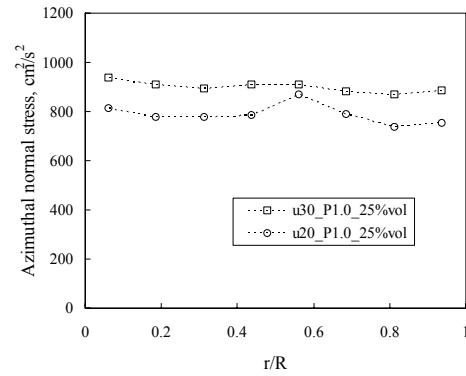
c) Solids shear stress



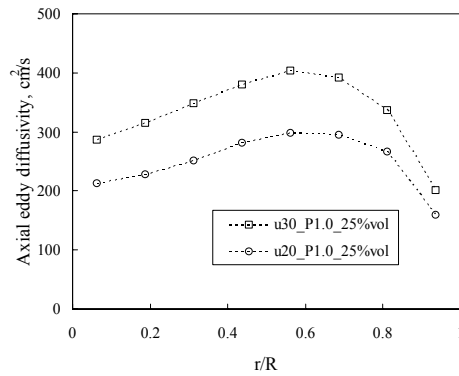
d) Solids axial normal stress



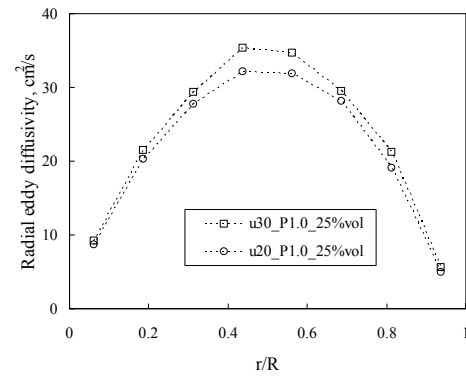
e) Solids radial normal stress



f) Solids azimuthal normal stress

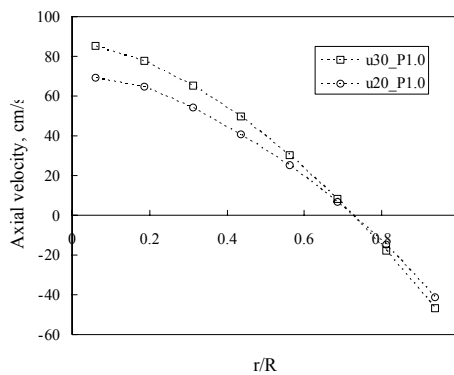


g) Solids axial eddy diffusivity

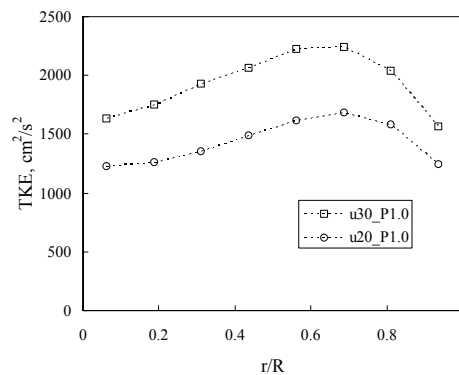


h) Solids radial eddy diffusivity

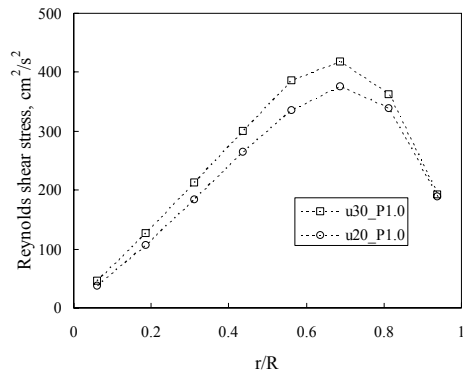
Figure A-19. u_g effects on the solids velocity and turbulence parameters, air-C₉C₁₁-FT Catalyst, 25% vol., 1.0 MPa, 0.20 m/s vs. 0.30 m/s



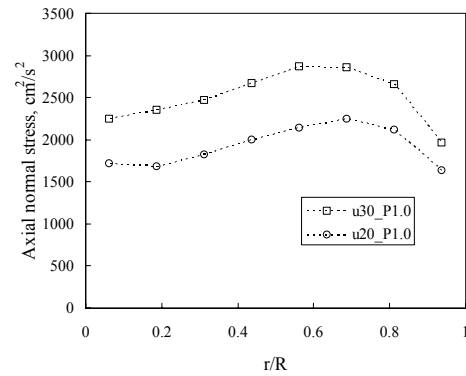
a) Liquid axial velocity



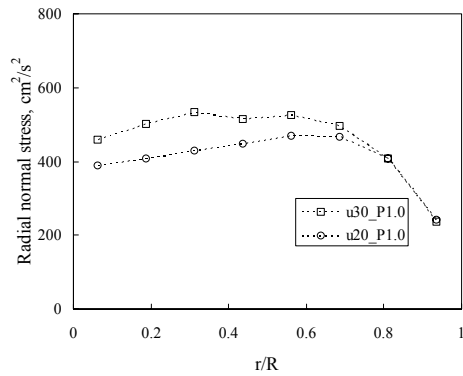
b) Liquid TKE



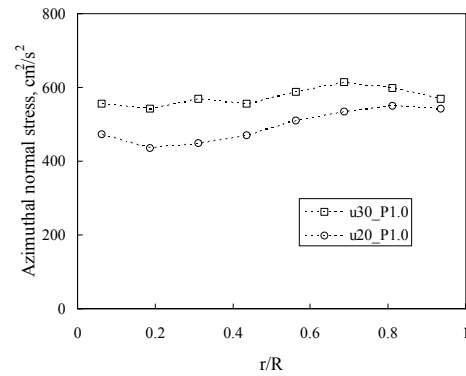
c) Liquid shear stress



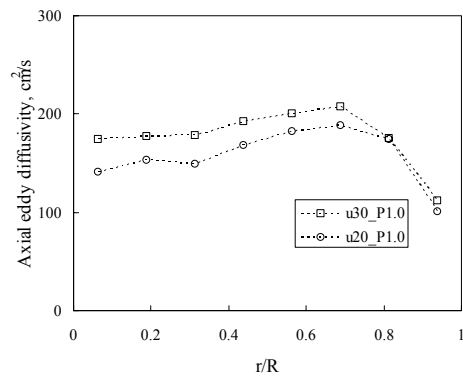
d) Liquid axial normal stress



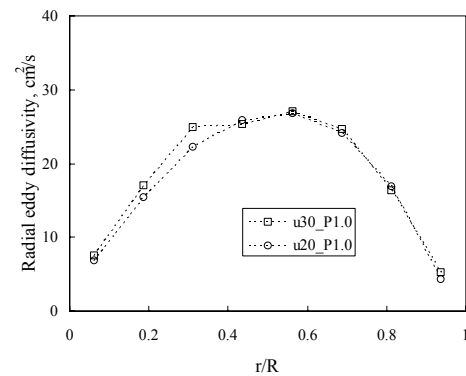
e) Liquid radial normal stress



f) Liquid azimuthal normal stress



g) Liquid axial eddy diffusivity



h) Liquid radial eddy diffusivity

Figure A-20. u_g effects on the liquid velocity and turbulence parameters, air-C₉C₁₁, 1.0 MP, 0.20 m/s vs. 0.30 m/s

A.2.2. Effects of the Operating Pressure on the Velocity and Turbulence parameter Profiles

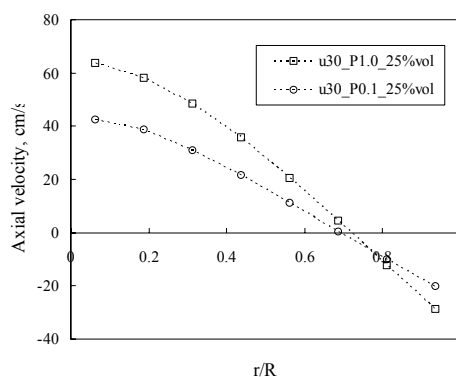
Effects of the operating pressure on the velocity and turbulence parameters were investigated at both SBCR and BCR conditions (Figures A-21 and A-22). The following summarizes the findings.

With the pressure escalated from 0.1 MPa to 1.0 MPa, the solids axial velocity in the SBCR increased by 60% (Figure A-21a), and the liquid axial velocity in the BCR increased by 50% (Figure A-22a). This pressure effect is similar to findings in the air-water system (Ong, 2003), the air-water-150 μ m glass beads system (Rados, 2003), and the air-Therminol-150 μ m glass beads system (Shaikh, 2007). The pressure effects on the solids and liquid axial velocities are due to the increased gas holdup and smaller bubbles generated, which are more efficient in dragging the solids or liquid. The pressure effect on the axial velocity can also be explained by the resulting larger radial density difference, proved by the holdup profiles from CT at the same conditions. When pressure increased, besides the faster recirculation, the inversion points of both the liquid in the BCR and the solids in the SBCR shifted slightly towards the wall. This is a reasonable change considering that the gas holdup became higher and its radial profiles became flatter in the center upward-flow region (CT data). Since the mass balance has to be kept, the cylindrical boundary of the time-averaged up-flowing and down-flowing zones moved slightly outwards.

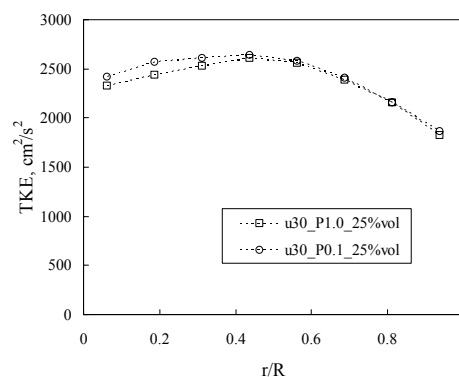
At the high pressure, the liquid TKE in the air-C₉C₁₁ system decreased significantly at the center, while remained about the same near the wall. This is also explained by the smaller bubbles generated by the high pressure (Reid et al., 1987, Lin et al., 1998; Luo et al., 1999; Xue, 2004). Since the large bubbles rise mostly in the center region, the pressure effect is more obvious in this region especially close to the centerline. This finding agrees with those in the air-water system (Ong, 2003), the air-water-glass beads system at 9.1% vol. solids loading (Rados, 2003), and the air-Therminol-glass beads system at 9.1% vol. solids loading (Shaikh, 2007). However, the pressure effects on the

TKE at high solids loading (25% vol.) are relatively small in the air-C₉C₁₁-FT catalyst system. As shown in Figure A-21 (b), only a slight increase in the TKE was observed at high pressure. This indicates that, even when the pressure was increased, the bubble interactions were dominated by the opposite effect of the high solids loading, which encourages large bubbles.

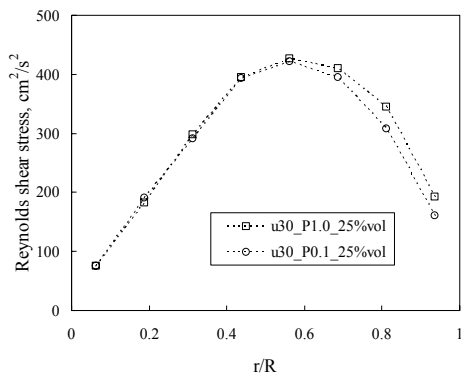
The peaks of the liquid or solids shear stress profiles moved towards the wall at high pressure, due to the similar shift of the axial velocity profiles and the inversion points. The Reynolds stress of the liquid flow decreased in the reactor center at high pressure. This indicates that the gradient of the axial velocity was smaller in the center region, as a result of the change in the bubble dynamics as discussed earlier. However, at the high solids loading, differences in the solids shear stress profiles between high and low pressures were small, indicating similar axial velocity gradients at high pressure. At two-phase conditions, the axial, radial, and azimuthal normal stresses decreased significantly with the pressure, in the similar trend to the liquid TKE.



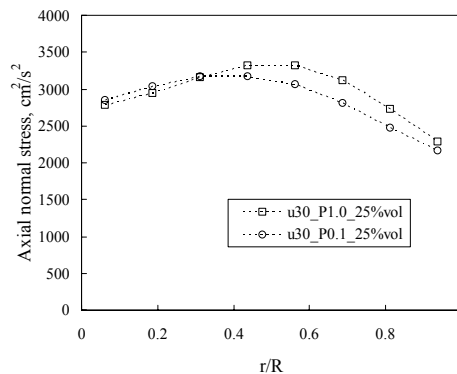
a) Solids axial velocity



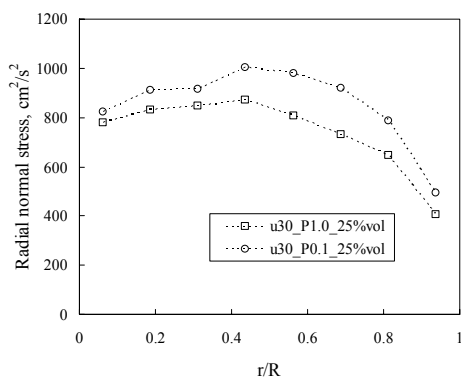
b) Solids TKE



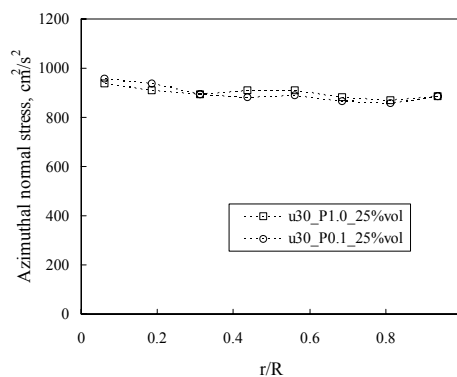
c) Solids shear stress



d) Solids axial normal stress

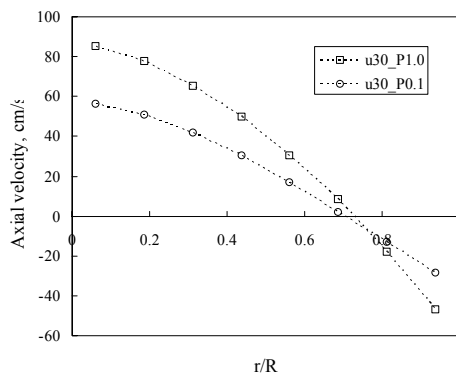


e) Solids radial normal stress

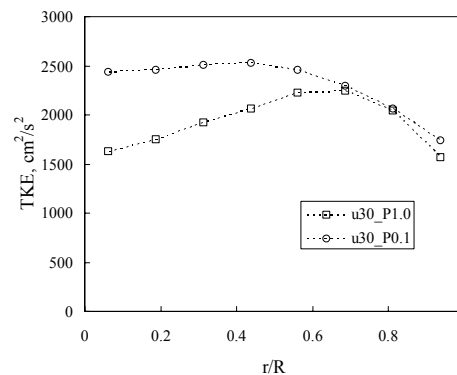


f) Solids azimuthal normal stress

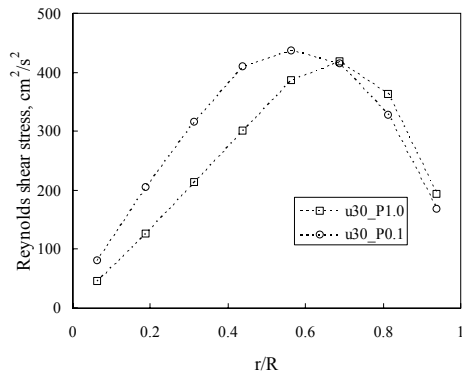
Figure A-21. Pressure effects on the solids velocity and turbulence parameters, air-C₉C₁₁-FT Catalyst, 0.30 m/s, 25% vol., 0.1 MPa vs. 1.0 MPa



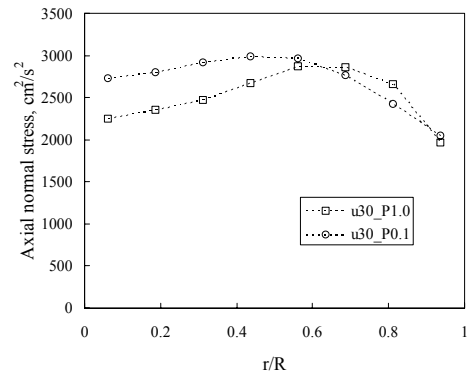
a) Liquid axial velocity



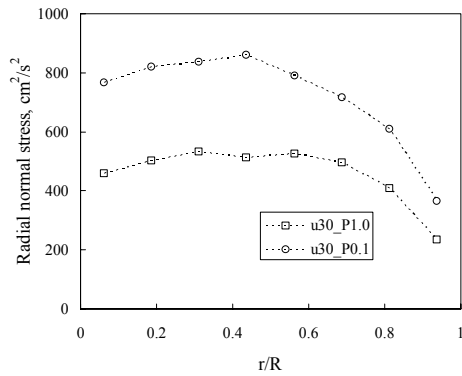
b) Liquid TKE



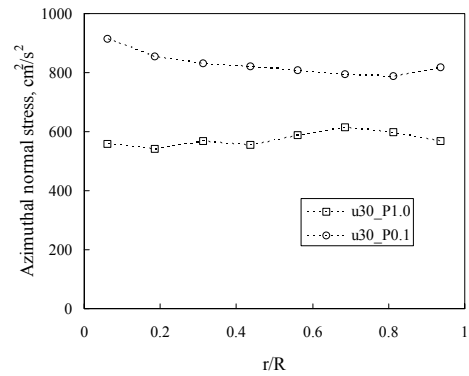
c) Liquid shear stress



d) Liquid axial normal stress



e) Liquid radial normal stress



f) Liquid azimuthal normal stress

Figure A-22. Pressure effects on the liquid velocity and turbulence parameters, air-C₉C₁₁, 0.30 m/s, 0.1 MPa vs. 1.0 MPa

Appendix B

Operating Procedures and Technical

Information of the Two Developed Techniques

This work developed a gaseous tracer technique to investigate the gas phase back-mixing and gas-liquid mass transfer, and an optical oxygen probe technique for the measurements of oxygen mass transfer. In addition to the discussion in the chapters, the necessary operating procedures and technical information of these two techniques are provided in this appendix.

B.1. Gaseous Tracer Technique

B.1.1. Components of the Gaseous Tracer Technique

1. Gas analyzer

The gas analyzer is a GOW-MAC 20 series binary analyzer, which contains a flowing reference thermal conductivity detector (TCD). Its accuracy is 3% of the full scale.

2. Gas sampling pump

The gas sampling pump used to draw the sampling gas is a GOW-MAC 59-300 model, which has been designed for GOW-MAC chromatography equipments.

3. Digital controller

The digital controllers (timers) are multifunction Dayton (model 6A855) time delay relays. They have contact current rating resistive of 10 Amps, maximum time of 999 minutes, and minimum time of 0.05 second.

4. Signal amplifier

The signal amplifier is a GOW-MAC 70-DACS-2CHAMP module, which has been designed for the DACS chromatography software. Supplied by a low voltage DC power, the amplifier has two channels (A and B) for both input and output signals.

5. Analog/digital converter

The A/D converter is a GOW-MAC 70-AD-12B module, with an effective $32.5 \mu\text{V/bit}$ response from 0–5V DC. It has two channels of analog input and an RS-232 port for the digital output.

6. Data acquisition software

The data acquisition was performed using the DACS Chromatography Software designed by GOW-MAC for MS Windows systems.

B.1.2. Operating Procedures of the Gaseous Tracer Technique

During measurements of gas tracer responses (either in the gas back-mixing or mass transfer studies), the following procedures were followed:

1. Properly setup the unit and connect the injection and sampling lines according to the schematic diagram of Figure 4-2.
2. Operate the SBCR at a desired condition for about an hour to reach stable hydrodynamics and solids distribution in the reactor.

3. Set the digital controller (I) that controls the injection to 0.05 second pulse; regulate the tracer gas pressure to obtain responses with proper magnitude which is neither too small (greatly affected by the noises) nor too large (exceeding the detector range). Set another digital controller (II), that controls digital controller (I), for precise repetition of measurements. The digital controller (II) is set with a time interval of several minutes depending on the experimental conditions.

4. Start the sampling pump, and adjust the sample rotameter on the TCD to set the sample flow rate as 1.0 SCFH.

5. Regulate the reference gas (ultra zero grade air) pressure at 40 psi. Adjust the reference rotameter on the TCD to set the reference flow rate as 1.0 SCFH.

6. After both the reference and the sample gas flows are set at the TCD, power on the gas analyzer. Settings on the gas analyzer include:

POLARITY (positive or negative) is set depending on the thermal conductivity difference of the tracer gas and the reference gas.

SPAN is usually set as 10 as long as the signal does not exceed the range of the A/D converter and amplifier, which never happened in this work.

ZERO is adjusted so that the signal baseline is slightly above the zero reading. This is because the based line can always be adjusted in the data processing, and being slightly above the zero avoids losing data below the zero line during small noise fluctuations.

7. Simultaneously start the data acquisition and turn on the switch to the digital controllers, which starts and repeats the measurements at the pre-set time intervals.

8. After sufficient data are obtained, stop the data acquisition and turn off the digital controllers, gas analyzer, gas pump, and amplifier. The measurement is completed.

B.2. Optical Oxygen Probe Technique

B.2.1. Components of the Optical Oxygen Probe System

The components of an optical oxygen probe system are listed below with technical information obtained from the manufacturer, Ocean Optics, Inc.

1. Optical probe

The T1000 model is a spectrometer-coupled sensor, designed for process environment and high pressure applications. Its specifications include:

Probe Assembly:	1000 μm optical fiber, stainless steel ferrule
Dimensions:	6.35 mm OD, 177.8 mm length
Pressure:	3000 psi
Typical Usage:	process environments, high-pressure applications

2. Optic fiber assembly

The optic fiber assembly used with the T1000 probe is the BIF600-VIS-NIR model from Ocean Optics, Inc. It consists of optic fiber in a diameter of 600 μm . The optic fiber assembly has a bifurcated design, which allows the probe to receive light from the light source and send fluorescence to the spectrometer.

3. Spectrometer assembly (including the USB A/D converter)

The USB2000 spectrometer detects light signal in the 360-1000 nm wavelength range. The integrated A/D converter then sends digital signals to the PC via the integrated the USB communication port. Specifications include:

Dimensions	63.34 mm x 89.10 mm x 34.37 mm
Power consumption:	90 mA @ 5 VDC
Wavelength range:	360-1000 nm
Detector:	2048-element linear CCD array
Entrance aperture:	200 μm wide slit
Focal length:	42 mm (input); 68 mm (output)
Optical resolution:	\sim 10 nm FWHM
Stray light:	<0.05% at 600 nm; <0.10% at 435 nm
Sensitivity:	600 nm -- 41 photons per count

4. Light source

The USB-LS-450 light source module is an integrated, multi-purpose LED device, designed for the USB2000 Spectrometers. It connects to the USB2000 Spectrometers via a connector on the front of the spectrometer, from which the light source receives power.

5. Data acquisition software

The OOIBase32 software was purchased from Ocean Optics and used as the data acquisition software for the optical oxygen probe technique.

B.2.2. Operating Procedures of the Optical Oxygen Probe Technique

During mass transfer measurements using the optical oxygen probe, the following procedures were followed:

1. Mount the optical probe to one of the threaded ports of the SBCR (II) at a desired axial location, and adjust the probe tip to the desired radial location in the column.
2. Properly couple the light source and the integrated spectrometer assembly. Connect the light source and spectrometer assembly with the optical probe using the bifurcated optic fiber assembly, and with the PC using an A-B USB cable.
3. Operate the SBCR at a desired condition for about an hour to reach stable hydrodynamics and solids distribution in the reactor. For the oxygen-enriched air method, regulate the oxygen pressure, which provides a small oxygen flow to the column at about 3% of the overall gas flow rate.
4. Set the digital timer that controls the small oxygen flow for measurement repetition. Sufficient time interval needs to be set depending on the time needed for a dynamic

response to reach the steady state. Three minutes are sufficient, for example, at $u_g=0.30$ m/s and $P=0.1$ MPa.

5. Run the data acquisition software at the PC and wait for its proper recognition of the oxygen probe system. Simultaneously start the data acquisition and the electric switch connected to the digital timer, which starts the measurement.

6. Data are recorded when the digital timer automatically and precisely starts and stops the small oxygen flow at the pre-set time interval. After sufficient data are obtained, stop the data acquisition and turn off the digital controller. The measurement is completed.

Appendix C

Solids Axial Dispersion with a Steady State

Method

In addition to the transient method presented in Chapter 4, a steady state method was evaluated to determine the solids axial dispersion coefficient. The solids concentration axial gradient was calculated from both the CARPT occurrence and the virtual tracer response curves. Using the obtained solids gradient data, the solids axial dispersion coefficient was fitted using the steady state sedimentation-dispersion model (SDM). This appendix provides the methods to obtain solids concentration axial gradient, the steady state SDM and its parameter fitting, and a comparison between the transient method and the steady state method.

C.1. Solids Concentration Axial Gradient

Since the solids tracer particle has the same physical properties (size and density) as the FT catalyst, the long-time averaged tracer particle occurrences proportionally represent the local solids holdup. An axial gradient of the solids holdup, $\varepsilon_s(z)$, can then be obtained from the cross-sectional average occurrences, $N_s(z)$, as

$$\varepsilon_s(z) = \bar{\varepsilon}_s \frac{N_s(z)}{N_{s,\text{tot}}}, \quad (\text{C-1})$$

where $\bar{\varepsilon}_s$ and $N_{s,\text{tot}}$ are the globally averaged solids holdup and tracer particle occurrences, respectively. For the calculation in the fully developed region, the cross-sectional average gas holdup, $\varepsilon_g(z)$, is assumed to be equal to the overall gas holdup, $\bar{\varepsilon}_g$, as also assumed in the CT/overall gas holdup reconstruction method. Based on this assumption, the solids concentration, defined as the volume fraction of glass beads in the gas-free slurry, is calculated from the solids holdup obtained in Equation C-1 as

$$C_s(z) = \frac{\varepsilon_s(z)}{1 - \varepsilon_g(z)} = \frac{\varepsilon_s(z)}{1 - \bar{\varepsilon}_g} = \frac{\bar{\varepsilon}_s}{1 - \bar{\varepsilon}_g} \frac{N_s(z)}{N_{s,\text{tot}}} = \bar{C}_s \frac{N_s(z)}{N_{s,\text{tot}}}, \quad (\text{C-2})$$

where \bar{C}_s is the globally averaged solids concentration in the gas-free slurry, equal to $\bar{\varepsilon}_s / (1 - \bar{\varepsilon}_g)$ according to the solids concentration definition in this work. \bar{C}_s can be easily calculated from the total amount of liquid and solids loaded into the reactor (9.1% vol. or 25% vol). The solids concentration was calculated in a discretized manner (Figure C-1a), using the tracer particle occurrences in a $2\Delta z$ section between $z_k - \Delta z$ and $z_k + \Delta z$, written as

$$C_s^{\text{Exp-S}}(z_k) = \bar{C}_s \frac{L}{2\Delta z} \frac{N_s(z_k)}{N_{s,\text{tot}}}, \quad (\text{C-3})$$

where L is the dynamic (aerated) height of the suspension, and Δz was selected as $0.1 d_c$ to have occurrences to calculate the solids concentration. Axial levels (z_k) were selected at 15 axial distances evenly distributed between $2.0 d_c$ and $9.0 d_c$. Figure C-1 (b) shows the obtained occurrence axial distribution, $N_s(z_k)$, based on which the solids concentration axial gradient, $C_s^{\text{Exp-S}}(z_k)$ (shown in Figure C-2), was calculated using Equation C-3. The solids concentration at $z=2 d_c$ is about 40% higher than that at $z=9 d_c$, indicating a significant axial gradient of the solids concentration.

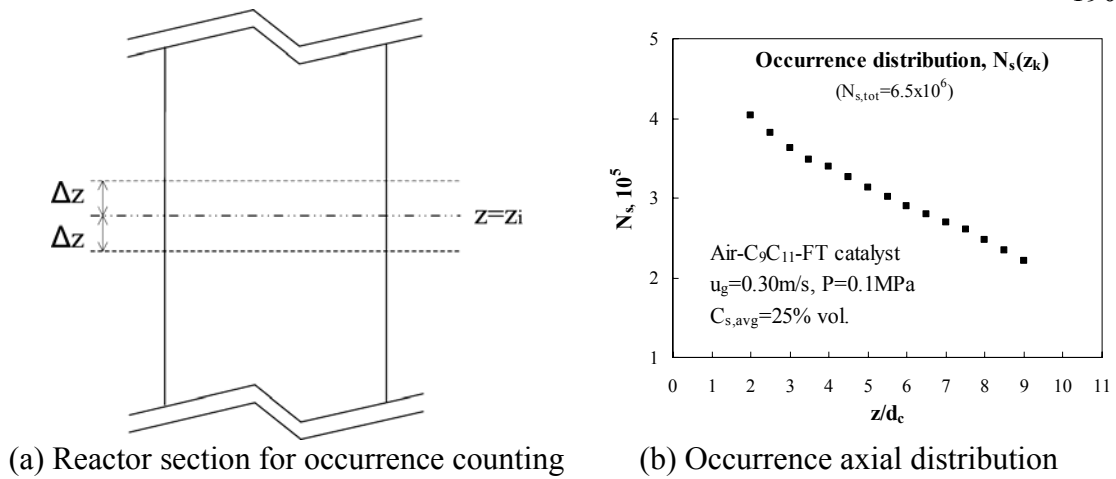


Figure C-1. Axial distribution (gradient) of the solids occurrences by CARPT

In addition to the CARPT occurrence method, solids concentration axial gradient was also calculated from the virtual tracer response curves obtained earlier. The virtual solids tracer concentration is proportional to the solids concentration in the slurry and can also be used for D_s estimation. Hence, the asymptotic values of the raw counts of the virtual tracer response curves (Figure 4-15 before the normalization) are considered to be proportional to the steady state solids concentration at various levels (Figure C-2).

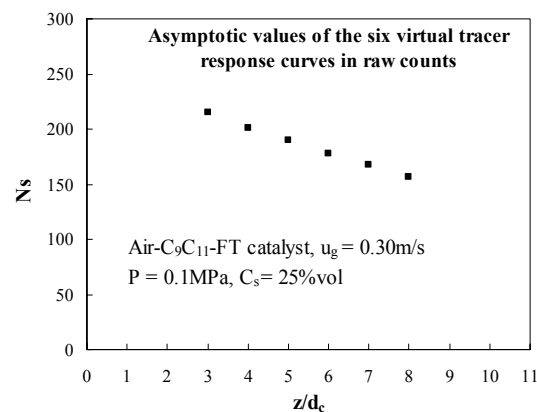


Figure C-2. Asymptotic values of the six virtual tracer response curves

Since transient method used the virtual tracer response curves, using the asymptotic values of the same curves for the steady state method yields a fair comparison between these two methods. However, the ratio between the solids concentration and the virtual tracer response raw counts was not directly known. This ratio was arbitrarily adjusted so that the magnitudes of these points match the steady state SDM, when fitting the gradient for the D_s estimation. Therefore, this method was only used as a secondary method to the CARPT occurrence method to provide solids concentration axial gradient for the steady state SDM.

C.2. Steady State SDM and its Parameter Fitting

The steady state SDM for a semi-batch SBCR is written as

$$D_s \frac{\partial^2 C_s}{\partial z^2} + u_{st} \frac{\partial C_s}{\partial z} = 0. \quad (C-4)$$

Boundary conditions are $z=0$, $D_s \frac{\partial C_s}{\partial z} + u_{st} C_s = 0$; $z=L$, $D_s \frac{\partial C_s}{\partial z} + u_{st} C_s = 0$.

With the boundary conditions, the analytical solution of Equation C-4 can be derived as

$$C_s(z) = C_{s,avg} \cdot \frac{(u_{st} L / D_s)}{1 - e^{-u_{st} L / D_s}} \cdot e^{-u_{st} z / D_s}. \quad (C-5)$$

Since the solids were in batch operation, the settling velocity, u_{st} , and D_s always appear in pairs in the equation and solution, in the form of u_{st}/D_s . Hence, the u_{st} value estimation proportionally affects the fitted D_s results. The values of u_{st} were calculated using the correlation of Matsumoto et al. (1989), same as for the earlier transient SDM. The results' sensitivity on the u_{st} estimation is discussed in the next section. D_s is the only unknown parameter in the model, fitted by minimizing the squared error defined as

$$\text{error} = \sum_{k=1}^{n_{z,S}} [C_s^{\text{Exp-S}}(z_k) - C_s^{\text{Mod-S}}(z_k)]^2. \quad (C-6)$$

Figure C-3 shows the solids concentration axial gradient obtained from the CARPT occurrences with the steady-state SDM fit. As discussed above, the six points obtained from the virtual tracer responses were also fitted with the steady state SDM (Figure C-4). At the same example condition, the D_s estimated in Figure C-4 is $158 \text{ cm}^2/\text{s}$, relatively close to the $133 \text{ cm}^2/\text{s}$ obtained using the CARPT occurrence (Figure C-3), when they are both compared to the transient method earlier ($526 \text{ cm}^2/\text{s}$ in Figure 4-15).

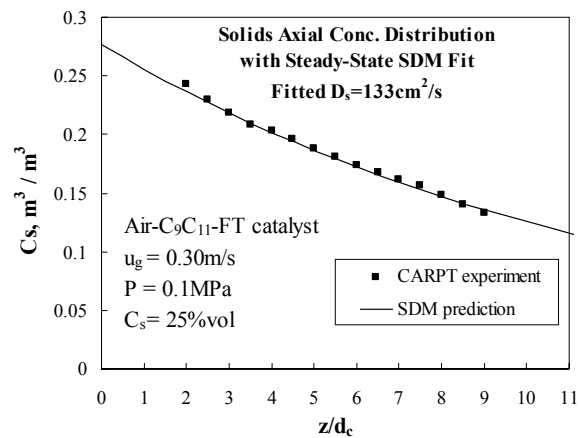


Figure C-3. Axial gradient of the solids concentration obtained from CARPT occurrences, with steady state SDM fit

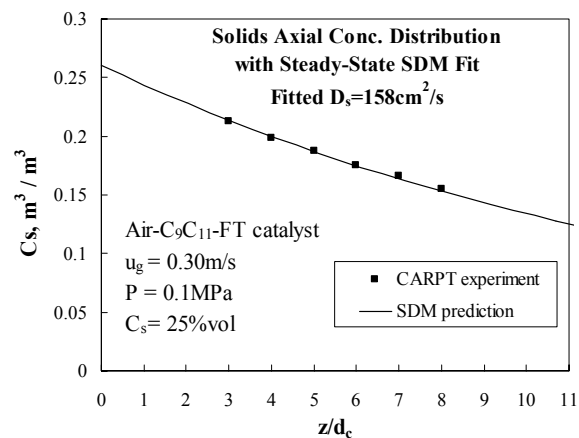


Figure C-4. Axial gradient of the solids concentration calculated (with arbitrary adjustments) from the asymptotic values of the virtual tracer response curves, with steady state SDM fit

C.3. Comparison of Transient and Steady State Methods

The solids axial dispersion coefficient can be estimated using either the transient SDM with the virtual tracer responses or the steady state SDM with the solids concentration axial gradient. The good model fits using both methods suggest that the solids dispersion and its axial distribution in this reactor can be described by the SDM with fitted D_s . However, although both methods gave good fits, the D_s value fitted by the steady state method (133 cm²/s in Figure C-3) is apparently lower than that fitted by the transient method (526 cm²/s in Figure 4-15). Similar difference was observed at other conditions. In this work, the solids settling velocity u_{st} was estimated by a literature correlation. Using a steady state SDM for this semi-batch operated SBCR, any error in the u_{st} estimation directly causes a same relative error in the fitted D_s , as explained in the model section earlier. In order to evaluate the error caused by u_{st} in the transient SDM method, D_s was fitted with arbitrarily varied u_{st} values. Since several different correlations predict the u_{st} values with a variation of about 50% for the conditions in this work, an u_{st} sensitivity test was performed by changing the u_{st} values estimated by Matsumoto et al. (1989) by $\pm 50\%$. It was found that increasing or decreasing the correlation estimated u_{st} by 50% only results in 5% increase or 3% decrease in the fitted D_s values using the transient method. The transient method obtains D_s values based on dynamic change of the solids concentration over a period of time, while the steady state method uses only the time-averaged solids axial gradient caused by the solids sedimentation. Therefore, the different D_s values fitted by the two SDMs are likely due to the higher u_{st} sensitivity of the steady state method. The smaller u_{st} sensitivity can be considered as an advantage of the transient method in D_s fitting, since accurate u_{st} estimation or measurement in a SBCR is difficult.

C.4. Evaluation of a C_s Axial Gradient Correlation

As introduced in Chapter 2, Rados (2003) presented a correlation (Equation C-7) for the solids concentration axial gradient, based on his data obtained in the air-water-glass

beads system. The correlation reflects Rados (2003)'s reporting of linear axial solids concentration profiles rather than exponential curves as described by the SDM.

$$\frac{C_s}{\bar{C}_s} = 1.86 - \frac{1}{6.4} \frac{z}{d_c} \quad (\text{C-7})$$

To further examine differences of the two solids, this work evaluated this correlation, developed using the air-water-glass beads data, with the solids concentration data obtained in the mimicked FT SBCR. The solids concentration axial gradients obtained above from both CARPT occurrences and the six solids tracer response curves are plotted with the correlation prediction in Figure C-5.

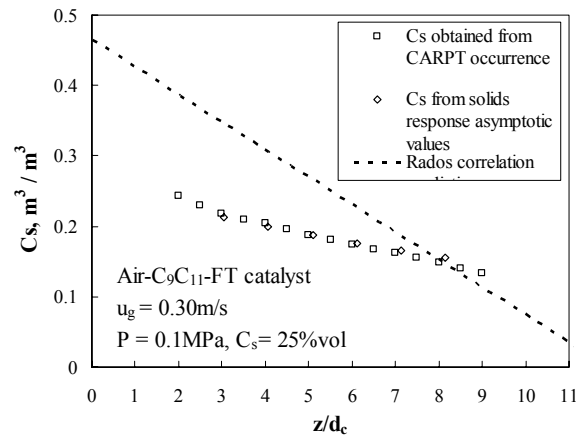


Figure C-5. Solids concentration axial gradients in the mimicked FT SBCR compared with the Rados (2003) C_s correlation

It was found that the correlation developed by Rados (2003) predicts a much higher axial gradient of the solids concentration than the data of this work. This evaluation suggests that the relative solids concentration axial gradient C_s / \bar{C}_s is not a simple function of only the relative axial position z / d_c , but also of the physical properties of phases. The FT catalyst used in this work, compared to the 150 μm glass beads, has smaller density and sizes and therefore a smaller settling velocity, which in turn results in a smaller axial gradient of solids concentration (i.e., more uniform slurry).

It should also be noted that the solids concentration axial gradients obtained in this work and the previous studies all have only slight curving. However, this does not necessarily mean a linear C_s - z relation, because the SDM also predicts small curving at these conditions. To further evaluate whether a linear relation or the SDM fits the data better, the solids concentration needs to be measured along the whole reactor length. If the introduced methods are to be used in the future, it is highly suggested that CARPT experiments are conducted within the whole reactor volume instead of only the fully developed region.

Appendix D

Development of Two Empirical k_{1a} Correlations

In addition to the current empirical k_{1a} correlations, two new empirical k_{1a} correlations were developed, based on a collected database using two different methods. The database was collected from the literature which covers mass transfer studies in BCRs and SBCRs reported from 1965 to 2004. The methods used for developing the correlations include an artificial neural network (ANN) method and a power law method.

D.1. Data Collection

Values of k_{1a} and operating parameters were collected at about 1800 data points from 43 literature studies (Abraham and Sawant, 1989; Behkish et al., 2000; Bhatia et al., 2004; Braulick et al., 1965; Cavatorta and Boehm, 1988; Charinpanitkul et al., 1993; Dewes et al., 1995; Dewes and Schumpe, 1997; Godbole et al., 1983; Godbole et al., 1984; Gopal and Sharma, 1983; Grund et al., 1992; Hikita et al., 1981; Hills, 1991; Jordan et al., 2002; Kang et al., 1999; Kataoka et al., 1979; Katnas et al., 1994; Kawase et al., 1987; Koide et al., 1983; Koide et al., 1984; Koide et al., 1985; Koranne et al.,

1985; Kratochvil et al., 1985; Laari et al., 1997; Letzel et al., 1999; Maalej et al., 2001; Nakao et al., 1983; Ozturk et al., 1987; Peeva et al., 2001; Pejanovic et al., 1993; Posarac and Tekic, 1987; Sada et al., 1987; Sauer and Hempel, 1987; Shah et al., 1995; Terasaka et al., 1998; Vandu et al., 2004; Vermeer and Krishna, 1981; Voyer and Miller, 1968; Winkler et al., 1988; Yang et al., 2001; Yang et al., 2001; and Yoshida and Akita, 1965). Values of k_{1a} , u_g , d_c , D_{AB} , ρ_g , ρ_l , μ_l , σ_l , g were collected as a set at each data point. In order to decrease the total number of inputs, dimensionless numbers were calculated from these parameters. Dimensionless numbers selected as the candidates during the correlation development are listed in Table D-1. The Sh number was used as the only output, and input dimensionless numbers were selected from the rest.

Table D-1. Dimensionless numbers considered for the k_{1a} correlation development

Symbol	Name	Expression	Physical basis
Sh	Sherwood number	$Sh = \frac{k_{1a} \cdot d_c^2}{D_{AB}}$	$\frac{\text{lengthscale}}{\text{diffusive boundary layer thickness}}$
Sc	Schmidt number	$Sc = \frac{\mu_l}{D_{AB}\rho_l}$	$\frac{\text{momentum diffusivity (viscosity)}}{\text{mass diffusivity}}$
Bo	Bond number	$Bo = \frac{g \cdot d_c^2 \cdot \rho_l}{\sigma}$	$\frac{\text{body (gravitational) forces}}{\text{surface tension forces}}$
Fr	Froude number	$Fr = \frac{u_g^2}{g \cdot d_c}$	$\frac{\text{inertial forces}}{\text{gravitational forces}}$
Ga	Galilei (Galileo) number	$Ga = \frac{g \cdot d_c^3 \cdot \rho_l^2}{\mu_l^2}$	$\frac{\text{gravitational forces}}{\text{viscous forces}}$
Ca	Capillary number	$Ca = \frac{u_g \cdot \mu_l}{\sigma}$	$\frac{\text{viscous forces}}{\text{surface tension forces}}$
Mo	Morton number	$Mo = \frac{\mu_l^4 \cdot g}{\rho_l \cdot \sigma_l^3}$	a combination of inertial, gravitational, surface tension, and viscous forces.
Re	Reynolds number	$Re = \frac{u_g \cdot \rho_l \cdot d_c}{\mu_l}$	$\frac{\text{inertial forces}}{\text{viscous forces}}$
R_ρ	Density ratio of the liquid/slurry to the gas	$R_\rho = \frac{\rho_g}{\rho_l}$	$\frac{\text{gas density}}{\text{liquid/slurry density}}$

D.2. k_a Correlation using the ANN

The ANN method gives good data fit and has been widely used in chemical engineering tasks (Bhat et al., 1990). The ANN model and the computer program NNFit used in this work were developed by Cloutier et al (1996). Figure D-1 is given by the developer to show an example ANN architecture with three-layers including an input layer (U_i), a hidden layer (H_j), and an output layer (S_k). The ANN model consists of a set of non-linear sigmoid functions as

$$S_k = \frac{1}{1 + \exp\left[-\sum_{j=1}^{J+1} w_{jk} H_j\right]} \quad (\text{D-1})$$

$$H_j = \frac{1}{1 + \exp\left[-\sum_{i=1}^{I+1} w_{ij} U_i\right]}, \quad (\text{D-2})$$

where S_k and U_i are the ANN model inputs and outputs, which are normalized from the actual input and output parameter values, respectively, as

$$U_i = \frac{\log(X_i / X_{\min})}{\log(X_{\max} / X_{\min})} \quad (\text{D-3})$$

$$S_k = \frac{\log(Y_k / Y_{\min})}{\log(Y_{\max} / Y_{\min})}. \quad (\text{D-4})$$

$I+1$, $J+1$, and K are the total numbers of the nodes in the input, hidden, and output layers. U_{I+1} and H_{J+1} are the bias constants which are set to be 1. Therefore, the fitting parameters in this ANN are the J number and the values of w_{ij} and w_{kj} , which are called the weights. Details of the procedures can be found in Cloutier's manual, Rarca et al. (2003), or Shaikh and Al-Dahhan (2003).

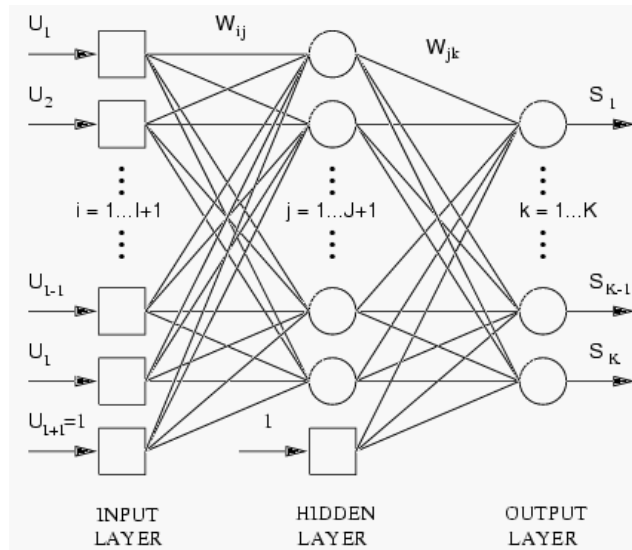


Figure D-1. Architecture of a neural network model with layers (Cloutier et al., 1996)

Similar to deciding the ANN model parameters, selection of input dimensionless numbers are also empirical. Many combinations of different groups have been tested, and one set of dimensionless groups was selected after evaluating the prediction at various conditions. The selected input groups are Sc, Fr, Mo, Re, and Rp for the ANN k_a correlation.

The J number was empirically determined as 7. The weight numbers were fitted as:

w_{ij}	1	2	3	4	5	6	7
1	-1.10E+00	-3.33E+00	7.26E-01	1.73E-01	1.07E+00	-7.17E-01	1.94E+00
2	-1.06E-01	2.97E-02	-2.84E-01	1.42E+00	1.43E+00	9.00E-01	-2.88E+00
3	6.59E-01	-1.12E-01	-3.03E-01	-2.98E-01	9.71E-01	-2.29E-01	-1.44E+00
4	-5.03E-01	-2.67E+00	-7.98E-01	-4.23E-01	2.76E+00	-5.55E-02	-2.02E+00
5	1.02E+00	1.78E+00	-8.56E-01	1.56E+00	-2.84E-01	1.38E+00	1.67E+00
6	2.34E+00	4.28E-01	9.55E-01	-1.52E+00	-6.96E-02	-5.80E-01	5.07E+00

w_{jk}	1	2	3	4	5	6	7	8
1	-3.16E+00	-4.84E+00	-1.94E+00	3.00E+00	3.62E+00	2.88E+00	-3.38E+00	1.72E+00

Figure D-2 plots the k_{1a} values predicted by the ANN correlation against the k_{1a} data. The average absolute relative error (AARE) was calculated to be 25%. Using some previously reported k_{1a} correlations to make predictions for these data, AAREs are 31% by Ozturk et al. (1987), 40% by Kawase et al. (1987), 43% by Schumpe et al. (1987), and 240% by Deckwer et al. (1981).

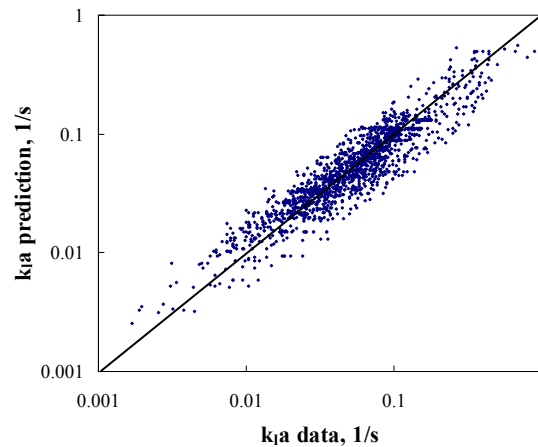


Figure D-2. Plot of predictions by the ANN k_{1a} correlation vs. data

It was found that this obtained ANN correlation can predict mass transfer coefficient with reasonable trends with respect to the operating conditions, such as the superficial gas velocity, liquid viscosity and surface tension, etc. Due to the nature of ANN models, this correlation should be used strictly within the data condition range, as shown in Table D-2.

Table D-2. Parameter ranges of the collected data

k_{1a}	1.14E-03 – 4.98E-01 1/s
u_g	1.30E-03 – 6.00E-01 m/s
d_c	3.70E-02 – 5.50E+00 m
D_{AB}	1.82E-10 – 5.06E-09 m ² /s
ρ_g	5.07E-02 – 1.20E+01 kg/m ³
ρ_l	6.94E+02 – 1.60E+03 kg/m ³
μ_l	3.06E-04 – 3.85E-02 Ns/m ²
σ_l	1.19E-02 – 7.50E-02 N/m

D.3. k_{1a} Correlation using Power Law Fit

Using an error minimization program, a power law k_{1a} correlation was also developed based on the same database. Dimensionless groups were empirically selected and the power constants were fitted. The obtained power law k_{1a} correlation is expressed as

$$\frac{k_{1a} \cdot d_c^2}{D_{AB}} = \left(\frac{\mu_1}{D_{AB} \cdot \rho_1} \right)^{0.735} \left(\frac{u_g^2}{g \cdot d_c} \right)^{0.378} \left(\frac{\mu_1^4 \cdot g}{\rho_1 \cdot \sigma^3} \right)^{0.133} \left(\frac{u_g \cdot \rho_1 \cdot d_c}{\mu_1} \right)^{1.458} \left(\frac{\rho_g}{\rho_1} \right)^{0.4} \quad (D-5)$$

Figure D-3 plots the k_{1a} values predicted by this power law correlation against the collected k_{1a} data. The AARE for the predictions of this correlation is 28%, which is slightly higher than the ANN k_{1a} correlation, but still better than others in the literature. Developed using the same database, this power law k_{1a} correlation should also be used within the condition range listed in Table D-2.

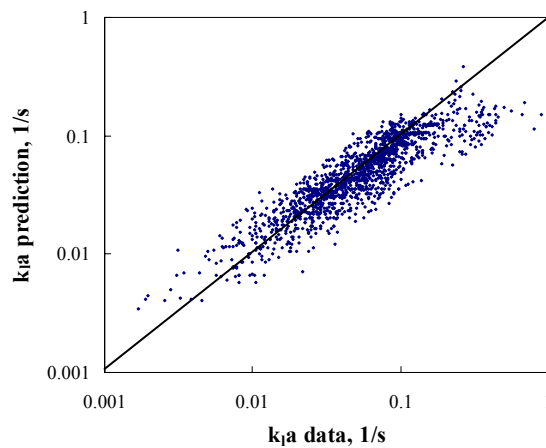


Figure D-3. Plot of predictions by the power law k_{1a} correlation vs. data

An MS Excel sheet for automatic calculation of the k_{1a} predictions using the two developed correlations was created and provided elsewhere.

References

- Ahon, V. R., Costa, E. F., Jr., Monteagudo, J. E. P., Fontes, C. E., Biscaia, E. C., Jr., Lage, P. L. C., 2005. A comprehensive mathematical model for the Fischer-Tropsch synthesis in well-mixed slurry reactors. *Chemical Engineering Science*, 60 (3), 677-694.
- Akita, K., Yoshida, F., 1973. Gas holdup and volumetric mass transfer coefficient in bubble columns. Effects of liquid properties. *Industrial & Engineering Chemistry Process Design and Development*, 12 (1), 76-80.
- Alexander, B. F., Shah, Y. T., 1976. Axial dispersion coefficients in bubble columns. *Chemical Engineering Journal (Amsterdam, Netherlands)*, 11 (2), 153-156.
- Argo, W. B., Cova, D. R., 1965. Longitudinal mixing in gas-sparged tubular vessels. *Ind. Eng. Chem., Process Design. Develop.*, 4 (4), 352-359.
- Asai, S., Yoshizawa, Hidekazu., 1992. Individual longitudinal dispersion coefficients of two immiscible liquids in bubble columns. *Industrial & Engineering Chemistry Research*, 31 (2), 587-592.
- Badgajar, M. N., Deimling, A., Morsi, B. I., Shah, Y. T., Carr, N. L., 1986. Solids distribution in a batch bubble column. *Chemical Engineering Communications*, 48 (1-3), 127-153.
- Baird, M. H. I., Rice, R. G., 1975. Axial dispersion in large unbaffled columns. *Chemical Engineering Journal*, 9 171-174.
- Baird, M. H. I., Rao, N. V. R., 1988. Characteristics of a countercurrent reciprocating plate bubble column. II. Axial mixing and mass transfer. *Canadian Journal of Chemical Engineering*, 66 (2), 222-231.
- Baird, M. H. I., Rao, N. V. R., 1998. Axial mixing in a 15 cm diameter reciprocating plate bubble column. *Canadian Journal of Chemical Engineering*, 76 (3), 370-378.
- Bandyopadhyay, B., Humphrey, A. E., Taguchi, H., 1967. Dynamic measurement of the volumetric oxygen transfer coefficient in fermentation systems. *Biotechnology and Bioengineering*, 9 (4), 533-544.
- Bartholomew, W. H., Karow, E. O., Sfat, M. R., Wilhelm, R. H., 1950. Oxygen transfer and agitation in submerged fermentations. Mass transfer of oxygen in submerged fermentation by *Streptomyces griseus*. *Journal of Industrial and Engineering Chemistry (Washington, D. C.)*, 42 1801-1809.

- Behkish, A., Men, Z., Morsi, B. I., 2000. Hydrodynamics of CO and H₂ in a slurry bubble column reactor with paraffin oil. Proceedings - Annual International Pittsburgh Coal Conference, 17th 2268-2287.
- Behkish, A., Men, Z., Morsi, B. I., 2000. Hydrodynamics of CO and H₂ in a slurry bubble column reactor with paraffin oil. Proceedings - Annual International Pittsburgh Coal Conference, 17th 2268-2287.
- Behkish, A., Men, Z., Inga, J. R., Morsi, B. I., 2002. Mass transfer characteristics in a large-scale slurry bubble column reactor with organic liquid mixtures. Chemical Engineering Science, 57 (16), 3307-3324.
- Behling, M., Mewes, D., 2004. X-ray computational tomography measurement of 3-phase flow in bubble columns. Bubbly Flows, 233-241.
- Bennett, M. A., West, R. M., Luke, S. P., Jia, X., Williams, R. A., 1999. Measurement and analysis of flows in a gas-liquid column reactor. Chemical Engineering Science, 54 (21), 5003-5012.
- Bhatia, B., Nigam, K. D. P., Auban, D., Hebrard, G., 2004. Effect of a new high porosity packing on hydrodynamics and mass transfer in bubble columns. Chemical Engineering and Processing, 43 (11), 1371-1380.
- Bhusarapu, S. B., 2005. Solids flow mapping in gas-solids risers. D.Sc. Thesis. Department of chemical engineering, Washington University, St. Louis.
- Bin, A. K., Duczmal, B., Machniewski, P., 2001. Hydrodynamics and ozone mass transfer in a tall bubble column. Chemical Engineering Science, 56 (21-22), 6233-6240.
- Breman, B. B., Beenackers, A. A. C. M., Bouma, M. J., van der Werf, M. H., 1996. The gas-liquid mass transfer coefficient (k_La) in the gas-liquid multi-stage agitated contractor (MAC). Chemical Engineering Research and Design, 74 (A8), 872-881.
- Brunner, E., 1985. Solubility of hydrogen in 10 organic solvents at 298.15, 323.15, and 373.15 K. Journal of Chemical and Engineering Data, 30 (3), 269-273.
- Bukur, D. B., Patel, S. A., Daly, J. G., 1990. Gas holdup and solids dispersion in a three-phase slurry bubble column. AIChE Journal, 36 (11), 1731-1735.
- Bukur, D. B., Daly, J. G., Patel, S. A., 1996. Application of g-ray Attenuation for Measurement of Gas Holdups and Flow Regime Transitions in Bubble Columns. Industrial & Engineering Chemistry Research, 35 (1), 70-80.

- Calderbank, P. H., Moo-Young, M. B., 1961. Continuous phase heat and mass transfer properties of dispersions. *Chemical Engineering Science*, 16 39-54.
- Camacho Rubio, F., Garcia, J. L., Molina, E., Chisti, Y., 1999. Steady-state axial profiles of dissolved oxygen in tall bubble column bioreactors. *Chemical Engineering Science*, 54 (11), 1711-1723.
- Camacho Rubio, F., Sanchez Miron, A., Ceron Garcia, M. C., Garcia Camacho, F., Molina Grima, E., Chisti, Y., 2004. Mixing in bubble columns: a new approach for characterizing dispersion coefficients. *Chemical Engineering Science*, 59 (20), 4369-4376.
- Campos, J. B. L. M., De Carvalho, J. R. F. Guedes., 1992. A new experimental technique to study backmixing in packed bubble columns. *Chemical Engineering Science*, 47 (15-16), 4063-4067.
- Cardoso, O. N., Sotto Mayor, T., Pinto, A. M. F. R., Campos, J. B. L. M., 2003. Axial dispersion of particles in a slugging column - the role of the laminar wake of the bubbles. *Chemical Engineering Science*, 58 (18), 4159-4172.
- Cassanello, M., Larachi, F., Guy, C., Chaouki, J., 1996. Solids mixing in gas-liquid-solid fluidized beds: experiments and modeling. *Chemical Engineering Science*, 51 (10), 2011-2020.
- Chang, H. N., Halard, B., Moo-Young, M., 1989. Measurement of KLa by a gassing-in method with oxygen-enriched air. *Biotechnology and Bioengineering*, 34 (9), 1147-1157.
- Chaouki, J., Larachi, F., Dudukovic, M. P., 1997. *Non-Invasive Monitoring of Multiphase Flows*. New York, Elsevier Science.
- Chaouki, J., Larachi, F., Dudukovic, M. P., 1997. Noninvasive Tomographic and Velocimetric Monitoring of Multiphase Flows. *Industrial & Engineering Chemistry Research*, 36 (11), 4476-4503.
- Chen, B., 1972. Effects of liquid flow on axial mixing of liquid in a bubble column. *The Canadian journal of chemical engineering*, 50 436-438.
- Chen, B. H., McMillan, A. F., 1982. Heat transfer and axial dispersion in batch bubble columns. *Canadian Journal of Chemical Engineering*, 60 (3), 436-439.
- Chen, B. H., Yang, N. S., 1989. Characteristics of a cocurrent multistage bubble column. *Industrial & Engineering Chemistry Research*, 28 (9), 1405-1410.

- Chen, B. H., Yang, N. S., 1989. Characteristics of a cocurrent multistage bubble column. *Industrial & Engineering Chemistry Research*, 28 (9), 1405-1410.
- Chen, J., Kemoun, A., Al-Dahhan, M. H., Dudukovic, M. P., Lee, D. J., Fan, L.-S., 1999. Comparative hydrodynamics study in a bubble column using computer-automated radioactive particle tracking (CARPT)/computed tomography (CT) and particle image velocimetry (PIV). *Chemical Engineering Science*, 54 (13-14), 2199-2207.
- Chen, P., Gupta, P., Dudukovic, M. P., Toseland, B. A., 2006. Hydrodynamics of slurry bubble column during dimethyl ether (DME) synthesis: Gas-liquid recirculation model and radioactive tracer studies. *Chemical Engineering Science*, 61 (19), 6553-6570.
- Clift, R., Grace, J. R., Weber, M. E., 1978. *Bubbles, Drops, and Particles*. New York, Academic Press.
- Comte, A., Kohls, O., Scheper, T., 1995. Fiber optical chemosensors and biosensors. *CLB Chemie in Labor und Biotechnik*, 46 (1), 18-22.
- Cova, D. R., 1966. Catalyst suspension in gas-agitated tubular reactors. *Ind. Eng. Chem., Process Design Develop.*, 5 (1), 20-25.
- Cova, D. R., 1974. Axial mixing in the liquid phase in gas sparged columns. *Industrial & Engineering Chemistry Process Design and Development*, 13 (3), 292-296.
- Da Silva, F. A., Pironti, F. F., Saez, A. E., 1995. The sedimentation-dispersion model for slurry bubble columns with a conical distributor. *Chemical Engineering Communications*, 138 157-170.
- Daiz, M., Vega, A., Coca, J., 1987. Correlation for the estimation of gas-liquid diffusivity. *Chemical Engineering Communications*, 52 (4-6), 271-281.
- Danckwerts, P. V., 1951. Significance of liquid-film coefficients in gas absorption. *Journal of Industrial and Engineering Chemistry (Washington, D. C.)*, 43 1460-1467.
- De Swart, J. W. A., Krishna, R., 2002. Simulation of the transient and steady state behaviour of a bubble column slurry reactor for Fischer-Tropsch synthesis. *Chemical Engineering and Processing*, 41 (1), 35-47.
- Deckwer, W. D., Burckhart, R., Zoli, G., 1974. Mixing and mass transfer in tall bubble columns. *Chemical Engineering Science*, 29 (11), 2177-2188.
- Deckwer, W. D., 1981. Access of hydrodynamic parameters required in the design and scale-up of bubble column reactors. *ACS Symposium Series*, 168 213-241.

- Deckwer, W. D., Nguyen-Tien, K., Kelkar, B. G., Shah, Y. T., 1983. Applicability of axial dispersion model to analyze mass-transfer measurements in bubble columns. *AIChE Journal*, 29 (6), 915-922.
- Deckwer, W. D., 1991. *Bubble column reactors*. West Sussex, England, John Wiley & Sons.
- Degaleesan, S., Roy, S., Kumar, S. B., Dudukovic, M. P., 1996. Liquid mixing based on convection and turbulent dispersion in bubble columns. *Chemical Engineering Science*, 51 (10), 1967-1976.
- Degaleesan, S., 1997. Fluid dynamic measurements and modeling of liquid mixing in bubble columns. D. Sc. Thesis. Department of Chemical Engineering, Washington University, St. Louis, MO, USA.
- Degaleesan, S., Dudukovic, M. P., Toseland, B. A., Bhatt, B. L., 1997. A Two-Compartment Convective-Diffusion Model for Slurry Bubble Column Reactors. *Industrial & Engineering Chemistry Research*, 36 (11), 4670-4680.
- Degaleesan, S., Dudukovic, M. P., 1998. Liquid backmixing in bubble columns and the axial dispersion coefficient. *AIChE Journal*, 44 (11), 2369-2378.
- Degaleesan, S., Dudukovic, M., Pan, Y., 2001. Experimental study of gas-induced liquid-flow structures in bubble columns. *AIChE Journal*, 47 (9), 1913-1931.
- Dempster, A. P., Laird, N. M. and Rubin, D. B., 1977. Maximum Likelihood Estimation from Incomplete data via the EM Algorithm. *Journal of the Royal Statistical Society*, 39 (B), 1-22.
- Devanathan, N., Moslemian, D., Dudukovic, M. P., 1990. Flow mapping in bubble columns using CARPT. *Chemical Engineering Science*, 45 (8), 2285-2291.
- Devine, W. D., Shah, Y. T., Morsi, B. I., 1985. Liquid phase axial mixing in a bubble column with viscous non-Newtonian liquids. *Canadian Journal of Chemical Engineering*, 63 (2), 195-201.
- Dewes, I., Kueksal, A., Schumpe, A., 1995. Gas density effect on mass transfer in three-phase sparged reactors. *Chemical Engineering Research and Design*, 73 (A6), 697-700.
- Dudukovic, M. P., Larachi, F., Mills, P. L., 1999. Multiphase reactors - revisited. *Chemical Engineering Science*, 54 (13-14), 1975-1995.

- Dudukovic, M. P., 2000. Opaque multiphase reactors: experimentation, modeling and troubleshooting. *Oil & Gas Science and Technology*, 55 (2), 135-158.
- Ellenberger, J., Krishna, R., 2002. Improving mass transfer in gas-liquid dispersions by vibration excitement. *Chemical Engineering Science*, 57 (22-23), 4809-4815.
- Fair, J. R., 1967. Designing gas-sparged reactors. *Chemical Engineering with Chemical and Metallurgical Engineering*, 74 (14), 67-74.
- Fair, J. R., 1967. Designing gas-sparged reactors. II. *Chemical Engineering with Chemical and Metallurgical Engineering*, 74 (5), 207-212.
- Fan, X., Parker, D. J., Smith, M. D., 2006. Labelling a single particle for positron emission particle tracking using direct activation and ion-exchange techniques. *Nuclear Instruments & Methods in Physics Research, Section A: Accelerators, Spectrometers, Detectors, and Associated Equipment*, 562 (1), 345-350.
- Farkas, E. J., Leblond, P. F., 1969. Solids concentration profile in the bubble column slurry reactor. *Canadian Journal of Chemical Engineering*, 47 (2), 215-217.
- Field, R. W., Davidson, J. F., 1980. Axial dispersion in bubble columns. *Transactions of the Institution of Chemical Engineers*, 58 (4), 228-236.
- Forret, A., Schweitzer, J-M., Gauthier, T., Krishna, R., Schweich, D., 2003. Influence of scale on the hydrodynamics of bubble column reactors: an experimental study in columns of 0.1, 0.4 and 1 m diameters. *Chemical Engineering Science*, 58 (3-6), 719-724.
- Gehrke, S., Wirth, K.-E., 2005. Application of conventional- and dual-energy X-ray tomography in process engineering. *IEEE Sensors Journal*, 5 (2), 183-187.
- George, D. L., Shollenberger, K. A., Torczynski, J. R., 2000. Sparger effects on gas volume fraction distributions in vertical bubble-column flows as measured by gamma-densitometry tomography. *FED (American Society of Mechanical Engineers)*, 251 1487-1494.
- George, D. L., Shollenberger, K. A., Torczynski, J. R., O'Hern, T. J., Ceccio, S. L., 2001. Three-phase material distribution measurements in a vertical flow using gamma-densitometry tomography and electrical-impedance tomography. *International Journal of Multiphase Flow*, 27 (11), 1903-1930.
- Godbole, S. P., Schumpe, A., Shah, Y. T., 1983. Hydrodynamics and mass transfer in bubble columns: effect of solids. *Chemical Engineering Communications*, 24 (4-6), 235-258.

- Godfroy, L., Larachi, F., Kennedy, G., Grandjean, B., Chaouki, J., 1997. Online flow visualization in multiphase reactors using neural networks. *Applied Radiation and Isotopes*, 48 (2), 225-235.
- Grund, G., Schumpe, A., Deckwer, W. D., 1992. Gas-liquid mass transfer in a bubble column with organic liquids. *Chemical Engineering Science*, 47 (13-14), 3509-3516.
- Gupta, P., Al-Dahhan, M. H., Dudukovic, M. P., Toseland, B. A., 2001. Comparison of single- and two-bubble class gas-liquid recirculation models - application to pilot-plant radioactive tracer studies during methanol synthesis. *Chemical Engineering Science*, 56 (3), 1117-1125.
- Gupta, P., Ong, B., Al-Dahhan, M. H., Dudukovic, M. P., Toseland, B. A., 2001. Hydrodynamics of churn turbulent bubble columns: gas-liquid recirculation and mechanistic modeling. *Catalysis Today*, 63 (3-4), 253-269.
- Gupta, P., 2002. Churn-turbulent bubble columns - experiments and modeling. D. Sc. Thesis. Department of Chemical Engineering, Washington University, St. Louis, MO, USA.
- Han, H., Fang, D., Zhu, B., 2003. Study of volumetric liquid-phase mass transfer coefficient in high solid-holdup three-phase bubble column slurry reactor and the comparison of its using two types of gas distributor. *Gaoxiao Huaxue Gongcheng Xuebao*, 17 (4), 383-388.
- Han, L., Al-Dahhan, M.H., 2007. Gas-liquid mass transfer in a high pressure bubble column reactor with different sparger designs. *Chemical Engineering Science*, 62 (1-2), 131-139.
- Hebrard, G., Bastoul, D., Roustan, M., 1996. Influence of the gas sparger on the hydrodynamic behavior of bubble columns. *Chemical Engineering Research and Design*, 74 (A3), 406-414.
- Hedrick, S. A., Chuang, S. S. C., 2003. Modeling the Fischer-Tropsch reaction in a slurry bubble column reactor. *Chemical Engineering Communications*, 190 (4), 445-474.
- Herbolzheimer, E., Iglesia, E., 1994. Slurry bubble column. U.S. Patent 5348982.,
- Hervieu, E., Jouet, E., Desbat, L., 2002. Development and validation of an X-ray tomograph for two-phase flow. *Annals of the New York Academy of Sciences*, 972 87-94.

- Hidaka, N., Mizuguchi, K., Matsumoto, T., 1998. Axial mixing of liquid in counter-current bubble columns. *Journal of Chemical Engineering of Japan*, 31 (6), 1016-1019.
- Higbie, R., 1935. The rate of absorption of a pure gas into a still liquid during short periods of exposure. *Transactions of American Institute of Chemical Engineers*, 31 365-389.
- Hikita, H., Kikukawa, H., 1974. Liquid-phase mixing in bubble columns. Effect of liquid properties. *Chemical Engineering Journal (Amsterdam, Netherlands)*, 8 (3), 191-197.
- Hikita, H., Asai, S., Tanigawa, K., Segawa, K., Kitao, M., 1981. The volumetric liquid-phase mass transfer coefficient in bubble columns. *Chemical Engineering Journal (Amsterdam, Netherlands)*, 22 (1), 61-69.
- Hu, T., Yu, B., Wang, Y., 1986. Holdups and models of three phase fluidized bed. *Fluidization* 5, 353-360.
- Hubers, J. L., Striegel, A. C., Heindel, T. J., Gray, J. N., Jensen, T. C., 2005. X-ray computed tomography in large bubble columns. *Chemical Engineering Science*, 60 (22), 6124-6133.
- Hurst, E. H., 1956. Methods of Using Long-Term Storage in Reservoirs. *Proceedings of the Institute of Civil Engineers*, 5 519-525.
- Imafuku, K., Wang, T. Y., Koide, K., Kubota, H., 1968. Behavior of suspended solid particles the bubble column. *Journal of Chemical Engineering of Japan*, 1 (2), 153-158.
- Inga, J. R., Morsi, B. I., 1998. Hydrodynamic and mass transfer characteristics in a large-scale slurry bubble column reactor. *Proceedings - Annual International Pittsburgh Coal Conference*, 15th 124-137.
- Jackson, N. B., Torczynski, J. R., Shollenberger, K. A., O'Hern, T. J., Adkins, D. R., 1996. Hydrodynamic characterization of slurry bubble-column reactors for Fischer-Tropsch synthesis. *Proceedings - Annual International Pittsburgh Coal Conference*, 13 (2), 1226-1231.
- Jamialahmadi, M., Branch, C., Mueller-Steinhagen, H., 1994. Terminal bubble rise velocity in liquids. *Chemical Engineering Research and Design*, 72 (A1), 119-122.
- Jean, R.-H., Tang, W.-T., Fan, L.-S., 1989. The sedimentation-dispersion model for slurry bubble columns. *AIChE Journal*, 35 (4), 662-665.
- Jordan, U., Schumpe, A., 2001. The gas density effect on mass transfer in bubble columns with organic liquids. *Chemical Engineering Science*, 56 (21-22), 6267-6272.

- Jordan, U., Terasaka, K., Kundu, G., Schumpe, A., 2002. Mass transfer in high-pressure bubble columns with organic liquids. *Chemical Engineering & Technology*, 25 (3), 262-265.
- Joseph, S., Shah, Y. T., Kelkar, B. G., 1984. A simple experimental technique to measure gas phase dispersion in bubble columns. *Chemical Engineering Communications*, 28 (4-6), 223-230.
- Joshi, J. B., 1980. Axial mixing in multiphase contactors - a unified correlation. *Transactions of the Institution of Chemical Engineers*, 58 (3), 155-165.
- Joshi, J. B., 1982. Gas phase dispersion in bubble columns. *Chemical Engineering Journal (Amsterdam, Netherlands)*, 24 (2), 213-216.
- Kago, T., Sasaki, Y., Kondo, T., Morooka, S., Kato, Y., 1989. Gas holdup and axial dispersion of gas and liquid in bubble columns of homogeneous bubble flow regime. *Chemical Engineering Communications*, 75 23-38.
- Kai, T., Misawa, M., Takahashi, T., Tiseanu, I., Ichikawa, N., 2005. Observation of 3-D structure of bubbles in a fluidized catalyst bed. *Canadian Journal of Chemical Engineering*, 83 (1), 113-118.
- Kang, Y., Fan, L. T., Min, B. T., Kim, S. D., 1991. Promotion of oxygen transfer in three-phase fluidized-bed bioreactors by floating bubble breakers. *Biotechnology and Bioengineering*, 37 (6), 580-586.
- Kang, Y., Cho, Y. J., Woo, K. J., Kim, S. D., 1999. Diagnosis of bubble distribution and mass transfer in pressurized bubble columns with viscous liquid medium. *Chemical Engineering Science*, 54 (21), 4887-4893.
- Kantak, M. V., Hesketh, R. P., Kelkar, B. G., 1995. Effect of gas and liquid properties on gas phase dispersion in bubble columns. *Chemical Engineering Journal (Lausanne)*, 59 (2), 91-100.
- Kastanek, F., 1977. The volume mass transfer coefficient in a bubble bed column. *Collection of Czechoslovak Chemical Communications*, 42 (8), 2491-2497.
- Kastanek, F., Zahradnik, J., Kratochvil, J., Cermak, J., 1993. *Chemical reactors for gas-liquid systems*. New York, Ellis Horwood.
- Katnas, S., Tosyali, C., Uysal, B. Z., 1994. Liquid phase mass transfer coefficients and interfacial area in a bubble column. *Turkish Journal of Engineering & Environmental Sciences*, 18 (3), 249-256.

- Kato, Y., Nishiwaki, Akio, Fukuda, Takashi, Tanaka, Shigenobu., 1972. Behavior of suspended solid particles and liquid in bubble columns. *Journal of Chemical Engineering of Japan*, 5 (2), 112-118.
- Kawase, Y., Moo-Young, M., 1986. Liquid phase mixing in bubble columns with Newtonian and non-Newtonian fluids. *Chemical Engineering Science*, 41 (8), 1969-1977.
- Kawase, Y., Halard, B., Moo-Young, M., 1987. Theoretical prediction of volumetric mass transfer coefficients in bubble columns for Newtonian and non-Newtonian fluids. *Chemical Engineering Science*, 42 (7), 1609-1617.
- Kelkar, B. G., Godbole, S. P., Honath, M. F., Shah, Y. T., Carr, N. L., Deckwer, W. D., 1983. Effect of addition of alcohols on gas holdup and backmixing in bubble columns. *AIChE Journal*, 29 (3), 361-369.
- Kelkar, B. G., Shah, Y. T., 1985. Gas holdup and backmixing in bubble column with polymer solutions. *AIChE Journal*, 31 (4), 700-702.
- Khang, S., Kothari, S. P., 1980. Experimental determination of axial dispersion coefficient in a bubble column. *Chemical Engineering Science*, 35 2203-2205.
- Kiared, K., Larachi, F., Cassanello, M., Chaouki, J., 1997. Flow Structure of the Solids in a Three-Dimensional Liquid Fluidized Bed. *Industrial & Engineering Chemistry Research*, 36 (11), 4695-4704.
- Kiared, K., Larachi, F., Guy, C., Chaouki, J., 1997. Trajectory length and residence-time distributions of the solids in three-phase fluidized beds. *Chemical Engineering Science*, 52 (21/22), 3931-3939.
- Kiared, K., Larachi, F., Chaouki, J., Guy, C., 1999. Mean and turbulent particle velocity in the fully developed region of a three-phase fluidized bed. *Chemical Engineering & Technology*, 22 (8), 683-689.
- Kim, J. O., Kim, S. D., 1990. Gas-liquid mass transfer in a three-phase fluidized bed with floating bubble breakers. *Canadian Journal of Chemical Engineering*, 68 (3), 368-375.
- Knesebeck, A., Guardani, R., 2004. Estimation of particle concentration profiles in a three-phase fluidized bed from experimental data and using the wake model. *Brazilian Journal of Chemical Engineering*, 21 (1), 47-57.
- Krishna, R., De Swart, J. W. A., Ellenberger, J., Martina, G. B., Maretto, C., 1997. Gas holdup in slurry bubble columns: effect of column diameter and slurry concentrations. *AIChE Journal*, 43 (2), 311-316.

- Krishna, R., Urseanu, M. I., Van Baten, J. M., Ellenberger, J., 1999. Influence of scale on the hydrodynamics of bubble columns operating in the churn-turbulent regime: experiments vs. Eulerian simulations. *Chemical Engineering Science*, 54 (21), 4903-4911.
- Krishna, R., Sie, S. T., 2000. Design and scale-up of the Fischer-Tropsch bubble column slurry reactor. *Fuel Processing Technology*, 64 (1-3), 73-105.
- Krishna, R., Urseanu, M. I., van Baten, J. M., Ellenberger, J., 2000. Liquid phase dispersion in bubble columns operating in the churn-turbulent flow regime. *Chemical Engineering Journal (Lausanne)*, 78 (1), 43-51.
- Krishna, R., van Baten, J. M., 2003. A Strategy for Scaling Up the Fischer-Tropsch Bubble Column Slurry Reactor. *Topics in Catalysis*, 26 (1-4), 21-28.
- Kulkarni, A., Shah, Y. T., 1984. Gas phase dispersion in a downflow bubble column. *Chemical Engineering Communications*, 28 (4-6), 311-326.
- Kumar, S. B., 1994. Computed tomographic measurements of void fraction and modeling of the flow in bubble columns. Ph.D. Thesis. Florida Atlantic University, Boca Raton.
- Kumar, S. B., Dudukovic, M. P., Toseland, B. A., 1997. Measurement techniques for local and global fluid dynamic quantities in two and three phase systems. *Non-Invasive Monitoring of Multiphase Flows*, 1-45.
- Kunii, D., Levenspiel, O., 1968. Bubbling bed model. Model for the flow of gas through a fluidized bed. *Industrial & Engineering Chemistry Fundamentals*, 7 (3), 446-452.
- Larachi, F., Kennedy, G., Chaouki, J., 1994. A g-ray detection system for 3-D particle tracking in multiphase reactors. *Nuclear Instruments & Methods in Physics Research, Section A: Accelerators, Spectrometers, Detectors, and Associated Equipment*, 338 (2-3), 568-576.
- Larachi, F., Chaouki, J., Kennedy, G., 1995. 3-D Mapping of solids flow field in multiphase reactors with RPT. *AIChE Journal*, 41 (2), 439-443.
- Lau, R., Peng, W., Velazquez-Vargas, L. G., Yang, G. Q., Fan, L.-S., 2004. Gas-Liquid Mass Transfer in High-Pressure Bubble Columns. *Industrial & Engineering Chemistry Research*, 43 (5), 1302-1311.

- Lee, D. H., Kim, J. O., Kim, S. D., 1993. Mass transfer and phase holdup characteristics in three-phase fluidized beds. *Chemical Engineering Communications*, 119 179-196.
- Lee, S. L. P., De Lasa, H. I., 1987. Phase holdups in three-phase fluidized beds. *AIChE Journal*, 33 (8), 1359-1370.
- Lehrer, I. H., 1976. A rational terminal velocity equation for bubbles and drops at intermediate and high Reynolds numbers. *Journal of Chemical Engineering of Japan*, 9 (3), 237-240.
- Leib, T. M., Mills, P. L., Lerou, J. J., Turner, J. R. , 1995. Evaluation of neural networks for simulation of three-phase bubble column reactors. *Chemical Engineering Research and Design*, 73 (A6), 690-696.
- Lemoine, R., Behkish, A., Morsi, B. I., 2004. Hydrodynamic and Mass-Transfer Characteristics in Organic Liquid Mixtures in a Large-Scale Bubble Column Reactor for the Toluene Oxidation Process. *Industrial & Engineering Chemistry Research*, 43 (19), 6195-6212.
- Letzel, H. M., Schouten, J. C., Krishna, R., Van den Bleek, C. M., 1999. Gas holdup and mass transfer in bubble column reactors operated at elevated pressure. *Chemical Engineering Science*, 54 (13-14), 2237-2246.
- Levenspiel, O., 1972. *Chemical reaction engineering*. New York, Wiley Eastern Press.
- Levenspiel, O., Fitzgerald, T. J., 1983. A warning on the misuse of the dispersion model. *Chemical Engineering Science*, 38 (3), 489-491.
- Lewis, W. K., Whitman, W. G., 1924. Principles of gas absorption. *Journal of Industrial and Engineering Chemistry (Washington, D. C.)*, 16 1215-1220.
- Lide, D. R., 2001. *CRC Handbook of Chemistry and Physics*, 82nd Edition. Boca Raton, CRC Press.
- Limtrakul, S., 1996. Hydrodynamics of liquid fluidized beds and gas-liquid fluidized beds. D.Sc. thesis. Department of chemical engineering, Washington University, St. Louis.
- Lin, T.-J., Tsuchiya, K., Fan, L.-S., 1998. Bubble flow characteristics in bubble columns at elevated pressure and temperature. *AIChE Journal*, 44 (3), 545-560.
- Linek, V., Sinkule, J., Benes, P., 1991. Critical assessment of gassing-in methods for measuring k_{La} in fermentors. *Biotechnology and Bioengineering*, 38 (4), 323-330.

- Liu, Z., Zheng, Y., 2004. A local model for gas-liquid mass transfer in a gas-liquid-solid circulating fluidized bed. *International Journal of Chemical Reactor Engineering*, 2 Article A13.
- Luo, H., Svendsen, H. F., 1991. Turbulent circulation in bubble columns from eddy viscosity distributions of single-phase pipe flow. *Canadian Journal of Chemical Engineering*, 69 (6), 1389-1394.
- Luo, H.-P., 2005. Analyzing and Modeling of Airlift Photobioreactors for Microalgal and Cyanobacteria Cultures. D.Sc. Department of chemical engineering, Washington University, St. Louis.
- Luo, X., Zhang, J., Tsuchiya, K., Fan, L.-S., 1997. On the rise velocity of bubbles in liquid-solid suspensions at elevated pressure and temperature. *Chemical Engineering Science*, 52 (21-22), 3693-3699.
- Luo, X., Lee, D. J., Lau, R., Yang, G., Fan, L.-S., 1999. Maximum stable bubble size and gas holdup in high-pressure slurry bubble columns. *AIChE Journal*, 45 (4), 655-680.
- Mandelbrot, B. B., Wallis, J.R., 1969. Robustness of the rescaled range R/S in the measurement of noncyclic long run statistical dependence. *Water Resources Research*, 5 967-968.
- Mangartz, K. H., Pilhofer, T., 1981. Interpretation of mass transfer measurements in bubble columns considering dispersion of both phases. *Chemical Engineering Science*, 36 (6), 1069-1077.
- Matsumoto, T., Hidaka, N., Morooka, S., 1989. Axial distribution of solid holdup in bubble column for gas-liquid-solid systems. *AIChE Journal*, 35 (10), 1701-1709.
- Matsumoto, T., Hidaka, N., Gushi, H., Morooka, S., 1992. Axial segregation of multicomponent solid particles suspended in bubble columns. *Industrial & Engineering Chemistry Research*, 31 (6), 1562-1568.
- Mendelson, H. D., 1967. The prediction of bubble terminal velocities from wave theory. *AIChE Journal*, 13 (2), 250-253.
- Men'shchikov, V. A., Aerov, M. E., 1967. Axial mixing of the gas in gas-liquid reactors. *Teoreticheskie Osnovy Khimicheskoi Tekhnologii*, 1 (6), 891-895.
- Miller, D. N., 1974. Scale-up of agitated vessels gas-liquid mass transfer. *AIChE Journal*, 20 (3), 445-453.

- Miller, S. A., Ekstrom, A., Foster, N. R., 1990. Solubility and mass-transfer coefficients for hydrogen and carbon monoxide in n-octacosane. *Journal of Chemical and Engineering Data*, 35 (2), 125-127.
- Mills, P. L., Dudukovic, M. P., 1989. Convolution and deconvolution of nonideal tracer response data with application to three-phase packed beds. *Computers & Chemical Engineering*, 13 (8), 881-898.
- Mills, P. L., Turner, J. R., Ramachandran, P. A., Dudukovic, M. P., 1996. The Fischer-Tropsch synthesis in slurry bubble column reactors: analysis of reactor performance using the axial dispersion model. *Topics in Chemical Engineering*, 8 339-386, 679-739.
- Mitra-Majumdar, D., Farouk, B., Shah, Y. T., Macken, N., Oh, Y. K. , 1998. Two- and Three-Phase Flows in Bubble Columns: Numerical Predictions and Measurements. *Industrial & Engineering Chemistry Research*, 37 (6), 2284-2292.
- Miyahara, T., Lee, M.-S., Takahashi, T., 1993. Mass transfer characteristics of a three-phase fluidized bed containing low-density and/or small particles. *International Chemical Engineering*, 33 (4), 680-686.
- Miyauchi, T., Furusaki, S., Morooka, S., Ikeda, Y., 1981. Transport phenomena and reaction in fluidized catalyst beds. *Advances in Chemical Engineering*, 11 275-448.
- Moslemian, D., Devanathan, N., Dudukovic, M. P., 1990. Liquid circulation in bubble columns via the CARPT facility. Effects of gas superficial velocity and column diameter. *HTD (American Society of Mechanical Engineers)*, 155 441-451.
- Moslemian, D., Devanathan, N., Dudukovic, M. P., 1992. Radioactive particle tracking technique for investigation of phase recirculation and turbulence in multiphase systems. *Review of Scientific Instruments*, 63 (10), 4361-4372.
- Moustiri, S., Hebrard, G., Thakre, S. S., Roustan, M., 2001. A unified correlation for predicting liquid axial dispersion coefficient in bubble columns. *Chemical Engineering Science*, 56 (3), 1041-1047.
- Myers, K. J., 1986. Liquid-phase mixing in churn-turbulent bubble columns. D.Sc. Department of chemical engineering, Washington University, St. Louis, Missouri.
- Myers, K. J., Dudukovic, M. P., Ramachandran, P. A., 1987. Modelling churn-turbulent bubble columns - I. Liquid-phase mixing. *Chemical Engineering Science*, 42 (10), 2301-2311.

- Nakanoh, M., Yoshida, F., 1980. Gas absorption by Newtonian and non-Newtonian liquids in a bubble column. *Industrial & Engineering Chemistry Process Design and Development*, 19 (1), 190-195.
- Nakao, K., Takeuchi, H., Kataoka, H., Kaji, H., Otake, T., Miyauchi, T., 1983. Mass transfer characteristics of bubble columns in recirculation flow regime. *Industrial & Engineering Chemistry Process Design and Development*, 22 (4), 577-582.
- Nakao, K., Bao, J., Harada, T., Yasuda, Y., Furumoto, K., 2000. Measurement and prediction of axial distribution of immobilized glucose oxidase gel beads suspended in bubble column. *Journal of Chemical Engineering of Japan*, 33 (5), 721-729.
- Nassos, G. P., Bankoff, S.G., 1967. Slip velocity ratios in an air-water system under steady-state and transient conditions. *Chemical Engineering Science*, 22 (4), 661-668.
- Nedeltchev, S., 2002. Penetration theory prediction of volumetric liquid-phase mass transfer coefficients in a high-pressure bubble column with water and organic liquids. *Bulgarian Chemistry and Industry*, 73 (3-4), 61-67.
- Nedeltchev, S., Ookawara, S., Ogawa, K., 2005. The effect of superficial gas velocity and aerated liquid height on the spatial distribution of local liquid-phase axial dispersion coefficients in a bubble column. *Journal of Chemical Engineering of Japan*, 38 (1), 1-11.
- Nedeltchev, S., Jordan, U., Schumpe, A., 2006. Correction of the penetration theory applied to the prediction of $k_L a$ in a bubble column with organic liquids. *Chemical Engineering & Technology*, 29 (9), 1113-1117.
- Nguyen-Tien, K., Patwari, A. N., Schumpe, A., Deckwer, W. D., 1985. Gas-liquid mass transfer in fluidized particle beds. *AIChE Journal*, 31 (2), 194-201.
- O'Dowd, W., Smith, D. N., Ruether, J. A., Saxena, S. C., 1987. Gas and solids behavior in a baffled and unbaffled slurry bubble column. *AIChE Journal*, 33 (12), 1959-1970.
- Ohki, Y., Inoue, H., 1970. Longitudinal mixing of the liquid phase in bubble columns. *Chemical Engineering Science*, 25 (1), 1-16.
- Ohnuki, A., Akimoto, H., 2001. Model development for bubble turbulent diffusion and bubble diameter in large vertical pipes. *Journal of Nuclear Science and Technology*, 38 (12), 1074-1080.
- Ong, B., 2003. Experimental investigation of bubble column hydrodynamics - effect of elevated pressure and superficial gas velocity. D. Sc. Thesis. Department of Chemical Engineering, Washington University, St. Louis, MO, USA.

- Ozturk, S. S., Schumpe, A., Deckwer, W. D., 1987. Organic liquids in a bubble column: holdups and mass transfer coefficients. *AIChE Journal*, 33 (9), 1473-1480.
- Parkinson, G., 1997. Fischer-Tropsch comes back. *Chemical Engineering & Technology*, 104 (4), 39-41.
- Patwari, A. N., Nguyen-Tien, K., Schumpe, A., Deckwer, W. D., 1986. Three-phase fluidized beds with viscous liquid: hydrodynamics and mass transfer. *Chemical Engineering Communications*, 40 (1-6), 49-65.
- Pilhofer, T., Bach, H. F., Mangartz, K. H., 1978. Determination of fluid dynamic parameters in bubble column design. *ACS Symposium Series*, 65 372-383.
- Rados, N., Al-Dahhan, M. H., Dudukovic, M. P., 2003. Modeling of the Fischer-Tropsch synthesis in slurry bubble column reactors. *Catalysis Today*, 79-80 211-218.
- Rados, N., 2003. Slurry bubble column hydrodynamics. D. Sc. Thesis. Department of Chemical Engineering, Washington University, St. Louis, MO, USA.
- Rados, N., Shaikh, A., Al-Dahhan, M., 2005a. Phase distribution in a high pressure slurry bubble column via a single source computed tomography. *Canadian Journal of Chemical Engineering*, 83 (1), 104-112.
- Rados, N., Shaikh, A., Al-Dahhan, M. H., 2005b. Solids flow mapping in a high pressure slurry bubble column. *Chemical Engineering Science*, 60 (22), 6067-6072.
- Reid, R. C., Prausnitz, J. M., Poling, B. E., 1987. *The Properties of Gases and Liquids*. Boston, McGraw-Hill.
- Reilly, I. G., Scott, D. S., De Bruijn, T. J. W., MacIntyre, D., Piskorz, J., 1990. Axial solids concentrations in three-phase bubble columns. *Chemical Engineering Science*, 45 (8), 2293-2299.
- Reith, T., Renken, S., Israel, B. A., 1968. Gas hold-up and axial mixing in the fluid phase of bubble columns. *Chemical Engineering Science*, 23 (6), 619-629.
- Rice, R. G., Littlefield, M. A., 1987. Dispersion coefficients for ideal bubbly flow in truly vertical bubble columns. *Chemical Engineering Science*, 42 (8), 2045-2053.
- Roy, S., Kemoun, A., Al-Dahhan, M. H., Dudukovic, M. P., 2005. Experimental investigation of the hydrodynamics in a liquid-solid riser. *AIChE Journal*, 51 (3), 802-835.

- Rustemeyer, U., Pauli, J., Menzel, Th., Buchholz, R., Onken, U., 1989. Liquid-phase mixing model for hydrodynamics of bubble columns. *Chemical Engineering and Processing*, 26 (2), 165-172.
- Ruthiya, K. C., Kuster, B.F.M., van der Schaaf, J., Schouten, J.C., 2006. Influence of particles and electrolyte on gas hold-up and mass transfer in a slurry bubble column. *International Journal of Chemical Reactor Engineering*, 4 Article A13.
- Salvacion, J. L., Ohta, A., Shimura, R., Ohtaguchi, K., Koide, K., 1996. Effects of alcohol and particle concentrations on longitudinal liquid dispersion coefficient in gel-particle-suspended bubble column. *Journal of Chemical Engineering of Japan*, 29 (5), 884-888.
- Sardeing, R., Painmanakul, P., Hebrard, G., 2006. Effect of surfactants on liquid-side mass transfer coefficients in gas-liquid systems: A first step to modeling. *Chemical Engineering Science*, 61 (19), 6249-6260.
- Schumpe, A., Saxena, A. K., Fang, L. K., 1987. Gas/liquid mass transfer in a slurry bubble column. *Chemical Engineering Science*, 42 (7), 1787-1796.
- Schumpe, A., Deckwer, W. D., Nigam, K. D. P., 1989. Gas-liquid mass transfer in three-phase fluidized beds with viscous pseudoplastic liquids. *Canadian Journal of Chemical Engineering*, 67 (5), 873-877.
- Sessieq, P., Mier, P., Gruy, F., Cournil, M., 1999. Solid particles concentration profiles in an agitated vessel. *Chemical Engineering Research and Design*, 77 (A8), 741-746.
- Shah, Y. T., Wisecarver, K., Borole, A., Salazar, A., Joshi, B., Guitian, J., 1995. Hydrodynamics, mixing and mass transfer in a large diameter jet bubble column. *Chemical Engineering Communications*, 136 95-117.
- Shaikh, A., Al-Dahhan, M., 2005. Characterization of the hydrodynamic flow regime in bubble columns via computed tomography. *Flow Measurement and Instrumentation*, 16 (2-3), 91-98.
- Shaikh, A., 2007. Bubble and slurry bubble column reactors for syngas to liquid fuel conversion: mixing, flow regime transition, and scale-up. D.Sc. Department of Energy, Environmental, and Chemical Engineering, Washington University, St. Louis, Missouri.
- Shawaqfeh, A. T., 2003. Gas holdup and liquid axial dispersion under slug flow conditions in gas-liquid bubble column. *Chemical Engineering and Processing*, 42 (10), 767-775.

- Shetty, S. A., Kantak, M. V., Kelkar, B. G., 1992. Gas-phase backmixing in bubble-column reactors. *AIChE Journal*, 38 (7), 1013-1026.
- Smith, D. N., Ruether, J. A., Stiegel, G. J., 1984. A modified sedimentation-dispersion model for solids behavior in coal liquefaction reactors. To be presented at the annual AIChE meeting, San Francisco, CA,
- Smith, D. N., Ruether, J. A., 1985. Dispersed solid dynamics in a slurry bubble column. *Chemical Engineering Science*, 40 (5), 741-754.
- Smith, D. N., Ruether, J. A., Shah, Y. T., Badgujar, M. N., 1986. Modified sedimentation-dispersion model for solids in a three-phase slurry column. *AIChE Journal*, 32 (3), 426-436.
- Song, H.-S., Ramkrishna, D., Trinh, S., Espinoza, R. L., Wright, H., 2003. Multiplicity and sensitivity analysis of Fischer-Tropsch bubble column slurry reactors: plug-flow gas and well-mixed slurry model. *Chemical Engineering Science*, 58 (12), 2759-2766.
- Soong, Y., Harke, F. W., Gamwo, I. K., Schehl, R. R., Zarochak, M. F., 1997. Hydrodynamic study in a slurry-bubble-column reactor. *Catalysis Today*, 35 (4), 427-434.
- Sotelo, J. L., Benitez, F.J., Beltran-Heredia, J., Rodriguez, C., 1994. Gas holdup and mass transfer coefficients in bubble columns. 1. Porous glass-plate diffusers. *International chemical engineering*, 34 (1), 82-90.
- Stern, D., Bell, A. T., Heinemann, H., 1983. Effects of mass transfer on the performance of slurry reactors used for Fischer-Tropsch synthesis. *Chemical Engineering Science*, 38 (4), 597-605.
- Stern, D., Bell, A. T., Heinemann, H., 1985. Experimental and theoretical studies of Fischer-Tropsch synthesis over ruthenium in a bubble-column reactor. *Chemical Engineering Science*, 40 (10), 1917-1924.
- Stern, D., Bell, A. T., Heinemann, H., 1985. A theoretical model for the performance of bubble-column reactors used for Fischer-Tropsch synthesis. *Chemical Engineering Science*, 40 (9), 1665-1677.
- Steynberg, A. P., 2004. Fischer-Tropsch technology. Amsterdam, Netherland, Elsevier.
- Syaiful, S., Wilhelm, A. M., Delmas, H., 1993. Bubble column and three phase fluidized beds: a comparison of axial dispersion and gas-liquid mass transfer by dynamic absorption. *Chemical Engineering and Processing*, 32 (3), 149-154.

- Terasaka, K., Hullmann, D., Schumpe, A., 1998. Mass transfer in bubble columns studied with an oxygen optode. *Chemical Engineering Science*, 53 (17), 3181-3184.
- Terasaka, K., Inoue, Y., Kakizaki, M., Niwa, M., 2004. Simultaneous measurement of 3-dimensional shape and behavior of single bubble in liquid using laser sensors. *Journal of Chemical Engineering of Japan*, 37 (8), 921-926.
- Therning, P., Rasmuson, A., 2001. Liquid dispersion and gas holdup in packed bubble columns at atmospheric pressure. *Chemical Engineering Journal (Lausanne)*, 81 (1-3), 69-81.
- Tinge, J. T., Drinkenburg, A. A. H., 1986. The influence of slight departures from vertical alignment on liquid dispersion and gas hold-up in a bubble column. *Chemical Engineering Science*, 41 (1), 165-169.
- Towell, G. D., Ackermann, G. H. (1972). Axial mixing of liquid and gas in large bubble reactors. *Proc. 5th European-2nd International Symposium on Chemical Reaction Engineering*, Amsterdam.
- Tung, H.-L., Chang, Y.-Y., Hwang, T.-K., Wu, W.-T., 1998. Liquid mixing and mass transfer in a modified bubble column with suspended particles. *Journal of the Chinese Institute of Chemical Engineers*, 29 (6), 467-472.
- Turner, J. R., Mills, P. L., 1990. Comparison of axial dispersion and mixing cell models for design and simulation of Fischer-Tropsch slurry bubble column reactors. *Chemical Engineering Science*, 45 (8), 2317-2324.
- Ueyama, K., Miyauchi, T., 1979. Properties of recirculating turbulent two phase flow in gas bubble columns. *AIChE Journal*, 25 (2), 258-266.
- Utomo, M. B., Warsito, W., Sakai, T., Uchida, S., 2001. Analysis of distributions of gas and TiO₂ particles in slurry bubble column using ultrasonic computed tomography. *Chemical Engineering Science*, 56 (21-22), 6073-6079.
- Van der Laan, G. P., Beenackers, A. A. C. M., Krishna, R., 1999. Multicomponent reaction engineering model for Fe-catalyzed Fischer-Tropsch synthesis in commercial scale slurry bubble column reactors. *Chemical Engineering Science*, 54 (21), 5013-5019.
- van Vuuren, D. S., Heydenrych, M. D., 1985. Multicomponent modeling of Fischer-Tropsch slurry reactors. *Chemical Engineering Research Group (CSIR) Report CENG 581*. Pretoria, South Africa.
- Vandu, C. O., Krishna, R., 2003. Gas holdup and volumetric mass transfer coefficient in a slurry bubble column. *Chemical Engineering & Technology*, 26 (7), 779-782.

Vandu, C. O., Krishna, R., 2004. Influence of scale on the volumetric mass transfer coefficients in bubble columns. *Chemical Engineering and Processing*, 43 (4), 575-579.

Vandu, C. O., Koop, K., Krishna, R., 2004. Volumetric mass transfer coefficient in a slurry bubble column operating in the heterogeneous flow regime. *Chemical Engineering Science*, 59 (22-23), 5417-5423.

Veera, U. P., Kataria, K. L., Joshi, J. B., 2004. Effect of superficial gas velocity on gas hold-up profiles in foaming liquids in bubble column reactors. *Chemical Engineering Journal (Amsterdam, Netherlands)*, 99 (1), 53-58.

Villiermaux, J., 1996. Trajectory length distribution (TLD), a novel concept to characterize mixing in flow systems. *Chemical Engineering Science*, 51 (10), 1939-1946.

Wachi, S., Nojima, Y., 1990. Gas-phase dispersion in bubble columns. *Chemical Engineering Science*, 45 (4), 901-905.

Walter, J. F., Blanch, H. W. , 1986. Bubble break-up in gas-liquid bioreactors: break-up in turbulent flows. *Chemical Engineering Journal (Amsterdam, Netherlands)*, 32 (1), B7-B17.

Wang, G., Wang, Y.-N., Yang, J., Xu, Y.-Y., Bai, L., Xiang, H.-W., Li, Y.-W., 2004. Modeling Analysis of the Fischer-Tropsch Synthesis in a Stirred-Tank Slurry Reactor. *Industrial & Engineering Chemistry Research*, 43 (10), 2330-2336.

Warsito, M. O., Maezawa, A., Uchida, S., 1997. Flow structure and phase distributions in a slurry bubble column. *Chemical Engineering Science*, 52 (21-22), 3941-3947.

Warsito, M. O., Kawata, N., Uchida, S., 1999. Cross-sectional distributions of gas and solid holdups in slurry bubble column investigated by ultrasonic computed tomography. *Chemical Engineering Science*, 54 (21), 4711-4728.

Warsito, W., Fan, L.-S., 2003. 3D-ECT velocimetry for flow structure quantification of gas-liquid-solid fluidized beds. *Canadian Journal of Chemical Engineering*, 81 (3-4), 875-884.

Warsito, W., Fan, L.-S., 2003. ECT imaging of three-phase fluidized bed based on three-phase capacitance model. *Chemical Engineering Science*, 58 (3-6), 823-832.

Warsito, W., Fan, L.-S., 2005. Dynamics of spiral bubble plume motion in the entrance region of bubble columns and three-phase fluidized beds using 3D ECT. *Chemical Engineering Science*, 60 (22), 6073-6084.

Wilcock, R. J., Battino, R., Danforth, W.F., Wilhelm, E., 1978. Solubilities of gases in liquids. II. The solubilities of helium, neon, argon, krypton, oxygen, nitrogen, carbon monoxide, carbon dioxide, methane, tetrafluoromethane, and sulfur fluoride (SF₆) in n-octane 1-octanol, n-decane, and 1-decanol. *Journal of Chemical Thermodynamics*, 10 (9), 817-822.

Wilkinson, P. M., 1991. Physical aspects and scale-up of high pressure bubble columns. Ph.D. Thesis. University of Groningen, Rijksuniversiteit Groningen, the Netherlands.

Wilkinson, P. M., Haringa, Herman, Stokman, Frans P. A., Van Dierendonck, Laurent L., 1993. Liquid mixing in a bubble column under pressure. *Chemical Engineering Science*, 48 (10), 1785-1791.

Wu, Y., Ong, B.C., Al-Dahhan, M. H., 2001. Predictions of radial gas holdup profiles in bubble column reactors. *Chemical Engineering Science*, 56 (3), 1207-1210.

Xue, J., Al-Dahhan, M., Dudukovic, M. P., Mudde, R. F., 2003. Bubble dynamics measurements using four-point optical probe. *Canadian Journal of Chemical Engineering*, 81 (3-4), 375-381.

Xue, J., 2004. Bubble velocity, size and interfacial area measurements in bubble columns. D. Sc. Thesis. Department of Chemical Engineering, Washington University, St. Louis, MO, USA.

Yang, G. Q., Fan, L. S., 2003. Axial liquid mixing in high-pressure bubble columns. *AIChE Journal*, 49 (8), 1995-2008.

Yang, W., Wang, J., Jin, Y., 2001. Gas-liquid mass transfer in a slurry bubble column reactor under high temperature and high pressure. *Chinese Journal of Chemical Engineering*, 9 (3), 253-257.

Yang, W., Wang, J., Jin, Y., 2001. Mass transfer characteristics of syngas components in slurry system at industrial conditions. *Chemical Engineering & Technology*, 24 (6), 651-657.

Yang, Y. B., Devanathan, N., Dudukovic, M. P., 1992. Liquid backmixing in bubble columns. *Chemical Engineering Science*, 47 (9-11), 2859-2864.

Yang, Y. B., Devanathan, N., Dudukovic, M. P., 1993. Liquid backmixing in bubble columns via computer-automated radioactive particle tracking (CARPT). *Experiments in Fluids*, 16 (1), 1-9.

Yang, Z., Parker, D. J., Fryer, P. J., Bakalis, S., Fan, X., 2006. Multiple-particle tracking - an improvement for positron particle tracking. *Nuclear Instruments &*

Methods in Physics Research, Section A: Accelerators, Spectrometers, Detectors, and Associated Equipment, 564 (1), 332-338.

Zehner, P., 1982. Momentum, mass, and heat transfer in bubble columns. Flow model of bubble columns and liquid velocity. . Institution of Chemical Engineers Symposium Series, 26 (22-35), 347-351.

Zhang, J.-Y., 1976. Computation of free-terminal velocity of spherical particle. Chemical Engineering (China), 1 18-31.

Zhang, J.-Y., Lin, C., Lin, C.-S., 2002. Axial distribution of solids holdup for both hydrophilic and hydrophobic particles in three-phase fluidized beds. Canadian Journal of Chemical Engineering, 80 (1), 37-43.

Zhang, J.-Y., Lin, C., Lin, C.-S., 2002. A sedimentation-dispersion model for both non-attached and attached particles in three-phase batchwise fluidized beds. Chinese Journal of Chemical Engineering, 10 (2), 170-176.

Zheng, C., Chen, Z., Feng, Y., Hofmann, H., 1995. Mass transfer in different flow regimes of three-phase fluidized beds. Chemical Engineering Science, 50 (10), 1571-1578.

Vita

Name	Lu Han
Date of Birth	October 19, 1976
Place of Birth	Jilin, China
Degrees	B.E. in Chemical Engineering, July 1999 Tsinghua University, Beijing, China M.E. in Chemical Engineering, July 2002 Tsinghua University, Beijing, China D.Sc. in Chemical Engineering, May 2007 Washington University, St. Louis, MO
Professional Societies	American Institute of Chemical Engineers

Publications

Lu Han; Muthanna Al-Dahhan. Gas-Liquid Mass Transfer in a High Pressure Bubble Column Reactor with Different Sparger Designs. *Chemical Engineering Science*. (2007), 62(1-2), 131-139.

M.H. Al-Dahhan, P.L. Mills, P. Gupta, L. Han, M.P. Dudukovic, T.M. Leib, J.J. Lerou. Liquid-phase tracer responses in a cold-flow counter-current trayed bubble column from conductivity probe measurements. *Chemical Engineering and Processing*, (2006), 45(11), 945-953.

Han, Lu; Luo, Wuxi; Liang, Weihua; Wang, Guangrun; Wang, Jinfu. Method and effect of catalyst dispersion in direct synthesis of DDS. *Journal of Chemical Industry and Engineering (China)* (2003), 54(3), 398-402.

Han, Lu; Luo, Wuxi; Liang, Weihua; Wang, Guangrun; Wang, Jinfu. Effect of reaction temperature on synthesis of methylchlorosilane. *Chemical Reaction Engineering and Technology (China)* (2002), 18(2), 187-192.

Han, Lu, Wang Guang-run, Liang Wei-hua, Luo Wu-xi, Wang Jinfu. Experimental Study of Direct Synthesis Process of MethylChlorosilane in Fluidized Bed Reactor. *Gaoxiao Huaxue Gongcheng Xuebao* (2002), 16(3), 287-292.

Liang, Wei-Hua; Wang, Jin-Fu; Han, Lu; Wang, Guang-Run; Jin, Yong. Prediction of minimum fluidization velocity of silicon particle system with the pressure fluctuation method. *Guocheng Gongcheng Xuebao* (2002), 2(1), 1-6.

Proceedings and Presentations

Lu Han; Muthanna Al-Dahhan. A new methodology to measure the solids dispersion in high pressure slurry bubble column reactor. Oral presentation (294f). AIChE annual meeting 2006, San Francisco.

Lu Han; Muthanna Al-Dahhan. Measurement of the solids axial dispersion and distribution in a slurry bubble column reactor. The 5th international symposium on measurement techniques for multiphase flows. Macao, China, December 2006.

Lu Han; Muthanna Al-Dahhan. A new methodology to determine true tracer response in bubble and slurry bubble column radioactive particle tracking data. Poster presentation (214). 19th ISCRE. Potsdam/Berlin, German, September 2006.

Muthanna Al-Dahhan, Novica Rados, Ashfaq Shaikh, Lu Han. Hydrodynamic studies in slurry bubble columns via CARPT and CT. 11th Asian pacific confederation of chemical engineering. Malaysia, Aug 2006.

Lu Han; Muthanna Al-Dahhan. Axial dispersion of gas phase in slurry bubble column reactor. Oral presentation (83g). AIChE annual meeting 2005, Cincinnati.

Lu Han; Muthanna Al-Dahhan. Study of gas-liquid volumetric mass transfer in bubble column reactors using axial dispersion model. Oral presentation (413g). AIChE annual meeting 2005, Cincinnati.

Wuxi Luo, Lu Han, Guangrun Wang, Jinfu Wang. Studies on the gas-solid-solid catalytic reaction - Synthesis of chlorosilanes with cuprous chloride as catalyst. Poster Presentation (M50), 17th ISCRE. Hong Kong, August 2002.

Han, Lu; Luo, Wuxi; Wang, Guangrun; Wang, Jinfu. Direct synthesis of methyl chlorosilane. 11th national symposium on chemical engineering technology. Xiangtan, China, May, 2002.

Patent

Wang, Guangrun; Wang, Jinfu; Han, Lu; Luo, Wuxi; Jin, Yong. Process for direct synthesis of organosilicon monomer from Si and hydrocarbon halide. Chinese Patent No.01136583, July 2004. (as the primary research student)

May, 2007

Short Title: Slurry Bubble Column Hydrodynamics Han, D.Sc. 2007